

LIGHT-INDUCED FOLDING CONTROL OF FLUORESCENT AND CATALYTICALLY ACTIVE SINGLE-CHAIN NANOPARTICLES

Zur Erlangung des akademischen Grades eines
DOKTORS DER NATURWISSENSCHAFTEN
(Dr. rer. nat.)

von der KIT-Fakultät für Chemie und Biowissenschaften
des Karlsruher Instituts für Technologie (KIT)

genehmigte
Dissertation
von

M.Sc. Patrick Heinrich Maag

1. Referent:	Prof. Peter Roesky
2. Referent:	Prof. Christopher Barner-Kowollik
3. Referent:	Prof. Hans-Achim Wagenknecht
Tag der mündlichen Prüfung:	19.04.2024

ABSTRACT

In the herein presented thesis, the field of single-chain nanoparticles (SCNPs) was critically enhanced, addressing key challenges and focusing on advanced application fields. SCNPs are a versatile class of soft-shell nanoparticles formed by intramolecular cross-links of precursor polymers. Originally inspired by natural analogues, i.e. enzymes, SCNPs fuse simple polymeric approaches with complex functionalities, i.e. catalytically active metals, fluorescence and biocompatibility. The intramolecular crosslinks fold the polymer chains into compact structures, which is the most critical step within the synthetic procedure controlling the size and conformation of the particles. The work presented in the current thesis uses light induced folding and unfolding reactions allowing for the temporal change of the conformation of SCNPs. Additional fluorescent crosslinks enable an enhanced characterization of the SCNPs' folded state through a simple fluorescent read-out method.

The first results, Chapter 4, focuses on fluorescent and catalytically active SCNPs folded *via* a photoinduced cross-linking reaction. The precursor copolymer contains phosphine ligands for gold coordination and catalysis along with photoreactive cross-linking moieties. Mild visible light ($\lambda_{\text{max}} = 415 \text{ nm}$) initiates folding, resulting in more compact structure. The catalytic activity of the incorporated gold(I) complexes was demonstrated utilizing an intramolecular hydroamination as a benchmark reaction. The formation of fluorescent cross-links allows for a visual read-out of the successful folding.

In Chapter 5 we investigate light responsive and water-soluble SCNPs. Bimane cross-linked SCNPs *via* an esterification reaction with a water-soluble backbone allow for unfolding in aqueous solution under mild visible light, returning to the original precursor polymer. By integrating fluorescent cross-linking units, we extend the potential SCNPs towards biomedical application, paving the way for enhanced tracing and imaging applications.

Chapter 6 introduces a method to visualize SCNP folding employing Förster Resonance Energy Transfer (FRET), a distance dependent interaction between a donor and acceptor fluorophore. We incorporate bimane as the donor fluorophore and cross-linking unit, and NBD as the acceptor fluorophore, into a polymer backbone. This approach allows for direct optical read-out of the SCNP folding state, evidenced by a strong FRET signal. The FRET-based strategy extends the range of characterisation methods for SCNPs avoiding complex analytical equipment.

ZUSAMMENFASSUNG

In dieser Arbeit erweitern wir das Forschungsgebiet der Einzelketten-Nanopartikel (ENPs) erheblich und gehen auf zentrale Herausforderungen und neue Anwendungen ein. ENPs sind eine vielseitige Klasse von weichschaligen Nanopartikeln, die durch intramolekulare Vernetzung von Ausgangspolymeren entstehen. Inspiriert durch die Natur, z.B. Enzymen, vereinen ENPs einfache polymerbasierte Ansätze mit komplexen Funktionalitäten, wie katalytisch aktiven Metalle, Fluoreszenz und Biokompatibilität. Wir stellen eine lichtinitiierte Vernetzungsreaktion vor, die eine räumlich-zeitliche Kontrolle des Faltens ermöglicht und somit die Größe der Partikel kontrolliert. Darüber hinaus haben wir wasserlösliche ENPs entwickelt, die sich durch sichtbares Licht in eine lineare Polymerkette entfalten lassen.

Im Hauptteil dieser Arbeit befasst sich Kapitel 3 mit fluoreszierenden und katalytisch aktiven ENPs, die durch eine lichtinduzierte Vernetzungsreaktion gefaltet werden. Das Ausgangs-Copolymer enthält Phosphinliganden zur Goldkoordination und Katalyse sowie photoreaktive Vernetzungseinheiten. Mildes sichtbares Licht initiiert das Falten und führt zu einer kompakteren Struktur. Die katalytische Aktivität der eingebetteten Gold(I)-Komplexe wurde mit einer intramolekularen Hydroaminierung als Referenzreaktion demonstriert. Die Bildung von fluoreszierenden Knotenpunkten visualisiert die erfolgreiche Faltung.

In Kapitel 4 untersuchen wir den umgekehrten Entfaltungsprozess wasserlöslicher SCNPs. Mit Bimaneinheiten vernetzte SCNPs, die durch eine intramolekulare Veresterungsreaktion mit einem wasserlöslichen Copolymer entstehen, können sich in wässriger Lösung unter sichtbarem Licht zu ihrem ursprünglichen Ausgangspolymer entfalten. Der Einbau fluoreszierender Vernetzungseinheiten erweitert das Potenzial der ENPs hin zur biomedizinischen Anwendungen und eröffnet neue Möglichkeiten für verbesserte Nachverfolgung und Bildgebung.

Kapitel 5 stellt eine Methode zur Visualisierung des Faltens von ENPs mit Förster-Resonanzenergietransfer (FRET) vor, einer distanzabhängigen Wechselwirkung zwischen einem Donor- und einem Akzeptor-Fluorophor. Wir haben Bimane als Donor-Fluorophor und Vernetzungseinheit sowie NBD als Akzeptor-Fluorophor in ein Polymer-Rückgrat eingebaut. Dieser Ansatz ermöglicht eine direkte optische Auslesung des Faltungszustandes der ENPs, wie durch ein starkes FRET-Signal belegt. Diese Strategie erweitert das Spektrum der Charakterisierungsmethoden für ENPs und vermeidet den Einsatz komplexer analytischer Geräte.

PUBLISHED PAPERS INCLUDED IN THIS PHD RESEARCH PROGRAM

Chapter 4

P. H. Maag, F. Feist, H. Frisch, P. W. Roesky, C. Barner-Kowollik, Fluorescent and Catalytically Active Single Chain Nanoparticles, *Macromolecules* **2022**, 55, 9918-9924.

Chapter 5

P. H. Maag, F. Feist, V. X. Truong, H. Frisch, P. W. Roesky, C. Barner-Kowollik, Visible-Light Induced Control over Reversible Single-Chain Nanoparticle Folding, *Angew. Chem. Int. Ed.* **2023**, 62, e202309259.

Chapter 6

P. H. Maag, F. Feist, H. Frisch, P. W. Roesky, C. Barner-Kowollik, Förster Resonance Energy Transfer within Single Chain Nanoparticles, *Chem. Sci.* **2024**, 15, 5218-5224.

CONFERENCE CONTRIBUTIONS

Visible-Light-Induced Control over Folding and Unfolding of Fluorescent and Catalytically Active Single-Chain Nanoparticles

P. H. Maag, F. Feist, V. X. Truong, H. Frisch, P. W. Roesky, C. Barner-Kowollik, *38th Australasian Polymer Symposium*, February **2024**, Auckland, New Zealand. Oral presentation.

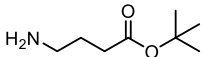
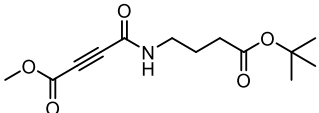
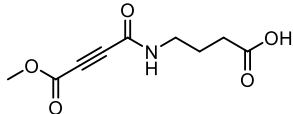
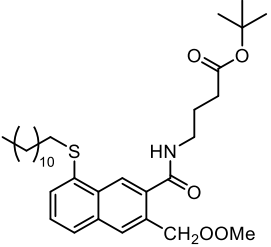
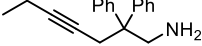
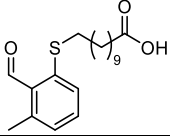
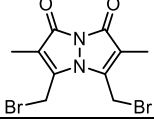
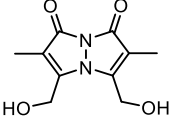
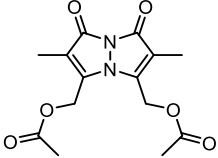
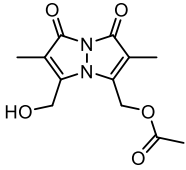
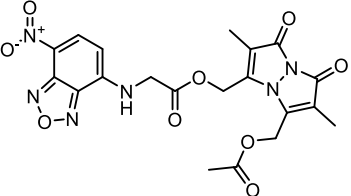
TABLE OF CONTENTS

Abstract	i
Zusammenfassung.....	ii
Published Papers Included in this PhD Research Program	iii
Conference Contributions	iii
Table of Contents	iv
Chemical Structures	vii
List of Abbreviations.....	x
Erklärung	xii
Acknowledgements.....	xiii
1 Introduction	1
2 Theoretical Background	3
2.1 Polymerization Techniques	3
2.1.1 Nitroxide-mediated polymerization (NMP).....	4
2.1.2 Reversible-addition-fragmentation chain-transfer (RAFT) polymerization	6
2.1.3 Copolymerization	10
2.2 Single-Chain Nanoparticles (SCNP).....	12
2.2.1 Synthetic strategies	12
2.2.2 Characterization of SCNPs	14
2.3 Photochemistry	17
2.3.1 Jablonski diagram	17
2.3.2 Beer-Lambert's law	19
2.3.3 [4+2] Cycloadditions	20
2.3.4 Bimane.....	22
2.3.5 Förster resonance energy transfer (FRET).....	22
2.4 Coordination Complexes	25
3 Motivation	27
4 Fluorescent and Catalytically Active Single-Chain Nanoparticles.....	29
4.1 Motivation	29
4.2 Results and Discussion.....	31
4.2.1 Photoinduced [4+2] cycloaddition	31
4.2.2 Synthesis of fluorescent and catalytically active SCNPs.....	33
4.2.3 SCNP-AuCl catalyzed intramolecular hydroamination	41
4.3 Summary.....	45
5 Visible Light Induced Control over Reversible Single-Chain Nanoparticle Folding	47
5.1 Motivation	47
5.2 Results and Discussion.....	49
5.2.1 Bimane photoinduced ester cleavage	50
5.2.2 Synthesis of water-soluble SCNPs	51
5.2.3 Photoinduced unfolding of SCNPs.....	55
5.2.4 Cross-linking density of SCNPs	57
5.2.5 Monte Carlo simulation of bond cleavage	61

5.2.6	Fluorescent SCNPs.....	64
5.2.7	Reusable SCNPs.....	66
5.3	Summary	67
6	Förster Resonance Energy Transfer within Single-Chain Nanoparticles	69
6.1	Motivation.....	69
6.2	Results and Discussion	71
6.2.1	Molecular FRET pair	71
6.2.2	FRET read-out of SCNP folding.....	76
6.3	Summary	81
7	Conclusions	83
8	Outlook.....	85
9	Experimental Section.....	89
9.1	Materials	89
9.2	Instrumentals	90
9.3	Synthesis of Molecular Structures	96
9.3.1	2,2,6,6-Tetramethyl-1-(1-phenylethoxy)piperidine.....	96
9.3.2	4-(Diphenylphosphino)styrene sulfide (S=PPh ₂ Sty).....	96
9.3.3	4-(Diphenylphosphino)styrene gold complex (ClAu-PPh ₂ Sty)	97
9.3.4	Tert-butyl 4-isocyanatobutanoate	97
9.3.5	Methyl 4-((4-(tert-butoxy)-4-oxobutyl)amino)-4-oxobut-2-ynoate (2)	98
9.3.6	4-(4-Methoxy-4-oxobut-2-ynamido)butanoic acid (3, A)	98
9.3.7	11-((2-Formyl-3-methylphenyl)thio)undecanoic acid (oMBA, B)	99
9.3.8	Catalyzed Intramolecular Hydroamination.....	99
9.3.9	2,6-dimethyl-1,7-dioxo-1H,7H-pyrazolo[1,2-a]pyrazole-3,5-diy]bis(methylene) diacetate, 8	102
9.3.10	Dihydroxybimane 7	103
9.3.11	tert-Butyl (7-nitrobenzo[c][1,2,5]oxadiazol-4-yl)glycinate (NBD-Gly-tert) ..	103
9.3.12	(7-Nitrobenzo[c][1,2,5]oxadiazol-4-yl)glycine (11)	104
9.3.13	(5-(Acetoxymethyl)-2,6-dimethyl-1,7-dioxo-1H,7H-pyrazolo[1,2-a]pyrazol-3-yl)methyl (7-nitrobenzo[c][1,2,5]oxadiazol-4-yl)glycinate (10)	104
9.3.14	N-(3-bromopropyl)-7-nitrobenzo[c][1,2,5] oxadiazol-4-amine (12)	105
9.4	Polymerizations.....	106
9.4.1	NMP copolymerization to form a poly(styrene-co-chloromethylstyrene-co-4-(diphenylphosphino sulfide)styrene) (P1).....	106
9.4.2	NMP copolymerization to form a poly(styrene-co-chloromethylstyrene-co-AuCl-PPh ₂ Sty) (P4).....	106
9.4.3	RAFT copolymerization to form poly(poly(ethylene glycol) methyl ether methacrylate-co-acrylic acid) (poly(MPEGMA-co-AA)).....	107
9.5	Polymer Post-Functionalization and Modification.....	108
9.5.1	Poly(styrene-co-bromomethylstyrene-co-4-(diphenylphosphino sulfide)styrene) (P2).....	108
9.5.2	Post-functionalization of P2 with the alkyne and oMBA (P3).....	108
9.5.3	Removing of remaining BMS groups with cesium acetate	109
9.5.4	Complexation of gold yielding in SCNP-AuCl	109
9.5.5	End group modification of poly(poly(ethylene glycol) methyl ether methacrylate-co-acrylic acid) (poly(MPEGMA-co-AA)) yielding P5	110
9.6	SCNPs Formation.....	111
9.6.1	Photoinduced Diels–Alder cycloaddition for the SCNP formation (SCNP1)	111

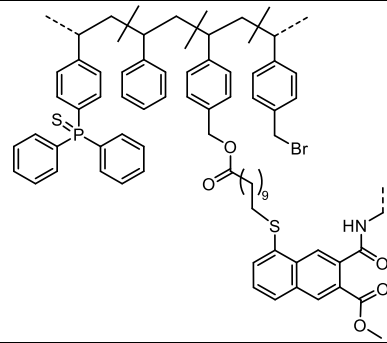
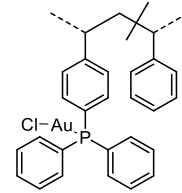
9.6.2	SCNPs formation by cross-linking with dibromobimane 6 (SCNP2).....	111
9.6.3	Post-functionalization and SCNPs formation (SCNP3)	112
9.6.4	Post-functionalization and SCNPs formation (SCNP4)	113
9.6.5	Post-functionalization and SCNPs formation (SCNP5)	113
9.7	Photoreactions	115
9.7.1	Photoreaction of <i>ortho</i> -methylbenzaldehyde thioether (<i>o</i> MBA) with tert-butyl protected 4-(4-methoxy-4-oxobut-2-ynamido)butanoic acid (alkyne).....	115
9.7.2	Unfolding of SCNP1 by radiation with visible light (P5')	115
9.7.3	Irradiation experiment of 10	116
9.7.4	Unfolding of SCNP4 by radiation with 415 nm.....	116
	Bibliography	117
	Lists of Figures, Schemes and Tables	127
	Appendices	141

CHEMICAL STRUCTURES

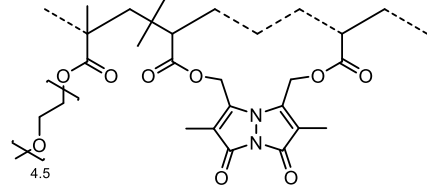
Number	Name, Synonym	Structure
Small molecules		
1	<i>tert</i> -butyl 4-aminobutanoate	
2	<i>tert</i> -butyl protected 4-(4-methoxy-4-oxobut-2-ynamido)butanoic acid	
3, A	4-(4-methoxy-4-oxobut-2-ynamido)butanoic acid	
4	<i>tert</i> -butyl 4-(8-(dodecylthio)-3-((methylperoxy)methyl)-2-naphthamido)butanoate	
5	2,2-diphenylhept-4-yn-1-amine	
oMBA, B	11-((2-formyl-3-methylphenyl)thio)undecanoic acid	
6	dibromobimane	
7	dihydroxybimane (3,5-bis(hydroxymethyl)-2,6-dimethyl-1H,7H-pyrazolo[1,2-a]pyrazole-1,7-dione)	
8	2,6-dimethyl-1,7-dioxo-1H,7H-pyrazolo[1,2-a]pyrazole-3,5-diyl)bis(methylene) diacetate	
9	monohydroxybimane ((5-(hydroxymethyl)-2,6-dimethyl-1,7-dioxo-1H,7H-pyrazolo[1,2-a]pyrazol-3-yl)methyl acetate)	
10	molecular FRET pair (5-(acetoxymethyl)-2,6-dimethyl-1,7-dioxo-1H,7H-pyrazolo[1,2-a]pyrazol-3-	

	yl)methyl (7-nitrobenzo[c][1,2,5]oxadiazol-4-yl)glycinate	
11	OH-NBD (7-nitrobenzo [c][1,2,5]oxadiazol-4-yl)glycine	
12	Br-NBD N-(3-bromopropyl)-7-nitrobenzo[c][1,2,5]oxadiazol-4-amine	
Polymers		
P1	poly(Sty-co-CMS-co-S=PPh ₂ Sty)	
P2	poly(Sty-co-BMS-co-S=PPh ₂ Sty)	
P3	poly(Sty-co-A/B-co-S=PPh ₂ Sty)	
P4	poly(Sty-co-CMS-co-AuCl-PPh ₂ Sty)	
P5, P5'	poly(MPEGMA-co-AA)	
P6 P7 P8	poly(MPEGMA-co-NBD)	

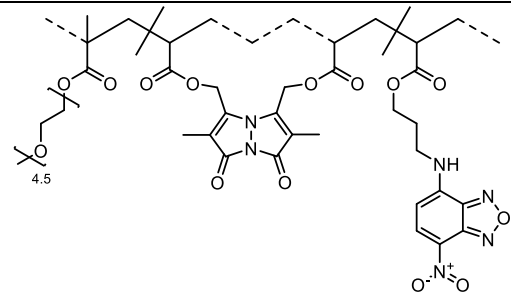
SCNPs

SCNP1SCNP(Sty-co-S=PPh₂Sty-cross-AB)**SCNP-AuCl**SCNP(Sty-co-AuCl-PPh₂Sty-cross-AB)**SCNP2**

SCNP(MPEGMA-cross-bimane)

**SCNP3**
SCNP4
SCNP5

SCNP(MPEGMA-co-NBD-cross-bimane)



LIST OF ABBREVIATIONS

Acronym	Name
AA	acrylic acid
ACN	acetonitrile
AIBN	2,2-azobisisobutyronitrile
AuCl(tht)	chloro(tetrahydrothiophene)gold(I)
BMS	bromomethylstyrene
CMS	chloromethylstyrene
<i>D</i>	diffusion coefficient
DCM	dichloromethane
DLS	dynamic light scattering
DMF	dimethylformamide
DMSO	dimethyl sulfoxide
DOSY	diffusion ordered spectroscopy
EDG	electron-donating group
EWG	electron withdrawing group
FRET	Förster resonance energy transfer
FRP	free radical polymerization
HAT	1,5-hydrogen atom transfer
Hz	hertz
IC	internal conversion
ISC	intersystem crossing
k_B	Boltzmann constant
LAMs	less activated monomers
LFRP	living free radical polymerization
MAMs	more activated monomers
M_n	molecular weight
NBD	nitrobenzoxadiazole
NMP	nitroxide-mediated radical polymerization
NMR	nuclear magnetic resonance
<i>o</i> MBA	orthomethylbenzaldehyde
<i>o</i> QDM	orthoquinodimethanes
PBu ₃	tributyl phosphine
PDI	polydispersity index
ppm	parts per million
RAFT	reversible addition-fragmentation chain transfer
RDRP	reversible-deactivation radical polymerizations
R_H	hydrodynamic radius
RID	refractive index detection
S_0	ground state
S_1	excited state

SCNPs	single-chain nanoparticles
<i>SD</i>	standard deviation
SEC	size exclusion chromatography
THF	tetrahydrofuran
TOF	turnover frequency
TON	turnover number
κ^2	orientation parameter

ERKLÄRUNG

Hiermit erkläre ich, die vorliegende Arbeit selbstständig angefertigt und keine anderen als die angegebenen Quellen und Hilfsmittel benutzt zu haben. Wörtlich oder inhaltlich übernommene Stellen habe ich als solche kenntlich gemacht. In Rahmen dieser Promotion wurden KI basierende online Tools zur Literatur Recherche, Schreiben von Code und zur Verbesserung der Lesbarkeit und Rechtschreibung von Texten verwendet. KI-generierte Texte z.B. Codes sind als solche gekennzeichnet. Rechtschreibung und Grammatik wurden mit *OpenAI (2024) ChatGPT 4* überprüft.

Die Regeln zur Sicherung der guten wissenschaftlichen Praxis des KIT in der jeweils gültigen Fassung wurden beachtet. Die elektronische Version dieser Arbeit stimmt mit der schriftlichen Version überein. Außerdem ist die Abgabe und Archivierung der Primärdaten gemäß Abs. A (6) der Regeln zur Sicherung guter wissenschaftlicher Praxis des KIT beim Institut gesichert.

Des Weiteren erkläre ich, dass ich mich derzeit in keinem laufenden Promotionsverfahren befinde und auch keine vorausgegangenen Promotionsversuche unternommen habe.

Brisbane, den 01.03.2024

Patrick Maag

ACKNOWLEDGEMENTS

I would like to start by acknowledging the Turrbal and Yugara, as the First Nations owners of the lands where QUT now stands and where a significant part of the experiments were performed. I recognize that these lands have always been places of teaching, research, and learning.

I would like to thank everyone who supported me during my PhD, both professionally and personally. Achieving this milestone would not have been possible without your help. It has been a great pleasure and honor to work within the macroarc and Roesky group. I would like to thank my entire supervisory team for the ongoing support, pleasant working atmosphere and productive meetings with innovative ideas that brought the projects forward.

I am grateful to Christopher Barner-Kowollik for guiding the joint PhD program between Australia and Germany. His discussions and passion for chemistry have been greatly motivating. Thank you for your support.

I am also very grateful to Peter Roesky for his support and time, particularly at the start of my PhD at KIT. Thank you for the joint PhD opportunity, the productive meetings, and your visit to Australia.

I want to thank Florian Feist for his support, especially during the early stages at INT. Your expertise was crucial for the success of this PhD. I am also thankful to Hendrik Frisch for his advice and insight, and the many corrections he did on drafts of all kinds.

Besides my supervisory team I want to thank Aaron Micallef for his help with NMR and DOSY measurements and I want to acknowledge QUT's Central Analytical Research Facility (CARF) supported by QUT's Research Portfolio. I acknowledge and I am grateful for the financial support from KIT and I thank QUT for a HDR Tuition Fee Scholarship.

I want to thank the macroarc team at both the QUT and KIT for the pleasant working atmosphere and support at any time. All our paper parties, end of the year parties and other social events are unforgettable memories. I also want to thank the inorganic group of Peter Roesky for their encouragement and help in Germany, and especially Conny for the whole organization at KIT and the planning of my stay in Australia.

Additionally, I want to thank all my friends for their mental support during my PhD and time abroad, for the memorable trips in Australia and Germany – be it camping, hiking, climbing, or other activities – and for keeping in touch across such a distance and over a long time.

Ich möchte mich auch ganz herzlich bei meiner Familie bedanken für all die Unterstützung während des Studiums und Promotion, all die Videoanrufe und Hilfe bei den Umzügen, die es ermöglicht haben, dass ich für so lange Zeit im Ausland bleiben konnte. Ich konnte mich immer auf euren bedingungslosen positiven Beistand verlassen und freu mich euch nach langer Zeit endlich wiederzusehen.

Finally, I want to thank my girlfriend Mackenna for all her support and understanding during this time and for all the commitment. I am looking back on a wonderful time with exciting trips and holidays. And thanks for reading and correcting the entire thesis.

Thank you very much!

1 Introduction

Single-chain nanoparticles (SCNPs) are a versatile class of soft-shell nanoparticles formed by intramolecular cross-links of precursor polymers, currently undergoing critical advancements in SCNPs formation, applications, and innovative characterization techniques.^[1-3] The current PhD thesis critically expands the scope of SCNPs by adding light induced spatiotemporal control of the folding state, influencing the particle size and compaction. Further, introducing catalytically active metals brings SCNPs one step closer to their natural analogues, i.e. enzymes. Consequently, water soluble SCNPs increase biocompatibility and expand their range towards biomedical applications. To improve the characterization and enable visualization of SCNPs formation, fluorescent cross-links were introduced. Lastly, Förster Resonance Energy Transfer (FRET) was exploited as a tool to probe the close proximity and compaction of SCNPs.

In recent years, SCNPs have witnessed remarkable progress, positioning them as tailored and recyclable macromolecular catalytic systems.^[4, 5] SCNPs are characterized as soft-shell nanoparticles with a hydrodynamic diameter typically ranging from 3 to 40 nm,^[6] and catalytic SCNPs combine the advantages of both homo- and heterogeneous catalysis.^[7] Homogeneous catalysts are generally more effective and selective under benign conditions, while heterogeneous catalysts provide the advantages of easier separation and recyclability.^[8]

Molecular organometallic complexes, acids, and enzymes are prominent examples for homogeneous catalysts and especially enzymes serve as blueprints for catalytically active SCNPs.^[9, 10] Although SCNPs are inspired by nature, they cannot mimic the specific and highly defined spatial conformation of proteins. However, they are significantly simpler to synthesize by utilizing radical polymerization techniques, which allow control over polymer chains' length and functionality.^[11-14] Several techniques have been developed to generate SCNPs from linear polymer precursors as described in the theoretical background section 2.2.^[15-17]

In Chapter 4 we describe the folding of SCNPs by a photoinduced reaction to create fluorescent and catalytically active nanoparticles. The folding mechanism is based on a photoenolization followed by a Diels-Alder reaction. Fluorescent and catalytically active SCNPs offer real-time catalyst visualization in reaction vessels upon light excitation. The

catalytically active metal center is equipped with gold complexes allowing the catalysis of a range of organic reactions.

In addition to catalysis, SCNPs are also promising candidates for biomedical applications such as drug delivery, target imaging, and enzyme mimicry,^[18] for which water-soluble and biocompatible polymer precursors are essential. Additionally, the size of SCNPs plays an important role, defining their biomedical efficacy by influencing cellular uptake^[19] and renal clearance^[20] in biological systems. The ability to change particle size and shape remotely could significantly enhance cellular interactions and biodistribution, thereby advancing controlled drug delivery, cell labelling, and imaging techniques.^[21, 22] However, current methods for remote control of SCNPs folding and unfolding are limited, especially in biomedical contexts due to incompatibilities with water^[23, 24] and the requirement for organic solvents as triggering agents.^[25]

Chapter 5 focuses on the remote unfolding and biocompatibility of SCNPs. Mild visible light is employed to control the macromolecular size, with bimane units serving as photolabile linkage points, resulting in an unfolded and reusable polymer. Water-soluble systems with fluorescent moieties allow for biomedical targeting and imaging applications.

The characterization of SCNP during and after folding is an ongoing challenge and often relies on techniques such as dynamic light scattering (DLS)^[26-28] or size exclusion chromatography (SEC).^[29, 30] In Chapter 6 we employed distance dependent interactions between two chromophores known as Förster Resonance Energy Transfer (FRET) to evidence SCNP folding. The novel FRET pair utilizes bimane units as a donor fluorophore and nitrobenzoxadiazole (NBD) as acceptor showing an efficient energy transfer. The pioneered simple spectroscopic readout allows tracking the folding status, and confirmation of high compaction.

2 Theoretical Background

The chapter Theoretical Background provides a comprehensive overview of the fundamental and advanced concepts in polymerization techniques, single-chain nanoparticles (SCNPs), photochemistry, and related fields that are important for understanding the context and scope of the current thesis. In the next section, polymerization techniques are described which are employed to synthesize precursor polymers with unique functionalities.

2.1 Polymerization Techniques

Polymerization describes the process of connecting molecular building blocks (monomers) to form polymer chains or complex networks. It can be characterized as step-growth polymerization or chain-growth polymerization. Step-growth polymerization summarizes all reactions where monomers with multiple functionalities react with each other, forming dimers, oligomers and small polymer chains that only combine to long polymer chains at high conversion rates. In a chain-growth polymerization, monomers add to a propagating polymer chain, extending its length. The active part of the chain, either a radical, cation, or anion reacts with monomers until side reactions lead to chain transfer or termination. Chain-growth polymerization techniques have the advantage of forming polymers with high molecular weight instantaneously after initiation at infinitesimal monomer conversion.^[31]

Free Radical Polymerization (FRP) is a common chain-growth polymerization method where highly reactive radicals attach to monomers in a repeating manner. Radical initiators, e.g. 2,2-azobisisobutyronitrile (AIBN), decompose forming radicals that start a polymerization, followed by a propagation reaction. However, the highly reactive radicals tend to undergo side reactions such as recombination and disproportionation, leading to termination and chain transfer, affording polymers with a broad molecular weight distribution. Therefore, regulation is required to control the molecular weight and the molecular weight distribution. Reversible-deactivation radical polymerizations (RDRP) summarize techniques used to control the propagation through an equilibrium of reversible activation/deactivation of the radical chains.^[32]

In the current thesis, the synthesis of precursor polymer chains is achieved by RDRP, allowing radical polymerization with so-called 'living character', which refers to the ability of polymer

chains to continuously grow without undergoing transfer and termination reactions, resulting in precise control over molecular weight and functionality.^[33] In comparison with free radical polymerization, RDRP maintains end-group fidelity and enables repetitive block-formation.^[34] Radical polymerizations with a 'living character' are based on the work of Szwarc in 1956,^[35] who established the foundational principle of a dynamic equilibrium between active and dormant species.^[36, 37]

In the scope of the current thesis, both nitroxide-mediated radical polymerization (NMP) and reversible addition-fragmentation chain transfer (RAFT) polymerization are employed to control the synthesis of defined structures.

2.1.1 Nitroxide-mediated polymerization (NMP)

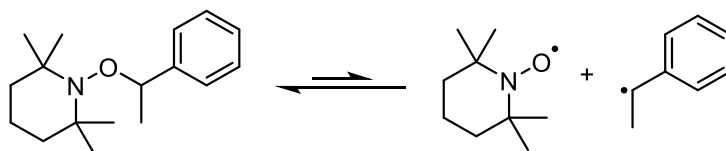
Nitroxide-mediated polymerization (NMP) is an important polymerization technique, which uses a dynamic equilibrium between active and dormant species to effectively minimize transfer and termination reactions.

Free radical polymerization has the ability to polymerize a wide variety of monomers to polymers with high molecular mass, but lack in narrow molecular weight distribution and end-group functionality. However, RDRP shows a linear progression of the molecular weight of the polymer, resulting in a low dispersity (\mathcal{D}) < 1.2. RDRP often allows chain extension based on their defined end groups. Therefore, the polymer chains can be readily reactivated from their dormant state forming block structures with different monomers.^[38]

NMP achieves a living character by utilizing persistent nitroxide radicals as mediating agent, which reversibly deactivate the propagating radicals and establish a rapid equilibrium between active and dormant species at elevated temperatures. During the reaction most radicals are reversibly trapped, minimizing the total concentration of the propagating free radicals. Both the termination rate and the propagation rate depend on the total radical concentration, but in contrast to the propagation, the termination by recombination requires two radicals and is therefore dependent on the square of the total radical concentration. The square dependence of the termination reaction on the concentration results in a drastic decrease of the termination rate, while the propagation rate is directly proportional to the total radical concentration and is thus less reduced.^[39-41]

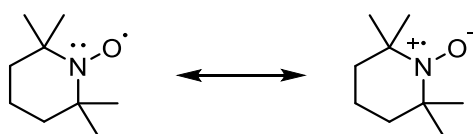
Originally, NMP was accomplished by adding the nitroxide radical 2,2,6,6-tetramethylpiperidin-1-yl)oxyl (TEMPO) to a free radical polymerization with conventional thermal initiators, such as AIBN. Above a certain temperature, TEMPO is capable of reversible

termination, allowing an equilibrium between active and dormant species (Scheme 3) to be established. Since then, a great variety of nitroxide compounds have been synthesized and investigated to overcome certain limitations of TEMPO, including high reaction temperatures typically above 130 °C and long reaction times. Additionally, TEMPO only allows living polymerization with styrene or styrene derivatives. A new generation of NMP initiators include SG1 (*N-tert*-butyl-*N*-[diethylphosphono-(2,2-dimethylpropyl)]nitroxide) and TIPNO (*N-tert*-butyl-*N*-[1-phenyl-2-methylpropyl] nitroxide), which allow controlled polymerization of monomers such as acrylates or acrylamides.^[38] However, TEMPO based alkoxyamines are still used for the polymerization of styrene based monomers (Scheme 1). *N*-alkoxyamines are often used instead of nitroxide radicals, allowing the thermal fragmentation into a persistent nitroxide radical and an initiating alkyl radical, avoiding the need of thermal initiators.^[42]



Scheme 1: Styryl-TEMPO alkoxyamine used in the current thesis for the polymerization of styrene derivatives, allowing thermal fragmentation into a persistent nitroxide radical and an initiating alkyl radical.

Nitroxide radicals are defined by their stability and are described as persistent radicals, implying that they do not self-terminate. The aminoxyl group with an unpaired electron shows two main mesomeric structures in which the radical is either depicted at the oxygen or at the nitrogen. The delocalization of the electron is the main reason for the stability of the radical (Scheme 2).^[43, 44]

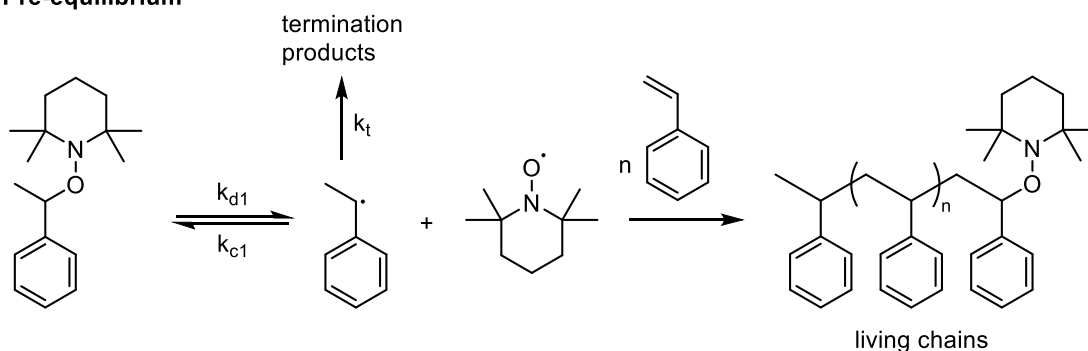


Scheme 2: Mesomeric structures of nitroxides showing the delocalization of the unpaired electron.^[38]

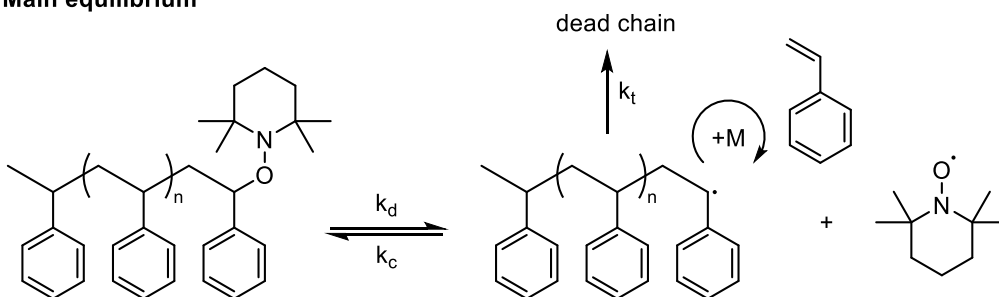
The NMP mechanism of styrene with styryl-TEMPO alkoxyamine is shown in Scheme 3. For the initiation, the homolysis of the O-R_{sty} bond is thermally induced, resulting in a stable radical (TEMPO) and reactive carbon-centered radical. The reactive radical undergoes a fast polymerization with the monomer (styrene), whereas the persistent radical is too stable to initiate a polymerization and is not able to self-terminate.^[45, 46] However, the persistent radical can recombine with the carbon radical to an alkoxyamine species, maintaining an

equilibrium between dormant and propagating chain. Self-termination of the carbon radical is possible but not favored due to the low concentration of radicals.^[47, 48]

Pre-equilibrium



Main equilibrium



Scheme 3: Mechanism of the NMP process. Starting with an alkoxyamine in the pre-equilibrium to generate a living chain. The main equilibrium shows the propagating chain. The monomer (M) is in this case styrene.^[38]

The control over the polymerization is achieved when the equilibrium between active and dormant chains is biased on the dormant site ($k_c \gg k_d$). Not only the temperature, but also the monomer-initiator-system is an essential criteria for controlled radical polymerization.^[49]

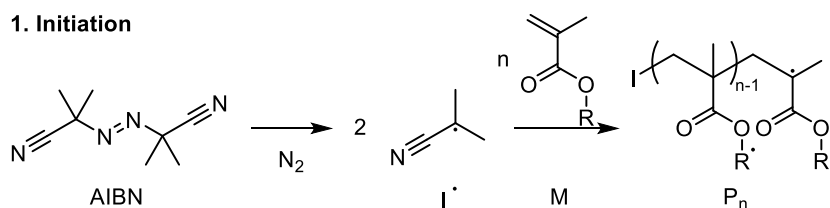
2.1.2 Reversible-addition-fragmentation chain-transfer (RAFT) polymerization

Reversible-addition-fragmentation chain-transfer (RAFT) polymerization is a variant of RDRP, as mentioned above, and first reported by Rizzardo, Moad, Thang and co-workers in 1998 in Australia.^[50] It has since become an important polymerization technique for well-defined polymers with a low dispersity and complex structure.

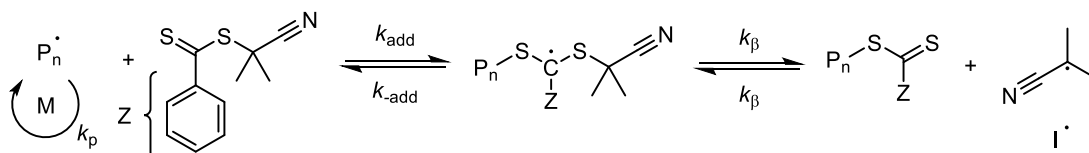
Control over the reaction is achieved by a reversible chain-transfer process, which activates and deactivates the propagating chain. The key steps in the mechanism of RAFT polymerization are shown in Scheme 4, with AIBN (initiator), methyl methacrylate substructure (monomer), and 2-cyano-2-propyl benzodithioate as RAFT agent, which were also used in the current thesis.

Similar to free radical polymerization, the RAFT process is initiated in the same way as free radical polymerization through the decomposition of an initiator (e.g. AIBN). The resulting radicals (I^{\bullet}) react with monomers (M) to form a propagating chain (P_n^{\bullet}). In the presence of a RAFT agent, P_n^{\bullet} forms a polymeric RAFT adduct radical which subsequently undergoes fragmentation, resulting in the formation of a polymeric RAFT agent alongside a reactive carbon-centered radical. An advantage of the RAFT agent 2-cyano-2-propyl benzodithioate is the formation of an identical radical (I^{\bullet}) compared to AIBN-derived radicals, generating a new propagating chain (P_m^{\bullet}). The propagating chains form an equilibrium with the polymeric RAFT agents, leading to rapid chain transfer between the active and dormant states of growing chains, thereby ensuring an equal distribution of propagation probability among all chains. It is important to note that in a RAFT process, the overall radical concentration remains consistent with that of a non-RAFT mediated process, ideally allowing it to proceed at a comparable rate. The rate at which radicals add to the RAFT agent also surpasses their bimolecular termination rate significantly because the RAFT adduct radical does not undergo bimolecular termination. As a result, RAFT polymerization provides control over the evolution of molecular weight and a dispersity.^[51, 52]

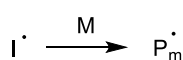
1. Initiation



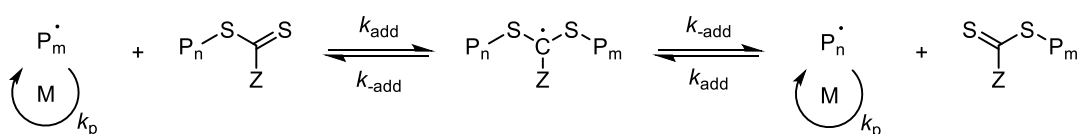
2. Reversible chain transfer/propagation



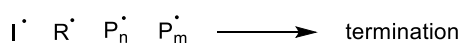
3. Reinitiation



4. Chain equilibration/propagation



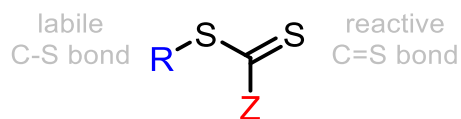
5. Termination



Scheme 4: General mechanism of a RAFT-polymerization. The activated initiator (I^\bullet) reacts with monomer units (M) forming a propagating chain (P_n^\bullet). In the presence of a RAFT agent, the P_n^\bullet forms a RAFT adduct radical which undergoes fragmentation, leading to a new propagating chain (P_m^\bullet). Step 4 describes the main equilibrium between the active chain and a dormant species.^[51]

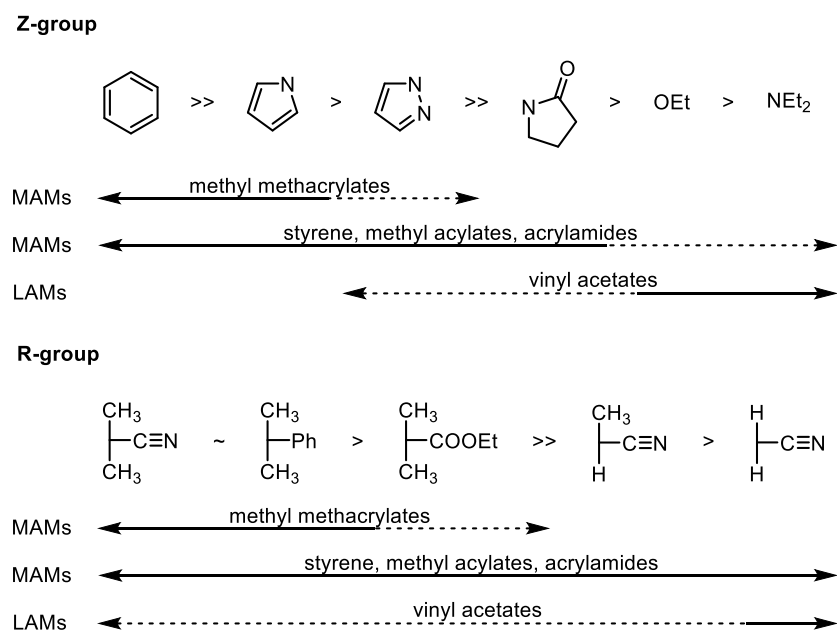
The RAFT polymerization leads to low dispersity and high molecular weight with a broad range of monomers. Depending on the monomers, the RAFT agent needs to be adapted to ensure a stable equilibrium and fast propagation. Therefore, monomers are typically distinguished in two classes, i.e. more activated monomers (MAMs) and less activated monomers (LAMs). MAMs form relatively stabilized radicals due to conjugated electron systems represented in butadiene, styrene, and acrylates. In comparison, LAMs have an electron-withdrawing group (nitrogen, oxygen and halogen) next to the vinyl group as represented in vinyl acetate, *N*-vinylpyrrolidone and vinyl chloride.^[53, 54]

The control of the RAFT polymerization mainly depends on the reactivity of the RAFT agents C=S bond compared to the monomer C=C bond towards radical addition. A more reactive C=S bond provides faster radical addition rates and can be achieved by adapting the R- and Z-group of the RAFT agent (Scheme 5).^[55]



Scheme 5: RAFT agent with a free-radical leaving group R and Z-group which controls the reactivity of the C=S bond.

The Z-group is mainly responsible for the radical addition and stabilization of the RAFT adduct radical during the polymerization, whereas the role of the R-groups is less pronounced here. For MAMs, the Z-Group needs to support the radical addition and stabilize the RAFT adduct radical to overcome an uncontrolled polymerization of the more stable radicals. In contrast, the less stabilized radicals from LAMs need support fragmentation towards propagating radicals, as a too stable RAFT adduct radical would trap propagating chains and prevent polymerization. A range of Z- and R-groups is shown in Scheme 6.

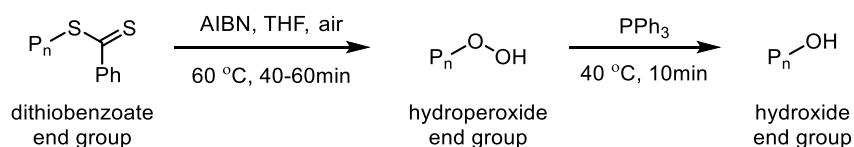


Scheme 6: Different Z- and R-groups for more activated monomers (MAMs) and less activated monomers (LAMs).

The R-group also has an important role in RAFT polymerization. Although less pronounced than the Z-group, the R-group also influences the radical addition to the C=S bond. In addition, the R-group must be a good radical leaving group and be able to initiate fast propagation. In the current thesis, the R-group mimics the initiator (AIBN), as it forms stable and reactive radicals that are able to react with most monomers and provides the same end groups.^[54]

Another advantage of RAFT polymerization is the end-group fidelity, which can be used for further functionalization and block extension. A broad range of reactions has been established to modify the thiocarbonylthio end-group, including the reduction to a thiol, radical-induced transformation or thermolysis.^[56-59] It is often necessary to remove the end group to prevent further side reactions. Within the scope of the current thesis, the dithiobenzoate group was removed to prevent visible light absorption due to its pink color and side reactions.

In a typical procedure, the RAFT polymer is exposed to AIBN in THF under the presence of atmospheric oxygen and heated to 60°C. The decomposition of AIBN initiates a radical oxidation cycle where the generated THF radicals react with the thiocarbonylthio end-group forming polymeric radicals P_n^* and tetrahydrofuranyl dithioesters. P_n^* reacts with oxygen dissolved in the reaction mixture yielding a hydroperoxide end group. Subsequently, the addition of triphenylphosphine reduces the hydroperoxide, resulting in a hydroxide end group. During this reaction, the color changes from pink to colorless (Scheme 7).^[60]



Scheme 7: End group modification of a RAFT polymer with dithiobenzoate group. A radical oxidation cycle initiated by AIBN yielding hydroperoxide groups which were reduced with triphenylphosphine to hydroxides.

2.1.3 Copolymerization

To increase the functionality or change the properties of a polymer, different monomers can be polymerized into one polymer. The properties of such copolymers depend on the structural units and their order along the chain. A distinction is made between statistical copolymers (ABAABAAABB), which show no periodic order between the monomers, alternating copolymers (ABABABAB), where monomers are particularly ordered, and block copolymers (AAABBB) where sequences of the same monomers are attached. In addition to linear copolymers, grafted or branched copolymers expand the range of polymeric architecture in which monomers form side chains attached to the polymer.

In the scope of the present thesis, all synthesized copolymers show a close to statistical order of the repeating units. However, the monomer feed ratio and the resulting polymer composition is often not identical, meaning that a change in the feed ratio does not

necessarily result in a proportional change in the polymer composition. Accordingly, during the course of a reaction, monomers are polymerized with different feed ratio leading to a change in the monomer concentration and therefore to different polymer compositions along the chain. The different ratios in which a monomer A or B adds to the propagating chain are defined as reactivity ratios and determine whether a monomer tends to react more readily with its own or with another type of monomer at the end of a propagating chain. The reactivity ratio of each monomer results from the rate constant of adding monomer A to the propagating chain with monomer A as chain end in relation to the rate constant for adding monomer A to the propagating chain with monomer B as chain end.

The copolymer composition can be determined by e.g. ^1H NMR spectroscopy, comparing resonances of the different repeating units with the backbone. To investigate if the copolymer composition changes gradually along the chain, their incorporation must be traced during the polymerization, which can be achieved by recording the kinetics of the polymerization.

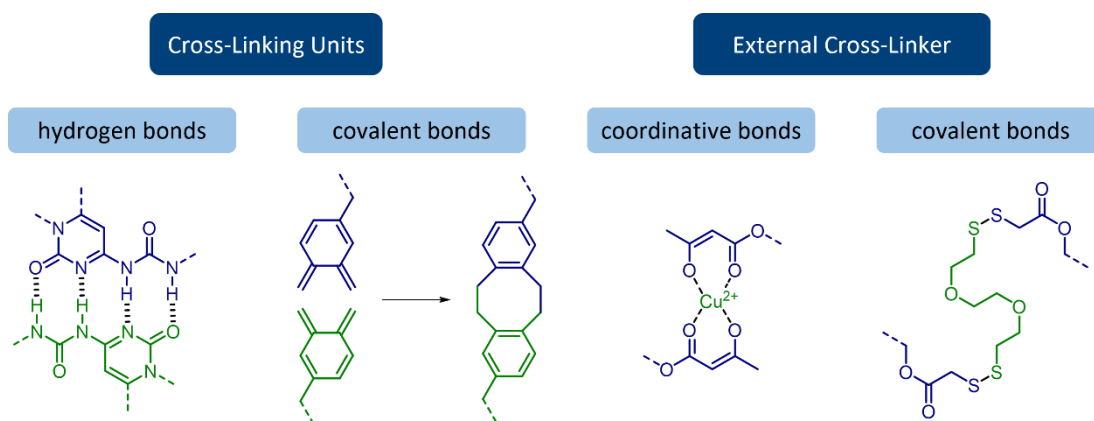
2.2 Single-Chain Nanoparticles (SCNP)

2.2.1 Synthetic strategies

Nanoparticles are defined by their size typically between 1 and 100 nm and they vary in shape and material.^[61] Single-chain nanoparticles (SCNPs) in particular are such nano-sized objects, obtained from a single polymer chain through intramolecular cross-linking, with a typical size between 3 to 30 nm.^[62] Polymerization techniques as discussed above are utilized to synthesize linear precursor polymers, and controlled folding into SCNPs allows precise control of size and tailored functionality. The defined cross-linked structure and functionality of natural biomacromolecules inspire the development of SCNPs, which have a wide range of potential applications in various fields. Enzymes in particular serve as blueprint for catalytically active SCNPs, focusing on reusability and selectivity.^[63] Further applications in the biomedical field include tailored release vectors or in *vivo* tissue targeting.^[10, 16, 64]

Complex synthetic designs are required to mimic biomacromolecules and their functions. Apart from the polymerization techniques (refer to 2.1 Polymerization Techniques), the main step towards the formation of SCNPs is the folding of the linear precursor polymers. The successful intramolecular cross-linking is dependent on the chain length and the rigidity of the polymer backbone, but also depends on the placement and type of cross-linking moieties. A broad range of pendant groups and external linkers can be used to form different bonds within the chain. To avoid inter-chain cross-linking, the folding of SCNPs is normally carried out in diluted solution (typically $<1 \text{ mg mL}^{-1}$).^[7]

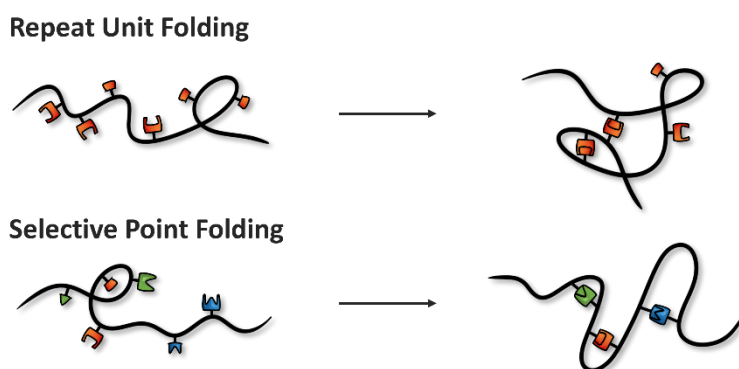
In nature, a large variety of cross-linkers are found, folding biomacromolecules into their specific structure. Disulfide bonds are frequently formed as covalent cross-links, whereas hydrogen bonds are a common form of non-covalent interactions. Within the scope of SCNPs, a wide range of hydrogen and covalent bonds are used.^[65] Furthermore, coordinative dynamic bonds with external metal-ions can be used to cross-link polymer chains.^[66, 67] Covalent and non-covalent cross-linking reactions can be categorized into reactions utilizing pendant groups, which react with each other in a e.g. [4+4] cycloaddition between benzocyclobutenes^[65], or cross-linking reactions that use small molecules such as an external linker to form a connection between two pendant groups. An example for a covalent cross-linking reactions is the disulfide bond formation as shown in Scheme 8.^[11]



Scheme 8: Examples of different ways of cross-linking polymer chains to obtain SCNPs with pendant groups and external cross-linker.

To avoid side reaction of the pendant groups during the polymerization, the cross-linking strategies often involve post-functionalization or protection groups. Post-functionalization is necessary if the cross-linking moieties contain alkenes, which react during a radical polymerization. An alternative way to avoid incompatibility is to use a highly reactive external cross-linker in combination with stable pendant groups. Moreover, light can be used as an external trigger to achieve spatiotemporal control.

In addition to the frequency, the placement of the pendant groups, leading to an intramolecular chain collapse, has a critical impact on the compaction of the SCNPs. Most common is the statistical copolymerization of pendant groups that can subsequently be utilized to initiate the collapse into SCNPs. More control can be achieved by selective point folding in which only specific orthogonal reaction partners form defined linkages between each other. Therefore, the functional groups must be placed in defined positions along the chain as shown in Scheme 9, requiring a high synthetic effort and orthogonal reaction partners.^[68]



Scheme 9: Folding of polymers *via* repeat unit folding and selective point folding.^[68]

A challenge during the cross-linking of single polymer chains is to avoid reactions between chains, normally achieved by highly diluting the polymer solutions, making intramolecular reactions more likely. However, an excess of solvent hinders upscaling and prevents large-scale industrial production of SCNPs. Recently, several groups have increased the concentration during SCNPs folding, enabling synthesis from up to 40 mg mL^{-1} by electrostatic-mediated intramolecular cross-linking.^[69]

In summary, many different synthesis strategies allow the formation of SCNPs with defined structures. However, to characterize the shape and the gain of compaction advanced characterization methods are required.^[16, 70]

2.2.2 Characterization of SCNPs

Beyond the synthetic strategies, characterizing the folding of SCNPs provides further challenges. While standard analytical methods such as NMR and UV/VIS spectroscopy can monitor molecular changes during the cross-linking reaction, they face limitations in differentiating between intra- and intermolecular cross-linking and cannot quantify the overall degree of compaction. To gain a deeper understanding of the folding process, more advanced characterization methods are necessary. Elaborated NMR spectroscopic experiments such as diffusion-ordered spectroscopy (DOSY) can identify intramolecular cross-links by determining the diffusion coefficient (D) of the cross-linked particles and comparing it with the smaller diffusion coefficients of linear polymer chains. In addition, size exclusion chromatography (SEC) is commonly used to determine the hydrodynamic diameter of the formed particles to ensure a interchain cross-linking.^[71] In the theoretical work of Pomposo and coworkers (2014),^[72] the structure of SCNPs was modeled using computer simulations, revealing that the collapse does not necessarily lead to high compaction, but often results in an open chain structure with local compactions. These results show that a high degree of pendant groups is required to reach high compaction and demonstrate the lack of characterization methods to further investigate the shape and structure of SCNPs to mimic globular proteins.^[73, 74]

A common method in polymer chemistry is SEC, also known as gel permeation chromatography (GPC), which separates macromolecules based on their hydrodynamic volume and enables calibration against molecular weight, displaying the molar mass distribution of a sample. In the scope of the current thesis, SEC is used to follow the SCNPs formation. The intramolecular collapse of a linear polymer chain results in a decrease of its

hydrodynamic volume, which indicates successful folding. However, the ability of SEC to resolve different substances into separated signals is limited, requiring a minimum mass difference for baseline separation.^[75] In principle, macromolecules are separated based on their hydrodynamic radius due to differential penetration depth in the porous stationary phase. The higher inclusion of smaller molecules increases the elution time and separates them from larger molecules that cannot access small pores. The column is filled with a gel, typically comprising cross-linked polymer particles based on polystyrene, divinyl benzene, or polyacrylamides, each having varied pore sizes. During the chromatography, the stationary phase is consistently flushed with a solvent, which dissolves the sample and carries it through the column. Ideally, the sample and the surface of stationary phase do not interact with each other.^[76]

To investigate SCNPs formation, the polymeric samples are compared before and after cross-linking, showing an increase in elution time in the case of successful compaction, resulting in a decreased hydrodynamic volume. The hydrodynamic volume during multi-chain aggregation increases, which leads to smaller elution times, but can also lead to insolubility of the polymer network.^[75, 77, 78] By default, SEC is used to determine the molecular weight and the molecular mass distribution of a polymeric sample employing a calibration curve of well-defined polymeric standards of the same polymer. In the field of SCNPs, the molecular weight is often specified as apparent molecular weight because a decrease in the hydrodynamic radius changes the elution time and therefore the molecular weight, which is based on a calibration, even the actual molecular weight does not change.

While SEC measurements are a commonly used method to investigate the folding of SCNPs, a second method is often used to confirm results. Dynamic Light Scattering (DLS) provides another practical way to measure the hydrodynamic radius of small particles. However, DLS is very sensitive to impurities and chain aggregations, and even a small amount will affect the measurement due to the proportion of the signal intensity to the power of 6 to the diameter of the particle. In addition, DLS reaches its resolution limit for SCNPs with small size differences after folding/unfolding.^[79]

A more complex method is diffusion ordered spectroscopy (DOSY). This 2D NMR technique is used to measure the diffusion coefficient of molecules, therefore the degree of Brownian molecular motion in solution. The diffusion coefficient of a molecule is affected by the size, shape, temperature, and viscosity of the solvent. DOSY NMR spectra contain the information of a sequence of NMR measurements by applying a pulse field gradient. Subsequently, the

decreasing signal intensity is plotted and analyzed in order to obtain the diffusion coefficients of each signal.

The pulsed field gradient sequence starts by labeling the nuclear spins with a phase factor based on their location in the NMR tube, followed by a short delay allowing for diffusion of the molecules. Another gradient pulse re-focuses (or undoes) the phase factors of the nuclear spins from the first gradient pulse.^[80] Depending on the amount of diffusion during the delay, the NMR signal will not be fully restored, leading to a weaker signal. DOSY spectra are primarily obtained from ¹H nucleus, resulting in a proton spectrum with diffusion data for each resonance. For the resonances of one molecule, the DOSY experiments show the same diffusion coefficient, which results from their hydrodynamic radius. Two molecules of different hydrodynamic radius will exhibit a different diffusion coefficient for each set of resonances. The average hydrodynamic radius (Stokes–Einstein radius, R_H) of each set of molecules can be calculated with the Stokes-Einstein relation (**1**) based on the diffusion coefficients (D) measured by DOSY. The Stokes-Einstein relation also includes the Boltzmann constant (k_B), the absolute temperature ($T = 294\text{K}$) and the dynamic viscosity (η) of the NMR solvent.

$$R_H = \frac{k_B \cdot T}{6\pi \cdot \eta \cdot D} \quad \mathbf{1}$$

Although DOSY experiments are a more complex measurement, they provide detailed insight into the molecular structure of macromolecules and are often used to support SEC data.^[81]

2.3 Photochemistry

In the scope of the current thesis, photoinduced reactions are used to trigger the folding of linear precursor polymer chains into compact SCNPs. Further, visible light was utilized to unfold SCNPs back to their linear structure. Light thereby enables spatiotemporal control and acts as a traceless reagent eliminates the need for a reactive external cross-linker or temperature as a trigger which might be limited in temperature sensitive application as living cells or with reactive functional sidechains. In general, photochemistry is defined as molecular changes caused by irradiation with ultraviolet, visible or infrared light.^[82] Photochemical reactions are natural processes that occur in many different ways. A well-known example is the complex process of photosynthesis, in which light energy is converted into chemical energy in the form of sugar.^[83, 84] Photochemistry allows to initiate specific reactions without having to rely on thermal activation energy, enabling spatiotemporal control.^[85] Specifically, visible light (400-800 nm) serves as an ideal mild trigger in many applications as it provides a clean, renewable, and cheap energy source.^[86]

2.3.1 Jablonski diagram

The wavelength at which light is being absorbed by a molecule depends on the electronic structure. For a photon to be absorbed, it must provide the right amount of energy required to excite an electron from the ground state to an excited state. Such behavior can be quantified in UV/VIS spectra, where the absorption is recorded for various wavelengths.^[87, 88] Different electronic states and transitions of a molecule are typically illustrated in a Jablonski diagram (Figure 1).^[89]

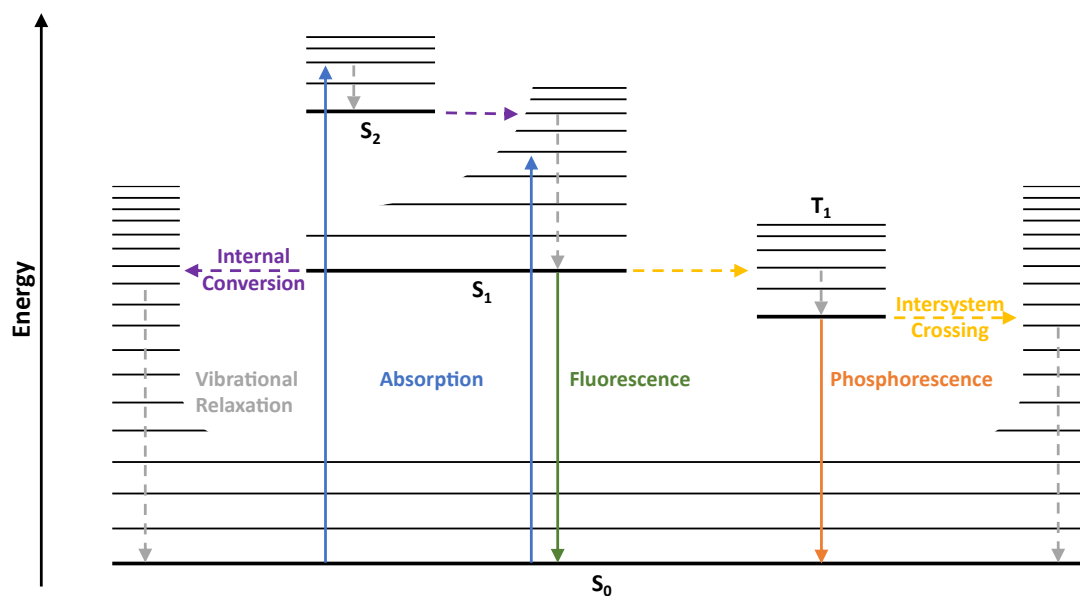


Figure 1: The Jablonski diagram shows the possible transitions after absorbing light from the ground state to excited state.

By irradiating a molecule with a suitable wavelength, a photon is absorbed, exciting a valence electron from the ground state (S_0) to an (S_1, S_2), which consists of many vibrational levels. The energy difference between the excited state (energy of the photon) and its lowest vibrational level ($S_{0,1,2}$) is called vibrational relaxation. The intermediate states are represented as thin lines and called vibrational states. After these relaxation processes, other so-called photophysical deactivation processes can occur to lower the energy of the electron from an excited state to the ground state.

Photophysical deactivation distinguishes between non-radiative and radiative deactivation. The non-radiative deactivation combines all transitions where no photons are emitted and is usually accomplished by vibrational relaxation. Internal conversion (IC) is one non-radiative transition that occurs between two excited states with different energetic levels, yet the same spin multiplicity. The electron passes from the excited state S_2 to the respective vibrational state of S_1 , followed by vibrational relaxation from the excited S_1 state to the lowest vibrational level of S_1 . Intersystem crossing (ISC) describes a similar transition, but differs due to the occurrence of spin multiplicity changes (e.g. $S_1 \rightarrow T_1$). Processes with different multiplicity are spin-forbidden, making them slower and only appearing for small energy differences.

Radiative deactivation describes the light emitting transitions, also known as luminescence. Fluorescence describes the transition from S_1 to S_0 under emission of light within a radiative

lifetime of about 10^{-9} s. Phosphorescence, on the other hand, takes place after ISC from S_1 to T_1 , followed by a radiative deactivation from T_1 to S_0 , emitting light with a longer radiative lifetime than fluorescence. Since the transition is spin-forbidden, radiative lifetime of phosphorescence is usually around 10^{-5} s but can go up to several hours.

Photochemical deactivation is not shown in a Jablonski diagram. It describes chemical reactions followed by light absorption including not only isomerization and bond forming processes, but also cycloadditions and cyclisation, converting excited molecules into ground state molecules.^[89-91]

2.3.2 Beer-Lambert's law

In the section above describes the absorption of light by a single molecule. To describe the absorption of light through a material or solution, the Beer-Lambert's Law is used. It relates the absorbance A with molar absorption coefficient ϵ for a certain substances and wavelength λ as well as the concentration c and the path length in cm. Shown in equation 2:

$$A = \epsilon_{\lambda} \cdot c \cdot l = \log \frac{I_0}{I} \quad 2$$

The absorption of light is determined using a UV/VIS spectrometer by measuring the intensity passing through a sample. The experimental design shown in Figure 2 depicts the light beam with full intensity (I_0) on the left side and with lower intensity (I) after passing through a solution of concentration c containing a substance with a wavelength-dependent molar absorptivity coefficient ϵ_{λ} .^[92] The quotient of I / I_0 is called transmittance and is used to calculate the absorbance.

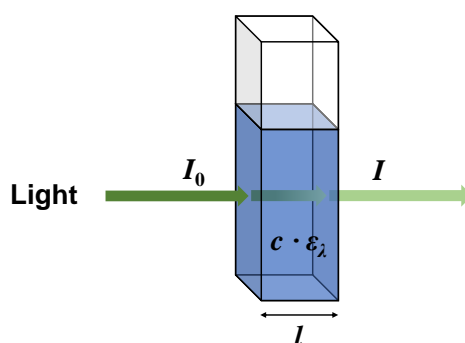


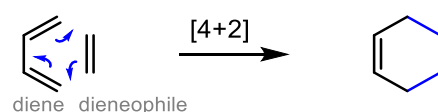
Figure 2: Light beam with full intensity (I_0) on the left side and with lower intensity (I) after passing through a solution of concentration c containing a substance with a wavelength-dependent molar absorptivity coefficient ϵ_{λ} .

Beer-Lambert's law is an essential principle for the analysis of light absorbing particles in solutions. It is a common way to calculate concentrations and the dimensions of a reaction vessel to ensure the most effective irradiation. With incorrect dimensioning, the reaction time might increase, as the intensity of the radiation decreases exponentially with increasing thickness of the reaction vessel. By working on larger scales, it is therefore necessary to stir the solution or use photo flow systems.^[89] The absorption coefficient can be determined for a solution with a known concentration, which can be further used to calculate the concentration of unknown samples. In the field of SCNPs it can give essential insight into the cross-linking density.

The absorption at different wavelengths of a molecule is defined as an absorption spectrum and displays the energy needed to excite a molecule. In contrast photochemical action plots determine the conversion of a photochemical reaction for different wavelengths with same number of photons. It is found that the highest conversion often does not align with the absorbance maximum. Instead, studies show a red shift of the conversion compared to the absorption spectrum.^[93, 94]

2.3.3 [4+2] Cycloadditions

Cycloaddition reactions describe the formation of a cyclic adduct by two or more double bonds. The unsaturated molecules form a cyclic transition state, which is followed by the formation of two new σ -bonds. Cycloadditions are highly valued for their regio- and stereoselectivity, making them versatile tools in chemistry. They are typically classified based on the number of π -electrons involved (e.g. [4+2], Scheme 10).^[95]

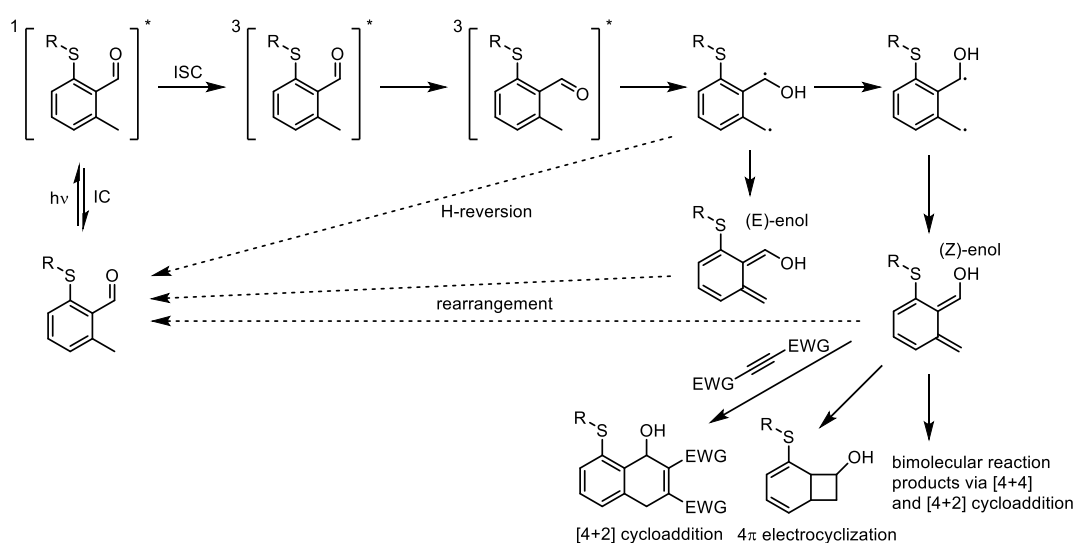


Scheme 10: Schematic overview of a [4+2] Diels-Alder cycloaddition between butadiene and ethene.

[4+2] Cycloadditions are also known as Diels–Alder reaction, named after their discoverers Otto Diels and Kurt Alder (1928). Importantly, Diels-Alder reactions can function under mild conditions when one component is substituted with an electron-donating group (EDG) and the reaction partner with an electron withdrawing group (EWG).

In the scope of the current thesis, a photoinduced Diels–Alder reaction is used to cross-link polymer chains into SCNPs. Orthomethylbenzaldehydes (oMBAs) serve as photocaged

dienes, generating orthoquinodimethanes (oQDM) intermediates, which react *in situ* with the corresponding dienophiles. The Diels–Alder reaction between the oQDM and the dienophile is thereby an important point considering the Woodward and Hoffmann rules which define if a cycloaddition is allowed (favored) or forbidden (unfavored), based on the number of π -electrons and their orbital alignment. Following these rules [4+2] cycloadditions are thermally allowed but photochemically forbidden. Therefore, a Diels–Alder reaction will not occur under irradiation but – as in our case – irradiation may provide the conjugated diene via a photoreaction which then reacts thermally with the dienophile. The mechanism of the oQDM formation is depicted in Scheme 11 using oMBA thioether as an example.^[96]



Scheme 11: Photoinduced mechanism for the formation of *o*-quinodimethanes and side products.

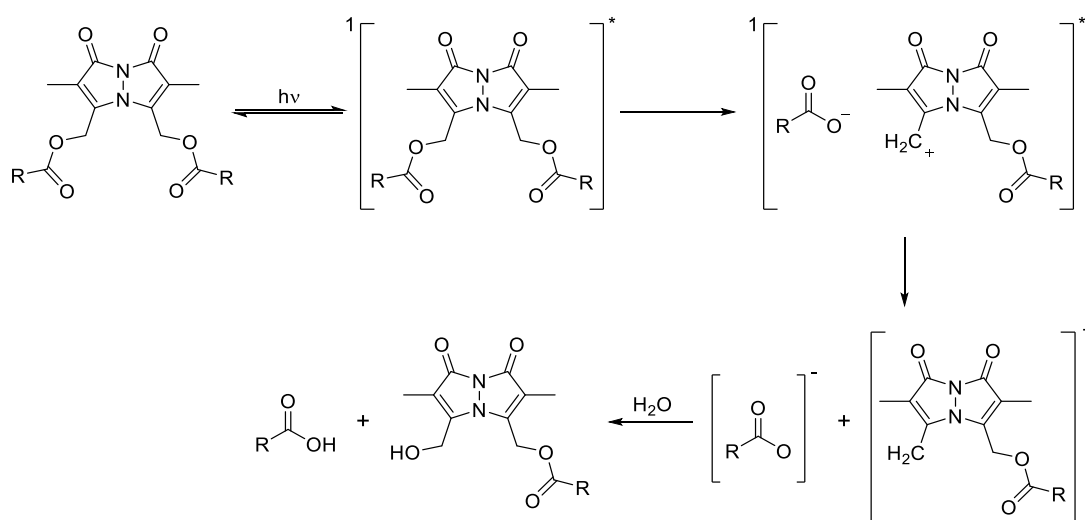
The irradiation of oMBA leads to a singlet excited state, which can undergo an ISC towards a triplet excited state. Compared to the singlet state, the triplet state has a longer half-life and allows free C-C bond rotation. Subsequently, biradicals are formed through H-abstraction leading to the (E)- or (Z)-enol. The (Z)-enol oQDM can rearrange back to the oMBA or undergo a side reaction, resulting in a 1-hydroxybenzocyclobutane or bimolecular reaction products. However, the [4+2]-cycloaddition with an electron poor dienophile (here alkyne) leads to 1,4-dihydro-1-naphthole. Notably, the (E)-enol oQDM does not react with dienophiles due to its short lifetime, and rearranges back to oQDM.^[97]

In the work of Feist *et al.* (2020)^[98] a photoinduced Diels–Alder reaction is reported, which led to fluorescent naphthalene *via* E1 elimination. In Chapter 4, this cycloaddition is utilized to gain spatiotemporal control over the SCNP formation and to form fluorescent cross-links, allowing an easy readout method of SCNP folding.

2.3.4 Bimane

Bimanes were first summarized and characterized by Kosower *et al.*,^[99, 100] as a new class of heterocyclic molecules. These authors introduced the name bimane (bi (two) and manus (hand)) as brief terms after their symmetric form of the core structure 1,5-diazabicyclo[3.3.0]octadienediones. Bimanes are an interesting field of study, used as small fluorophores for labeling and tracing application and have been widely used as fluorescent photoremovable protecting group or for labeling and tracing in biomedical applications.^[101, 102]

The photolysis of bimane caged esters was reported by Chaudhuri *et al.*^[103] who suggested that the photon excited bimane undergoes a relaxation to the lowest excited singlet state (S_1). Subsequently, a heterolytic C–O bond cleavage forms a singlet ion pair. To prevent recombination, the ion pair is separated and quenched by water, yielding the photoproduct alcohol and carboxylic acid (Scheme 12).^[103]



Scheme 12: Photoinduced cleavage mechanism of bimane diesters in the presence of water.

Bimanes are often used as fluorescent labeling agents in biological systems, as bromoderivatives (monobromobimane or dibromobimane) are non-fluorescent but become fluorophores after nucleophilic substitution with a substrate.^[100, 104]

2.3.5 Förster resonance energy transfer (FRET)

As previously mentioned, fluorescence is a radiative deactivation process of a molecule to release absorbed energy, typically between the first excited state and the ground state of a molecule. The process, in the range of 10^{-9} to 10^{-7} seconds, is relatively slow and involves energy loss through internal conversion and vibrational relaxation, resulting in emission

spectra with a higher wavelength than the absorption spectra. The difference between absorption spectra and emission spectra is also known as Stokes shift.

Energy can be transferred if two different chromophores are in close proximity, resulting in a redshift of the fluorescence spectra, which is called Förster resonance energy transfer (FRET).^[105] Here, an excited donor chromophore can transfer energy to an acceptor chromophore *via* nonradiative dipole-dipole coupling. The efficiency of this energy transfer is highly dependent on the distance between donor and acceptor molecules. FRET is often used as a molecular ruler to confirm that two objects of interest are close together. The general principle of FRET is depicted in Figure 3.^[106]

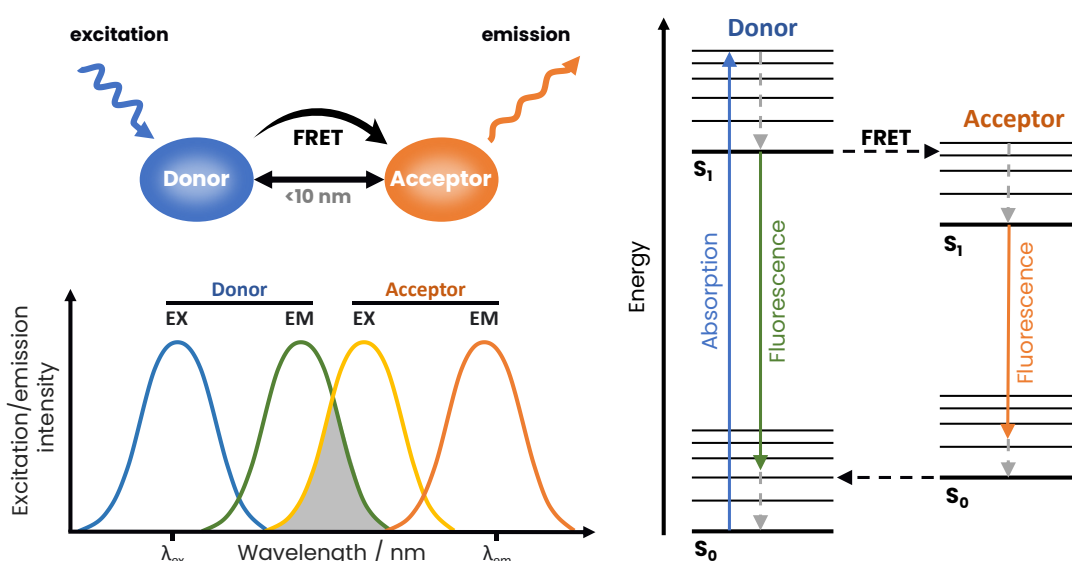


Figure 3: Concept of Förster resonance energy transfer (FRET) with fluorescence spectra and Jablonski diagram of FRET.

FRET only occurs if the chromophores are sufficiently close for Coulombic dipole-dipole interactions, which is within 10 nm. The FRET efficiency is highly dependent on the distance between the donor and acceptor, due to its correlation to the power of sixth. Additionally, the energy transfer is improved by a high extinction coefficient and a high quantum yield of the donor. To enable FRET, a spectral overlap between the donor's emission spectrum and the acceptor's absorption spectrum is required, allowing an energy transfer from the excited state of the donor to the acceptor. The spectral overlap between two chromophores is illustrated in Figure 3. Another factor influencing FRET is the orientation of the fluorophores to each other. The spatial alignment is described by the orientation parameter (κ^2). The orientation parameter ranges from 0 to 4, with 0 indicating that the dipoles are perpendicular to each other, while a value of 4 indicates that the dipoles are collinear. When the two

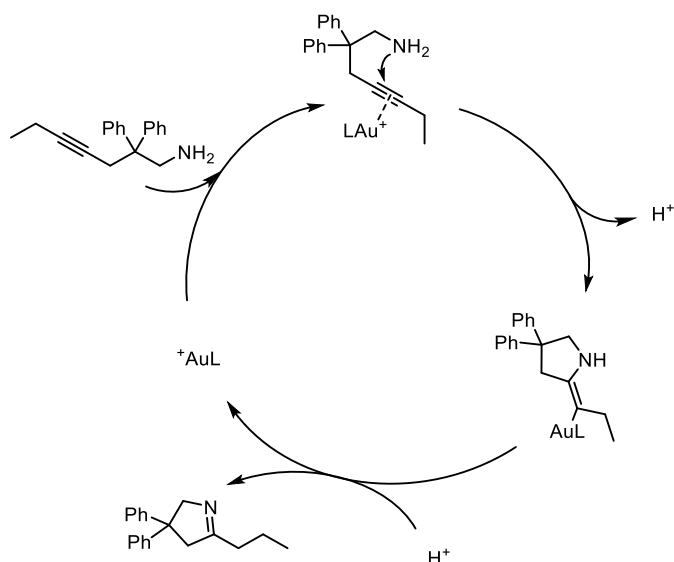
transition dipoles are parallel, κ^2 equals 1. However, a value of 2/3 is expected for a freely rotatable system.^[107, 108]

2.4 Coordination Complexes

An important goal of the current thesis was to implement catalytic activity in SCNPs to mimic the catalytic behaviour of enzymes. A basic understanding of metal-to-ligand interactions is necessary to understand the metal and ligand selection to avoid orthogonality problems with other functional groups. A coordination complex consists of a centralized metal surrounded by ligands that coordinate with the metal. The geometry of the complex is determined by the metal and its oxidation state, as well as the type and number of ligands. The interactions between metal and ligand are mostly considered as covalent bonds where the ligand provides electrons to an empty orbital of the metal. Also, metal to ligand back donation may occur.

In the scope of this thesis, we chose gold(I) as catalytically active metal center due to its ability to form stable (but unreactive) chlorides which can readily be activated using a cocatalyst. Gold complexes are able to catalyze a wide range of organic reactions^[109, 110] and are a promising study area in application as liquid crystals,^[111] metalorganic vapour-phase epitaxy (MOCVD),^[112, 113] luminescence,^[114] and cancer therapy.^[115, 116]

Gold(I) catalyzed organic reactions are often based on alkyne activation followed by C-C, C-O or C-N bond formation. In the last years, studies have shown the efficiency of gold in catalyzing cross-coupling reactions *via* an Au(I)/Au(III) cycle, based on nucleophilic addition to unsaturated C-C bonds, hydroarylation, enyne cyclization, and cycloaddition reactions.^[109, 117] To demonstrate the catalytic activity of our gold(I) equipped SCNPs, we performed an intramolecular hydroamination of an aminoalkyne as a benchmark reaction.^[118] The proposed mechanism is shown in Scheme 13.



Scheme 13: Mechanism for the Au(I)-catalyzed intramolecular hydroamination of an aminoalkyne.

Phosphine ligands coordinate to transition metals by donating their lone pair to the empty d-orbital of the metal center. However, phosphines are readily oxidized, leading to a significant change in their coordination behavior. The oxidation product, phosphine oxide, changes from bonding with soft metal centers to favoring hard acids due to its transformation from a phosphorus-based donor to an oxygen-based one. To prevent oxidation, we utilized sulfur as a stable protection group during the polymerization and SCNPs formation. Phosphines also allow monitoring of their chemical surroundings using the NMR active ^{31}P nuclei. Phosphor NMR is a commonly used NMR technique, as it is highly sensitive due to the 100% isotopic abundance with a nuclear spin of $\frac{1}{2}$ and high gyromagnetic ratio of ^{31}P . This enables tracking of the reaction state during protection, deprotection and coordination. Additionally, any unwanted oxidation would be observed.^[119]

SCNPs equipped with catalytic active metal complexes combine the advantages of homo- and heterogeneous catalysis. Homogeneous catalysts are generally more effective and selective under mild conditions, while heterogeneous catalysts provide the advantages of easier separation and recyclability.^[8] Molecular organometallic complexes, acids and enzymes are examples of homogeneous catalysts.^[9, 10] In the work of Knöfel and Rothfuss *et al.* (2017),^[120] platinum(II) cross-linked SCNPs have been demonstrated as homogeneous yet recyclable catalysts, by utilizing the amination of allyl alcohol as a benchmark reaction.

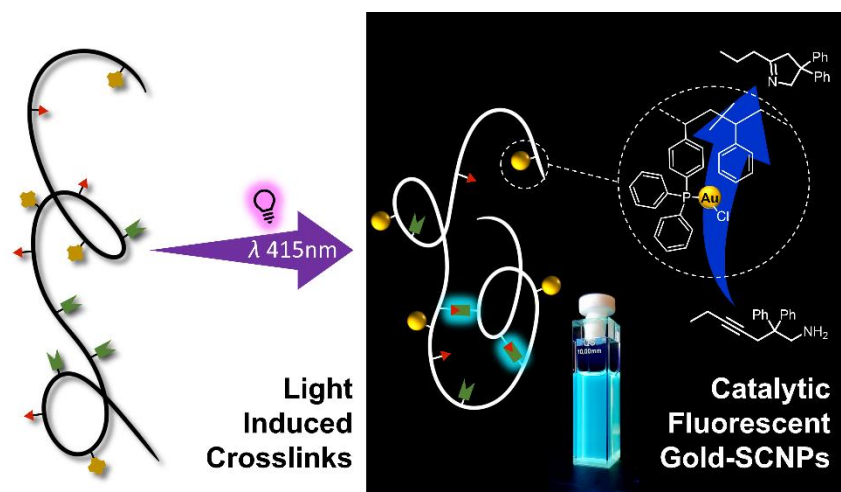
3 Motivation

Single-chain nanoparticles (SCNPs) are a versatile class of soft-shell nanoparticles, currently undergoing critical advancements, aiming for applications in the field of catalysis, biomedical application and responsive materials.^[64, 121, 122] Many examples have been shown in the literature highlighting the use of SCNPs as catalysts, with catalytically active metals or e.g. photosensitizers.^[118, 123] Compared to traditional homogeneous and heterogeneous catalysts, such as metals and metal complexes, SCNPs merge the benefits of both, offering homogeneous reaction conditions, enhanced recyclability, high activity, and potentially high substrate specificity.^[7] In the field of biomedical applications, literature showed that SCNPs can be used for drug delivery and in tracing and imaging applications.^[124] Furthermore, it was shown that the conformation of the SCNPs – linear polymer chain versus compact particle – can influence the cellular uptake within a biological system.^[19]

With the current body of work we aim to contribute to the research field of SCNPs and make critical enhancements for the use of SCNPs in catalysis and biomedical applications. To allow for changing the conformation by light, we introduced photoactive cross-links which fold or unfold the polymer under irradiation, allowing for temporal control. Changing the conformation of SCNPs by light could be used to influence the cellular uptake in biological systems or influencing the catalytic active center within a polymeric pocket. To improve the characterization of the folded state of SCNPs fluorescent cross-links are incorporated, indicating the successful folding and unfolding allowing for an optical readout method. Those fluorescent SCNPs could further be used in tracing and imaging applications.

The overall research strategy is implemented within three projects, where project one focuses on the light induced folding resulting in the formation of fluorescent SCNPs. In addition, the polymer backbone contains phosphine ligands to coordinate gold and allow for catalysis. The second project focuses on the remote unfolding and biocompatibility of SCNPs. Mild visible light is employed to control the conformation and size, with bimeane units serving as photolabile linkage points. Water-soluble systems with fluorescent moieties allow for biomedical tracing and imaging applications. In the last project, we employed distance-dependent interactions between two chromophores known as Förster Resonance Energy Transfer (FRET) to evidence SCNP folding and pave the way for further optical read out methods and improved characterization.

4 Fluorescent and Catalytically Active Single-Chain Nanoparticles



Abstract: Fluorescent and catalytically active SCNPs enable homogeneous catalysis and simultaneous monitoring of the catalyst distribution within a reaction vessel. Linear polymer chains are folded into compact polymer nanoparticles *via* a photoactivated reaction under visible light irradiation ($\lambda_{\text{max}} = 415$ nm), resulting in the formation of fluorescent cross-links. The polymer backbone was obtained by NMP and contains functional groups for the coordination of catalytically active gold complexes and the photoactive cross-linking moieties. Reprinted with permission from P. H. Maag *et al.*, *Macromolecules* **2022**, 55 (22), 9918-9924. Copyright 2022 American Chemical Society.

4.1 Motivation

In the current chapter, the synthesis of catalytically active single-chain nanoparticles (SCNPs), utilizing a photoinduced folding reaction, is explored. The photoreaction also results in fluorescent cross-links enabling the read-out of the folding status. Catalytic SCNPs benefit from their tailored structure, combining the advantages of homo- and heterogeneous catalysis (refer to Chapter 2.4). SCNPs are inspired by nature, but do not reach the same level of precise folding as proteins with their specific spatial conformation yet. However, they are significantly simpler to synthesize utilizing radical polymerization techniques, which allow control over polymer chains' length and functionality.^[11-14] Several techniques have been developed to prepare SCNPs from linear polymer precursors as described in the theoretical background 2.2.^[15-17]

The current chapter explores a photoinduced cross-linking reaction to fold linear polymer chains into SCNPs. The [4+2] cycloaddition is initiated by the photoenolization of *ortho*-methylbenzaldehyde (*o*MBA), generating *ortho*-quinodimethane (*o*QDM).^[125, 126] Mechanistically, a 1,5-hydrogen atom transfer (HAT) takes place on the triplet manifold, leading to a (Z)-enol, a highly reactive diene.^[96, 97, 127] Subsequently, the intermediate diene undergoes a Diels–Alder reaction with an electron deficient dienophile. When alkynes are employed as dienophiles, the initially produced cycloadduct is a 1,4-dihydro-1-naphthole, which is non-fluorescent, but can be transformed quantitatively into the corresponding fluorescent naphthalene-derivative through an E1-elimination in the presence of a catalytic amount of acid. Importantly, photochemical processes reach higher conversion within the compact structure of SCNPs compared to small molecule reactions in solution due to increased quantum efficiency.^[128, 129]

The synthesis of fluorescent and catalytically active SCNPs utilizes a photoinduced [4+2] cycloaddition to cross-link the polymer chain and create a more compact structure. The resulting naphthalene cross-links are stable fluorophores that remain intact under both light irradiation and high temperatures. These fluorophores serve the purpose of reporting the cross-linking reaction directly, and further enable the tracking of the resulting SCNPs in reaction vessels.^[130] Additionally, a phosphine ligand is introduced during the nitroxide mediated polymerization (NMP), which enables gold(I) coordination and catalysis. Gold complexes can catalyze various organic reactions, including hydroarylation, addition of nucleophilic heteroatoms, and cycloaddition reactions, often initiated by forming π -complexes with unsaturated carbon bonds.^[110, 131-133]

For the results described in the current chapter, F. Feist closely supervised the synthesis of polymeric and molecular structures, analytics and the catalysis experiments. C. Barner-Kowollik, P. W. Roesky and H. Frisch motivated and supervised the project. The chapter “Fluorescent and Catalytically Active Single Chain Nanoparticles” is adapted from Patrick H. Maag, Florian Feist, Hendrik Frisch, Peter W. Roesky, and Christopher Barner-Kowollik, *Macromolecules* **2022**, 55 (22), 9918-9924, DOI: 10.1021/acs.macromol.2c01894. AI-based language models were used to improve readability and spelling (*OpenAI* (2024) ChatGPT 4).

4.2 Results and Discussion

In the current chapter, the synthesis of fluorescent SCNPs through a photoinduced cross-linking reaction of a linear precursor polymers is described. These nanoparticles were later post-functionalized with catalytically active metals (**SCNP-AuCl**). In Figure 4, the synthesis steps are depicted, beginning with the polymerization of the polymer backbone (step 1), consisting of sulfur-protected triarylphosphine (S=PPh₂Sty) and chloromethylstyrene (CMS) units (**P1**). These CMS units were subsequently replaced with bromide (**P2**, step 2), preparing the polymer for the post-functionalization with a photo-active *o*MBA and an electron-deficient alkyne (**P3**, step 3). Both pendant groups underwent a photoinduced Diels–Alder cycloaddition, leading to the formation of fluorescent cross-links and folding **P3** into SCNPs (**SCNP1**, step 4). The triarylphosphine pendant groups allowed for gold(I) coordination, resulting in both fluorescent and catalytically active (**SCNP-AuCl**, step 5-6).

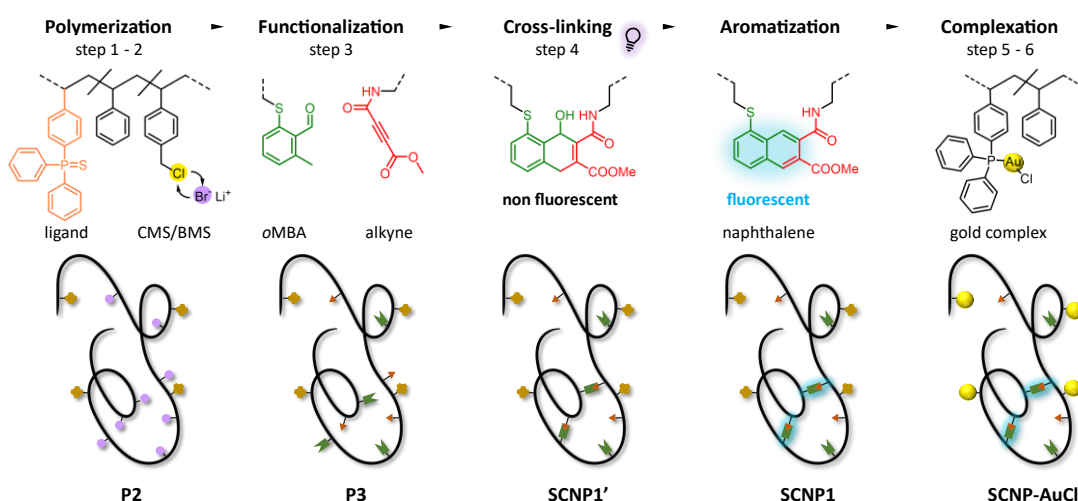
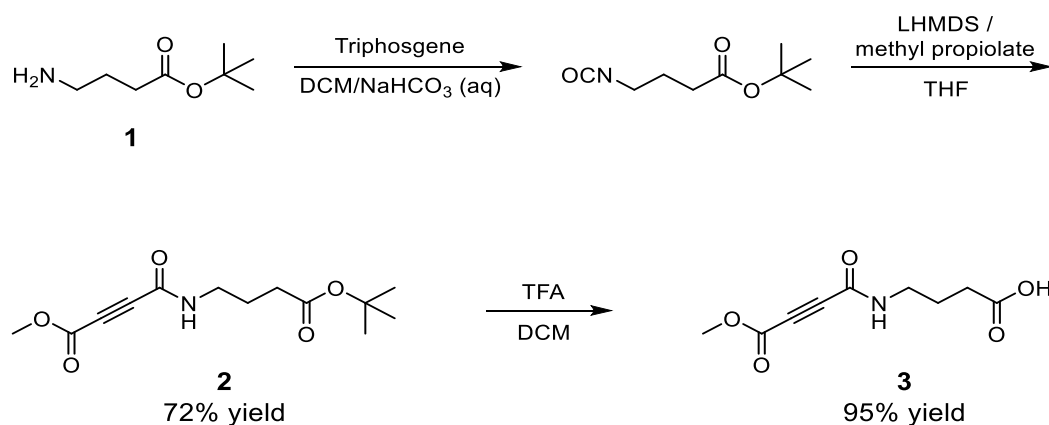


Figure 4: Overview of the SCNPs synthesis in 6 steps. Polymerization and exchange reaction affording a styrene-based copolymer containing S=PPh₂Sty (orange) ligand and bromomethylstyrene (BMS, yellow), followed by the post-functionalization with an *o*MBA (green) and an alkyne (red), which are utilized to fold the polymer chain into SCNPs with fluorescent naphthalene cross-links (light blue) in the third step. Finally, the phosphine ligands are deprotected and coordinated with a catalytically active gold complex (metallic yellow). Reprinted with permission from P. H. Maag *et al.*, *Macromolecules* **2022**, 55 (22), 9918-9924. Copyright 2022 American Chemical Society.

4.2.1 Photoinduced [4+2] cycloaddition

The folding step in the formation of SCNPs involved the [4+2] cycloaddition reaction initiated by visible light, in which *o*MBA and an alkyne combined to form a fluorescent naphthalene.^[98] Utilizing an *o*MBA thioether enabled this photochemical reaction under visible light exposure ($\lambda_{\text{max}} = 415 \text{ nm}$), as described in Chapter 2.3.^[134, 135] Increasing the reactivity of the alkyne (dienophile) towards the *o*QDM contributes to a high formation of cross-links, resulting in

more compact SCNPs.^[72] Consequently, the 4π -electrocyclization side-reaction of the *o*MBA is reduced. Compared to terminal alkynes, bifunctional alkynes with two electron-withdrawing groups demonstrate increased reactivity. However, to link such alkynes to the polymer backbone, one side must carry a functional handle. The development of a functional asymmetric electron-deficient alkyne is depicted in Scheme 14.^[136]



Scheme 14: Synthesis of 4-(4-methoxy-4-oxobut-2-ynamido)butanoic acid (**3**) starting with tert-butyl 4-aminobutanoate (**1**).

The electron-deficient alkyne (4-(4-methoxy-4-oxobut-2-ynamido)butanoic acid, **3**) was synthesized from *tert*-butyl 4-aminobutanoate (**1**) which was converted to an isocyanate using triphosgene. Subsequently, the isocyanate was reacted with deprotonated methyl propiolate using lithium bis(trimethylsilyl)amide as a strong base. The educt already contained a *tert*-butyl ester protected carboxylic acid group, enabling post-functionalization in a S_N2 -reaction with the existing bromomethylstyrene (BMS) pendant groups in the polymer (Scheme 16). The protective group was removed using TFA, yielding 4-(4-methoxy-4-oxobut-2-ynamido)butanoic acid (**3**, refer to Chapter 9.3 in the experimental section). The intermediate product, *tert*-butyl protected 4-(4-methoxy-4-oxobut-2-ynamido)butanoic acid (**2**), was employed in a molecular photoreaction to determine its suitability as an alkyne for the Diels–Alder cycloaddition. Consequently, a mixture of *o*MBA and the alkyne (**2**) in deuterated benzene was irradiated at $\lambda_{\max} = 415$ nm for 20 minutes and the photoreaction was monitored by ¹H NMR spectroscopy (Figure 5, refer to Chapter 9.7 in the experimental section).

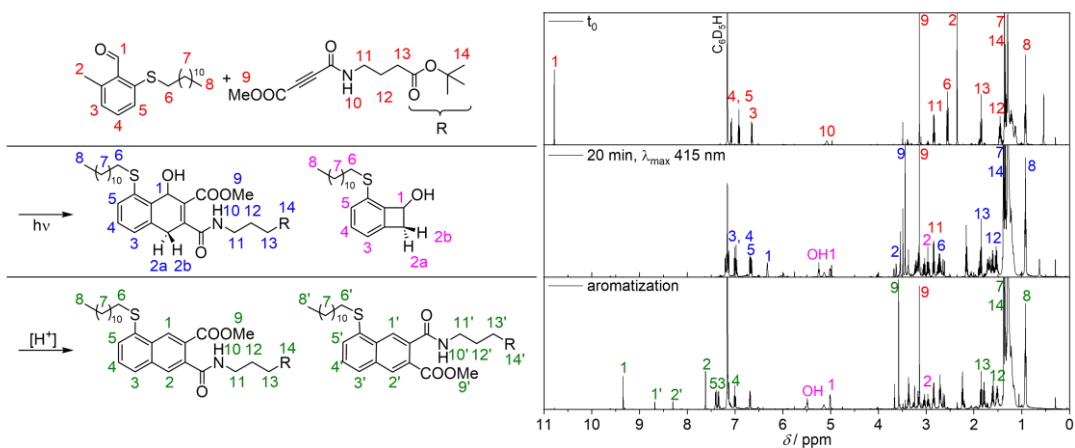


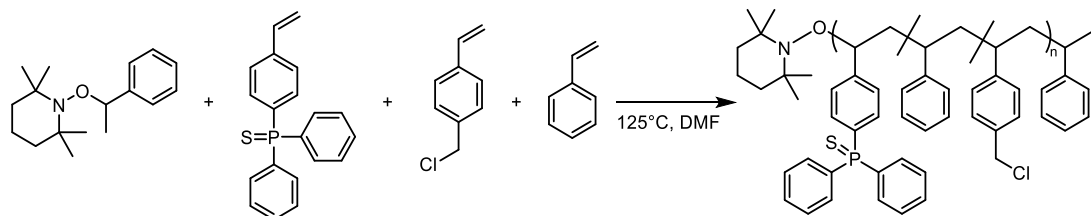
Figure 5: Left: Photoreaction of *o*MBA with the alkyne (**2**) in benzene (red numbers), initially leading to the non-fluorescent 1,4-dihydro-1-naphthole (blue numbers) and benzocyclobutane as side product (pink numbers), resulting in two regioisomers of the fluorescent naphthalene through an E1-elimination (green numbers). Right: Reaction monitoring *via* ^1H NMR spectroscopy in benzene- d_6 . The top spectrum was recorded prior to the irradiation. The middle spectrum was obtained after 20 min of irradiation at $\lambda_{\text{max}} = 415$ nm. The bottom spectrum was recorded after the addition of *p*-TsOH. Reprinted with permission from P. H. Maag *et al.*, *Macromolecules* **2022**, 55 (22), 9918-9924. Copyright 2022 American Chemical Society.

The conversion of *o*MBA during the photoreaction can be observed by the decrease of the aldehyde resonance at $\delta = 10.68$ ppm in the ^1H NMR spectrum. Within 20 minutes, the *o*MBA was fully consumed, resulting in two regioisomers of the non-fluorescent 1,4-dihydro-1-naphthole. The addition of a catalytic amount of acid led to the formation of two regioisomers of the fluorescent naphthalene through an E1-elimination, which can be observed by the appearance of two resonances between 7.5 ppm and 9.5 ppm corresponding to the naphthalene structure. Simultaneously, a side reaction generated benzocyclobutane *via* a 4π electrocyclozation from the *o*QDM, as described in Chapter 2.3.^[98] In contrast to the higher local concentration in SCNPs, the lower local concentration of molecular reaction partners in this test reaction favored the unimolecular 4π electrocyclozation. However, in SCNPs with a high local concentration, this reaction was less favored compared to the bimolecular Diels–Alder reaction.

4.2.2 Synthesis of fluorescent and catalytically active SCNPs

To post-functionalize the polymer chain with pendant groups for cross-linking and metal coordination, a synthetic strategy was required, taking into account the functional group compatibility^[137] and stability throughout the successive polymer modification steps. In the first step, the polymeric backbone was synthesized by a nitroxide-mediated polymerization (NMP) of styrene, CMS (chloromethylstyrene), and sulfur-protected 4-(diphenylphosphino)styrene (S=PPh₂Sty, refer to Chapter 9.4 in the experimental section).

The protection group of the phosphine monomer successfully prevented a side reaction with CMS and oxidation, leading to the synthesis of the copolymer poly(Sty-*co*-CMS-*co*-S=PPh₂Sty) (**P1**, $M_n = 21 \text{ kg mol}^{-1}$, Scheme 15).



Scheme 15: Step 1, NMP copolymerization to form **P1** using 2,2,6,6-Tetramethyl-1-(1-phenylethoxy)piperidine as initiator, incorporating styrene, CMS and S=PPh₂Sty.

It is critical to know the exact monomer composition of the polymer to be able to calculate the amounts of reactants needed for post-functionalization and catalysis. Two techniques were used to determine this. The first method monitors the conversion of each monomer during the polymerization and uses this to deduce the monomer composition of the polymer. Herein, the conversion was monitored by ¹H NMR spectroscopy, utilizing 1,4-dimethoxybenzene as an internal standard. The polymerization was stopped after a conversion of 47 mol% styrene, 56 mol% CMS and 80 mol% S=PPh₂Sty. Considering the molar quantities of reactants used in the copolymerization, the polymer **P1** contains 18 mol% CMS and 6 mol% S=PPh₂Sty (Table 1).

Table 1: Analysis of the copolymer composition by monomer conversion.

	Group	¹ H \int -Area ppm	conversion %	eq	composition %
Styrene	CH=CH ₂	5.25 – 5.19	47	300	75
CMS	CH ₂	4.60 – 4.54	56	30	18
S=PPh ₂ Sty	CH=CH ₂	5.40 – 5.33	80	15	6

An alternative way to calculate the monomer composition of a polymer is by comparing the peak integrals of different functional groups of the repeating units with the integrals of the polymeric backbone. Using the integral of the CH₂ resonance of CMS and comparing it with the CH-CH₂ signals of the polystyrene polymer backbone enabled calculation of the monomer composition *via* equation 3. For S=PPh₂Sty, an isolated aromatic resonance of 6 protons was used.

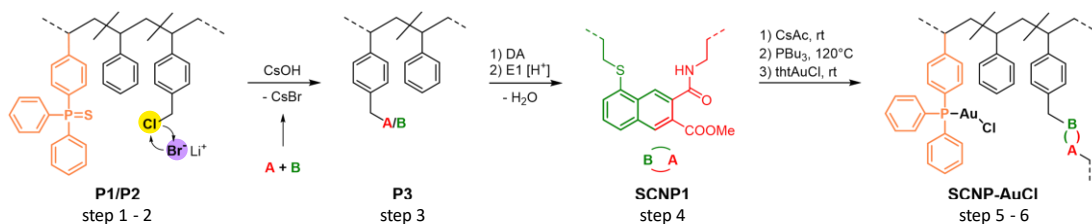
$$x_{CMS} = \frac{\int (CH_2)_{CMS}}{2} \div \frac{\int (CHCH_2)_{backbone}}{3} \quad 3$$

Using the second method, the composition of **P1** consisting of 23 mol% CMS and 5 mol% S=PPh₂Sty was determined (Table 2). As the analysis can be repeated at any time, it allows for easier comparison with other polymers. These results were used to calculate the amounts of reactants for the post-functionalization and catalysis.

Table 2: Analysis of copolymer composition calculated from ¹H NMR of the polymer.

	Group	protons	¹ H δ -Area ppm	¹ H \int	composition %
CMS	CH ₂	2	4.61 – 4.33	0.15	23
S=PPh ₂ Sty	Ar	6	7.81 – 7.56	0.09	5
Backbone	CH-CH ₂	3	2.39 – 1.18	1.00	

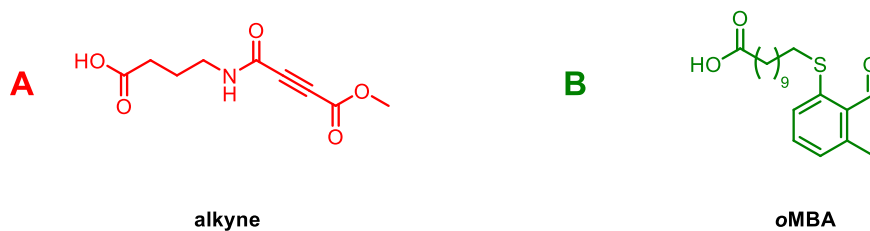
To enhance the reactivity of **P1** for the subsequent post-functionalization of CMS with cross-linking units, chlorine was substituted with bromine using lithium bromide, resulting in poly(Sty-co-BMS-co-S=PPh₂Sty) (**P2**, Scheme 16, refer to Chapter 9.5 in the experimental section). The conversion of CMS to BMS was monitored using ¹H NMR spectroscopy, which showed high conversion. Nevertheless, the resonances were not sufficiently distinct to precisely calculate the conversion.



Scheme 16: Overview of the detailed synthetic strategy showing the poly(Sty-co-BMS-co-S=PPh₂Sty) (**P2**) and the post-functionalization with the DA reagents the *o*MBA (B) and alkyne (A) (**P3**), as well as the resulting cross-links of **SCNP1** and the final gold(I) coordinated SCNPs (**SCNP-AuCl**). Reprinted with permission from P. H. Maag *et al.*, *Macromolecules* **2022**, 55 (22), 9918-9924. Copyright 2022 American Chemical Society.

The sulfur protecting group of S=PPh₂Sty also prevented side reaction between the phosphine and the alkyne during the post-functionalization of both the *o*MBA and alkyne (shown in Scheme 17, refer to Chapter 9.5 in the experimental section). In step 3 the cross-linking units were introduced through an esterification reaction with the BMS pendant

groups of **P3** ($M_n = 17 \text{ kg mol}^{-1}$, $D = 1.55 \cdot 10^{10} \text{ m}^2\text{s}^{-1}$, $R_H = 2.48 \text{ nm}$). Cesium carbonate served as the base, which enhanced the solubility of the carboxylate in dimethylformamide (DMF), leading to a more rapid reaction compared to the sodium salts,^[138] and achieving a conversion of 53% of the BMS pendant groups, as confirmed by ^1H NMR spectroscopy. A ratio of *o*MBA to alkyne at 1:0.6 was achieved. The post-functionalization also enabled the use of highly reactive alkynes which are otherwise unstable during NMP.



Scheme 17: *o*MBA and alkyne used for the light introduced [4+2] cycloaddition, leading to fluorescent cross-links of the polymer chains. To attach both to the polymer backbone, the carboxylic acid group is used, which allows a post-functionalization with the BMS repeating units.

After post-functionalizing of the polymeric backbone with the cross-linking units, **SCNP1** ($M_n = 15 \text{ kg mol}^{-1}$, $D = 2.09 \cdot 10^{10} \text{ m}^2\text{s}^{-1}$, $R_H = 1.84 \text{ nm}$) was formed through a photoinduced [4+2] cycloaddition as described in Chapter 2.3.3 in the theoretical background or the in the experimental section Chapter 9.6.1, resulting in a more compact structure. The SCNP formation was monitored using size exclusion chromatography (SEC) and diffusion-ordered spectroscopy (DOSY). Both analytical techniques implied a decrease in the hydrodynamic radius, R_H , after cross-linking. DOSY experiments measure the diffusion coefficient of each ^1H NMR resonance and were therefore also able to confirm that the *o*MBA (10.7 ppm) and the alkyne (3.8 ppm) were part of the polymer. The diffusion coefficients, D , increased by 34.8% after cross-linking and consequently the calculated hydrodynamic radius decreased, R_H .

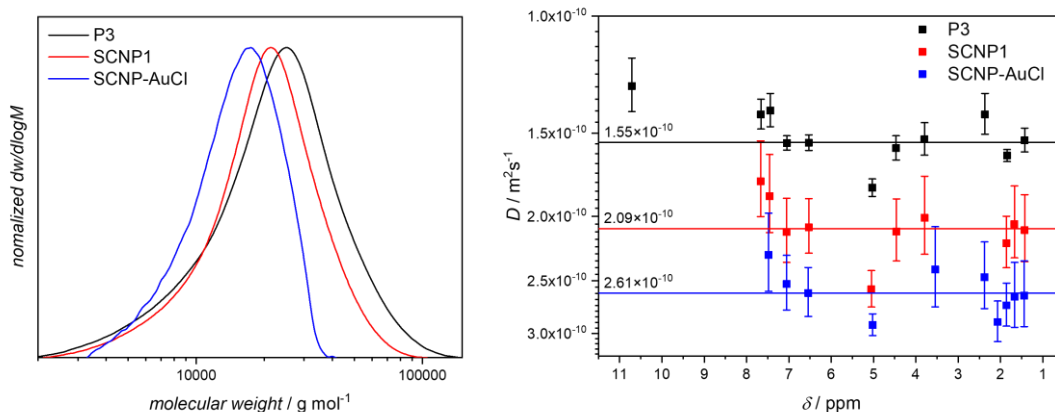


Figure 6: THF-SEC and diffusion coefficients, D , measured by DOSY of **P3**, **SCNP1** and **SCNP-AuCl**. Both analytic methods show a significant decrease in the hydrodynamic radius after cross-linking. Reprinted with permission from P. H. Maag *et al.*, *Macromolecules* **2022**, 55 (22), 9918-9924. Copyright 2022 American Chemical Society.

The hydrodynamic radius (Stokes–Einstein radius, R_H) was calculated using the Stokes–Einstein relation (4) and the diffusion coefficients (D) measured by DOSY. Additionally, the Boltzmann constant (k_B), the absolute temperature ($T = 294\text{K}$), and the dynamic viscosity ($\eta = 0.56 \text{ mPa s}$) of the solvent CDCl_3 were used.

$$R_H = \frac{k_B \cdot T}{6\pi \cdot \eta \cdot D} \quad 4$$

Subsequently, the folded SCNPs were prepared for metal coordination and catalysis. Remaining pendant groups such as the BMS functionality and unreacted alkyne needed to be deactivated to prevent side reactions with the triarylphosphine or the deprotection reagent tributyl phosphine (PBu_3). An easy approach is the esterification of BMS with cesium acetate, which also reacts with the remaining alkynes (refer to Chapter 9.5 in the experimental section). Step 5 was monitored using ^1H NMR spectroscopy until full conversion was observed.

In step 6, the protected triphenylphosphine was deprotected with PBu_3 at 120°C (refer to Chapter 9.5 in the experimental section). Full conversion was confirmed by ^{31}P NMR spectroscopy. Step 6 also included the coordination of the deprotected SCNPs with gold(I) for catalysis. The complexation of chloro(tetrahydrothiophene)gold(I) ($\text{AuCl}(\text{tht})$) with the triarylphosphine pendant groups of the SCNPs resulted in gold(I) decorated nanoparticles (**SCNP-AuCl**, $M_n = 15 \text{ kg mol}^{-1}$, $D = 2.61 \cdot 10^{10} \text{ m}^2\text{s}^{-1}$, $R_H = 1.47 \text{ nm}$). The ^{31}P NMR spectrum of the **SCNP-AuCl** showed a resonance at 32.2 ppm (chloro(4-(diphenylphosphino)styrene)gold(I) ($\text{AuCl-PPH}_2\text{Sty}$): 32.5 ppm) associated with this phosphorous-gold complex, indicating full conversion (Figure 7).

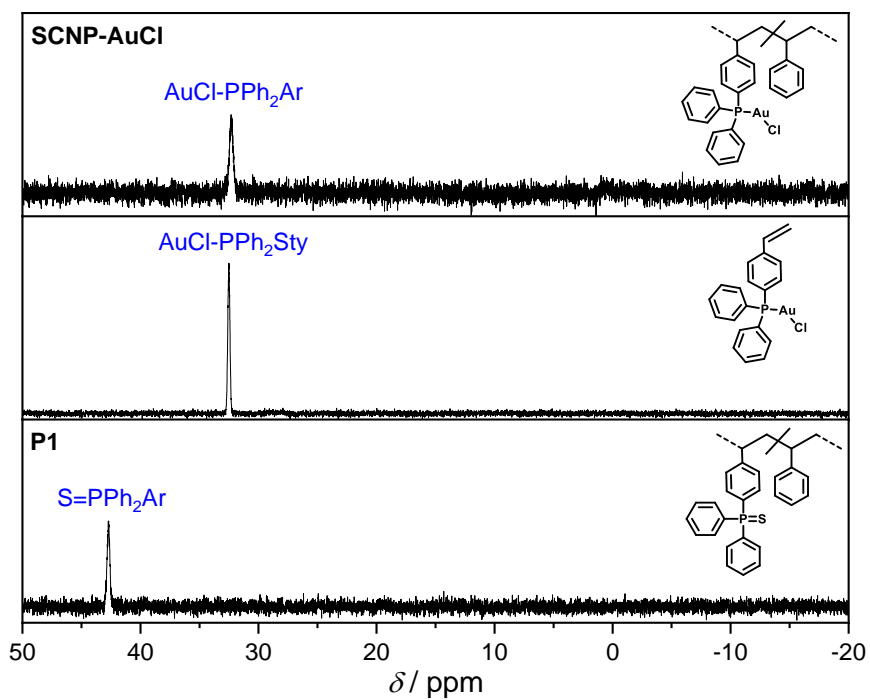


Figure 7: $^{31}\text{P}\{^1\text{H}\}$ NMR spectra of **SCNP-AuCl**, **AuCl-PPh₂Sty** and **P1** recorded in CDCl_3 , showing a resonance at 32.2 ppm for the gold(I) complex in comparison to the sulfur protected triphenylphosphine. Reprinted with permission from P. H. Maag *et al.*, *Macromolecules* **2022**, 55 (22), 9918-9924. Copyright 2022 American Chemical Society.

Furthermore, the coordinated of gold(I) was confirmed *via* UV/VIS spectroscopy, as indicated by an increasing absorption below 300 nm after gold complexation similar to a small molecule analogue chloro((4-(diphenylphosphino)styrene)gold(I) complex (shown in Figure 8).

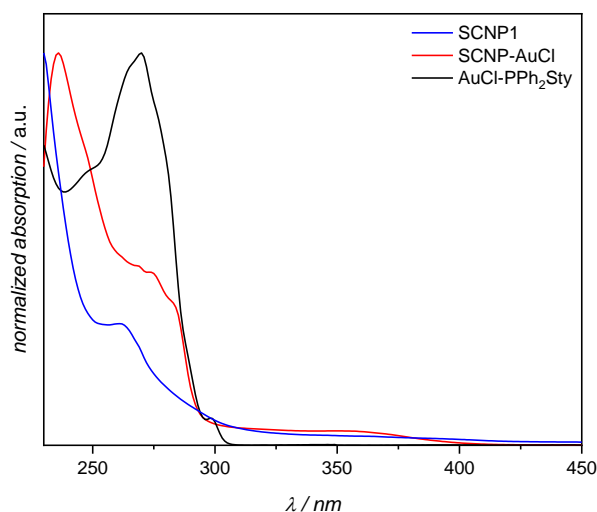


Figure 8: UV/VIS spectra of **SCNP-AuCl** showing an increasing absorption band below 300 nm compared to **SCNP1**. Reprinted with permission from P. H. Maag *et al.*, *Macromolecules* **2022**, 55 (22), 9918-9924. Copyright 2022 American Chemical Society.

The formation of fluorescent naphthalene cross-links provided an additional indication that the linear precursor polymer formed **SCNP1** *via* a light-induced Diels–Alder cycloaddition. The recorded emission and excitation spectra were similar to the spectra of the corresponding non-polymer bound small molecule **4**, which was used as comparison (shown in Figure 9).

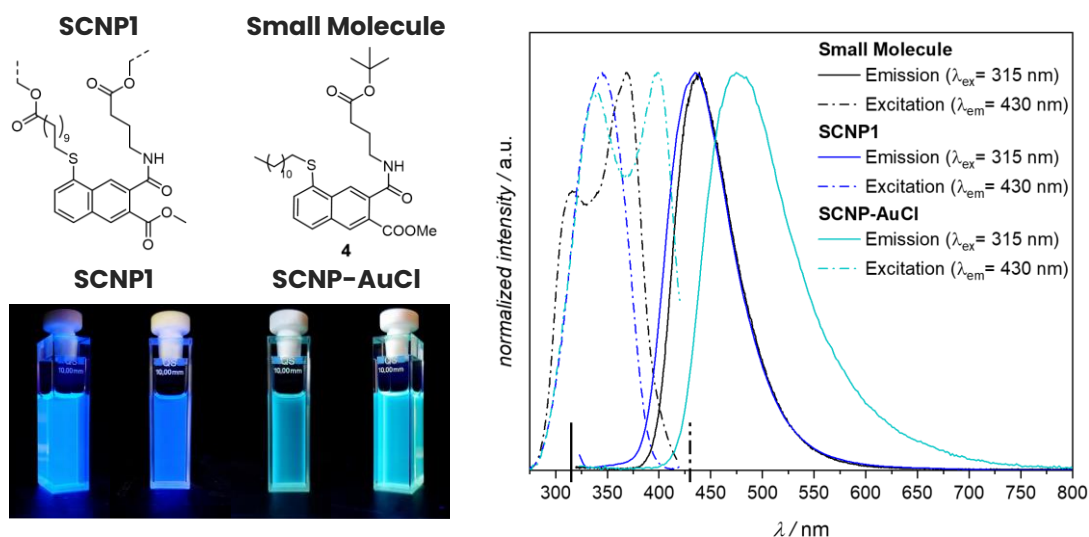


Figure 9: Fluorescence spectra of **SCNP1** and gold coordinated SCNPs (**SCNP-AuCl**) in comparison with the small molecule model of the fluorescent cross-linking units. The fluorescence spectra of the **SCNP1** and the small molecules **4** show an emission and excitation band at the same wavelength, but redshifted emission and excitation band for **SCNP-AuCl**. Reprinted with permission from P. H. Maag *et al.*, *Macromolecules* **2022**, 55 (22), 9918-9924. Copyright 2022 American Chemical Society.

However, the emission spectrum of **SCNP-AuCl** showed a redshift compared to the emission spectra of **SCNP1**. To further investigate the origin of the red-shift, fluorescence spectra of all intermediates were recorded, indicating that the shift appeared after the esterification reaction with cesium acetate to eliminate unreacted BMS or alkyne units. To enable a comparison of fluorescence spectra with the chemical structure, small molecule **4** was exposed to the same reaction conditions as those used in step 5. After the reaction of **4** with acetic acid and cesium hydroxide in dimethylformamide (DMF) for 3 d under N_2 , the resulting spectra exhibited a similar yet less pronounced redshift compared to **SCNP + CsAc**. We suggest that a transformation at the cross-links of the SCNPs are responsible for the red shift and conclude that this side reaction has no effect on the functionality as SCNPs or on the following catalysis.

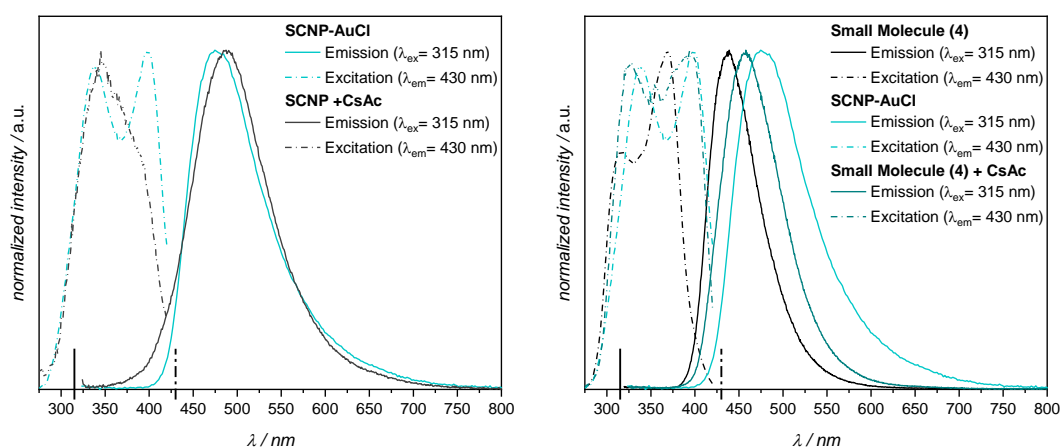


Figure 10: Left: Fluorescence spectra of **SCNP-AuCl** compared with **SCNP + CsAc**. Right: Fluorescence spectra of **SCNP-AuCl** compared with small molecule (**4**) before and after treatment with CsAc. Reprinted with permission from P. H. Maag *et al.*, *Macromolecules* **2022**, 55 (22), 9918-9924. Copyright 2022 American Chemical Society.

LCMS traces of **4** after the reaction with cesium acetate indicated that the ester and amid group attached at the naphthalene formed a phthalimide or an isobaric structure, causing the redshift of the emission spectrum (Figure 11).

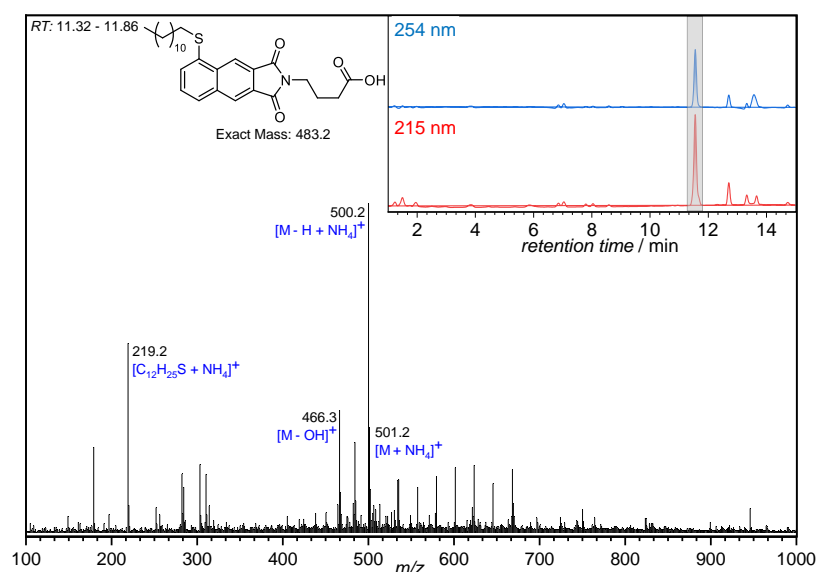
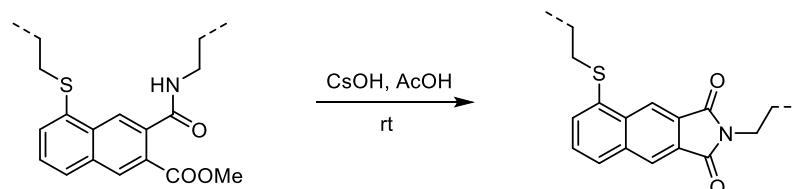


Figure 11: LCMS spectra of **4** after treatment with acetic acid and cesium hydroxide in DMF for 3 d under N₂. Reprinted with permission from P. H. Maag *et al.*, *Macromolecules* **2022**, 55 (22), 9918-9924. Copyright 2022 American Chemical Society.

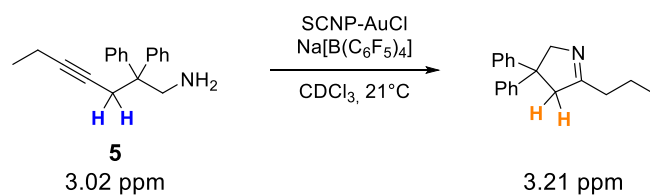
Reactions similar to the one proposed in Scheme 18 are known in the literature, with early reports from Balenović *et al.* (1957).^[139]



Scheme 18: Proposed reaction scheme for the naphthalene formation within SCNPs.

4.2.3 SCNP-AuCl catalyzed intramolecular hydroamination

To demonstrate the catalytic activity of **SCNP-AuCl**, an intramolecular hydroamination of an aminoalkyne (**5**)^[118] was undertaken as previously reported by Bohlen and Kulendran *et al.*,^[118] serving as a benchmark reaction (Scheme 19, refer to Chapter 9.3.7 in the experimental section).



Scheme 19: Intramolecular hydroamination of 2,2-diphenylhept-4-yn-1-amine (**5**) utilizing **SCNP-AuCl** as catalyst and $\text{Na[B(C}_6\text{F}_5)_4]$ as cocatalysts forming a nitrogen-containing heterocycle.

To monitor the conversion, a sequence of ^1H NMR spectra was recorded at constant 21°C (Figure 12). The conversion was calculated by comparing the integrals of the characteristic resonances of substrate **5** (3.02 ppm) and the product (3.21 ppm), using ferrocene (4.19 ppm) as an internal standard (equation 5).

$$X_S = 1 - \frac{\int (\text{CH}_2)_S}{\int (\text{CH}_2)_S + \int (\text{CH}_2)_P} \quad \mathbf{5}$$

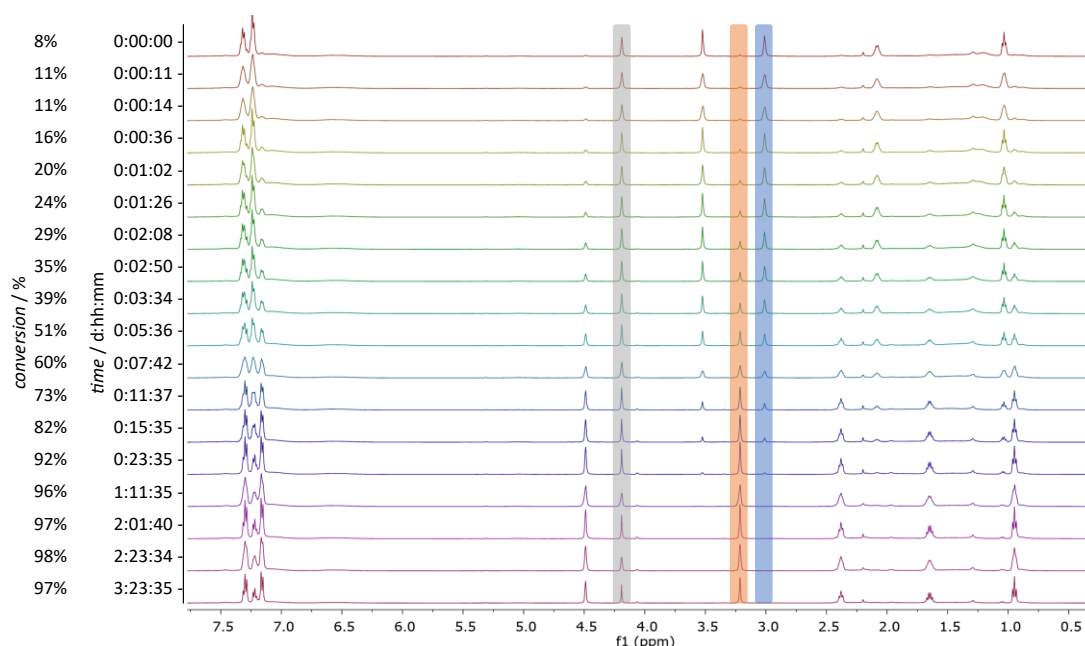


Figure 12: ^1H NMR spectra of the hydroamination of **5** with 2 mol% **SCNP-AuCl** as a time series recorded in CDCl_3 . The conversion was calculated from the marked resonances: internal standard ferrocene (4.19 ppm, grey), product (3.21 ppm, orange) and **5** (3.02 ppm, blue). Reprinted with permission from P. H. Maag *et al.*, *Macromolecules* **2022**, 55 (22), 9918-9924. Copyright 2022 American Chemical Society.

Additionally, to evaluate the impact of the folded SCNPs design, the catalytic activity of the SCNPs was compared with linear polymer chains containing incorporated $\text{AuCl-PPh}_2\text{Sty}$ units

(P4) and molecular AuCl-PPh₂Sty complexes. The catalyzed intramolecular hydroamination requires the cocatalyst Na[B(C₆F₅)₄], which was tested in a control experiment with no catalytic activity (blank). The catalyst, along with ferrocene as an internal standard, was dissolved in CDCl₃ and mixed with the cocatalyst. Fully dissolved, the mixture was frozen, and the substrate (5) was added. The sample was thawed prior to the sequence of ¹H NMR spectra. Figure 20 illustrates the determined conversion rates of the catalysis at varying concentrations of SCNP-AuCl.

Furthermore, the SCNPs were compared with linear polymer chains with incorporated AuCl-PPh₂Sty units (P4) and AuCl-PPh₂Sty complexes to study the effect of the local surroundings of the SCNPs. A cocatalyst Na[B(C₆F₅)₄] was used and tested in a control experiment, which showed no catalytic activity (blank). The catalyst and ferrocene (internal standard) were dissolved in CDCl₃ and mixed with the cocatalyst. After dissolving, the mixture was frozen and the substrate (5) was added. The sample was thawed before recording the ¹H NMR spectra over time. The conversion for different concentrations of SCNP-AuCl and reference experiments is depicted in Figure 13.

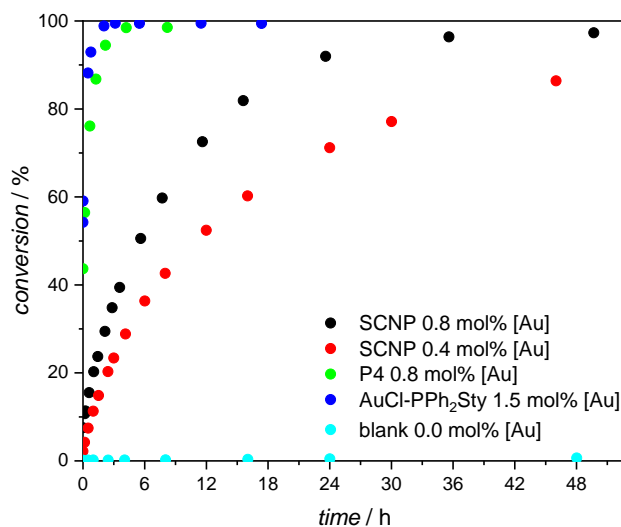


Figure 13: Kinetics of the catalyzed intramolecular hydroamination monitored by ¹H NMR with calculated conversion for SCNP-AuCl (0.8 mol%, 0.4 mol% [Au]), P4 (0.8 mol% [Au]) and AuCl-PPh₂Sty (1.5 mol% [Au]). Na[B(C₆F₅)₄] was used as cocatalyst and tested in a control experiment, which showed no catalytic activity (blank). Reprinted with permission from P. H. Maag *et al.*, *Macromolecules* **2022**, 55 (22), 9918-9924. Copyright 2022 American Chemical Society.

The mole fraction of gold was quantified using ³¹P NMR spectroscopy, using triphenyl phosphate as an internal standard, and is based on the amount of substrate. These results demonstrate the catalytic activity of SCNP-AuCl in the intramolecular hydroamination of 5

used as benchmark reaction. The conversion rate exceeding 90% after 24 hours using a catalyst concentration of 0.8 mol% [Au] relative to the substrate. Higher catalytic activities were observed for **P4** and AuCl-PPh₂Sty. However, the primary aim of SCNPs is not to surpass in catalytic activity but rather to be more selective, as their natural analogues, i.e. enzymes.

The recorded data of the SCNPs-AuCl catalyzed intramolecular hydroamination of **5** with 0.8 mol% [Au] were also used to determine the reaction order of the reaction. The relative concentration of the substrate $[S]_{rel}$ was determined from the ¹H NMR spectra (**5**: 3.02 ppm, shown in Figure 12) using ferrocene (4.19 ppm) as internal standard. $[S]_{rel}$ was plotted over time, showing an exponential decrease. The logarithm of $[S]_0/[S]_t$ was plotted over time and fitted with a linear fit ($[S]_{rel} = 100\% - 10\%$, Figure 14). The linear correlation indicates a first order reaction with a reaction rate coefficient (k) of $1.53 \cdot 10^{-3} \text{ s}^{-1}$ (2.20 d^{-1}).

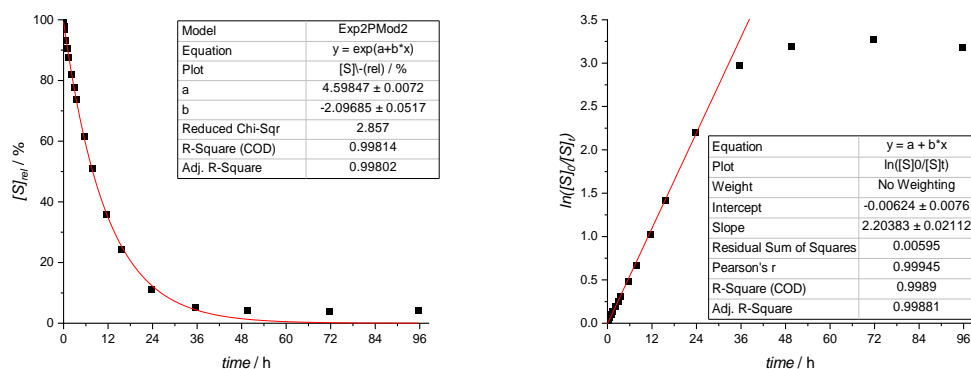


Figure 14: Left: $[S]$ over time of the SCNPs-AuCl catalyzed intramolecular hydroamination with 0.8 mol% [Au]. Right: $\ln([S]_0/[S]_t)$ over time and fitted with a straight line. Reprinted with permission from P. H. Maag *et al.*, *Macromolecules* **2022**, 55 (22), 9918-9924. Copyright 2022 American Chemical Society.

Furthermore, the turnover frequency (TOF) was calculated *via* equation 6 using the turnover number (TON) and time at 90% conversion. These results underline the kinetics with a TOF of the unfolded polymer chain **P4** (68 h^{-1}), which is 13 times higher than the folded SCNPs-AuCl (5 h^{-1}).

$$TOF = \frac{dTON}{dt} \quad \mathbf{6}$$

The TON was calculated using the amount of gold determined by ³¹P NMR spectroscopy and the amount of substrate (**5**, 30.75 mg). However, the implementation of the catalyzation and the determination of the gold fraction by ³¹P NMR with triphenyl phosphate as internal standard and thereby the calculation of TOF was beset with a significant error.

Table 3: TON and TOF for the catalyzed intramolecular hydroamination of 5.

Catalyst	^{31}P J ^a	m(PO ₄ Ph ₃) ^b mg	[Au] ^c mol%	TON _{90%} ^d	t _{90%} ^e h	TOF _{90%} ^f h ⁻¹
SCNP-AuCl	0.36	0.8411	0.8	113	22.1	5
P4-AuCl	1.08	0.2595	0.8	113	1.7	68
AuCl-PPh ₂ Sty	1.20	0.4666	1.5	61	0.6	102

^aIntegral of the ^{31}P NMR spectroscopy of AuCl-PPh₂Sty units compared to ^bthe internal standard PO₄Ph₃. ^cMole fraction of gold compared with the substrate, measured by ^{31}P NMR with triphenyl phosphate as internal standard. ^dTON_{90%}: turnover number for a conversion of 90%. ^eTime to reach a conversion of 90%. ^fTOF_{90%}: turnover frequency for a conversion of 90%.

Comparing **SCNP-AuCl** with **P4** (poly(Sty-co-CMS-co-AuCl-PPh₂Sty), $M_n = 20 \text{ kg mol}^{-1}$) it must be considered that the polymers are not identical in molecular weight and chemical structure.

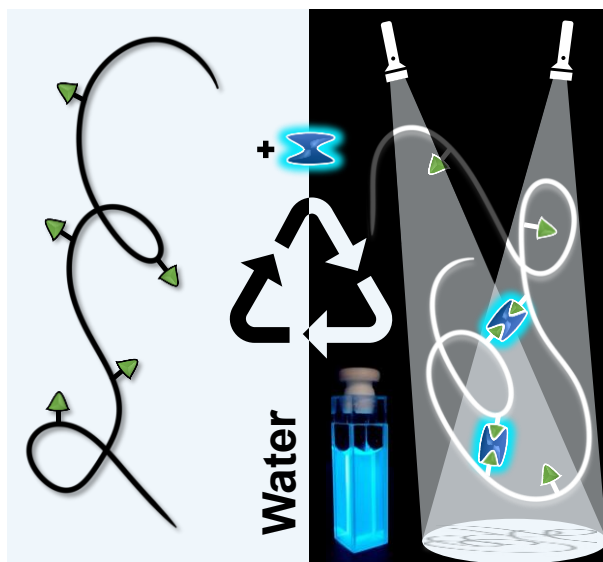
4.3 Summary

Herein, we successfully synthesized SCNPs utilizing a visible light induced Diels–Alder cycloaddition. We were able to equip such SCNPs with gold(I) and demonstrate their catalytic activity. Even though these SCNPs are not water soluble, they form the first step to mimic their natural analogues, i.e. enzymes. Furthermore, the fluorescent cross-links provided a visual read-out of their folding state.

The fluorescent and catalytically active SCNPs were synthesized, based on linear styrene copolymer (**P1**, poly(Sty-co-CMS-co-S=PPh₂Sty)). The precursor polymer contains protected phosphine moieties and CMS, which are functionalized with a photocaged diene and alkyne moieties, resulting in a photoreactive parent polymer (**P3**). Under irradiation with visible light ($\lambda_{\text{max}} = 415 \text{ nm}$), a [4+2] cycloaddition takes place, leading to the formation of pro-fluorescent intramolecular cross-links within the folded **SCNP1**. The compaction process was monitored using SEC and DOSY NMR spectroscopy, both of which showed a decrease in the hydrodynamic radius after cross-linking. Taking advantage of the tailored SCNPs, gold-complexes were introduced to enable catalysis. An intramolecular hydroamination reaction was monitored using ^1H NMR, with **SCNP-AuCl** as catalyst. The conversion exceeded 90% after 24 hours at 0.8 mol% [Au] per substrate. As the fluorescent properties of **SCNP-AuCl** are a direct result of its cross-linking and not due to an additional fluorophore, they allow for a visual read-out of the folding state.

In the current project, the compaction of linear polymer chains using visible light was applied. The next Chapter will expand on photoinduced control over SCNPs by investigating the reverse process e.g. the unfolding of SCNPs by light. Furthermore, we focus on water-soluble SCNPs to increase the biocompatibility to enable biomedical tracing and imaging applications.

5 Visible Light Induced Control over Reversible Single-Chain Nanoparticle Folding



Abstract: Bimanes allow for the synthesis of water-soluble single-chain nanoparticles (SCNPs) and enable the effective unfolding with visible light from a compact structure into a linear chain. The unfolding of the fluorescent nanoparticles is reversible and occurs in aqueous systems, making it promising for controlling and tracing the SCNPs in biological environments. Reprinted with permission from P. H. Maag *et al. Angew. Chem. Int. Ed.* **2023**, 62, e202309259. Open access under a CC BY-NC 4.0 DEED license by John Wiley & Sons.

5.1 Motivation

Chapter 4 focused on catalytically active SCNPs folded by a light induced [4+2] cycloaddition. In the current Chapter, the rarely investigated reverse process is explored e.g. the light induced unfolding of SCNPs. In addition, we combine the ability of remote unfolding with water solubility of the polymer to enable application in a biological environment. Similar to the previous Chapter, the cross-linking units are fluorescent and thereby allow for a simple read-out of the folding state, paving the way towards biomedical tracing and imaging applications with SCNPs.

The structure and functionality of soft-shell particles such as SCNPs can be tailored for application in different fields, e.g. catalysis^[140] (demonstrated in Chapter 4) and sensing,^[141] but also for biomedical science.^[16, 122, 142] Particularly in biomedical contexts, SCNPs are

gaining attention due to their size (3 to 20 nm) and their ability to mimic proteins in functionality and folding.

As discussed in the introduction of the present thesis, biocompatible SCNPs are primarily explored in drug delivery, target imaging, and enzyme mimicry.^[18] For their biomedical efficacy, the size and compaction of SCNPs plays an important role, influencing their cellular uptake^[19] in biomedical application. The ability to change particle size and compaction remotely with spatiotemporal control could allow a change in cellular uptake as one area of interest and therefore advancing controlled drug delivery, cell labeling, and imaging techniques.^[21, 22] However, current methods for remote control of SCNP folding and unfolding are limited, especially in biomedical contexts since many conventional processes are incompatible with water.^[23-25] In the realm of biological applications, utilizing visible light is essential to prevent the degradation of biomolecules, thereby imposing limitations on the available options.^[143, 144]

Light, especially visible light, emerges as a prime candidate for triggering SCNP unfolding due to its precise spatiotemporal control capabilities and minimal photodamage, facilitating tissue penetration.^[143] However, the selection of photochemical reactions suitable for this purpose is limited. Within SCNPs, the internal environment markedly influences photoreaction kinetics, favoring certain reactions over others, which poses additional challenges in biomedical applications.^[128, 129] Photocycloadditions e.g. [2+2] cycloadditions exhibit a higher kinetic preference within the high local concentration of SCNPs as compared to the corresponding photocycloreversion process. This preferential behavior effectively hinders the unfolding of SCNPs triggered by photocycloreversion.^[145]

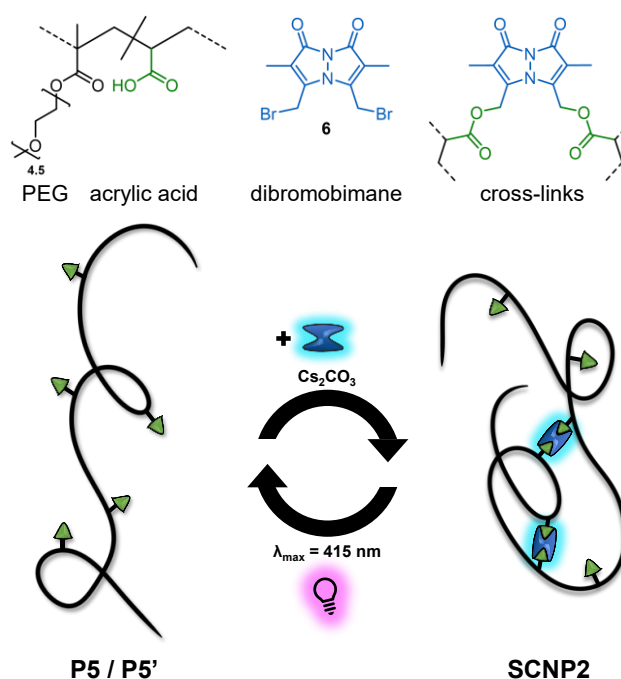
In the current Chapter, the unfolding of SCNPs is presented using visible light as an external trigger. Bimane moieties, a heterocyclic fluorescent molecule characterized by Kosower and co-workers, are utilized as photolabile linkage points.^[100, 103, 146, 147] The bimanes undergo cleavage under mild conditions, resulting in an unfolded, reusable polymer. We were able to control folding and unfolding of a water-soluble single polymer chain. By integrating fluorescent moieties into a water-soluble system, we extend SCNPs' potential towards biocompatibility, paving the way for enhanced tracing and imaging applications.^[64, 101, 102]

For the results described in the current chapter, the diffusion ordered NMR spectra of **P5**, **SCNP2** and **P5'** were recorded by Aaron Micallef. Daniel Kodura and Vinh X. Truong performed preliminary experiments of the photocleavage of bimanes, which preceded the

project. C. Barner-Kowollik, P. W. Roesky, H. Frisch and F. Feist motivated and supervised the project. The chapter “Visible Light Induced Control over Reversible Single-Chain Nanoparticle Folding” is adapted from P. H. Maag, F. Feist, V. X. Truong, H. Frisch, P. W. Roesky, C. Barner-Kowollik, *Angew. Chem. Int. Ed.* **2023**, 62, e202309259 with permission from John Wiley & Sons. AI-based language models were used to improve readability and spelling (*OpenAI* (2024) ChatGPT 4).

5.2 Results and Discussion

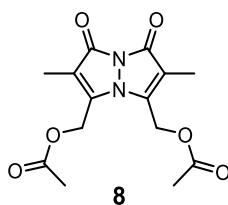
In the following section, we describe our strategy for unfolding SCNPs by visible light, which results in the original linear polymer chains and enables subsequent refolding. The process utilizes fluorescent bimane cross-links, which are capable of photocleavage under light irradiation. Scheme 20 illustrates the reversible folding process of the water-soluble linear polymer chain.



Scheme 20: Folding and unfolding of poly(MPEGMA-*co*-acrylic acid), utilizing dibromobimane **1** as fluorescent, photoreactive cross-linker. In the folding reaction, the acrylic acid (AA) units react in a base-mediated SN2 reaction with **1**. The generated cross-links can be cleaved by visible light resulting in the original polymer and dihydroxybimane **2**. Reprinted with permission from P. H. Maag *et al.* *Angew. Chem. Int. Ed.* **2023**, 62, e202309259. Open access under a CC BY-NC 4.0 DEED license by John Wiley & Sons.

5.2.1 Bimane photoinduced ester cleavage

The photolysis of bimane caged esters was reported by Chaudhuri *et al.*^[103] and is described in the theoretical background section 2.3.4. To further study the bimane cleavage reaction used to unfold the SCNPs into linear polymer chains, the photoreaction was performed with a molecular bimane caged acetate ester (**8**, Scheme 21) under similar conditions to the SCNPs unfolding.



Scheme 21: Bimane caged acetate ester ((2,6-dimethyl-1,7-dioxo-1H,7H-pyrazolo[1,2-a]pyrazole-3,5-diyl)bis(methylene) diacetate, **8**).

Therefore **8** was dissolved in water, degassed by passing through a stream of N₂, and the solution irradiated with $\lambda_{\text{max}} = 415$ nm for 30 min (refer to Chapter 9.3.9 in the experimental section). The subsequently freeze-dried reaction mixture was analyzed by LC-MS, showing the formed monohydroxybimane **9** and dihydroxybimane **7** along with a small amount of an unknown side product (Figure 15). After 30 min of irradiation, the reaction mixture still contained a significant amount of educt which can easily be adjusted by changing the concentration, the irradiation intensity or the reaction time. The quantitative and a fast cleavage shows the potential of bimane moieties as photocleavable cross-linking units.

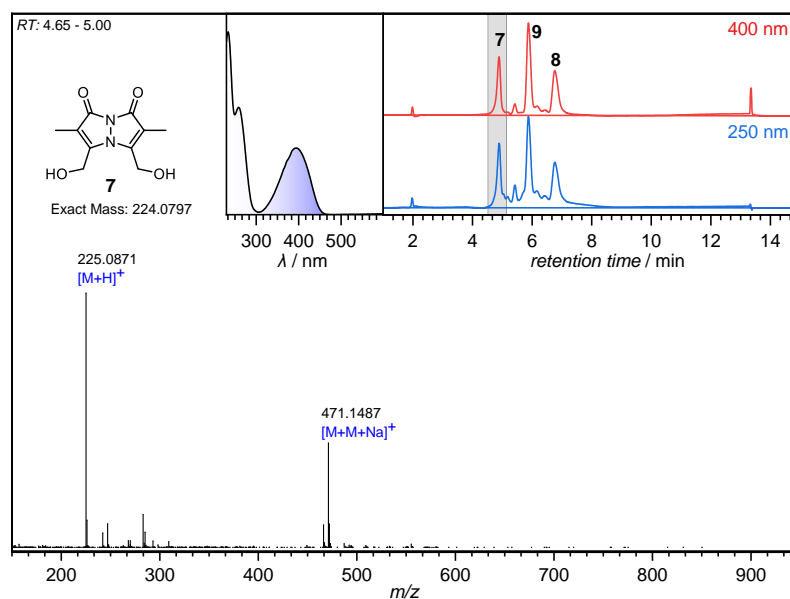


Figure 15: LC-MS trace (250 nm, 400 nm detector wavelength), absorption spectra and accumulated mass spectra of irradiation products and side products of **8**. Reprinted with permission from P. H. Maag *et al. Angew. Chem. Int. Ed.* **2023**, 62, e202309259. Open access under a CC BY-NC 4.0 DEED license by John Wiley & Sons.

5.2.2 Synthesis of water-soluble SCNPs

The polymeric backbone of the SCNPs was designed to be water-soluble, allowing for application in biological systems, but to also support the bimane cleavage reaction as described in the theoretical background 2.3.4. The polymer was synthesized by reversible addition fragmentation chain transfer (RAFT) copolymerization of poly(ethylene glycol) methyl ether methacrylate (MPEGMA, $M_n = 300 \text{ g mol}^{-1}$) and acrylic acid (AA). The monomer composition within the polymer was 16% AA units, as shown by ^1H NMR spectroscopy in deuterated chloroform. The resonances of the solvent DMF ($(\text{CH}_3)_2\text{NC(O)H}$, 7.62 – 8.59 ppm) were used as internal standard to calculate the monomer conversion after 22 h of polymerization, resulting in a conversion of 79 mol% MPEGMA and 46 mol% AA. Figure 16 shows the crude ^1H NMR spectra before and after 5 and 22 h of reaction time, respectively.

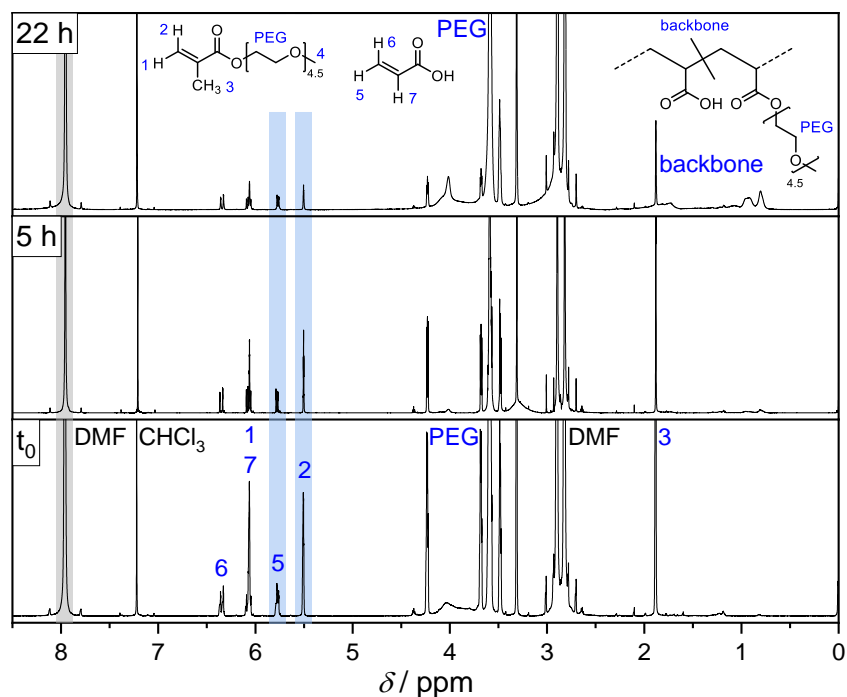


Figure 16: ^1H NMR spectrum of the reaction mixture before and after copolymerization for 5 and 22 h. The spectrum obtained after 22h was used for the calculation of the copolymer composition. Reprinted with permission from P. H. Maag *et al.* *Angew. Chem. Int. Ed.* **2023**, 62, e202309259. Open access under a CC BY-NC 4.0 DEED license by John Wiley & Sons.

Based on the conversion, the monomer composition within the copolymer poly(MPEGMA-*co*-AA) was calculated to be 84 mol% MPEGMA units and 16 mol% AA, while taking the equivalents of the reactant used into account (Table 4).

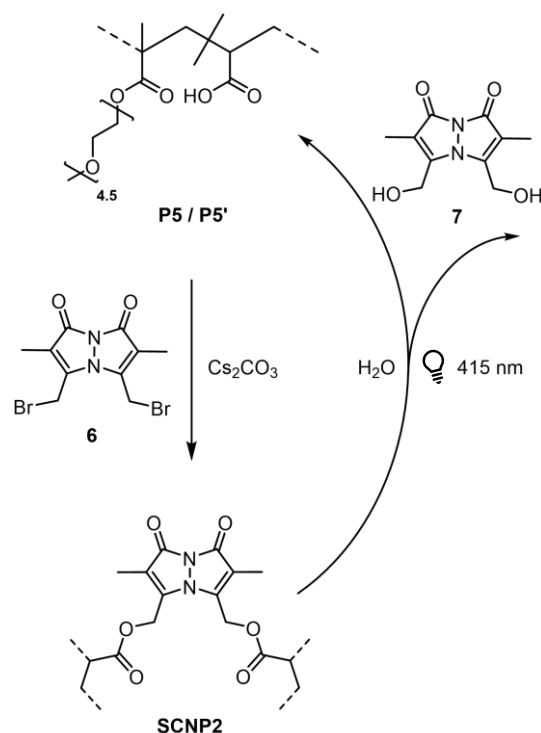
Table 4: Analysis of copolymer composition by conversion of the polymerization.

Monomer	Group	^1H f -Area ppm	conversion %	eq	composition %
MPEGMA	$\text{CH}_3\text{C}=\text{CH}_2$	5.45 – 5.57	78.6	300	84
AA	$\text{HC}=\text{CH}_2$	5.72 – 5.82	45.5	100	16

The monomer conversion also enabled calculation of the theoretical molecular weight (M_{theo}), which can be used for further calculation and is more accurate than the apparent molecular weight measured by SEC or DOSY because of the grafted copolymer structure. M_{theo} is calculated based on the monomer conversion multiplied with the equivalents of monomer units per RAFT agent, considering the molecular weight of the monomers, resulting in $M_{\text{theo}} = 74.02 \text{ kg mol}^{-1}$. The theoretical molecular weight is expected to be higher than the

molecular weight obtained by SEC due to the PEG side chains and the applied PMMA calibration.

To prepare the polymer backbone for further modification and photoreactions, the RAFT end-groups were hydrolyzed to form hydroxy groups (refer to Chapter 9.5.5 in the experimental section)^[60] affording poly(MPEGMA-*co*-AA) (**P5**, $M_n = 36.53 \text{ kg mol}^{-1}$, $D = 8.53 \pm 0.23 \cdot 10^{-11} \text{ m}^2 \text{ s}^{-1}$, $R_H = 4.62 \pm 0.13 \text{ nm}$, $x_{AA} = 16\%$). The RAFT end-groups could otherwise undergo side reactions and affect the photo cleavage. Additionally, the apparent molecular weight (M_n) was determined by size exclusion chromatography (SEC) based on the hydrodynamic volume of the polymer in dimethylacetamide. To support these data, the diffusion coefficient, D , was determined by diffusion-ordered spectroscopy (DOSY) in deuterated chloroform. The diffusion coefficient D can be inserted into the Stokes-Einstein equation to calculate the hydrodynamic radius (R_H). The end-group modified polymer **P5** was cross-linked into SCNPs by an esterification reaction of the carboxylic acid pendant groups with dibromobimane **6** in a highly diluted solution in tetrahydrofuran (THF, 0.2 mg mL^{-1}) and cesium carbonate as base (**SCNP2**, $M_n = 31.34 \text{ kg mol}^{-1}$, $D = 1.14 \pm 0.05 \cdot 10^{-10} \text{ m}^2 \text{ s}^{-1}$, $R_H = 3.46 \pm 0.16 \text{ nm}$, refer to Chapter 9.6.2 in the experimental section). Scheme 22 illustrates the folding reaction as well as the light induced unfolding.



Scheme 22: Synthesis route for folding poly(MPEGMA-co-acrylic acid) (**P5**) with dibromobimane **6** in an esterification reaction with the AA units using cesium carbonate as base resulting in **SCNP2**. The bimane caged esters – functioning as cross-links – can be cleaved by visible light, resulting in the original polymer and dihydroxybimane **7** as side product. Reprinted with permission from P. H. Maag *et al. Angew. Chem. Int. Ed.* **2023**, *62*, e202309259. Open access under a CC BY-NC 4.0 DEED license by John Wiley & Sons.

During the intramolecular cross-linking reaction, the hydrodynamic volume of the polymer decreased, resulting in a decrease of the apparent molecular weight by 17% (refer to SEC, Figure 17). This compaction can be evidenced by the shift of the **SCNP2** SEC retention time compared to the **P5** (red arrow). The SCNP formation was further monitored by the UV/VIS absorption of the polymer in the SEC elugram, normalized by the refractive index detection (RID), returning the amount of incorporated bimane units within the polymer. We observed a linear increase in absorption over time at 400 nm, the absorption maxima of bimane, which correlated with the decrease in molecular weight and confirmed the incorporation and role as cross-linking agents of the bimane units. The linear increase of absorption indicates a constant incorporation of bimane units, which might occur from the low concentration of bimane and carboxylic acid pendant groups in THF, resulting in a concentration independent trend. A higher bimane ratio may lead to an increased reaction rate, but also incorporate single binding bimanans, which do not contribute to cross-linking. However, the apparent molecular weight indicates a higher compaction rate at the beginning of the cross-linking reaction.

5.2.3 Photoinduced unfolding of SCNPs

Next, we unfolded the bimane cross-linked **SCNP2** by irradiation with visible light ($\lambda_{\max} = 415$ nm) in an aqueous solution, cleaving the ester bonds and releasing dihydroxybimane **2** and the original polymer with carboxylic acid groups (**P5'**, $M_n = 37.29 \cdot 10^3$ g mol⁻¹, $D = 6.97 \pm 0.20 \cdot 10^{-11}$ m² s⁻¹, $R_H = 5.65 \pm 0.17$ nm, refer to Chapter 9.7.2 in the experimental section). The unfolding process of **SCNP2** was monitored using SEC and DOSY measurements. The unfolding was visually observed in the SEC traces by a shift in the elution time of **P5'** compared to **SCNP2** (blue arrow), indicating an increase in the hydrodynamic volume, which results in an increase in the apparent molecular weight by 19%.

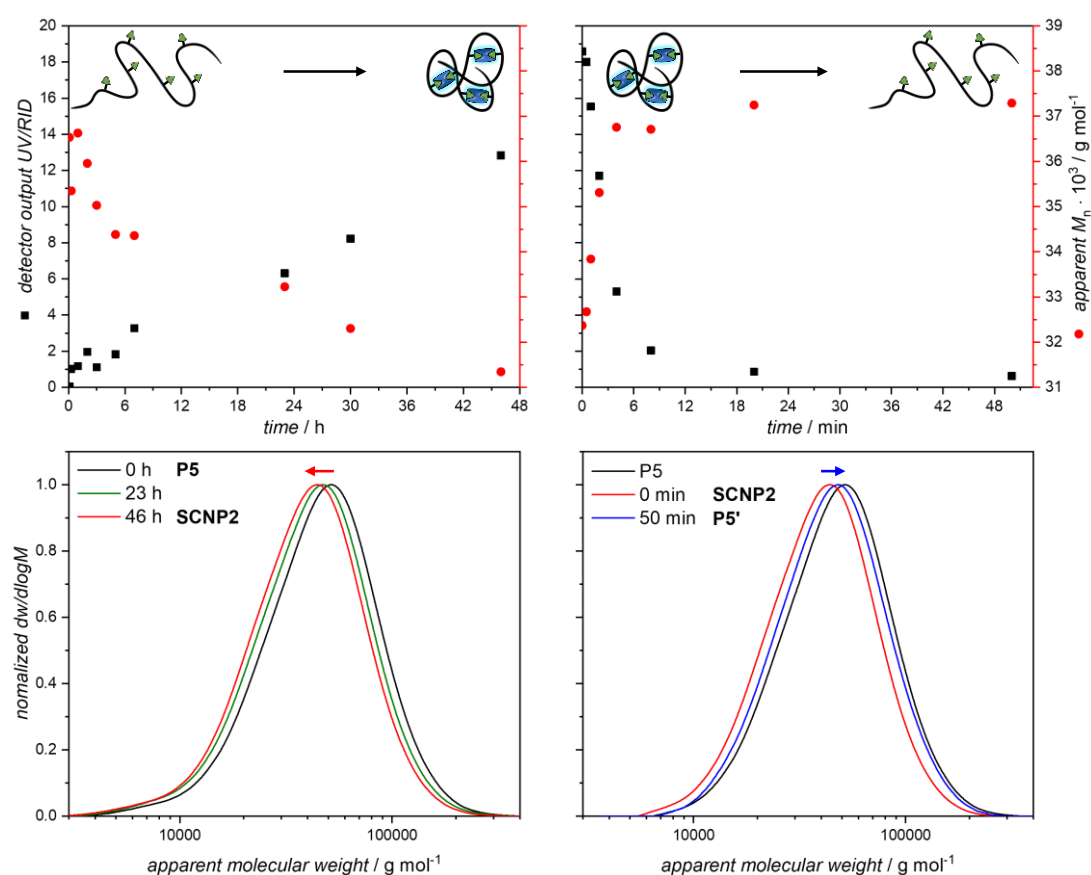


Figure 17: **Top left:** Kinetics of the folding reaction of **P5** to **SCNP2** monitored by UV/VIS absorption at 400 nm and apparent molecular weight determined by size SEC. The cross-linking of the polymer chain leads to a higher compaction and consequently to a smaller hydrodynamic volume appearing with a smaller molecular weight in the SEC. **Bottom left:** RID SEC traces of **P5** folding to **SCNP2**. **Top right:** Kinetics of the unfolding reaction of **SCNP2** to **P5'** by irradiation with visible light monitored by UV/VIS absorption at 400 nm and apparent molecular weight by SEC. The cleavage of the cross-links leads to unfolding and consequently to a higher hydrodynamic volume appearing with a higher molecular weight in the SEC. **Bottom right:** RID SEC traces of **SCNP2** unfolding to **P5'** compared to **P5**. Reprinted with permission from P. H. Maag *et al. Angew. Chem. Int. Ed.* **2023**, 62, e202309259. Open access under a CC BY-NC 4.0 DEED license by John Wiley & Sons.

The observed shift in the SEC elugram during unfolding (toward **P5'**) does not appear as pronounced as in the initial folding (toward **SCNP2**), even though both polymers (**P5** and **P5'**) must have similar molecular weights (refer to SEC, Figure 17). The incomplete unfolding may be caused by remaining bimane cross-links tethered to the polymer chain or by side reactions occurring during the photocleavage of the ester bonds. During irradiation, the UV/VIS absorption of the polymer in the SEC trace decreases asymptotically, indicating high cleavage of the bimane units from the polymer as the polymer does not absorb light at 400 nm. Consequently, the apparent molecular weight response with a simultaneous increase.

The pH was measured during the unfolding to evidence the release of the carboxylic acid groups by photocleavage. The pH value decreased rapidly within the first 5 min of irradiation, aligning with the kinetics monitored using absorption and molecular weight. The lower pH values indicate the release of the carboxylic acid groups and a full recovery of the original polymer (Figure 18).

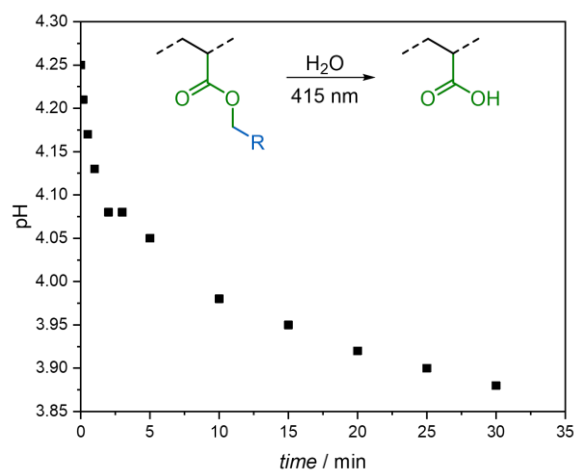


Figure 18: pH-value over time during radiation of **SCNP2** (25 mg) in 80 mL water. Reprinted with permission from P. H. Maag *et al. Angew. Chem. Int. Ed.* **2023**, 62, e202309259. Open access under a CC BY-NC 4.0 DEED license by John Wiley & Sons.

The change in the pH value during the reaction was recorded using a similar setup as during the **SCNP2** unfolding, equipped with a pH meter within the reaction mixture (refer to Chapter 9.2 in the experimental section). The aqueous solution was degassed by passing through a stream of nitrogen, which was continued during irradiation.

In addition, the diffusion coefficient (D) was determined by DOSY measurements to support the shifts in the molecular weight during folding and unfolding observed by SEC. The results show the same trend, an increase of D by close to 34% after folding. Consequently, the

calculated R_H decreases from 4.62 ± 0.13 nm (**P5**) to 3.46 ± 0.16 nm (**SCNP2**, Figure 19) indicating the compaction.

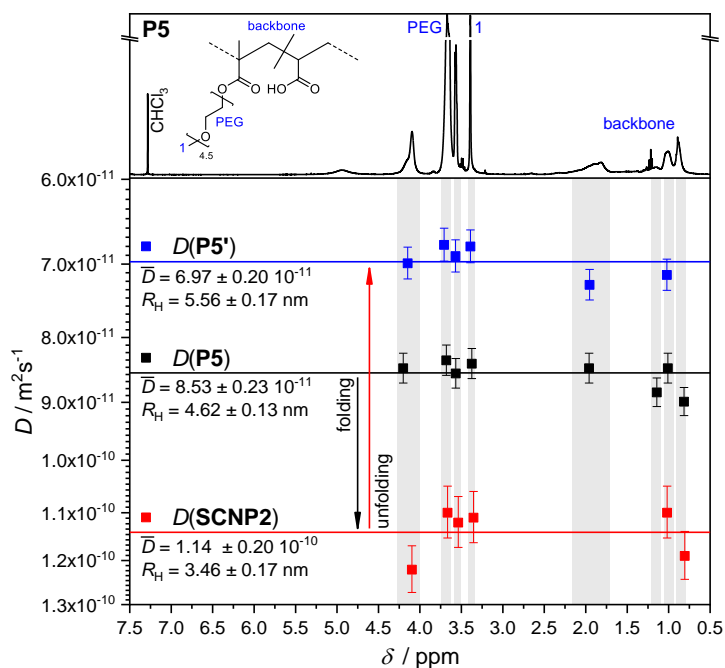


Figure 19: Diffusion coefficients (D) determined by diffusion-ordered spectroscopy (DOSY) in deuterated chloroform of integrated polymer resonances for the original polymer **P5**, the folded **SCNP2** and the unfolded **P5'**. The defined integrals are compared with the ^1H NMR spectrum of **P5** displayed above. The D of the corresponding chemical shifts is displayed as a colored square (\blacksquare) within the integral areas. For each polymer, the arithmetic mean was calculated and displayed as a colored line (—), wherefrom the hydrodynamic radius (R_H) was calculated. D increased after folding, correlated with a smaller R_H and decreases after irradiation, indicating an unfolding of the SCNPs. Reprinted with permission from P. H. Maag *et al. Angew. Chem. Int. Ed.* **2023**, 62, e202309259. Open access under a CC BY-NC 4.0 DEED license by John Wiley & Sons.

D decreased by 63.5% after unfolding, resulting in an increased R_H of 5.65 ± 0.17 nm (**P5'**). We assume that the higher R_H might be caused due to the same factors which cause the less pronounced shift in the SEC trace. Remaining bimane moieties could influence the hydrodynamic volume of the polymer, depending on the solvent. This could lead to slightly different trends of R_H in dimethylacetamide (SEC) and chloroform (DOSY).

5.2.4 Cross-linking density of SCNPs

Different methods were used to quantify the cross-linking density in both the SCNPs and the unfolded polymer (**P5'**). The first approach compared ^1H NMR resonances of the polymer backbone with the resonances from the cross-linking units. The second approach attempted to determine the cross-linking density indirect based on the ^1H NMR resonances of the

cleaved dihydroxybimane **7** after irradiation. Lastly, the molar absorption coefficient of the bimane caged acetate ester (**3**) was compared to the absorption spectra of **SCNP2** and **P5'**.

The first method determines the cross-linking density of **SCNP2** and unfolded polymer (**P5'**), by comparing the backbone resonances with the resonances from the cross-linking units. Therefore ^1H NMR spectra of **P5**, **SCNP2** and **P5'** were recorded and compared. The resonances of the cross-linking bimane (indicated with a blue 2 and 3 in Figure 20) are expected at close to 5.1 ppm (2, CH_2) and 2.1 ppm (3, CH_3), respectively. The CH_2 -groups are observed as a broad resonance in the 5.0 to 5.5 ppm range after the SCNP formation (**SCNP2**). The resonances of the CH_3 -groups overlap with the backbone (CH , CH_2), but an increase in the integral area was measured after folding. Upon unfolding, the integral areas of both resonances decrease again, indicating a successful release. These data provide qualitative support for the folding and unfolding processes, although they do not allow for precise calculation of the exact cross-linking density due to high experimental uncertainty.

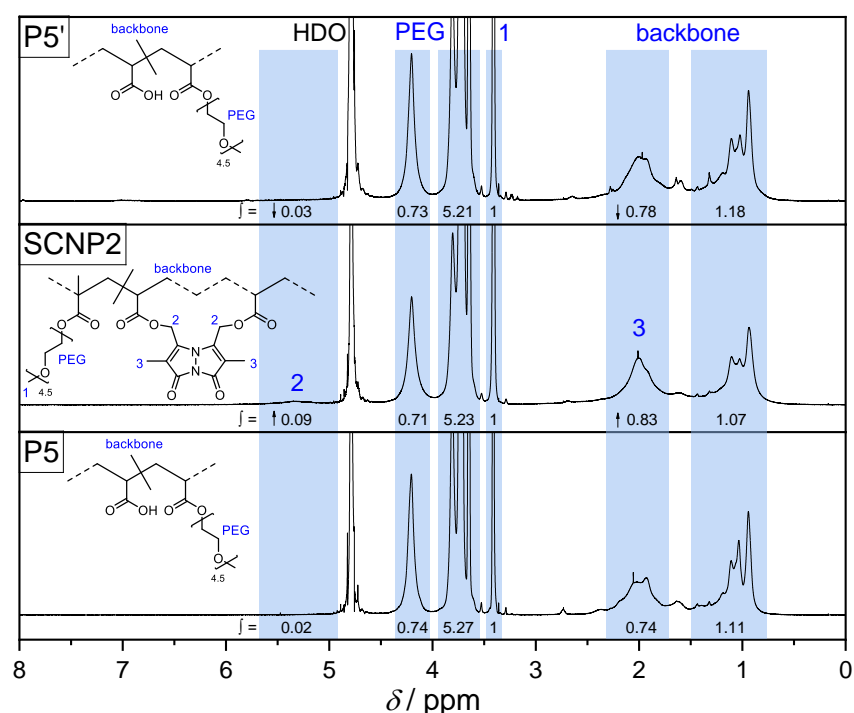


Figure 20: ^1H NMR of the original polymer (**P5**), folded (**SCNP2**) and unfolding (**P5'**) polymer with integrals areas compared to the backbone. Reprinted with permission from P. H. Maag *et al.* *Angew. Chem. Int. Ed.* **2023**, 62, e202309259. Open access under a CC BY-NC 4.0 DEED license by John Wiley & Sons.

Another indirect way to determine the cross-linking density is to determine the quantity of the cleaved dihydroxybimane **7** after irradiation. Therefore, ^1H NMR spectra of **SCNP2** were

compared with **P5'** after irradiating for 20 min with 415 nm LED in D₂O without purification. The resonances of the cleaved dihydroxybimane **7**, indicated by the blue numbers 3 and 4 in Figure 21 are integrated and compared with the methyl group of the MPEGMA side chains.

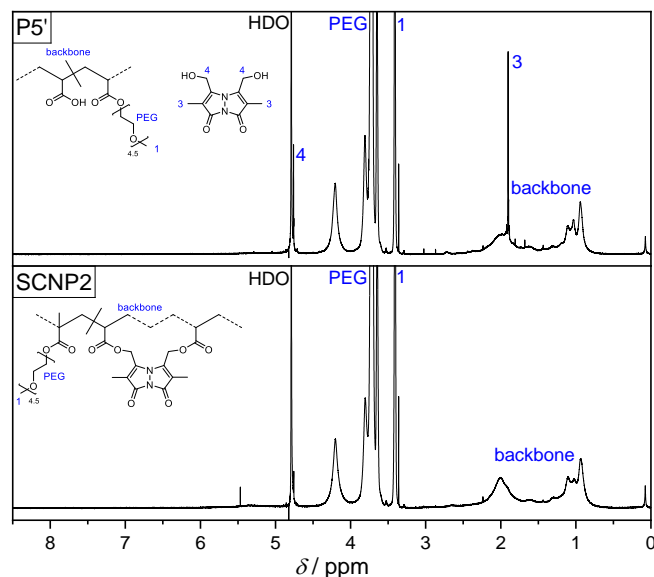


Figure 21: ¹H NMR spectra of **SCNP2** and **P5'** after irradiating for 20 min with 415 nm LED in D₂O. The resonances of the bimane cross-link (CH₃, CH₂) are not separated from the polymer resonances, but can be observed after cleaved of as dihydroxybimane **7** indicated by the blue numbers 3 and 4. Reprinted with permission from P. H. Maag *et al. Angew. Chem. Int. Ed.* **2023**, 62, e202309259. Open access under a CC BY-NC 4.0 DEED license by John Wiley & Sons.

The integral area of the methyl MPEGMA side chains was used to calculate the overall monomer content, based on the monomer cooperation of the copolymer **P5**, as discussed above, of 16% acrylic acid and 84% MPEGMA units. Compared with the integral areas of dihydroxybimane **7**, 1 bimane unit is released per 33 monomer units. Considering the theoretical molecular weight of the polymer calculated from the conversion of the polymerization of 74 kg mol⁻¹, 8.5 bimane units are released per SCNP. This second approach evidences the cleavage of dihydroxybimane **7** during irradiation and provides a minimum estimate on cross-links released. However, the experiment cannot return the absolute number of cross-linking before and after irradiation and systematic error might result from side reactions accruing. Furthermore, the experiment is not directly comparable with the original unfolding experiments of **SCNP2**, as it was performed in an NMR tube and might differ in conversion after 20 min of irradiation due to higher concentrations and differences in light penetration.

In addition to NMR experiments, the cross-linking density of the SCNPs was determined by comparing the molar absorption coefficient of the bimane caged acetate ester (**8**, $\epsilon_{385\text{nm}} =$

$5.91 \pm 0.38 \cdot 10^3 \text{ L mol}^{-1} \text{ cm}^{-1}$), as a close comparison of the bimane cross-links in the SCNPs, with **SCNP2** and **P5'**. **8** was synthesized from **6** with cesium acetate in DMF with an additional purification step by column chromatography on silica gel to remove any impurities (refer to Chapter 9.3.9 in the experimental section). The calculated molar absorption is displayed in Figure 22 for wavelengths between 205 nm and 800 nm in methanol, showing a peak absorbance at 230 nm and 385 nm.

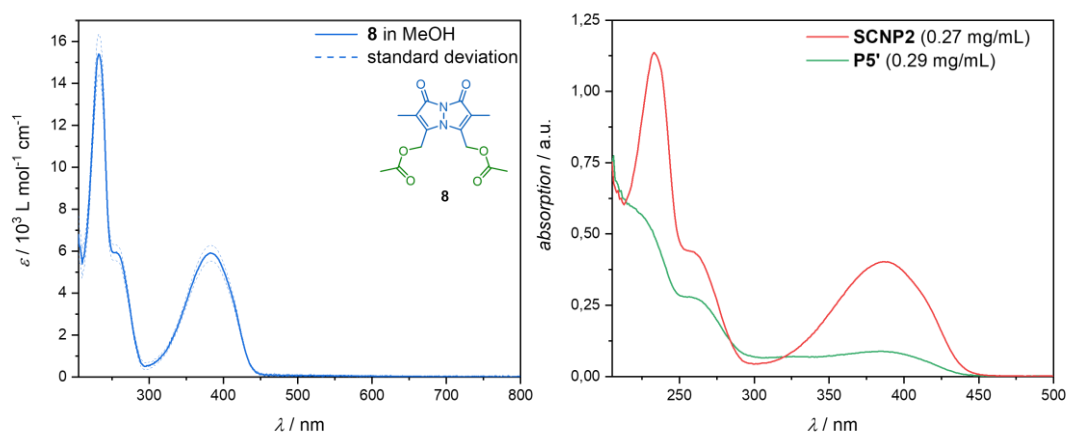


Figure 22: Left: Molar absorption of **8** in methanol with standard deviation. Right: Absorption spectra of **SCNP1** and **P1'** for similar concentrations. Reprinted with permission from P. H. Maag *et al.* *Angew. Chem. Int. Ed.* **2023**, 62, e202309259. Open access under a CC BY-NC 4.0 DEED license by John Wiley & Sons.

Subsequently, the absorbance of both **SCNP2** and **P5'** at the peak absorbance was compared with the molar absorption coefficient of **8**. From it the number of bimane units per polymer chain was determined, using the theoretical molecular weight of the polymer derived from a polymerization conversion of 74 kg mol^{-1} . Using this calculation, **SCNP2** contained 18.5 ± 0.6 bimane units per polymer ($X_{AA} = 81\%$), whereas **P5'** bound 3.6 ± 0.2 bimane units per polymer ($X_{AA} = 16\%$). This corresponded to a decrease of 80% after 20 min of irradiation (Table 5).

Table 5: Calculation of the cross-linking density for **SCNP1** and **P1'**.

Sample	$\epsilon_{3, 385\text{nm}}^{[1]}$ L mol ⁻¹ cm ⁻¹	$SD^{[2]}$	$cd^{[3]}$ mmol g ⁻¹	$SD^{[2]}$	$M_{\text{theo}}^{[4]}$ g mol ⁻¹	$CLD^{[5]}$	$SD^{[2]}$	$X_{AA}^{[6]}$ %	decrease %
SCNP2	5908.80	377	0.2495	0.0084	74019	18.5	0.62	81.2	
P5'	5908.80	377	0.0487	0.0027	74019	3.6	0.20	15.9	80

[1] molar absorption coefficient (ϵ) of **8** at peak absorbance of 385 nm. [2] Standard deviation (SD). [3] Cross-linking density ($cd = n(\text{bimane})/m(\text{polymer})$) calculated from the absorption (a) of the sample at different concentration, $\epsilon(\mathbf{8})$ and the mass concentration (θ) of the samples ($cd = a / \epsilon(\mathbf{8}) / \theta$). [4] Theoretical molecular weight (M_{theo}) obtained from the monomer composition. [5] Number of cross-links per polymer chain ($CLD = cd * M_{\text{theo}}$). [6] Conversion of acrylic acid units (X_{AA}).

The results shown in Table 5 provide an overview of the cross-linking density within the SCNPs, with around 81% functionalized AA units. However, these results come with a significant error as the number of bimane units per polymer is highly dependent on the calculated theoretical molecular weight. The decrease in intensity by 80% aligns with the decrease in the ratio of UV trace at 400 nm with the RID trace observed via SEC during unfolding (Figure 17).

5.2.5 Monte Carlo simulation of bond cleavage

A high degree of unfolding after a cleavage of 80% of bimane units is supported by a Monte Carlo simulation, modelling the probability of single to double bonded bimane units. Experimental results of the ester bond cleavage of **8** over irradiation time showed similar composition of single (**9**) and double (**7**) cleaved bimanies. According to both methods, only one quarter of the remaining 20% bimane units are double bonded (i.e., representing cross-links in SCNPs), whereas the other three quarters are cleaved on one side and do not cross-link the polymer chain anymore.

The Monte Carlo simulation distinguished between units which cross-link the chain (double bonded) and single bonded bimane units, which are cleaved off on one side and do not cross-link the chain. The obtained absorption of the UV/VIS detector normalized by the RID in the SEC trace was proportional to the amount of cleaved bimane units, but does not distinguish between double bonded and single bonded bimane units. This simulation allows us to address this question further and obtain the mathematic probabilities of the double bonded to single bonded bimane units. An important assumption we are making is that single bonded and double bonded bimane units are equal in reactivity towards irradiation. The results are displayed in Figure 23 as percentage of fully cleaved bimane units (*X*-axis), which aligns with the decrease of absorption, against the remaining bimane units (*Y*-axis), which are either single or double bonded to the polymer chain.

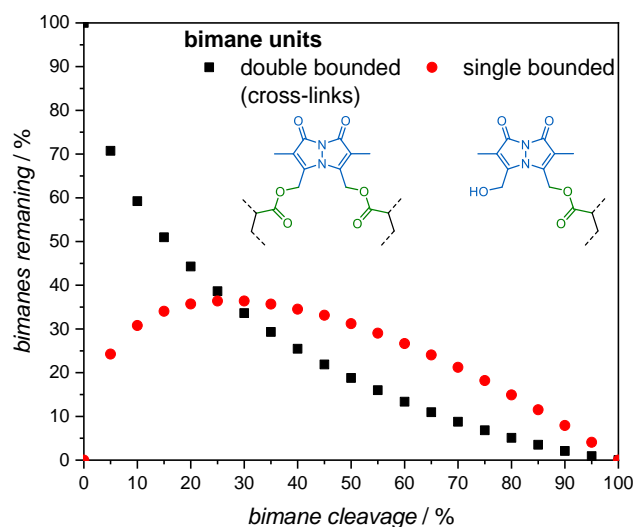


Figure 23: Probability of double bonded and single bonded bimeane units for different conversion simulated by a Monte Carlo method. Reprinted with permission from P. H. Maag *et al. Angew. Chem. Int. Ed.* **2023**, 62, e202309259. Open access under a CC BY-NC 4.0 DEED license by John Wiley & Sons.

For example, after 10% of the bimeane units are cleaved, 90% bimeane units are still attached to the polymer chain, of which around 60% are double bonded and 30% are singly bonded, demonstrating that 40% of SCNPs are already unfolded after a 10% decrease in absorption. The Monte Carlo method simulated this probability of single or double bonded bimeane units for every 5% and lists the results in a table. In the case of our experiment discussed above, where a decrease of 80% in absorption was observed, it is assumed that 80% of the bimeane units were fully cleaved and according to the simulation, 5.1 % of the remaining 20% are double bonded (cross-links) and 14.9 % are cleaved off on one side and do not cross-link the polymer chain. The results support the high degree of unfolding we observe in the SEC traces, which show a similar molecular weight to the original polymer **P5**. The simulation was performed on MatLab R2022b using a code generated by *Bing*, an AI-powered language model (refer to Appendix D: MatLab code).

We supported the simulated probabilities with empiric data. A small molecule analogue to the polymeric cross-links, the bimeane caged acetate ester **8**, was irradiated with 415 nm in degassed water/acetonitrile at ambient temperature. A sequence of samples was taken over time and analyzed by LC-MS. The signals were assigned to dihydroxybimeane **7** ($RT = 4.9$ min), monohydroxybimeane **9** ($RT = 5.8$ min), and **8** ($RT = 6.7$ min). The composition of the main irradiation products is shown in Figure 24. The irradiation time of nearly 90 min until full conversion could have been required due to the addition of acetonitrile to ensure complete solubility or to a higher concentration of bimeane units compared to SCNP unfolding.

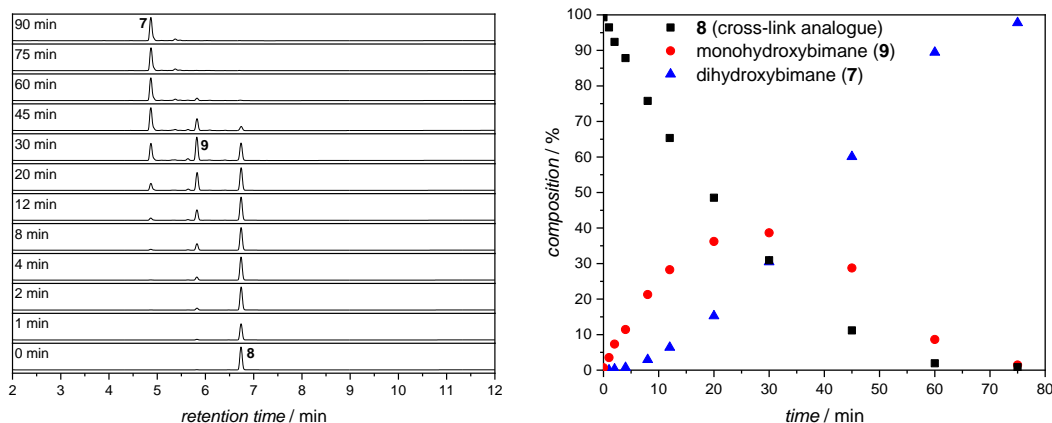


Figure 24: Left: UV traces (380-400 nm) of LC-MS during irradiation of **8**. Over time the ester groups are cleaved resulting in **9** and further into **7**. Right: Composition of **7**, **8** and **9** over time. Reprinted with permission from P. H. Maag *et al. Angew. Chem. Int. Ed.* **2023**, 62, e202309259. Open access under a CC BY-NC 4.0 DEED license by John Wiley & Sons.

Particularly, **8** was selected as a close comparison of the bimane units in the SCNPs. Consequently, **9** represents the single bound bimane unit, which is cleaved off on one side from the polymer chain. The final irradiation product **7** is identical to the cleaved product obtained after unfolding of **SCNP2** as obtained in our NMR spectroscopic studies. By comparing the results from the Monte Carlo simulation with the irradiation experiment of **8**, it can be observed that both curves align closely, supporting the assumption that single bonded and double bonded bimane units are equal in reactivity towards irradiation (Figure 25). A small uncertainty remains due to the assumption that the bimane esters have similar photocleavage kinetics in the single-chain nanoparticle **SCNP2** and as solvated individual molecules (i.e. **8** and **9**).

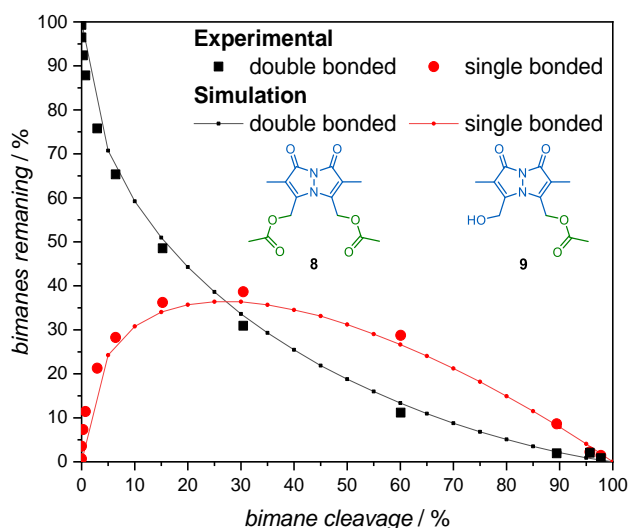


Figure 25: Experimental (scattered) and simulated (line) results of bimanane ester photocleavage. Reprinted with permission from P. H. Maag *et al. Angew. Chem. Int. Ed.* **2023**, 62, e202309259. Open access under a CC BY-NC 4.0 DEED license by John Wiley & Sons.

5.2.6 Fluorescent SCNPs

The fluorescent bimanane cross-links allow for a simple read-out of the folding state and could be further used in biomedical tracing and imaging applications. Bimananes are often used as fluorescent labeling agents in biological systems as bromoderivatives (monobromobimane or dibromobimane, **6**). They are non-fluorescent but become fluorophores after nucleophilic substitution with a substrate,^[100, 104] enabling visual read-out of the folding and unfolding, showing a strong emission at around 470 nm ($\lambda_{\text{ex}} = 395$ nm) also visible under a TLC-UV lamp (Figure 26).

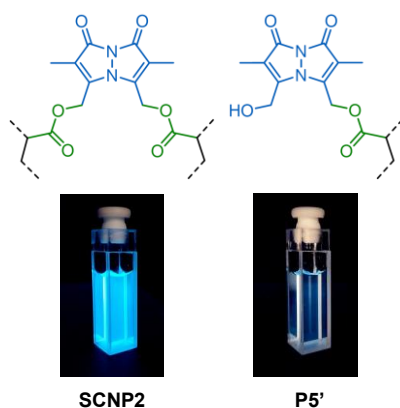


Figure 26: Fluorescence of **SCNP2** and **P5'** in water under a UV lamp showing a lower intensity after unfolding. Reprinted with permission from P. H. Maag *et al. Angew. Chem. Int. Ed.* **2023**, 62, e202309259. Open access under a CC BY-NC 4.0 DEED license by John Wiley & Sons.

The fluorescence spectra of **SCNP2** and the unfolded **P5'** were recorded, showing similar emission and excitation spectra, with an emission maximum at around 475 nm. The fluorescence of **P5'** mainly occurs from residual bimane units along the chain, in addition to cleaved dihydroxybimane **7**, which was not removed during purification (Figure 27, left side). To ensure complete purification, polymer **P5'** was separated from small molecules by dialysis (cellulose membrane, 10 kDa MWCO in methanol). Subsequently, the intensity of the emission of **P5'** decreased by 95% compared to **SCNP2** (Figure 27, right side). The remaining emission intensity is caused by residual bimane moieties which are primarily single bonded according to the Monte Carlo simulation and bimane studies (refer to Chapter 5.2.5).

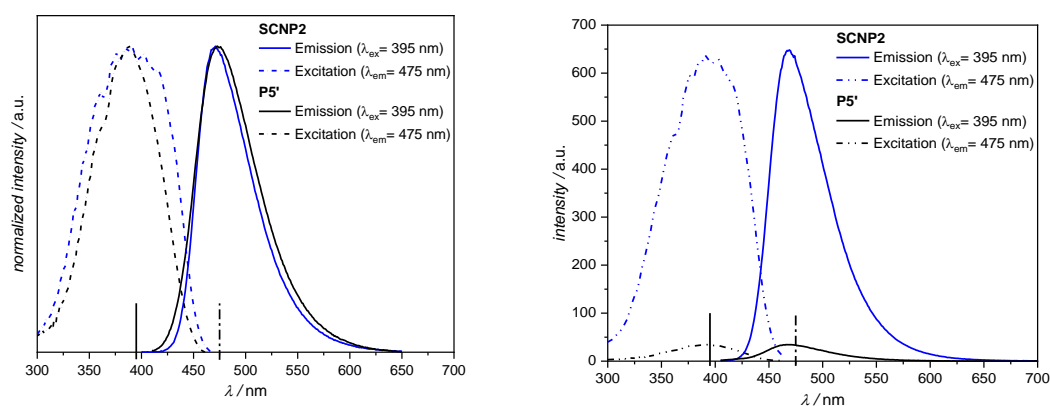


Figure 27: Left: Normalized emission and excitation spectra of **SCNP2** compared with **P5'**. Right: Emission and excitation spectra after purification by dialysis. The intensity at 475 nm decreases by 95% after unfolding. Reprinted with permission from P. H. Maag *et al.* *Angew. Chem. Int. Ed.* **2023**, 62, e202309259. Open access under a CC BY-NC 4.0 DEED license by John Wiley & Sons.

Understanding the different fluorescence intensities and spectra of the resulting products is essential for effective utilization of fluorescent SCNPs in labeling and tracing applications. To examine the fluorescence characteristics of compound **8** and its photoreaction products, the reaction mixture of **8** after irradiation with $\lambda_{max} = 415$ nm for 30 minutes was analyzed using an HPLC system equipped with a fluorescence detector. The analysis revealed comparable fluorescence spectra and intensities to the absorption of the educt (7.44 min, **8**), the product (5.17 min, dihydroxybimane **7**), and the intermediate (6.45 min, monohydroxybimane, **9**), as identified by LCMS (Appendix A: LCMS).

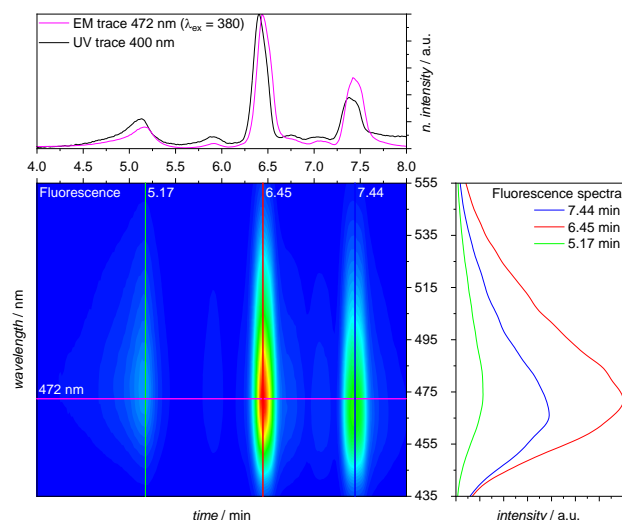


Figure 28: Spectral fluorescence slices obtained by HPLC coupled with a fluorescence detector of **8** after radiation with $\lambda_{\text{max}} = 415 \text{ nm}$ for 30 min showing the emission trace at 472 nm (pink) in comparison with the UV/VIS absorption trace at 400 nm (black). As well as the fluorescence spectra of the assigned signals. Reprinted with permission from P. H. Maag *et al. Angew. Chem. Int. Ed.* **2023**, *62*, e202309259. Open access under a CC BY-NC 4.0 DEED license by John Wiley & Sons.

5.2.7 Reusable SCNPs

A major benefit of the bimeane folded SCNPs is the reusability of the unfolded polymer (**P5'**). The folding/unfolding cycle was successfully repeated for a second time, using the same conditions as the first cycle, after recovering the crude polymer through freeze-drying. After the second folding cycle, **SCNP2'** was obtained, and a second unfolding yielded **P5''**, demonstrating the successful release of the carboxylic acid groups and enabling the polymer's reuse, as depicted in Figure 29.

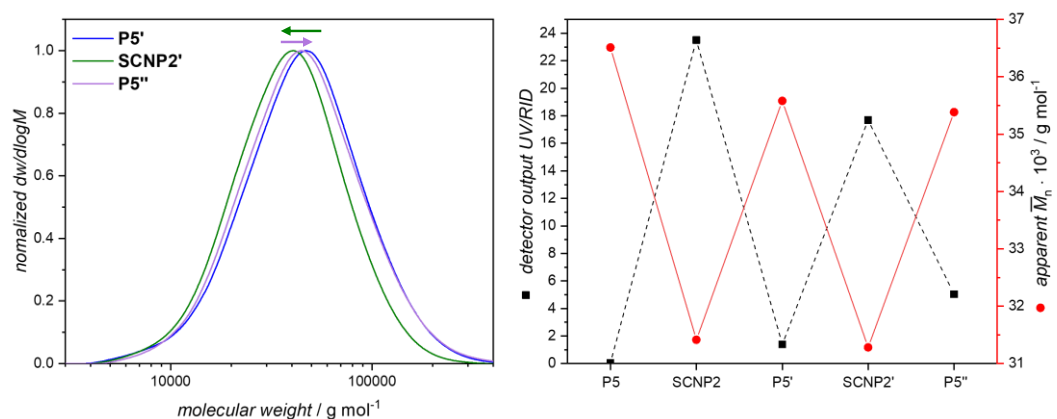


Figure 29: Folding of poly(MPEGMA-co-acrylic acid) (**P5**) with dibromobimane **6** and unfolding with visible light in a repetitive fashion. **Left:** The second cycle shows a similar shift of the SEC trace compared to the first cycle (Figure 17) resulting in a lower molecular weight for **SCNP2'** and increasing molecular weight for **P5''**. **Right:** Depicts the molecular weight and absorption at 400 nm for every step in the cycle showing alternating values. Reprinted with permission from P. H. Maag *et al. Angew. Chem. Int. Ed.* **2023**, 62, e202309259. Open access under a CC BY-NC 4.0 DEED license by John Wiley & Sons.

The shift in SEC elution times observed during the second cycle closely resembles that of the first cycle, leading to alternating changes in molecular weights after each folding and unfolding event. At the same time, the UV/VIS absorption increases with each folding process and decreases upon unfolding, demonstrating the release and incorporation of bimane cross-links.

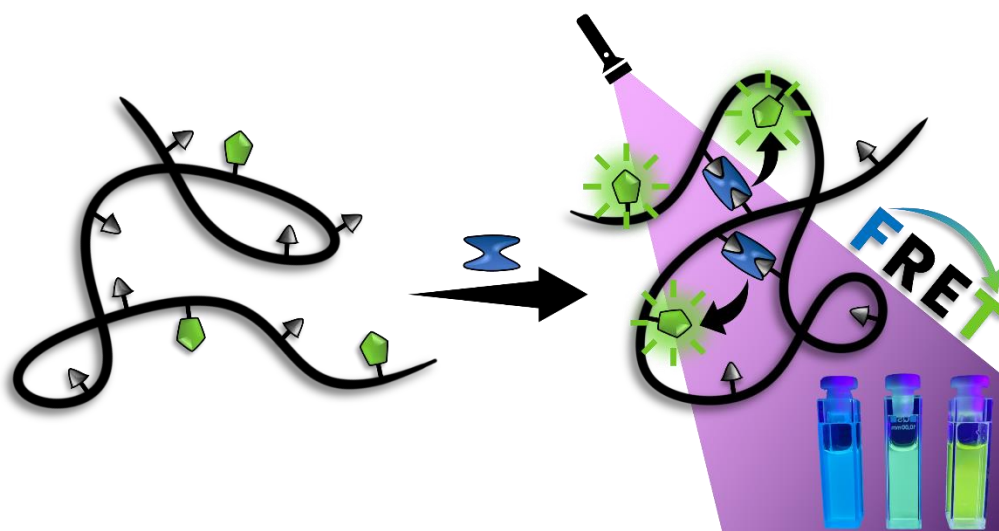
5.3 Summary

The present chapter describes the synthesis of SCNPs that respond to visible light ($\lambda_{\text{max}} = 415$ nm), transitioning from a compact structure to linear chain analogues. The SCNPs are folded by an esterification reaction of the polymer backbone, containing acrylic acid pendant groups with commercially available dibromobimane cross-links. The bimane moieties facilitate the photochemical unfolding by cleaving the ester-bond and restoring the original polymer. In addition, the fluorescent cross-links indicate successful cross-linking and unfolding reactions after purification. The different conformation after folding and light-driven unfolding can be monitored using size exclusion chromatography (SEC) and diffusion ordered NMR spectroscopy (DOSY), which observe changes in the hydrodynamic radius (R_H) resulting from the different conformations. Both the folding reaction and the light-induced unfolding are repeatable, supported by a highly efficient photocleavage.

The SCNPs were designed with MPEGMA sidechains to make the particles water soluble and with bimeane cross-links which allow for an unfolding reaction in aqueous media, indicating potential for controlling the unfolding of SCNPs in biological environments. However, to allow applications in biological environments, the toxicity of the particles and released dihydroxybimeane units must be investigated, as well as the cleavage reaction in such environments.

In contrast to the previous chapters, where the folding or unfolding of SNCPs was followed by conventional analysis techniques, in the following we studied how the folding process can be monitored by a simpler optical readout.

6 Förster Resonance Energy Transfer within Single-Chain Nanoparticles



Abstract: In this chapter we introduce a method using Förster Resonance Energy Transfer (FRET) to visualize the folding of single polymer chains into single-chain nanoparticles (SCNPs). A molecular FRET pair, consisting of a bimane and a nitrobenzoxadiazole (NBD) unit, is used for small molecule fluorescence studies. Subsequently, a polymer chain with incorporated NBD units was synthesized and folded *via* difunctional bimane cross-links into compact SCNPs. The close proximity of bimane and NBD units in the resulting SCNP reports itself as a distinct FRET fluorescence signal, evidencing the folded state of the SCNPs. The herein introduced readout method offers a simpler way to monitor SCNP folding without relying on complex analytical techniques. Reproduced from P. H. Maag *et al. Chem. Sci.* **2024**, *15*, 5218-5224 with permission from the Royal Society of Chemistry. Open access under a CC BY 3.0 DEED license.

6.1 Motivation

As described in the theoretical background Chapter 2.2, SCNPs have been synthesized in various structures through different intramolecular cross-linking methods and with a wide range of functionalities.^[2, 24, 67, 148-150] Their morphology and molecular structure have been analyzed using techniques such as molecular dynamic simulations,^[151] microscopy,^[81] NMR spectroscopy,^[152] and high-resolution mass spectrometry.^[21, 153] Most common methods for evidencing SCNP compaction are dynamic light scattering (DLS)^[26-28] and size exclusion chromatography (SEC).^[29, 30, 154] However, these methods require complex analytical

equipment. Therefore, determining the folding state of SCNPs through a simple optical readout would mark a significant advancement in easily establishing and tracking their folding status.

In the previous chapter, we studied the light induced unfolding of SCNPs in aqueous solution utilizing photolabile bimane moieties for cross-linking. In the current chapter, we introduce a method to visualize the folding reaction of the bimane cross-linked SCNPs described above, using Förster Resonance Energy Transfer (FRET).

FRET uses distance-dependent energy transfer FRET to visualize the folding state of SCNPs by a fluorescence indication. FRET is a common technique, especially in molecular biology to evidence the close proximity of two fluorophore labeled systems.^[108] As described in the theoretical background Chapter 2.3.5, FRET is defined as energy transfer between two fluorophores. The donor fluorophore absorbs light and can transfer the energy to an acceptor fluorophore *via* nonradiative dipole–dipole interactions.^[106, 155-157] FRET induced changes in fluorescence has been widely used in various of fields, including studies on the stability and encapsulation behavior of drug delivery nanogels or micelles,^[158, 159] as well as in understanding the aggregation patterns of amphiphiles into micelles.^[160]

To visualize SCNPs folding by a FRET induced change in fluorescence, we initially developed a molecular FRET pair (**10**, Scheme 24) using bimane and nitrobenzoxadiazole (NBD) as fluorophores, to preliminarily study the system. Bimane was selected for its fluorescent properties and its availability as a difunctionalized symmetric cross-linker. NBD was chosen due to its high fluorescence intensity and shifted emission spectrum, resulting in an ideal spectral overlap of donor emission and acceptor absorption.

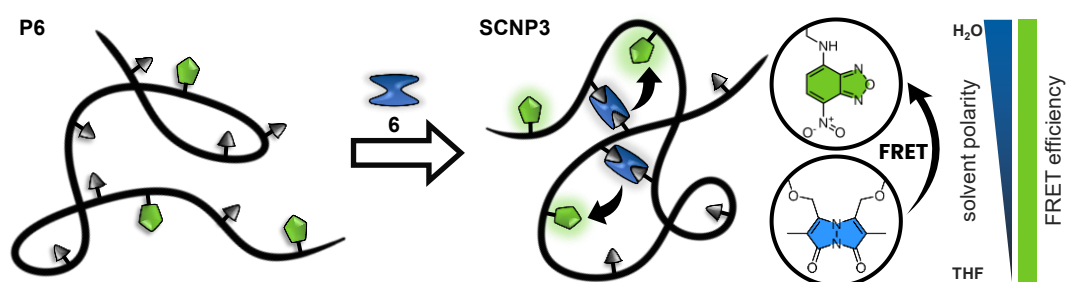
Furthermore, both fluorophores were incorporated in a water-soluble precursor polymer using carboxylic acid functionalities for post-functionalization and intramolecular cross-linking. Folding the polymer chain with dibromobimane **6** into SCNPs positions the bimane and NBD units in close proximity allows the FRET pair to self-report the folding status. This optical method offers a unique way to understand and monitor the folding state of SCNPs.

C. Barner-Kowollik, P. W. Roesky, H. Frisch and F. Feist motivated and supervised the project. The chapter “Förster Resonance Energy Transfer within Single-Chain Nanoparticles” is adapted from P. H. Maag, F. Feist, H. Frisch, P. W. Roesky, C. Barner-Kowollik, Förster Resonance Energy Transfer within Single Chain Nanoparticles, *Chem. Sci.* **2024**, 15, 5218-

5224 with permission from Royal Society of Chemistry. AI-based language models were used to improve readability and spelling (*OpenAI* (2024) ChatGPT 4).

6.2 Results and Discussion

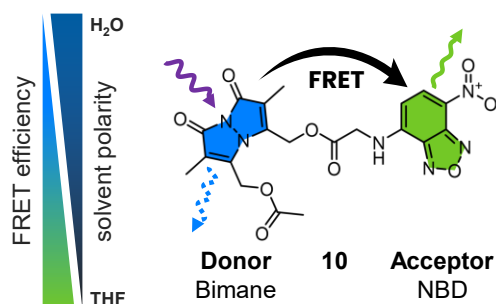
In the current chapter, we evidence the SCNP folding using FRET as a distance dependent fluorescence response. Initially, we investigate the efficiency of the energy transfer between two fluorophores based on a molecular FRET pair (**10**, Scheme 24) consisting of the donor fluorophore bimane and acceptor NBD. Both fluorophores show an ideal spectral overlap between donor emission and acceptor absorption, a criterion for an efficient energy transfer. Subsequently, we introduced both fluorophores into a water-soluble SCNPs, using dibromobimane **6** as intramolecular cross-links, thereby enabling FRET interactions between the bimane units and NBD (Scheme 23).



Scheme 23: Linear polymer chain **P6** with incorporated FRET acceptor (NBD, green), folded *via* intramolecular cross-links utilizing dibromobimane (**6**, blue). The introduced bimane units act as energy donor, absorbing light at shorter wavelengths and transferring this energy to the NBD units, which emits light in its unique spectral range, allowing the optical read out of the folding state *via* the characteristic FRET spectrum. Reproduced from P. H. Maag *et al. Chem. Sci.* **2024**, *15*, 5218-5224 with permission from the Royal Society of Chemistry. Open access under a CC BY 3.0 DEED license.

6.2.1 Molecular FRET pair

To examine the efficiency and photochemical characteristics of a FRET bimane and NBD system, both fluorophores were combined into a molecular FRET pair (**10**, Scheme 24) with glycine as a short linker. The emission spectra of **10** show an efficient energy transfer in organic solvents as THF and (dichloromethane) DCM, yet emission was less pronounced in acetonitrile (ACN) or methanol and displayed up to no FRET in polar solvents such as water.



Scheme 24: Structure of the molecular FRET pair (**10**) composed of bimane (blue) and NBD (green), connected with a short linker. Bimane, the energy donor, absorbs light at shorter wavelengths and transfers this energy to the acceptor (NBD), which in turn emits light in its characteristic spectra. Reproduced from P. H. Maag *et al. Chem. Sci.* **2024**, 15, 5218-5224 with permission from the Royal Society of Chemistry. Open access under a CC BY 3.0 DEED license.

Bimane derivatives, like dihydroxybimane (**7**) or the corresponding diacetate (refer to Chapter 9.3.9 in the experimental section), exhibited fluorescence spectra with a peak emission at 450 nm and an excitation maximum at 380 nm in THF. In comparison, NBD derivatives, such as (7-nitrobenzo[*c*][1,2,5]oxadiazol-4-yl)glycine (**11**), show similar fluorescence spectra but red-shifted by around 100 nm compared to the bimane (Figure 30). **11** shows a peak emission at 530 nm and an excitation maximum at 460 nm in THF. The local excitation minimum of **11** overlapped with the excitation maximum of **7**, enabling selective excitation of **7** at 380 nm (Figure 30, top left).

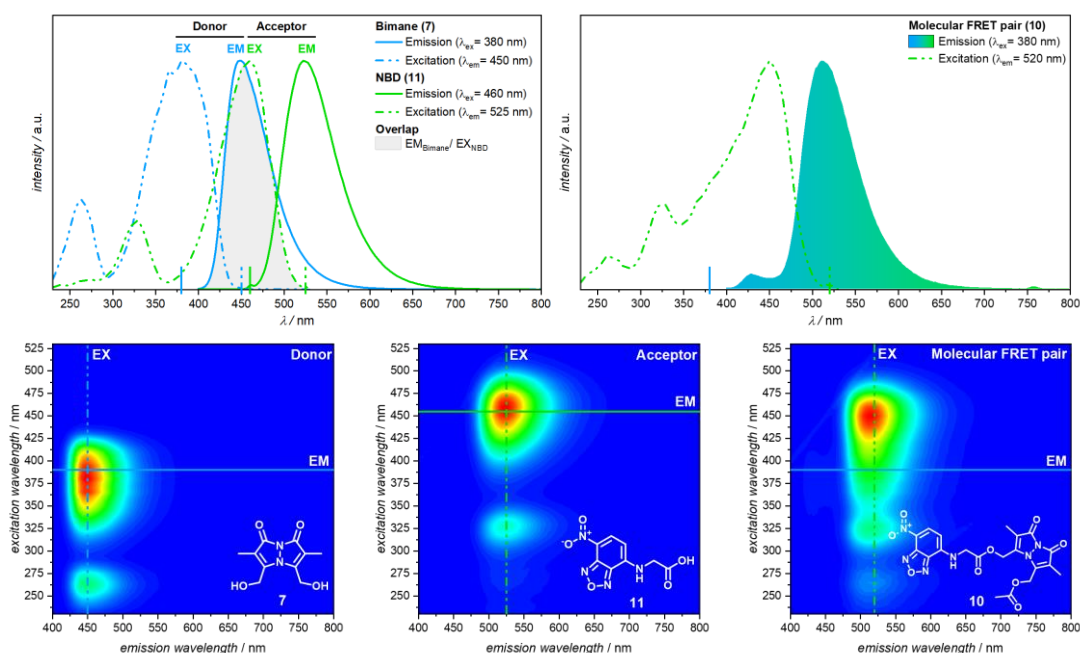


Figure 30: Top left: Overlaid fluorescence spectra of **7** and **11** in THF with spectral overlap of the donor emission spectrum with the acceptor excitation spectrum. Top right: Fluorescence spectrum of **10** in THF. Bottom: 3D Fluorescence spectra of **7** (left), **11** (middle) and **10** (right) in THF with indicated

2D slices of spectra above. Reproduced from P. H. Maag *et al. Chem. Sci.* **2024**, 15, 5218-5224 with permission from the Royal Society of Chemistry. Open access under a CC BY 3.0 DEED license.

The overlap between the emission spectrum of the donor and the absorbance spectrum of the acceptor is an important parameter influencing the FRET efficiency.^[107] For the acceptor NBD, the excitation spectrum overlaps perfectly with its absorbance spectrum (as shown in the appendix). After combining bimane and NBD with a short linker (**10**), the bimane emission shifted towards longer wavelengths as a result of energy transfer from the donor (bimane) to the acceptor (NBD). In addition, the excitation spectrum, resulting in the emission at 520 nm, merges the excitation spectra of both fluorophores. 3D fluorescence spectra of **10** compared to the individual fluorophores can also be used to visualize FRET. Compounds **7** and **11** each show a distinct emission spectrum depending on the excitation wavelength displayed in a heat map Figure 30, bottom). Bringing both compounds into close proximity enabled the energy transfer from the donor to the acceptor, returning the emission spectrum characteristic of NBD.

Fluorescence spectra of **10**, **7** and **11** were recorded in THF, showing an efficient energy transfer, indicating close proximity and free orientation of both fluorophores. FRET was also observed in DCM, but was less efficient in ACN and methanol. No FRET was observed in polar solvents such as dimethylformamide (DMF), dimethyl sulfoxide (DMSO), and water (Figure 31).

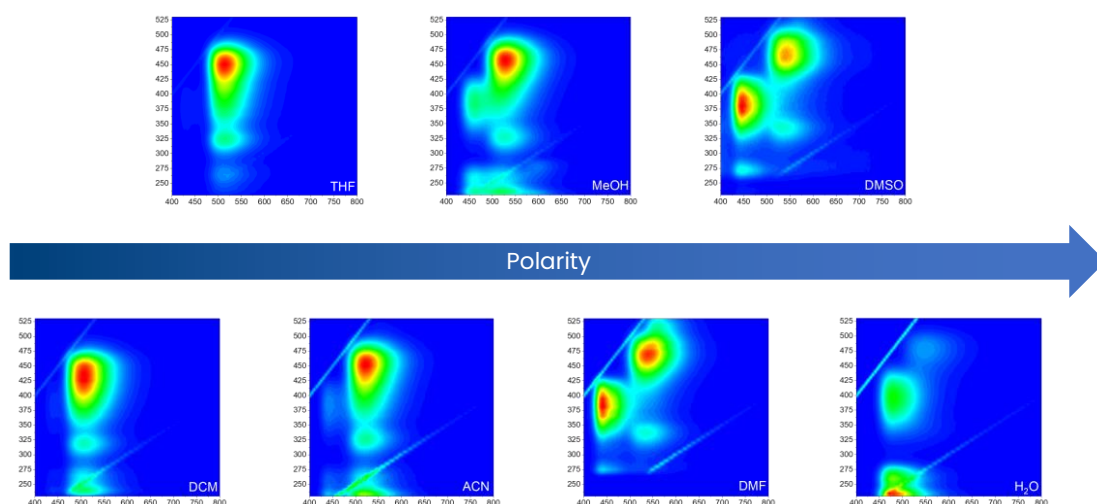


Figure 31: 3D Fluorescence spectra of **10** in different solvents sorted by polarity. Less polar solvents show a more efficient energy transfer between donor (bimane) and acceptor (NBD) than polar solvents. Reproduced from P. H. Maag *et al. Chem. Sci.* **2024**, 15, 5218-5224 with permission from the Royal Society of Chemistry. Open access under a CC BY 3.0 DEED license.

The differences in FRET efficiencies observed for **10** in the different solvents may result from different orientations of the fluorophores to each other. The orientation parameter (κ^2) is an important factor influencing the Förster distance, which describes the separation of both fluorophores at which the corresponding FRET has an efficiency of 50%. κ^2 can theoretically range from 0 to 4, but a value of 2/3 is typically assumed for a system with free rotation of the emission transition dipole in comparison to the absorption dipole.^[107] Another explanation could be the impact of the solvent on the rate coefficient of intramolecular energy transfer, as shown in previous research, which could have changed the efficiency of FRET.^[161] With regard to **10**, the solvent may restrict the free orientation of the donor and acceptor, or could reduce the transfer efficiency by changing the transfer rate coefficient. Further investigation of this specific FRET pair would require time-resolved fluorescence spectroscopy.

To further quantify fluorescence measurements, the changes in emission had to be in a linear range. Thus, the absorption at 475 nm was compared to the emission intensity at 550 nm of **1**. Figure 32 shows a linear behavior of the absorption at different dilutions in water. However, the emission intensity is only linear until an absorption of 0.2 %. To ensure a linear behavior of the emission intensity during bleaching experiments or photoreactions, fluorescence spectra were recorded for solutions with an absorptivity adjusted to 0.1 %.

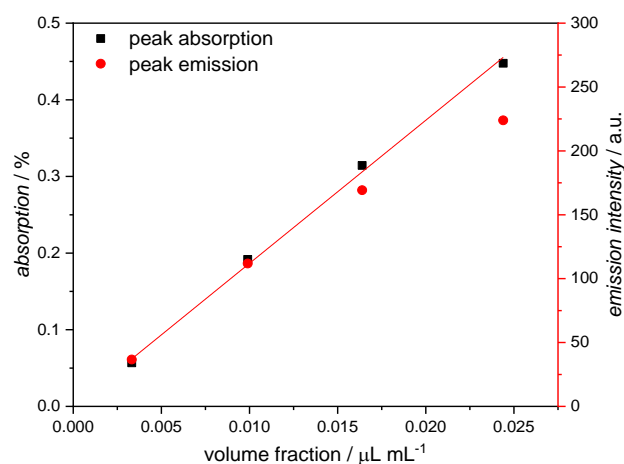


Figure 32: Comparison of peak absorption (470 nm) to peak emission (550 nm) intensity for different volume fractions of a stock solution of **10** in water ($l = 1$ cm). Reproduced from P. H. Maag *et al. Chem. Sci.* **2024**, 15, 5218-5224 with permission from the Royal Society of Chemistry. Open access under a CC BY 3.0 DEED license.

The efficiency of the energy transfer in the fluorescence spectra above was determined by photobleaching experiments of the acceptor, comparing the emission of the bimane before

and after bleaching. Additional cleavage experiments were conducted, separating bimane and NBD photochemically (Figure 33).

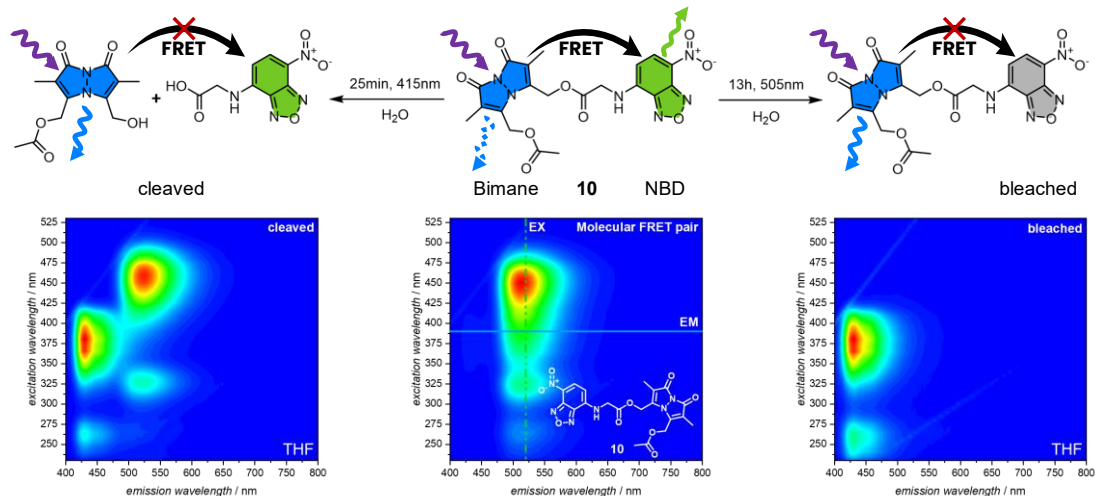


Figure 33: Reaction pathway of photobleaching and cleavage followed by 3D fluorescence spectra in THF. To photo-bleach the acceptor NBD, **10** was irradiated in water for 13 h with $\lambda_{\max} = 505$ nm, resulting in an increasing intensity of the bimane emission. The cleavage reaction was performed in water for 25 min with $\lambda_{\max} = 415$ nm resulting in an increasing intensity of the bimane emission. Reproduced from P. H. Maag *et al. Chem. Sci.* **2024**, 15, 5218-5224 with permission from the Royal Society of Chemistry. Open access under a CC BY 3.0 DEED license.

The bleaching experiment of **10** was performed at $\lambda_{\max} = 505$ nm, irradiating for 13 h until the emissions of the NBD were no longer detectable, leading to an 80% increase in the intensity of the bimane emission. Consequently, the FRET efficiency is estimated to be approximately 80% (refer to appendix). A different approach to demonstrate the FRET efficiency utilizes the photochemical cleavage abilities of bimane moieties through an ester bond cleavage, which was reported in the work of Chaudhuri *et al.*^[103] and described in the theoretical background Chapter 2.3.4. Using this approach, **10** was irradiated for 25 minutes at $\lambda_{\max} = 415$ nm in water, leading to the generation of a carboxylic acid and an alcohol (as shown in Figure 33, left). The resulting 3D fluorescence spectrum displays the distinct patterns of each fluorophore individually, indicating that the ester bond linking the donor-acceptor pair has been cleaved.

The photo cleavage reaction was monitored by LCMS, showing the expected reaction products with minor side products (Figure 34). The main products are derived from the cleaved bimane unit converting the ester to an alcohol function and the NBD connected to the glycine linker. A side product which was identified is the NBD with cleaved glycine linker. All compounds show the expected absorption spectra and the masses could be assigned.

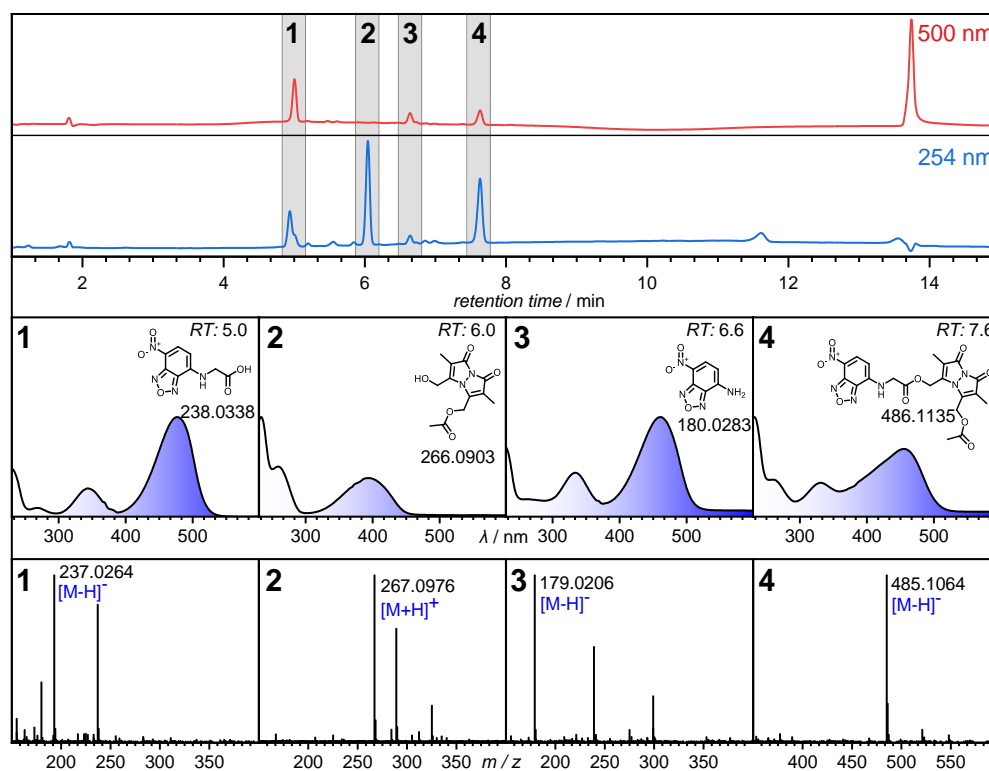
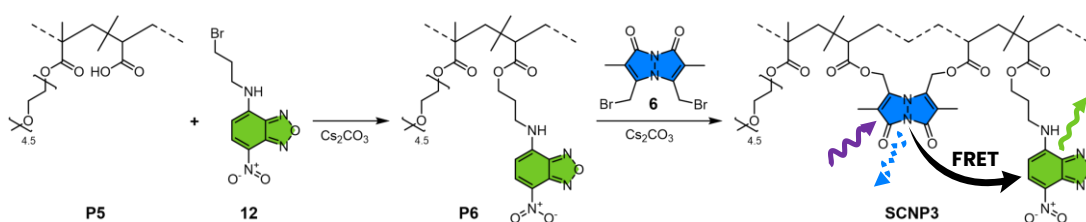


Figure 34: LC-MS trace (254 nm, 500 nm detector wavelength), absorption spectra and accumulated mass spectra of **10** irradiated with 415 nm for 25 min. Reproduced from P. H. Maag *et al. Chem. Sci.* **2024**, *15*, 5218-5224 with permission from the Royal Society of Chemistry. Open access under a CC BY 3.0 DEED license.

6.2.2 FRET read-out of SCNP folding

To evidence the SCNP folding *via* FRET and to use the discovered features of **10** within SCNPs, we introduced both fluorophores into water-soluble SCNPs. Dibromobimane **6** served as intramolecular cross-links, thereby enabling FRET interactions between the bimane units and NBD (Scheme 23). As water-soluble polymeric backbone, we utilized the same copolymer from Chapter 5, a statistic RAFT copolymer of poly(ethylene glycol) methyl ether methacrylate (MPEGMA, $M_n=300 \text{ g mol}^{-1}$), and acrylic acid (AA). The polymer composition was determined based on the conversion of the monomers during polymerization. 16% AA was determined *via* ^1H NMR spectroscopy using DMF as an internal standard (Figure 16, Table 4). The RAFT end-groups were hydrolyzed to avoid side reactions and to decrease light absorption (refer to Chapter 9.5.5 in the experimental section), affording poly(MPEGMA-co-AA) (**P5**, $M_n = 42.62 \text{ kg mol}^{-1}$, $x_{AA} = 16 \%$).^[60] To equip **P5** with a FRET acceptor, **P5** was post-functionalized with *N*-(3-bromopropyl)-7-nitrobenzo[*c*][1,2,5] oxadiazol-4-amine (**12**) by an

esterification reaction of the carboxylic acid pendant groups in a solution of THF and cesium carbonate as base (**P6**, $M_n = 47.27 \text{ kg mol}^{-1}$, Scheme 25).



Scheme 25: Post-functionalization of **P5** with the fluorophores **12** and **6** to incorporating the FRET pair. **6** concomitantly acts as cross-linker, folding **P5** into **SCNP3**. Reproduced from P. H. Maag *et al. Chem. Sci.* **2024**, 15, 5218-5224 with permission from the Royal Society of Chemistry. Open access under a CC BY 3.0 DEED license.

After the post-functionalization of **12** within the polymer, changes in the hydrodynamic volume led to an 11% increase of the apparent molecular weight (M_n), which appeared as a shift in the SEC elution time of **P6** compared to **P5** (as shown in SEC, Figure 42). The incorporation of **12** was also monitored by comparing the UV/Vis absorption of the polymer in the SEC trace with RID. An increase in absorption at 450 nm over time confirmed the successful tethering of the NBD units to the polymer chain. Subsequently, **P6** was cross-linked into a SCNP by another esterification with the difunctional dibromobimane **6** in a highly diluted reaction mixture (0.2 mg mL^{-1} **P2** in THF) to form **SCNP3** ($M_n = 35.67 \text{ kg mol}^{-1}$, Scheme 24, refer to Chapter 9.6.3 in the experimental section). The folding process resulted in compact SCNPs with a decreased hydrodynamic volume, leading to a 25% reduction in the apparent M_n , appearing as a shift in the SEC elution time of **SCNP3** compared to **P6**.

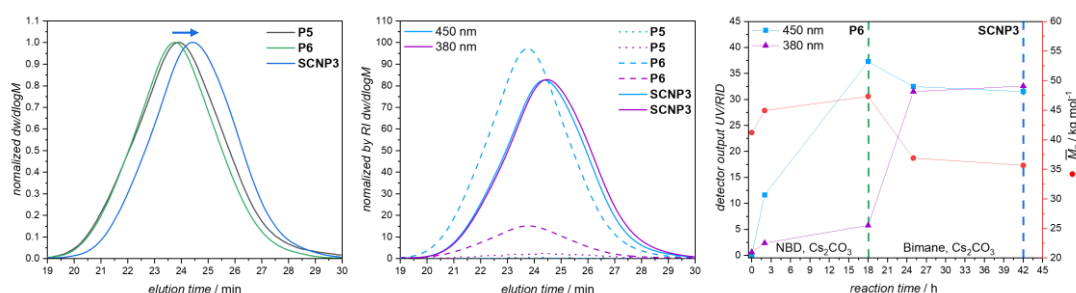


Figure 35: Left: RID SEC traces of **P5**, post-functionalized to **P6** and folded into **SCNP3**. Middle: UV/Vis absorption SEC trace at 380 nm and 450 nm normalized by RID of **P5**, **P6** and **SCNP3**. Right: Kinetics of the post-functionalization of **P5** to **P6** and folding of **P6** to **SCNP3** monitored by UV/Vis absorption and M_n by SEC. The cross-linking of the polymer chain leads to a compaction and consequently to a smaller hydrodynamic volume e.g. a smaller apparent molecular weight in the SEC. M_n : apparent molecular weight. Reproduced from P. H. Maag *et al. Chem. Sci.* **2024**, 15, 5218-5224 with permission from the Royal Society of Chemistry. Open access under a CC BY 3.0 DEED license.

Additionally, the increase of the UV/Vis absorption at 380 nm of the polymer in the SEC trace over time confirms the effective addition of bimeane units into the polymer chain, leading to a decreased apparent molecular weight, indicating that the bimeanes function as cross-links. After 2 h of folding, the absorption at 380 nm reaches a plateau, indicating a full conversion of the carboxylic acid repeating units.

A 3D fluorescence spectrum of **SCNP3** in water was recorded and compared with the molecular FRET pair **10** (Figure 36, top left). The 3D spectrum of **SCNP3** displays a similar pattern compared to **10**, suggesting an efficient FRET between bimeane and NBD within the SCNP structure, likely due to the close proximity of the cross-links (donor) and the polymer-bound fluorophore (acceptor).

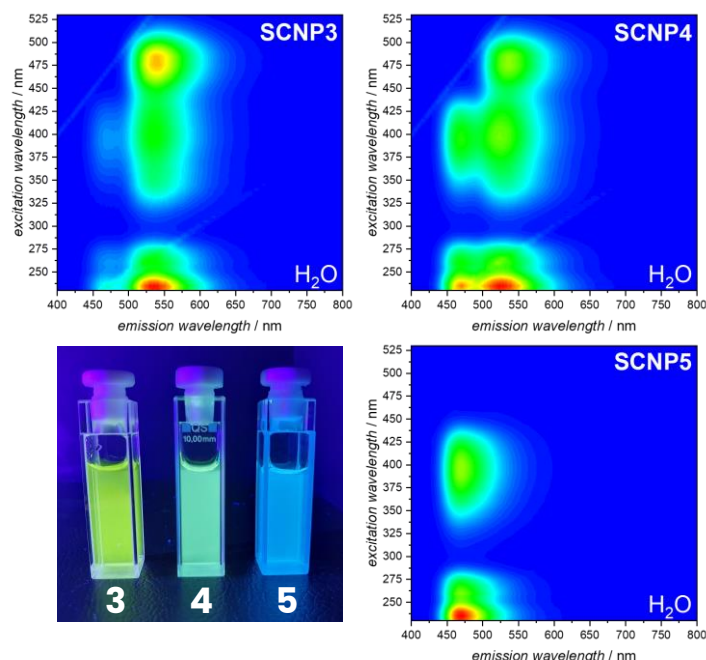


Figure 36: 3D fluorescence spectra of **SCNP3-5** in water as well as an image of the cuvettes irradiated with $\lambda_{\max} = 380$ nm. M_n : apparent molecular weight. Reproduced from P. H. Maag *et al. Chem. Sci.* **2024**, *15*, 5218-5224 with permission from the Royal Society of Chemistry. Open access under a CC BY 3.0 DEED license.

By bleaching experiments, it was confirmed that the observed fluorescence pattern is the result of FRET. After irradiating for 8 h at 505 nm, the intensity of the bimeane emission at around 470 nm increases, evidencing the interrupted energy transfer (refer to appendix E). Notably, FRET is now also observed in water and other polar solvents whereas **10** did not show any energy transfer, perhaps suggesting a change in the orientation parameter in different solvents, as previously discussed in Chapter 6.2.1.

To investigate how different ratios of NBD pendant groups influence the FRET efficiency, SCNPs were synthesized with adjusted reaction time and NBD (**12**) concentration to stepwise decrease the NBD incorporation. **P5** was functionalized with decreasing amounts of NBD units (**12**), utilizing the carboxylic acid pendant groups, leading to the formation of **P7** ($M_n = 42.62 \text{ kg mol}^{-1}$) and **P8** ($M_n = 41.64 \text{ kg mol}^{-1}$), both with a slight increase in apparent M_n compared to **P5**. The incorporation of NBD units was monitored by UV/Vis absorption at 450 nm in the SEC elugram. Without purification, **P7** and **P8** were cross-linked with equal amounts of dibormobimane **6** in a highly diluted solution of 0.2 mg mL^{-1} in THF, resulting in **SCNP4** ($M_n = 36.13 \text{ kg mol}^{-1}$) and **SCNP5** ($M_n = 38.62 \text{ kg mol}^{-1}$). The changes in molecular weight, as shown in Figure 37, along with the absorption of the polymer at 380 nm and 450 nm, also presented in Figure 37, confirm the incorporation of bimane and NBD units.

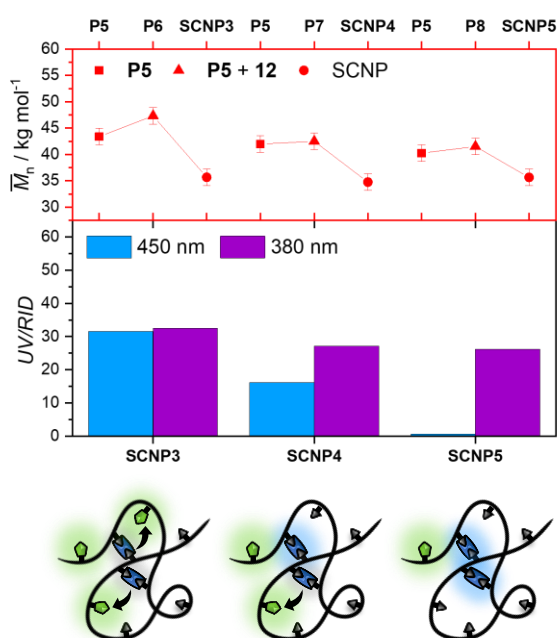


Figure 37: Bottom: Illustration of SCNPs with different incorporation of NBD analyzed by SEC showing different absorption at 450 nm compared to the RID and similar incorporation of bimane units according to the absorption at 380nm. The apparent M_n (red) slightly increases after post-functionalization and decreases with folding to SCNPs. Reproduced from P. H. Maag *et al. Chem. Sci.* **2024**, *15*, 5218-5224 with permission from the Royal Society of Chemistry. Open access under a CC BY 3.0 DEED license.

The folding of the linear polymer chain into SCNPs resulted in a decreased hydrodynamic volume, correlating with a decrease in the apparent M_n , as determined from a change in the SEC elution time. 3D fluorescence measurements indicated a decreasing FRET efficiency with decreasing number of NBD moieties, with no FRET observed in **SCNP5**. The difference in emission can be visually observed by irradiating with $\lambda_{\text{max}} = 380 \text{ nm}$ LED (Figure 36).

The photochemical behavior of **SCNP3** and **SCNP4** was further investigated to study the differences between the small molecule **10** and the SCNPs. To demonstrate the efficiency of the FRET, **SCNP3** was irradiated for 8 h with $\lambda_{\max} = 505$ nm until no emission of the NBD could be observed anymore. This resulted in an increasing intensity of the bimane emission, with no significant changes in the apparent M_n (Figure 38, Figure 39, left).

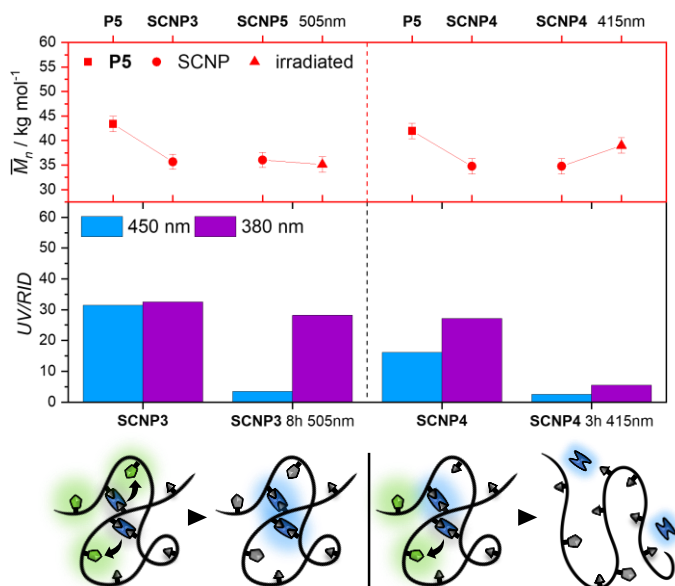


Figure 38: Left: **SCNP3** and **SCNP4** analyzed by SEC showing different absorption at 450 nm and 380 nm. The apparent M_n (red) increases after irradiating with 415 nm for 3 h in water indicating an unfolded of the SCNPs. M_n : apparent molecular weight. Reproduced from P. H. Maag *et al. Chem. Sci.* **2024**, 15, 5218-5224 with permission from the Royal Society of Chemistry. Open access under a CC BY 3.0 DEED license.

Furthermore, **SCNP4** was irradiated with $\lambda_{\max} = 415$ nm for 3 h in water, leading to a strong decrease of absorption at 380 nm and 450 nm. In addition, the apparent M_n increased, indicating that the SCNPs were unfolded to linear chains. The irradiation of the SCNPs led to ester bond cleavage, releasing dihydroxybimane **7** and the carboxylic acid pendant groups of the polymer. The increased hydrodynamic volume of the irradiated SCNPs compared to **SCNP4** was evidenced by a shift in the SEC elution time, as indicated by the red arrow (Figure 39, left).

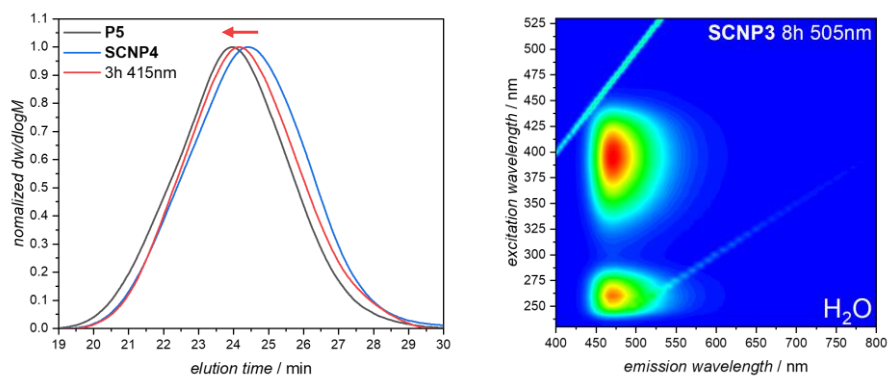


Figure 39: Left: RID SEC traces of **SCNP4** unfolding compared to **P5**. Right: 3D fluorescence spectrum of **SCNP4** irradiated with 505 nm for 8 h in water. Reproduced from P. H. Maag *et al. Chem. Sci.* **2024**, 15, 5218-5224 with permission from the Royal Society of Chemistry. Open access under a CC BY 3.0 DEED license.

The change of the SEC elution time after unfolding was less pronounced than for the initial folding, perhaps caused by remaining bimane cross-links within the chain or side reactions that occur during the photocleavage and bleaching of the NBD units.

6.3 Summary

We introduce a method to monitor the folding of polymer chains into single-chain nanoparticles (SCNPs) by fluorescence, utilizing Förster Resonance Energy Transfer (FRET). We designed a molecular FRET pair by linking the two judiciously chosen fluorophores bimane and nitrobenzoxadiazole (NBD) together into one molecule which exhibited efficient energy transfer in solvents such as tetrahydrofuran (THF) or dichloromethane (DCM), while displaying no FRET in more polar solvents such as dimethylformamide (DMF) and water.

SCNPs were folded from linear polymer chains equipped with NBD units using the difunctional bimane units for intramolecular chain collapse. Upon cross-linking, the donor fluorophore bimane and the acceptor fluorophore NBD reach close proximity, leading to a strong FRET fluorescence signal of the SCNPs, signaling their folded state. The presented visual read-out method on the folding state of SCNPs allows for future real-time analysis of the folding process and reduces the need for complex analytical devices, paving the way for in-situ monitoring of SCNP folding and unfolding.

FRET is a useful tool to determine the close proximity of two fluorophores evidencing the folded state of the polymer, however, this method could be further developed to allow for a

quantification of the actual compaction of SCNPs by monitoring the increasing FRET efficiency during folding.

7 Conclusions

With the results presented in this thesis we are contributing to the research field of SCNPs and addressing various challenges. Key challenges are for example the controlled folding of SCNPs, the characterization of the folded state but also the incorporation of functionalities. We focused on the remote folding control by visible light which could be used to influence the conformation and size within a biological system or affecting the catalytic center of a metal coordinated SCNP. To improve the characterization of the folded state of SCNPs fluorescent cross-links were incorporated, indicating the successful folding and unfolding, allowing for an optical readout method. Those fluorescent SCNPs could further be used in tracing and imaging applications.

In Chapter 4 we introduce fluorescent and catalytically active SCNPs, synthesized through a photoinduced cross-linking reaction. The precursor copolymer contains phosphine ligands for gold coordination among the photoreactive cross-linking moieties. Visible light ($\lambda_{\text{max}} = 415$ nm) initiates the folding and leads to a compacted structure. The catalytic activity of the introduced gold(I) complexes is demonstrated in an intramolecular hydroamination reaction, with high conversion rates observed.

Chapter 5 focuses on light induced unfolding of SCNP with a water-soluble backbone, making them suitable for further investigations using biological media. The SCNPs are initially cross-linked through an esterification reaction with bimeane moieties. The unfolding proceeds in water under mild conditions yielding in the original precursor polymer which can be repeatedly folded and unfolded. This light-responsive behavior in water positions these SCNPs as promising candidates for biological applications, given their ability to respond to external triggers and the potential for manipulating their size.

In Chapter 6 we present a method to visualize SCNP folding using Förster Resonance Energy Transfer (FRET). A molecular FRET pair, containing bimeane as donor fluorophore and cross-linking unit as well as NBD acceptor fluorophores, were attached to the polymer backbone and employed to monitor the folding state of SCNPs. The incorporation of this FRET pair into the polymer chain enables direct optical readout of SCNP formation, as indicated by a strong FRET signal. This method eliminates the need for complex analytical tools and paves the way for in-situ observation of SCNP folding.

8 Outlook

The results of the thesis address specific challenges in the field of SCNPs. Focusing on synthesis strategies such as the folding control and characterization of the folding state. Light induced crosslinking thereby enables spatiotemporal control over the folding state but does not affect the spatial arrangement of the cross-links and backbone. At present, synthetic SCNPs do not reach the level of precision in their folding as proteins with their highly specific spatial conformation. Such spatial control may ultimately only be achievable by starting from sequence-defined polymer chains. More control over the folded shape of SCNPs could be implemented using alternating copolymers with alternating amphiphilic groups, creating a micelle-like structure but much smaller and cross-linked.^[162] Block polymers and grafted polymers could also add a degree of structure to the folded state, creating pockets for catalysis or drug delivery.

Furthermore, the pocket design of SCNPs could be used to catalyze sequential reactions, where one substrate undergoes a cascade of reaction steps catalyzed by different metals in the same polymeric pocket. Ebensperger *et al.*^[163] reported a two-step reaction in aqueous solution where the catalytic center is located within an artificial protein containing a dual-metal-tagged guest protein, potentially serving as a blueprint for a similar reaction within SCNPs. Instead of two metals the SCNPs could also contain different catalysts like organic catalysts or photo catalysts. To catalyze a sequential cascade reaction within one type of SCNPs a defined polymeric particle is required – ideally forming a pocket – hosting the substrate for the duration of the reaction. The cascade reaction then could be a combination of a metal, organic and photo catalyzed reaction. Therefore, metals could be used fold the polymeric chains into SCNPs and catalyze a first reaction step followed by a second reaction step catalyzed by a photoreaction or organic catalysts along the backbone.

In addition to the interest in catalytic SCNPs, there is a high interest to study SCNPs in biological environments. A promising way to synthesize and unfold such potentially biocompatible SCNPs is demonstrated in our project on water-soluble SCNPs described in Chapter 5.^[64] Water-soluble SCNPs likely allow for biomedical applications and are one step closer to their natural analogues, i.e. enzymes. However, the availability of water-soluble and biocompatible polymer backbones suitable for folding into SCNPs remains limited, requiring additional research in this area.

Another limitation for biocompatible photo responsive SCNPs is the presence of oxygen in biological environments. Many photoreactions that proceed *via* the triplet excited state are sensitive to oxygen, as it quenches the triplet state, converting the oxygen into singlet oxygen. Photosensitizers could potentially use this to eliminate the oxygen around the SCNPs and enable photoreactions within the SCNPs.^[164] Alternatively, photoreaction could be used which are more oxygen tolerant and more suitable for biological environments. Afterwards, SCNPs could be designed carrying functional units e.g. drugs which are released in a photo induced cleavage reaction. Additionally, the unfolding reaction could be used to cleave not only the cross-links but also degrade the polymer backbone in smaller parts to enable an enhanced clearance of the SCNPs from a biological system. To achieve this, short polymer chains would be connected at their end groups with a photolabile linker to longer linear chains and intramolecular cross-linked into SCNPs with the same linker. In an additional step functional units e.g. drugs would be attached to the remaining not saturated linking units. Under irradiation the SCNPs would simultaneously be unfolded, degraded and the drug released (Figure 40).

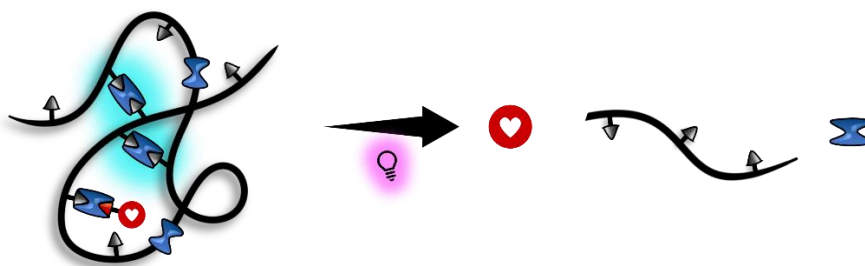


Figure 40: Illustration of a photoinduced drug release and degradation of SCNPs.

As mentioned in Chapter 5, FRET is a common tool to determine the close proximity of two fluorophores and we employed it to indicate the folded state of SCNPs. However, additional research is necessary to determine the exact degree of compaction in SCNPs by FRET efficiency. To achieve this, two fluorophores would be attached to the backbone of a linear polymer chain and the folding monitored by SCE or DOSY compared with the FRET efficiency to obtain a calibration curve for this system.

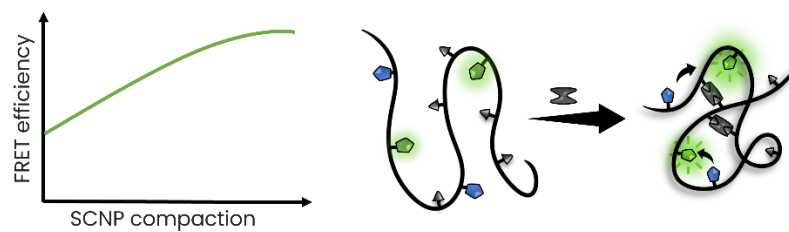


Figure 41: Illustration of two fluorophores attached to a linear polymer chain which get closer by folding the polymer chain into SCNPs and report their folding and increasing compaction by a strong FRET signal.

Overall SCNPs are an existing ongoing research field with a high potential in application as catalysis and in biomedical science.

9 Experimental Section

9.1 Materials

All chemicals were used as received unless noted otherwise. 11-mercaptoundecanoic acid (95%, Sigma-Aldrich), 2-Cyano-2-propyl benzodithioate (Sigma-Aldrich, >97%), 2-fluoro-6-methylbenzaldehyde (fluorochemicals), 4-chloro-7-nitrobenzofurazan (Sigma-Aldrich, 98%), 4-chloromethylstyrene (90%, abcr, stabilized with TBC, ONP, *o*-nitrocresol), acetic acid (Fisher chemical, >99.0%), acetic acid (ROTIPURAN® 100 %, p.a., Roth), acetonitrile (ACN, Fisher chemical, >99.9%), acrylic acid (AA, anhydrous, Sigma-Aldrich, contains 200 ppm MEHQ as inhibitor, 99%), azobisisobutyronitrile (AIBN, Sigma-Aldrich, 12.-wt% in acetone), cesium carbonate (>98.0%, TCI), cesium carbonate (Alfa Aesar, 99.5%), cesium hydroxide monohydrate (99.95%, thermo scientific), chloroauric acid (Acros Organics), chloroform D (99.8%, Eurisotop), cyclohexane (Sigma-Aldrich, EMSURE®), dibromobimane (**6**, Synchem, 98%), dichloromethane (fischer scientific, >99.8%) diethyl ether (Ajax Finechem, >99.5), diethyl ether (Ajax Finechem, >99.5), dimethyl sulphoxide (Ajax Finechem, >99.0), ethanol (Ajax Finechem, absolute, >99.5%), ethyl acetate (Fisher chemical, ≥99.8%), ferrocene (98%, Sigma-Aldrich), geduran® Si 60 for column chromatography silicagel 60 (40-63 μm, Merck), glycine *tert*-butyl ester HCl (Combi-Blocks, 98%), lithium bis(trimethylsilyl)amide solution (1.0 M in THF, Sigma-Aldrich), lithium bromide (anhydrous, 99% min, Alfa Aesar), magnesium sulfate anhydrous (Sigma-Aldrich), magnesium sulphate hydrate (≥99%, dried, Roth), methanol (Ajax Finechem, >99.9), methyl 4-(bromomethyl)benzoate (98%, ABCR), *N,N*-Dimethylformamide (99.8%, extra dry, over molecular sieve, AcroSeal®, Acros organics), *N,N*-Dimethylformamide (DMF, Sigma-Aldrich, 99.8%), *n*-pentane (Ajax Finechem, absolute, >98%), poly(ethylene glycol) methyl ether methacrylate (average Mn 300, MPEGMA, Sigma-Aldrich, contains 100 ppm MEHQ as inhibitor, 300 ppm BHT as inhibitor), raney nickel catalyst activated for hydrogenation (~50% water, Merck), sodium formate (Sigma-Aldrich), sodium hydrogen carbonate (Ajax Finechem, absolute, >99.7%), styrene (≥99%, Sigma-Aldrich, stabilizer: 15 ppm 4-*tert* butylcatechol), tetrachloroauric(III) acid trihydrate (99%, Acros organics), tetrahydrofuran (THF, Fisher chemical, >99.9%), tetrahydrothiophene (>99%, TCI), toluene (HPLC grade, VWR BDH Chemicals), toluene-4-sulfonic acid monohydrate (≥99%, Merck), triethylsilane (Sigma-Aldrich, >99%), trifluoroacetic acid (thermos scientific, 99%), tri-*n*-butylphosphine (95%, AcroSeal, Acros Organics), triphenylphosphine (ChemSupply,

>99%), triphenylphosphine (Sigma-Aldrich), triphosgene (98%, Sigma-Aldrich), 1,4-Dimethoxybenzene (98%, Alfa Aesar).

Styrene and CMS were purified by passing through a column of basic alumina before use.

9.2 Instrumentals

DMAC-Size Exclusion Chromatography (DMAC-SEC)

DMAC-SEC measurements were conducted on a PSS SEcurity2 system consisting of a PSS SEcurity Degasser, PSS SEcurity TCC6000 Column Oven (60 °C), PSS GRAM Column Set (8x150 mm 10 µm Precolumn, 8x300 mm 10 µm Analytical Columns, 1000 Å, 1000 Å and 30 Å) and an Agilent 1260 Infinity Isocratic Pump, Agilent 1260 Infinity Standard Autosampler, Agilent 1260 Infinity Diode Array and Multiple Wavelength Detector (A: 400 nm, B: 360 nm), Agilent 1260 Infinity Refractive Index Detector (RID, 35 °C). HPLC grade DMAc, 0.01 M LiBr, is used as eluent at a flow rate of 1 mL min⁻¹. Narrow disperse linear poly(styrene) (M_n : 266 g mol⁻¹ to 2.52x10⁶ g·mol⁻¹) and poly(methyl methacrylate) (PMMA, M_n : 202 g mol⁻¹ to 2.2x10⁶ g mol⁻¹) standards (PSS ReadyCal) were used as calibrants. All samples were passed over 0.22 µm PTFE membrane filters. Molecular weight and dispersity analysis were performed in PSS WinGPC UniChrom software (version 8.2).

THF-Size Exclusion Chromatography (THF-SEC)

THF-SEC measurements were conducted on a PSS SEcurity2 system consisting of a PSS SEcurity Degasser, PSS SEcurity TCC6000 Column Oven (35 °C), PSS SDV Column Set (8 x 150 mm 5 µm Precolumn, 8 x 300 mm 5 µm Analytical Columns, 100000 Å, 1000 Å, and 100 Å) and an Agilent 1260 Infinity Isocratic Pump, Agilent 1260 Infinity Standard Autosampler, Agilent 1260 Infinity Diode Array and Multiple Wavelength Detector (A: 254 nm, B: 360 nm), Agilent 1260 Infinity Refractive Index Detector (RID, 35 °C). HPLC grade THF, stabilized with BHT, is used as eluent at a flow rate of 1 mL min⁻¹. Narrow disperse linear poly(methyl methacrylate) (PMMA, M_n : 202 g mol⁻¹ to 2.2x10⁶ g·mol⁻¹) standards (PSS ReadyCal) were used as calibrants. All samples were passed over 0.22 µm PTFE membrane filters. Molecular weight and dispersity analysis were performed in PSS WinGPC UniChrom software (version 8.2).

Nuclear Magnetic Resonance (NMR) Spectroscopy

1D spectra (^1H , ^{13}C -APT, ^{31}P) as well as 2D spectra (COSY, HSQC, HMBC, NOESY) were recorded using a Bruker Ultrashield plus 500 spectrometer (^1H : 500.28 MHz, ^{13}C 125.81 MHz, ^{31}P 202.51 MHz), a Bruker Avance III 600 MHz, equipped with a BBO-Probe (5 mm) with z-gradient (^1H : 600.13 MHz, ^{13}C : 150.90 MHz,) or a Bruker Avance III 400 MHz spectrometer equipped with a Quattro Nucleus Probe (QNP) with an operating frequency of 400 MHz (^1H). All measurements were carried out in deuterated solvents. The chemical shift (δ) is recorded in parts per million (ppm) and relative to the residual solvent protons.^[165] The measured coupling constants were calculated in Hertz (Hz). Spectra were analyzed with *Mestrelab* MNova 11.0. The signals were quoted as follows: s = singlet, d = doublet, t = triplet, and m = multiplet.

Diffusion Ordered Spectroscopy (DOSY) NMR

All samples were measured in amber NMR-tubes to prevent exposure to ambient light. DOSY experiments based on ^1H -NMR were performed in CDCl_3 at 301.0 K on a Bruker 400 UltraShield spectrometer equipped with a Quattro Nucleus Probe (QNP) with an operating frequency of 400 MHz (^1H). A double-stimulated echo sequence using bipolar gradients was used in order to compensate convection. A bipolar gradient δ of 4.8 ms and a diffusion delay Δ of 129.9 ms were found to be a good compromise for all samples in order to maintain comparability of the samples. Gradient strength was linearly incremented from 2% at 0.96 G to 95% in 20 steps. The obtained data was processed with TopSpin 4.2 and Dynamics Center 2.8.3. After Fourier transformation of the 1D spectra, the signal decay along the gradients G was fitted to:

$$f(G) = I_0 \cdot e^{-DG^2\gamma^2\delta^2\left(\Delta-\frac{\delta}{3}\right)} \cdot 10^4$$

With the gyromagnetic ratio γ and the full signal intensity I_0 .

$$R_H = \frac{k_b T}{6\pi\eta D}$$

Hydrodynamic radii R_H were calculated from the Stokes-Einstein equation: Where k_b is the Boltzmann constant, T the temperature and η the solvent viscosity (CHCl_3 : 0.537 mPa).^[166]

Liquid Chromatography – Mass Spectrometry (LC-MS)

LC-MS measurements were performed on an *UltiMate* 3000 UHPLC System (*Dionex*) consisting of a pump (LPG 3400SZ), autosampler (WPS 3000TSL), and a temperature-controlled column compartment (TCC 3000). Separation was performed on a C18 HPLC column (*Phenomenex* Luna 5 μ m, 100 Å, 250 \times 2.0 mm) operating at 40 °C. Water (containing 5 mmol L⁻¹ ammonium acetate) and acetonitrile were used as eluents. A gradient of acetonitrile: H₂O, 5:95 to 100:0 (v/v) in 7 min at a flow rate of 0.40 mL·min⁻¹ was applied. The flow was split in a 9:1 ratio, where 90% of the eluent was directed through a DAD UV-detector (VWD 3400, *Dionex*) and 10% was infused into the electrospray source. Spectra were recorded on an LTQ Orbitrap Elite mass spectrometer (*Thermo Fisher Scientific*) equipped with a HESI II probe. The instrument was calibrated in the m/z range 74-1822 using premixed calibration solutions (*Thermo Scientific*). A constant spray voltage of 3.5 kV, a dimensionless sheath gas, and a dimensionless auxiliary gas flow rate of 5 and 2 were applied, respectively. The capillary temperature was set to 300 °C, the S-lens RF level was set to 68, and the aux gas heater temperature was set to 100 °C.

Flash Column Chromatography

Flash chromatography was performed on a CombiFlash Rf+ (Teledyne ISCO). Fractions were collected *via* a UV detector (254, 280, 320 or 344 nm and detection of the full UV-Vis spectrum). Puriflash cartridges of 12, 25, 40 and 120 g (interchim, F0012, F0025, F0040, F0120, 30 μ m, SI-HP) or an Uptisphere Strategy silica column (100 Å, 15 μ m, interchim) were employed for the purification in direct mode and puriflash C18-HP cartridges of 12 and 40 g (interchim, F0012, F0040, 15 μ m) for the reverse mode. The analyte was dried on celite and was transferred into an adapted pre-column prior to purification.

UV-VIS Spectroscopy

UV/vis spectra were recorded on a *Shimadzu* UV-2700 spectrophotometer equipped with a CPS-100 electronic temperature control cell positioner. Samples were dissolved, filtered, and subsequently measured in *Hellma Analytics* quartz high precision cells with a path length of 10 mm at ambient temperature.

Fluorescence Spectroscopy

The fluorescence intensities were measured using a Cary Eclipse Fluorescence Spectrophotometer from *Agilent Technologies*. Voltage was adjusted between low (400 V) and medium (600 V) with an excitation and emission slit of 5 nm (scan rate 600 nm min⁻¹) and the excitation wavelength was set to 395 nm if not noted otherwise. Samples were prepared in deionized water and measured at ambient temperature in *Hellma Analytics* quartz high precision cells with a path length of 10 mm. 3D spectra were recorded in the emission scan mode with an excitation wavelength of 230 nm to 530 nm with increments of 5 nm. To ensure a linear behavior of the emission intensity as a function of concentration, the absorption of the solution was adjusted to 0.1 %.

HPLC- Fluorescence Measurements

The fluorescence spectra of the crude mixture of **8** and its photoreaction products were separated and recorded using a HPLC system (UltiMate 3000, UHPLC+ focused, *Thermo Scientific*) comprising a quaternary solvent delivery pump, diode array and fluorescence detectors and an auto sampler was used to follow OII concentration-time profiles. Separation was performed on a C18 HPLC column (*Phenomenex* Luna 5 μ m, 100 Å, 250 × 2.0 mm) operating at 40 °C. Water (containing 5 mmol L⁻¹ ammonium acetate) and acetonitrile were used as eluents. A gradient of acetonitrile: H₂O, 5:95 to 100:0 (v/v) in 7 min at a flow rate of 0.40 mL·min⁻¹ was applied. The injection volume was 10 μ l and detection was achieved with the diode array detector and fluorescence detectors in scan mode. Data was analyzed with Chromeleon 7.2.9.0.

Photoreactor

The photoreactions were performed using a 250 mL round-bottom flask or a NMR-tubes (NORELL ST500-7 5mm, high-throughput 7" standard series) and LED (10W Violet LED, 410-420nm EPILED from futureeden) with an emission centered at 415 nm. The LEDs were powered by a variable power supply (1.00 A current) and positioned in a distance of 4 cm measured from the center of the vials (Figure 42). The LEDs and vials were cooled by two small ventilators to maintain ambient temperature of 20 to 24 °C. Individual procedures are described at Chapter 9.7.

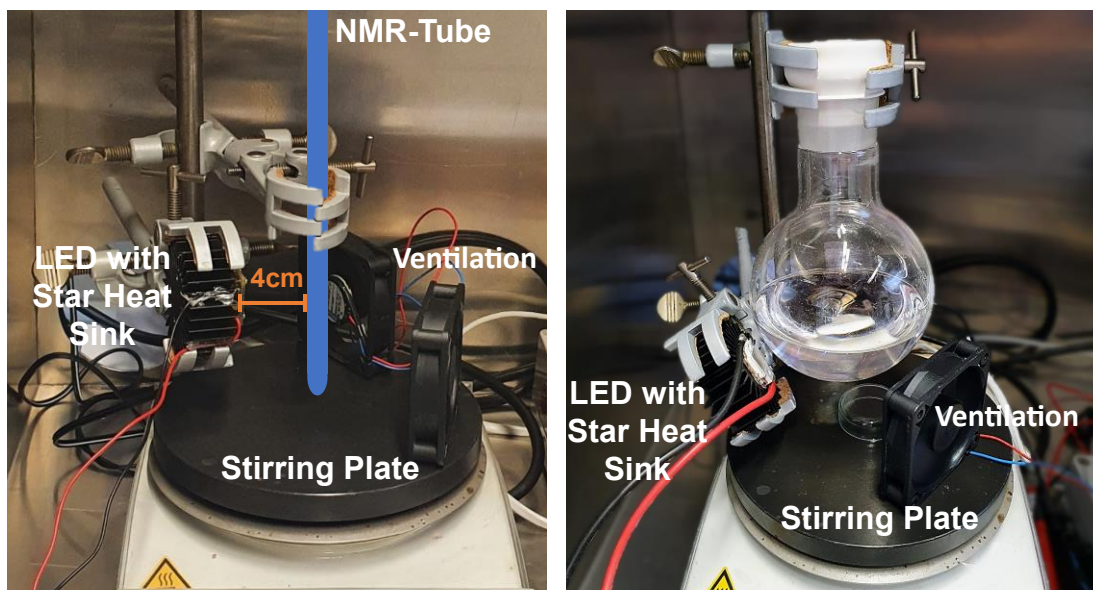


Figure 42: Left: Setup for small scale batch photoreactions performed in NMR-tubes. Right: Batch photoreaction setup for the cross-linking of linear polymers to SCNPs (Step 4). The LEDs and the reaction mixture were cooled using two small ventilators.

The change in the pH value during the reaction was recorded using a similar setup with a 100 mL two neck flask and the pH electrode AQUA-pH from TPS. Two small fans were used to maintain ambient temperature of 20 °C. The aqueous solution was degassed by passing through a stream of nitrogen for at least 10 min, which was continued during radiation (Figure 43).

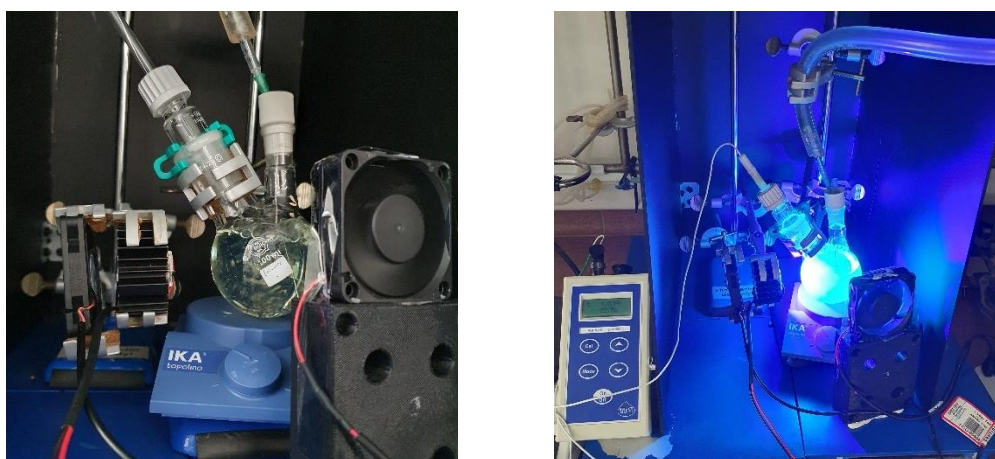


Figure 43: Irradiation setup for the photo cleavage of bimane with pH electrode to track the pH over time. The degassed sample in water was stirred with an electric stir bar and further flushed with N₂ to prevent contamination with oxygen. The LED and reaction mixture was cooled by small electric fans to maintain ambient temperature. Both pictures show the same setup from different angles without and under irradiation in a lightproof box.

LED emission spectra were recorded using an Ocean Insight Flame-T-UV-Vis spectrometer, with an active range of 200-850 nm and an integration time of 10 ms. The emission spectra of the employed LEDs are depicted in Figure 44.

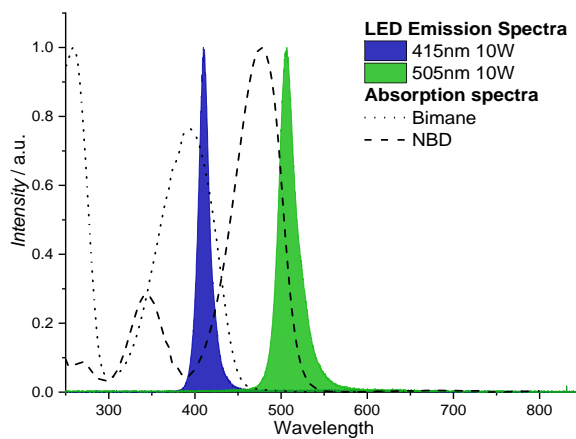
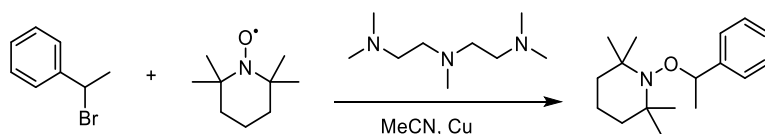


Figure 44: Emission spectrum of 415 nm (green) and 505 nm (blue) 10 W LEDs and absorbance spectrum of bimane and NBD (black).

9.3 Synthesis of Molecular Structures

9.3.1 2,2,6,6-Tetramethyl-1-(1-phenylethoxy)piperidine

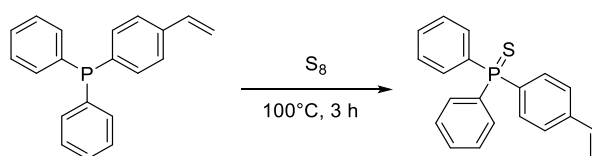


The procedure was adapted from Harrisson *et al.*, 2011.^[135, 167] (1-Bromoethyl)benzene (0.75 mL, 5.5 mmol, 1.00 eq) and 2,2,6,6-tetramethyl-1-piperidinyloxy (TEMPO, 0.94 g, 6.0 mmol, 1.10 eq) were dissolved in dry acetonitrile (10 mL). Copper powder (0.17 g, 2.7 mmol, 0.50 eq) was added, and the solution was degassed by purging with nitrogen for 10 min. *N,N,N',N'',N''*-Pentamethyldiethylenetriamine (PMDETA, 0.65 mL, 3.3 mmol, 0.60 eq) was added by syringe. The reaction was stirred overnight at ambient temperature. Afterwards the solvent and volatiles were removed under reduced pressure. The crude product was isolated by column chromatography on basic aluminum oxide with toluene as eluent. The solvent was removed under reduced pressure, yielding in the final product of a white, crystalline solid (1.1 g, 81%).

¹H NMR (400 MHz, CDCl₃) δ 7.29 – 7.11 (m, 5H), 4.72 (q, *J* = 6.7 Hz, 1H), 1.42 (d, *J* = 6.7 Hz, 3H), 1.37 – 0.60 (m, 18H).

¹³C{¹H} NMR (101 MHz, CDCl₃) δ 145.8, 127.9, 126.7, 126.5, 83.0, 59.6, 40.3, 34.4, 34.1, 23.5, 20.3, 17.2.

9.3.2 4-(Diphenylphosphino)styrene sulfide (S=PPh₂Sty)

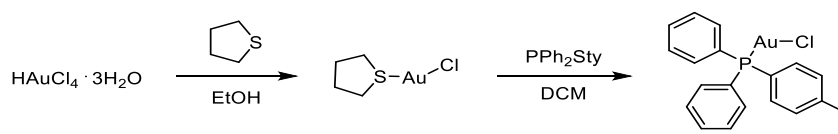


The procedure was adapted from Goodwin *et.al.*, 2020.^[168] Toluene (30 mL) was added to a mixture of S₈ (0.11 g, 3.5 mmol, 1.00 eq) and 4-(diphenylphosphino)styrene (1.0 g, 3.5 mmol, 1.00 eq) in a round bottom flask. The clear solution was heated at 110 °C for 3 h. The clear solution was concentrated to 15 mL, causing some colorless precipitate to form, which was redissolved by heating. Pentane (15 mL) was layered on top of the solution, which was subsequently stored overnight at -20 °C to give the product as large colorless needles (0.65 g, 59%).

$^1\text{H NMR}$ (400 MHz, CDCl_3) δ 7.80 – 7.60 (m, 6H), 7.56 – 7.38 (m, 8H), 6.74 (dd, $J = 17.6, 10.9$ Hz, 1H), 5.85 (d, $J = 17.6$ Hz, 1H), 5.38 (dd, $J = 10.8, 0.7$ Hz, 1H).

$^{31}\text{P}\{^1\text{H}\}$ NMR (162 MHz, CDCl_3) δ 42.9.

9.3.3 4-(Diphenylphosphino)styrene gold complex (ClAu-PPh₂Sty)



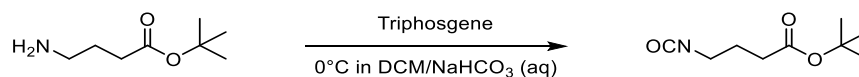
The procedure was adapted from Harper *et al.*, 2017.^[169] Chloroauric acid ($\text{HAuCl}_4 \cdot 3\text{H}_2\text{O}$, 0.10 g, 0.25 mmol, 1.00 eq) in EtOH (2.5 mL) was added to a solution of tetrahydrothiophene (0.11 g, 1.3 mmol, 5.00 eq) at ambient temperature. After stirring for 10 min, the precipitate was filtered and washed with cold EtOH (3×2 mL) and dried in *vacuo* to afford the intermediate chloro(tetrahydrothiophene)gold(I), $[(\text{tth})\text{AuCl}]$, as a white amorphous solid. $[(\text{tth})\text{AuCl}]$ was redissolved in DCM (2 mL) and 4-(diphenylphosphino)styrene (PPh₂Sty, 0.50 mmol, 2.00 eq) was added at room temperature. After stirring for 1h, the solution was concentrated to afford a colorless solid. The solid was dissolved in DCM and the solution was layered with hexane and allowed to stand overnight during which colorless crystals were formed. The crystals were filtered, washed with pentane (2×10 mL) and dried in *vacuo* to afford the pure product as colorless crystals (280 mg, 87%).

$^1\text{H NMR}$ (500 MHz, CDCl_3) δ 7.59 – 7.42 (m, 14H), 6.73 (dd, $J = 17.6, 10.9$ Hz, 1H), 5.86 (d, $J = 17.6$ Hz, 1H), 5.41 (d, $J = 10.9$ Hz, 1H).

$^{13}\text{C}\{^1\text{H}\}$ NMR (126 MHz, CDCl_3) δ 141.3, 135.6, 134.6, 134.5, 134.3, 134.1, 132.1, 132.1, 129.4, 129.3, 129.1, 128.6, 127.9, 127.4, 127.0, 126.9, 117.2.

$^{31}\text{P}\{^1\text{H}\}$ NMR (203 MHz, CDCl_3) δ 32.5.

9.3.4 Tert-butyl 4-isocyanatobutanoate

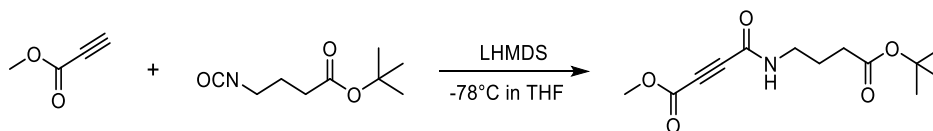


The procedure was adapted from Avalos *et al.*, 2008.^[170] Triphosgene (125 mg, 0.42 mmol, 0.30 eq) was added to a mixture of *tert*-butyl 4-aminobutanoate (250 mg, 1.28 mmol, 1.00 eq) in DCM (50 mL) and a saturated solution of NaHCO_3 (30 mL). The resulting mixture was stirred vigorously at 0°C for 30 min. The organic layer was separated and washed with distilled water and brine, dried (MgSO_4), and evaporated to dryness.

$^1\text{H NMR}$ (500 MHz, CDCl_3) δ 3.37 (t, $J = 6.6$ Hz, 2H), 2.32 (t, $J = 7.2$ Hz, 2H), 1.87 (p, $J = 6.9$ Hz, 2H), 1.44 (s, 9H).

$^{13}\text{C}\{^1\text{H}\}$ NMR (126 MHz, CDCl_3) δ 172.0, 122.1, 80.8, 44.7, 33.0, 28.0, 26.6.

9.3.5 Methyl 4-((4-(tert-butoxy)-4-oxobutyl)amino)-4-oxobut-2-ynoate (2)

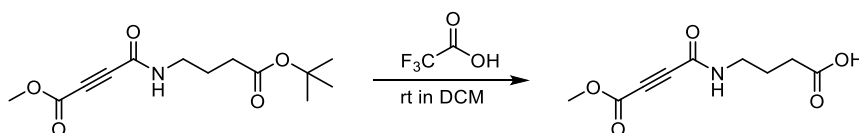


The procedure was adapted from Aioub *et al.*, 2018.^[171] Methyl propiolate (272 μL , 3.1 mmol, 1.00 eq) was dissolved in dry THF (10 mL) and cooled at -78°C in a dry ice/acetone bath under nitrogen atmosphere. LHMDS (1 M in THF, 3.2 mL, 3.2 mmol, 1.10 eq) was added dropwise. The resulting solution was stirred for an additional 30 min at -78°C . Subsequently, *tert*-butyl 4-isocyanatobutanoate (567 mg, 1.1 mmol, 1.00 eq) was added slowly to the reaction mixture and the resulting solution was stirred for an additional 30 min. The reaction was quenched by addition of saturated NH_4Cl (20 mL) at -78°C . The mixture was allowed to warm to ambient temperature, extracted with ethyl acetate (2x20 mL) and the combined organic layers were washed with NaHCO_3 and brine, dried over MgSO_4 , and concentrated at reduced pressure. The crude product was purified by column chromatography on silica gel (gradient CH:EE 100:0-30:70 v/v) to afford the product as a yellow oil (592 mg, 72%).

$^1\text{H NMR}$ (500 MHz, CDCl_3) δ 6.84 – 6.55 (m, 1H), 3.80 (s, $J = 0.9$ Hz, 3H), 3.40 – 3.30 (m, 2H), 2.34 – 2.23 (m, 2H), 1.94 – 1.74 (m, 2H), 1.49 – 1.36 (m, 9H).

$^{13}\text{C}\{^1\text{H}\}$ NMR (126 MHz, CDCl_3) δ 172.7, 152.8, 150.8, 81.0, 77.6, 73.5, 53.4, 39.7, 32.9, 28.1, 24.1.

9.3.6 4-(4-Methoxy-4-oxobut-2-ynamido)butanoic acid (3, A)

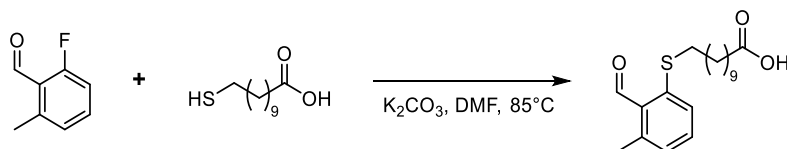


The procedure was adapted from Zhou *et al.*, 2020.^[172] Methyl 4-((4-(tert-butoxy)-4-oxobutyl)amino)-4-oxobut-2-ynoate (100 mg, 0.37 mmol, 1.00 eq) in dichloromethane (5 mL) was added dropwise at ambient temperature to a solution of TFA (422 mg, 3.72 mmol, 10.0 eq). The solution was stirred over night at room temperature, and volatiles removed under reduced pressure. The brown oil was coevaporated with toluene and dichloromethane to afford the final product as a yellow oil (75 mg, 95%).

$^1\text{H NMR}$ (500 MHz, CDCl_3) δ 6.70 (d, $J = 6.3$ Hz, 1H), 3.84 (s, $J = 12.3$ Hz, 3H), 3.40 (q, $J = 6.6$ Hz, 2H), 2.44 (t, $J = 7.0$ Hz, 2H), 1.91 (dp, $J = 13.8, 6.8$ Hz, 2H).

$^{13}\text{C}\{^1\text{H}\}$ NMR (126 MHz, CDCl_3) δ 178.2, 152.9, 151.2, 77.5, 73.8, 53.5, 39.5, 31.2, 24.0.

9.3.7 11-((2-Formyl-3-methylphenyl)thio)undecanoic acid (*o*MBA, B)



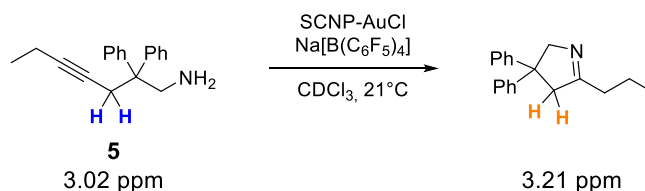
The procedure was adapted from Feist *et al.*, 2022.^[134] A dry Schlenk round bottom flask was charged with K_2CO_3 (2.50 g, 18.10 mmol, 2.50 eq), 2-fluoro-6-methylbenzaldehyde (1.00 g, 7.24 mmol, 1.00 eq), and 11-mercaptoundecanoic acid (1.90 g, 8.69 mmol, 1.20 eq) and the mixture was dissolved in 25 mL dry DMF. The solution was degassed by passing through a stream of N_2 for 10 min and stirred overnight at 85°C for 12 h. The crude mixture was cooled to ambient temperature, dissolved in 200 mL ethyl acetate, the organic phase was washed with 50 mL 1 N HCl, 2x 25 brine and dried over MgSO_4 . After recrystallization from DCM and *n*-hexane in a freezer the product was obtained as yellowish solid (2.10 g, 86 % yield).

$^1\text{H NMR}$ (500 MHz, CDCl_3) δ 10.68 (s, 1H), 7.35 (t, $J = 7.7$ Hz, 1H), 7.28 (d, $J = 7.9$ Hz, 1H), 7.04 (d, $J = 7.4$ Hz, 1H), 2.90 (t, $J = 7.4$ Hz, 2H), 2.60 (s, 3H), 2.35 (t, $J = 7.5$ Hz, 2H), 1.71 – 1.58 (m, 5H), 1.47 – 1.39 (m, 2H), 1.37 – 1.23 (m, 12H).

$^{13}\text{C}\{^1\text{H}\}$ NMR (126 MHz, CDCl_3) δ 192.6, 179.1, 142.8, 141.9, 132.8, 128.8, 126.7, 34.0, 33.8, 29.3, 29.3, 29.1, 29.1, 29.0, 28.9, 28.6, 24.6, 20.6.

9.3.8 Catalyzed Intramolecular Hydroamination

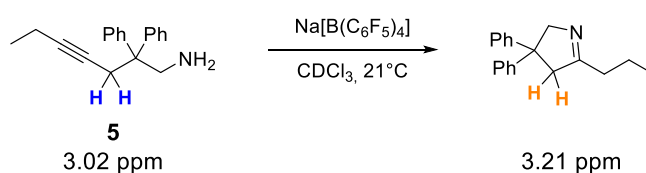
Intramolecular Hydroamination with SCNP-AuCl as Catalyst



The procedure was adapted from Bohlen *et al.*, 2021.^[118] A stock solution of the substrate (**5**, 123.26 mg, 0.468 mmol) in 800 μL CDCl_3 and the internal standard ferrocene (8.72 mg, 0.0468 mmol) in 1000 μL CDCl_3 were prepared. SCNP-AuCl (0.0029 mmol, 0.02 eq or 0.0005 mmol, 0.004 eq, $[\text{PPh}_2\text{Sty-AuCl}]$ units calculated by $^{31}\text{P}\{^1\text{H}\}$ NMR with internal standard PO_4Ph_3) and the cocatalyst $\text{Na}[\text{B}(\text{C}_6\text{F}_5)_4]$ (2.16 mg, 0.0023 mmol, 0.02 eq) were

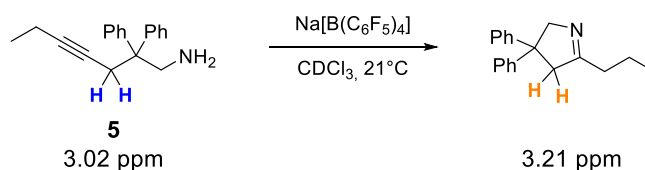
mixed with 200 μL CDCl_3 and 200 μL of ferrocene stock solution (1.741 mg, 0.0094 mmol, 0.08 eq) in a 10 mL vial with screw cap. The mixture was stirred and treated in an ultrasonic bath until the cocatalyst reacts with the gold complex and therefore dissolves. The solution was transferred to a Young NMR tube and the vial rinsed with 200 μL CDCl_3 . The solution was frozen with liquid nitrogen and 200 μL of the stock solution of the substrate (**5**, 30.82 mg, 0.117 mmol, 1 eq) was added and frozen. The open Young NMR tube was warmed up until the solution thawed and inserted into the NMR spectrometer (t_0). To monitor the conversion, ^1H NMR spectra were recorded as a time series at constant temperature of 21°C. The conversion was determined *via* comparison of the integrals of the characteristic resonances of substrate **5** (3.02 ppm) and the product (3.21 ppm), using ferrocene (4.19 ppm) as internal standard.

Intramolecular Hydroamination with AuCl-PPh₂Sty as catalyst



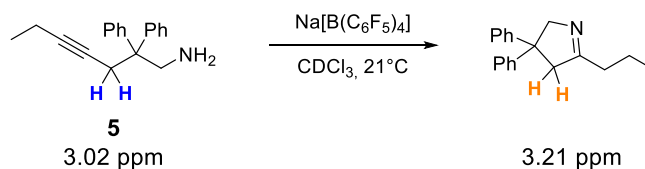
The procedure was adapted from Bohlen *et al.*, 2021.^[118] A stock solution of the substrate (**5**, 123.26 mg, 0.468 mmol) in 800 μL CDCl_3 and the internal standard ferrocene (8.72 mg, 0.0468 mmol) in 1000 μL CDCl_3 were prepared. AuCl-PPh₂Sty (0.0017 mmol, 0.015 eq calculated by $^{31}\text{P}\{^1\text{H}\}$ NMR with internal standard PO_4Ph_3) and the cocatalyst Na[B(C₆F₅)₄] (2.16 mg, 0.0023 mmol, 0.02 eq) were mixed with 200 μL CDCl_3 and 200 μL of ferrocene stock solution (1.741 mg, 0.0094 mmol, 0.08 eq) in a 10 mL vial with screw cap. The mixture was stirred and treated in an ultrasonic bath until the cocatalyst reacts with the gold complex and therefore dissolves. The solution was transferred to a Young NMR tube and the vial rinsed with 200 μL CDCl_3 . The solution was frozen with liquid nitrogen and 200 μL of the stock solution of the substrate (**5**, 30.82 mg, 0.117 mmol, 1 eq) was added and frozen. The open Young NMR tube was warmed up until the solution thawed and inserted into the NMR spectrometer (t_0). To monitor the conversion, ^1H NMR spectra were recorded as a time series at constant temperature of 21°C. The conversion was determined *via* comparison of the integrals of the characteristic resonances of substrate **5** (3.02 ppm) and the product (3.21 ppm), using ferrocene (4.19 ppm) as internal standard.

Intramolecular Hydroamination with P4 as catalyst



The procedure was adapted from Bohlen *et al.*, 2021.^[118] A stock solution of the substrate (**5**, 123.26 mg, 0.468 mmol) in 800 μL CDCl_3 and the internal standard ferrocene (8.72 mg, 0.0468 mmol) in 1000 μL CDCl_3 were prepared. **P4** (0.0001 mmol, 0.008 eq calculated by $^{31}\text{P}\{^1\text{H}\}$ NMR with internal standard PO_4Ph_3) and the cocatalyst $\text{Na}[\text{B}(\text{C}_6\text{F}_5)_4]$ (2.16 mg, 0.0023 mmol, 0.02 eq) were mixed with 200 μL CDCl_3 and 200 μL of ferrocene stock solution (1.741 mg, 0.0094 mmol, 0.08 eq) in a 10 mL vial with screw cap. The mixture was stirred and treated in an ultrasonic bath until the cocatalyst reacts with the gold complex and therefore dissolves. The solution was transferred to a Young NMR tube and the vial rinsed with 200 μL CDCl_3 . The solution was frozen with liquid nitrogen and 200 μL of the stock solution of the substrate (**5**, 30.82 mg, 0.117 mmol, 1 eq) was added and frozen. The open Young NMR tube was warmed up until the solution thawed and inserted into the NMR spectrometer (t_0). To monitor the conversion, ^1H NMR spectra were recorded as a time series at constant temperature of 21°C. The conversion was determined *via* comparison of the integrals of the characteristic resonances of substrate **5** (3.02 ppm) and the product (3.21 ppm), using ferrocene (4.19 ppm) as internal standard.

Intramolecular Hydroamination without catalyst (blank)

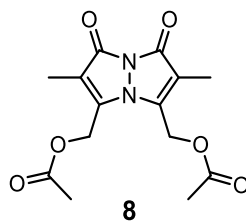


The procedure was adapted from Bohlen *et al.*, 2021.^[118] A stock solution of the substrate (**5**, 123.26 mg, 0.468 mmol) in 800 μL CDCl_3 and the internal standard ferrocene (8.72 mg, 0.0468 mmol) in 1000 μL CDCl_3 were prepared. The cocatalyst $\text{Na}[\text{B}(\text{C}_6\text{F}_5)_4]$ (2.16 mg, 0.0023 mmol, 0.02 eq) were mixed with 200 μL CDCl_3 and 200 μL of ferrocene stock solution (1.741 mg, 0.0094 mmol, 0.08 eq) in a 10 mL vial with screw cap. The mixture was stirred and treated in an ultrasonic bath for 20 min. The solution was transferred to a Young NMR tube

and the vial rinsed with 200 μL CDCl_3 . The solution was frozen with liquid nitrogen and 200 μL of the stock solution of the substrate (**5**, 30.82 mg, 0.117 mmol, 1 eq) was added and frozen. The open Young NMR tube was warmed up until the solution thawed and inserted into the NMR spectrometer (t_0). To monitor the conversion, ^1H NMR spectra were recorded as time series at a constant temperature of 21°C. The conversion was determined *via* comparison of the integrals of characteristic resonances of starting material (**5**: 3.02 ppm) and product (3.21 ppm), using ferrocene (4.19 ppm) as internal standard.

9.3.9 2,6-dimethyl-1,7-dioxo-1H,7H-pyrazolo[1,2-a]pyrazole-3,5-diyl)bis(methylene) diacetate, **8**

To study the photo induced cleavage of the bimane ester bonds, the photoreaction was performed with the bimane caged acetate ester ((2,6-dimethyl-1,7-dioxo-1H,7H-pyrazolo[1,2-a]pyrazole-3,5-diyl)bis(methylene) diacetate, **8**) with similar conditions to the SCNPs unfolding.



Dibromobimane **6** (10.00 g, 0.03 mmol, 1.00 eq), cesium carbonate (23.30 mg, 0.07 mmol, 2.50 eq) and acetic acid (8.20 μL , 0.14 mmol, 5.00 eq) were dissolved in THF and stirred at ambient temperature overnight. The reaction mixture was mixed with water (5 mL) and extracted with ethyl acetate (2 mL) four times. The organic phase was washed with brine (2 mL) and dried over MgSO_4 . The obtained product **8** was characterized by LC-MS (Figure 46) and NMR.

^1H NMR (600 MHz, CDCl_3) δ 5.12 (s, 2H), 2.14 (s, 3H), 1.97 (s, 3H).

$^{13}\text{C}\{^1\text{H}\}$ NMR (151 MHz, CDCl_3) δ 169.8, 160.0, 142.3, 117.0, 77.4, 77.2, 77.0, 54.6, 20.7, 7.3.

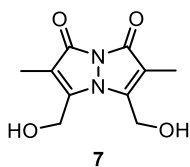
8 was dissolved in 8 mL H_2O and degassed by passing through a stream of N_2 for 10 min. The solution was irradiated with $\lambda_{\text{max}} = 415$ nm for 30 min (Irradiation Experiments) and subsequently freeze dried. The obtained product was analyzed by LC-MS (Figure 15 - Figure 50).

The LC-MS traces show a mixture of the monohydroxybimane **9** ((5-(hydroxymethyl)-2,6-dimethyl-1,7-dioxo-1H,7H-pyrazolo[1,2-a]pyrazol-3-yl)methyl acetate) and dihydroxybimane **7** (3,5-bis(hydroxymethyl)-2,6-dimethyl-1H,7H-pyrazolo[1,2-a]pyrazole-1,7-dione) along

with a small amount of side product. After 30 min of irradiation the reaction mixture still contains a significant amount of educt. Compared with the SCNPs unfolding were full conversion after 20 min according the UV/VIS absorption was observed, the conversion of **8** is lower. This might be due to a higher concentration of **8** in water compared to the SCNPs unfolding.

9.3.10 Dihydroxybimane **7**

To study the stability of dihydroxybimane **7** during radiation **7** was synthesized and irradiated for 30 min.

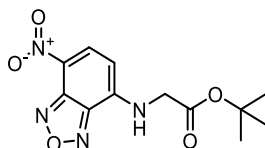


Dibrombimane (10.00 mg, 0.03 mmol, 1.00 eq) was dissolved in ethanol and sodium formate (19.40 mg, 0.29 mmol, 10.00 eq) was added. The reaction mixture was heated overnight at 80 °C, cooled at ambient temperature, filtered and the solvent evaporated to obtain the product **7** without further purification. The product was characterized by LC-MS (Figure 51).

7 was dissolved in 8 mL H₂O and degassed by passing through a stream of N₂ for 10 min. The solution was irradiated for 30 min (IrRadiation Experiments) and subsequently freeze dried. The obtained product was analyzed by LC-MS (Figure 15, Figure 52).

After 30 min of radiation no significant conversion of **7** or formation of side products could be observed.

9.3.11 *tert*-Butyl (7-nitrobenzo[*c*][1,2,5]oxadiazol-4-yl)glycinate (NBD-Gly-*tert*)



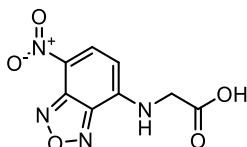
The procedure was adapted from Greco *et al.*^[173] Glycine *tert*-butyl ester (1.68 g, 5.01 mmol, 2.00 eq), 4-chloro-7-nitrobenzo-2-oxa-1,3-diazole (0.51 g, 2.51 mmol, 1.00 eq) and NaHCO₃ (0.63 g, 7.52 mmol, 3.00 eq) were dissolved in 25 mL of methanol. The mixture was stirred under light exclusion at room temperature. After 16 h, the solvent was evaporated and the residue dissolved in 100 mL of ethyl acetate, the organic phase was washed with 3x 50 mL of 1 N HCl, 25 brine, dried over MgSO₄ and filtered. The solvent was evaporated. The crude

product was purified by column chromatography on silica gel (gradient CH:EE 70:30-20:80 v/v) to afford the product as an orange powder.

$^1\text{H NMR}$ (600 MHz, CD_3CN) δ 8.50 (d, $J = 8.7$ Hz, 1H), 7.28 (s, 1H), 6.28 – 6.24 (m, 1H), 4.20 (s, 2H), 1.47 (s, 9H).

$^{13}\text{C}\{^1\text{H}\}$ NMR (151 MHz, CD_3CN) δ 168.5, 145.7, 145.3, 137.9, 125.0, 100.8, 83.5, 46.4, 28.2.

9.3.12 (7-Nitrobenzo[*c*][1,2,5]oxadiazol-4-yl)glycine (11)

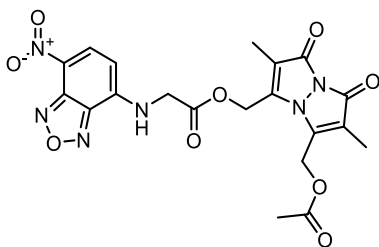


tert-Butyl (7-nitrobenzo[*c*][1,2,5]oxadiazol-4-yl)glycinate (50.00 mg, 0.17 mmol, 1.00 eq) was dissolved in 1 mL of trifluoroacetic acid and 0.1 mL triethylsilane was added. After 90 min, the reaction mixture was dissolved in 50 mL ethyl acetate, the organic phase was washed with 3x 50 mL of 1 N HCl, 25 brine, dried over MgSO_4 and filtered. The product was afforded as an orange powder.

$^1\text{H NMR}$ (600 MHz, MeOD) δ 8.52 (d, $J = 8.7$ Hz, 1H), 6.30 (s, 1H), 4.32 (s, 2H).

$^{13}\text{C}\{^1\text{H}\}$ NMR (151 MHz, MeOD) δ 171.8, 145.9, 145.4, 138.0, 127.8, 124.5, 100.6, 45.4.

9.3.13 (5-(Acetoxymethyl)-2,6-dimethyl-1,7-dioxo-1H,7H-pyrazolo[1,2-*a*]pyrazol-3-yl)methyl (7-nitrobenzo[*c*][1,2,5]oxadiazol-4-yl)glycinate (10)

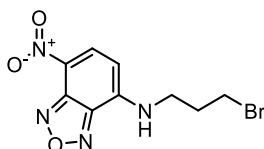


11 (10.00 mg, 0.04 mmol, 1.00 eq), dibromobimane (22.00 mg, 0.04 mmol, 1.50 eq), and Cs_2CO_3 (6.84 mg, 0.02 mmol, 0.50 eq) were dissolved in 5 mL of THF and stirred at ambient temperature for 6 h. Cs_2CO_3 (123 mg, 0.38 mmol, 9.00 eq) and acetic acid (0.024 mL, 0.42 mmol, 10.00 eq) were added and stirred for additional 2 h. The reaction mixture was dissolved in 50 mL of ethyl acetate, the organic phase was washed with 3x 50 mL of 1 N HCl, 25 brine, dried over MgSO_4 and filtered. The crude product was purified by column chromatography on silica gel (gradient DCM:MeOH 98:2-92:8 v/v) to afford the product as an orange powder.

$^1\text{H NMR}$ (600 MHz, CD_3CN) δ 8.48 (d, $J = 8.6$ Hz, 1H), 6.29 (d, $J = 6.5$ Hz, 1H), 5.24 (s, 2H), 5.01 (s, 2H), 4.40 (s, 2H), 2.05 (s, 3H), 1.88 (s, 3H), 1.83 (s, 3H).

$^{13}\text{C}\{^1\text{H}\}$ NMR (151 MHz, CD_3CN) δ 170.8, 161.0, 144.0, 143.3, 137.5, 116.5, 56.4, 55.5, 20.7, 7.2, 7.1.

9.3.14 *N*-(3-bromopropyl)-7-nitrobenzo[*c*][1,2,5]oxadiazol-4-amine (12)



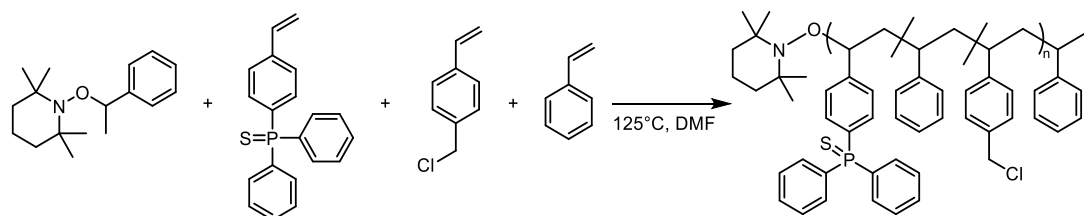
The procedure was adapted from Buscher *et al.*^[174] 4-Chloro-7-nitrobenzo[*c*][1,2,5]oxadiazole (100 mg, 0.50 mmol, 1.00 eq.) was dissolved in EtOAc (3.0 mL). 3-Bromopropylamine (109.70 mg, 0.50 mmol, 1.00 eq.) and NaHCO_3 (126.26 mg, 1.50 mmol, 3.00 eq.) were added and the suspension was stirred at 50 °C for 3 d. The reaction mixture was diluted with 50 mL of ethyl acetate, the organic phase was washed with 3x 50 mL 1 N HCl, 25 brine, dried over MgSO_4 and filtered. The crude product was purified by column chromatography on silica gel (gradient CH:EE 75:25-45:55 v/v) to afford the product as an orange powder (63 mg).

$^1\text{H NMR}$ (600 MHz, CD_3CN) δ 8.49 (d, $J = 8.8$ Hz, 1H), 7.39 (s, 1H), 6.34 (d, $J = 8.8$ Hz, 1H), 3.66 (s, 2H), 3.58 (t, $J = 6.5$ Hz, 2H), 2.27 (p, $J = 6.6$ Hz, 2H).

$^{13}\text{C}\{^1\text{H}\}$ NMR (151 MHz, CD_3CN) δ 144.4, 145.3, 144.9, 137.8, 123.5, 99.5, 42.5, 31.5, 31.4.

9.4 Polymerizations

9.4.1 NMP copolymerization to form a poly(styrene-co-chloromethylstyrene-co-4-(diphenylphosphino sulfide)styrene) (P1)



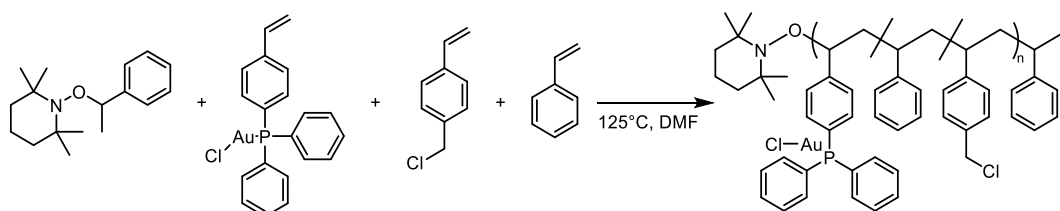
The procedure was adapted from Hooker *et al.*, 2020.^[135] Initiator 2,2,6,6-Tetramethyl-1-(1-phenylethoxy)piperidine (9.0 mg, 0.034 mmol, 1.00 eq), styrene (0.98 mL, 10.3 mmol, 300 eq), chloromethylstyrene (CMS) (0.34 mL, 2.07 mmol, 60.0 eq) and 4-(diphenylphosphino sulfide)styrene (165.5 mg, 0.52 mmol, 15.0 eq) were added to a 10 mL Schlenk tube and dissolved in DMF (2.5 mL). As internal standards 1,4-dimethoxybenzene (15.0 eq) and triphenylphosphate (5.00 eq) were used. The reaction mixture was degassed by passing through a stream of N₂ for 10 min. Subsequently, the reaction mixture was sealed and heated at 125 °C. After 6 h, the reaction was stopped by cooling the flask to ambient temperature. The crude mixture was dissolved in a small amount of THF (2 mL) and added dropwise to a solution of cold methanol (-20°C). The precipitate was collected by centrifugation and purified in the same way a second time before the polymer was dried under high vacuum. The product was obtained as white powder.

SEC characterization (THF, RI): $M_n = 21\,000\text{ g}\cdot\text{mol}^{-1}$, $D = 1.28$.

¹H NMR (500 MHz, CDCl₃) δ 7.73 – 6.22 (m, aromatic protons of S=PPh₂Sty, CMS and Sty), 4.58 (bs, CH₂Cl), 2.19 – 1.12 (m, aliphatic protons, backbone).

³¹P{¹H} NMR (203 MHz, CDCl₃) δ 42.7 (s, S=PPh₃).

9.4.2 NMP copolymerization to form a poly(styrene-co-chloromethylstyrene-co-AuCl-PPh₂Sty) (P4)



The procedure was adapted from Hooker *et al.*, 2020.^[135] Initiator 2,2,6,6-Tetramethyl-1-(1-phenylethoxy)piperidine (9.0 mg, 0.034 mmol, 1.00 eq), styrene (0.98 mL, 10.3 mmol, 300 eq), chloromethylstyrene (CMS) (0.17 mL, 1.03 mmol, 30.0 eq) and (chloro(4-

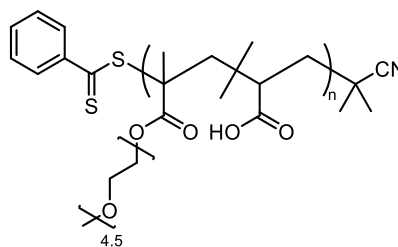
(diphenylphosphino) styrene)gold(I) (264.8 mg, 0.52 mmol, 15.0 eq) were added to a 10 mL Schlenk tube and dissolved in DMF (2.5 mL). As internal standards 1,4-dimethoxybenzene (15.0 eq) and triphenylphosphate (5.00 eq) were used. The reaction mixture was degassed by passing through a stream of N₂ for 10 min. Subsequently, the reaction mixture was sealed and heated at 125 °C. After 6 h, the reaction was stopped by cooling the flask to ambient temperature. The crude mixture was dissolved in a small amount of THF (2 mL) and added dropwise to a solution of cold methanol (-20°C). The precipitate was collected by centrifugation and purified in the same way a second time before the polymer was dried under high vacuum. The product was obtained as white powder.

SEC characterization (THF, RI): $M_n = 20\,000\text{ g}\cdot\text{mol}^{-1}$, $\mathcal{D} = 1.34$.

¹H NMR (500 MHz, CDCl₃) δ 7.63 – 6.26 (m, aromatic protons of AuCl-PPh₂Sty, CMS and Sty), 4.57 (bs, CH₂Cl), 2.31 – 1.23 (m, aliphatic protons, backbone).

³¹P{¹H} NMR (203 MHz, CDCl₃) δ 32.3 (s, AuCl-PPh₂Sty), -17.68 (s, internal standard PO₄Ph₃).

9.4.3 RAFT copolymerization to form poly(poly(ethylene glycol) methyl ether methacrylate-*co*-acrylic acid) (poly(MPEGMA-*co*-AA))

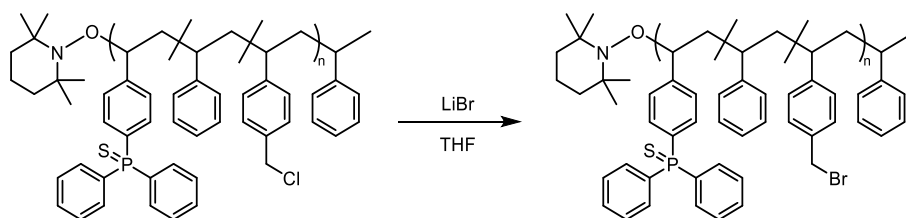


The procedure was adapted from Irshadeen *et al.*, 2022.^[175] Poly(ethylene glycol) methyl ether methacrylate and acrylic acid was passed through a short neutral alumina column to remove the inhibitor before being utilized in the polymerization. Poly(ethylene glycol) methyl ether methacrylate ($M_n = 300\text{ g mol}^{-1}$, 2.79 mL, 300.00 eq, 13.52 mmol), acrylic acid (309.00 μL , 100.00 eq, 4.51 mmol), 2-cyano-2-propyl benzodithioate (9.97 mg, 1.00 eq, 45.06 μmol) and AIBN (12 wt. % in acetone, 9.97 μL , 0.20 eq, 9.01 μmol) were added to a 10 mL Schlenk tube and dissolved in 10 mL of DMF. The reaction mixture was degassed by passing through a stream of N₂ for 10 min. The mixture was subsequently heated at 70 °C for 22 h. The polymer was purified by twice precipitation into cold Et₂O/pentane (5:1) and centrifuged.

SEC characterization (THF, RI): $M_n = 47.24 \cdot 10^3\text{ g mol}^{-1}$, $\mathcal{D} = 1.37$.

9.5 Polymer Post-Functionalization and Modification

9.5.1 Poly(styrene-co-bromomethylstyrene-co-4-(diphenylphosphino sulfide)styrene) (P2)



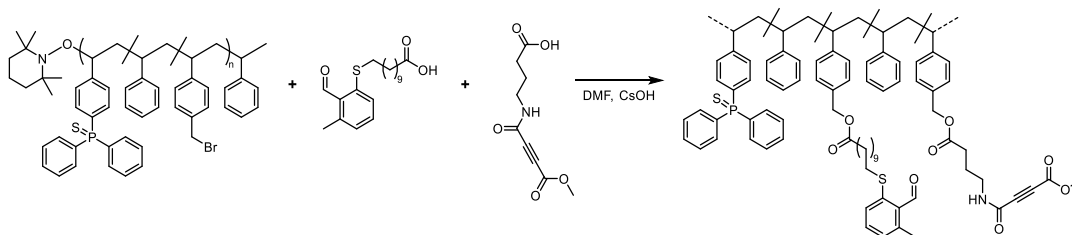
P1 (450.0 mg, equivalent to 1.15 mmol CMS units, 1.00 eq) and lithium bromide (1.50 g, 17.27 mmol, 15.02 eq) were dissolved in 12 mL of anhydrous THF resulting in a clear solution. The solution was degassed by passing through a stream of N_2 for 10 min and stirred overnight at ambient temperature. The crude mixture was added dropwise to a solution of cold methanol ($-20^\circ C$). The precipitate was collected by centrifugation and dried under high vacuum. The product was obtained as white powder.

SEC characterization (THF, RI): $M_n = 16\ 000\ g\cdot mol^{-1}$, $D = 1.50$.

1H NMR (500 MHz, $CDCl_3$) δ 7.91 – 6.12 (m, aromatic protons of $S=PPh_2Sty$, BMS and Sty), 4.42 (bs, CH_2Br), 2.51 – 0.83 (m, aliphatic protons, backbone).

$^{31}P\{^1H\}$ NMR (203 MHz, $CDCl_3$) δ 42.7 (s, $S=PPh_3$).

9.5.2 Post-functionalization of P2 with the alkyne and oMBA (P3)



P2 (50.00 mg, equivalent to 0.13 mmol BMS units, 1.00 eq), 11-((2-formyl-3-methylphenyl)thio)undecanoic acid (86.10 mg, 0.26 mmol, 2.00 eq) and 4-(4-methoxy-4-oxobut-2-ynamido)butanoic acid (81.80 mg, 0.38 mmol, 3.00 eq) were dissolved in DMF (3 mL) and degassed by passing a stream of N_2 for 10 min through the solution. Subsequently, CsOH (85.90 mg, 0.51 mmol, 4 eq) was added and the mixture stirred at ambient temperature for 2 h under exclusion of light. The crude mixture was added dropwise to a solution of cold methanol ($-20^\circ C$) and the precipitate was collected by centrifugation. The white solid was immediately dissolved in a small amount of DCM and purified in the same

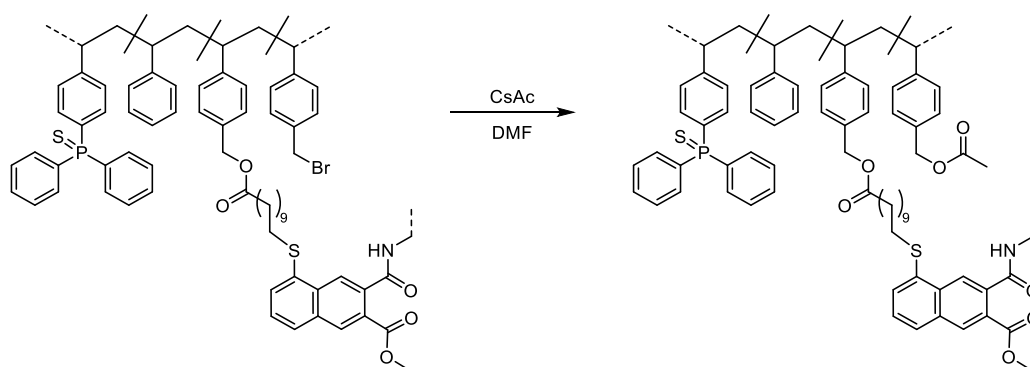
way. For better flocculation, CsCl was added as a coagulant. The product was stored in DCM solution.

SEC characterization (THF, RI): $M_n = 17\,000\text{ g mol}^{-1}$, $\mathcal{D} = 1.68$.

$^1\text{H NMR}$ (500 MHz, CDCl_3) δ 10.68 (s, CHO), 7.87 – 6.03 (m, aromatic protons of $\text{S}=\text{PPh}_2\text{Sty}$, BMS and Sty), 5.04 (bs, $\text{CH}_2\text{-OOC}$), 4.47 (bs, CH_2Br), 3.76 (bm, alkin- CH_3), 3.41 (bd, $\text{CH}_2\text{-N}$, $\text{CH}_2\text{-S}$), 2.24 – 0.64 (m, aliphatic protons, backbone).

$^{31}\text{P}\{^1\text{H}\}$ NMR (203 MHz, CDCl_3) δ 42.7 (s, $\text{S}=\text{PPh}_3$).

9.5.3 Removing of remaining BMS groups with cesium acetate

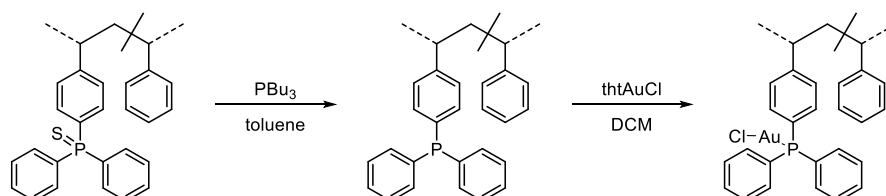


SCNP1 (20 mg) were dissolved in 3 mL DMF and mixed with acetic acid (100 μL , 1.74 mmol) and cesium hydroxide (263 mg, 1.57 mmol). The solution was degassed by passing through a stream of N_2 for 10 min and stirred at room temperature for 3 d. The crude mixture was added dropwise to a solution of cold methanol (-20°C) and the precipitate was collected by centrifugation.

SEC characterization (THF, RI): $M_n = 10\,000\text{ g}\cdot\text{mol}^{-1}$, $\mathcal{D} = 1.28$.

$^1\text{H NMR}$ (500 MHz, CDCl_3) δ 7.86 – 6.03 (m, aromatic protons of $\text{S}=\text{PPh}_2\text{Sty}$, BMS and Sty), 4.96 (bs, $\text{CH}_2\text{-OOC}$), 3.12 – 0.63 (m, aliphatic protons, backbone).

9.5.4 Complexation of gold yielding in SCNP-AuCl



Protected SCNPs (20 mg, from section 9.5.3) were dissolved in 5 mL toluene and degassed by passing a stream of N_2 for 10 min through the solution. Tributylphosphine (0.35 mL, 1.42 mmol) was added and heated at 120°C using a pressure tube. After 24 h, the reaction

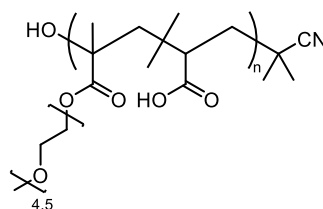
mixture was cooled to ambient temperature and added dropwise to a solution of cold methanol (-20°C). The precipitate was collected by centrifugation, dissolved in a small amount of DCM, and purified again in cold methanol (-20°C). For better flocculation CsCl was added as a coagulant. The brown solid product was diluted in DCM and degassed by passing through a stream of N₂ for 10 min. Chloro(tetrahydrothiophene)gold(I) ([tthtAuCl], 5 mg, 0.02 mmol, approximately 1.5 eq per PPh₃ unit) was added and stirred for 1 h. The crude mixture was added dropwise to a solution of cold diethyl ether (-20°C) and the precipitate was collected by centrifugation. For better flocculation CsCl was added as a coagulant. The product was obtained as yellow solid.

SEC characterization (THF, RI): $M_n = 15\,000\text{ g mol}^{-1}$, $D = 1.14$.

¹H NMR (500 MHz, CDCl₃) δ 7.75 – 6.12 (m, aromatic protons of S=PPh₂Sty, BMS and Sty), 5.00 (bs, CH₂-OOC), 2.77 – 0.52 (m, aliphatic protons, backbone).

³¹P{¹H} NMR (203 MHz, CDCl₃) δ 32.3 (s, AuCl-PPh₃), 29.1 (s, O=PPh₃).

9.5.5 End group modification of poly(poly(ethylene glycol) methyl ether methacrylate-co-acrylic acid) (poly(MPEGMA-co-AA)) yielding P5



The procedure was adapted from Dietrich *et al.*, 2010.^[60] A solution of 2,2'-azobis(isobutyronitrile) (14.79 mg, 0.09 mmol, 10 mmol L⁻¹) in 9 mL of THF was heated at 60 °C for 60 min under ambient atmosphere. A solution of 3.00 g RAFT-polymer in the pre-treated THF (10 mmol L⁻¹ based on M_n) was prepared in a 50 mL round flask under ambient atmosphere. The flask was subsequently heated to 60 °C under vigorous stirring. After the discoloration of the solution indicated full conversion of the RAFT end group, the temperature was reduced to 40 °C and 3.00 eq triphenylphosphine were added. After 15 min the polymer was precipitated twice in cold Et₂O/pentane (5:1) and centrifuged.

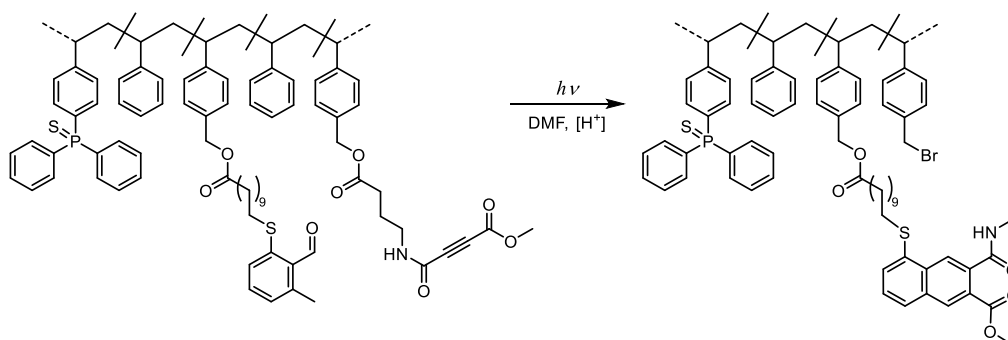
SEC characterization (DMAc, RI): $M_n = 36.53 \cdot 10^3\text{ g mol}^{-1}$, $D = 1.50$.

SEC characterization (THF, RI): $M_n = 47.95 \cdot 10^3\text{ g mol}^{-1}$, $D = 1.36$.

¹H NMR (400 MHz, CDCl₃) δ 4.43 – 3.92 (m), 3.75 – 3.60 (m), 3.59 – 3.53 (m), 3.39 (bs), 2.25 – 1.68 (m), 1.21 – 1.08 (m), 1.09 – 0.94 (m), 0.94 – 0.82 (m).

9.6 SCNPs Formation

9.6.1 Photoinduced Diels–Alder cycloaddition for the SCNP formation (SCNP1)



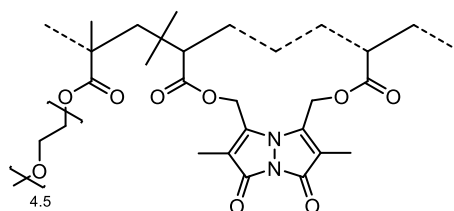
A **P3** (10 mg in 1 mL DCM, from step 3) solution in DCM was passed through a 0.2 μm PTFE membrane filter and diluted with toluene (100 mL, $c(\text{poly}) = 0.1 \text{ mg/mL}$). The solution was degassed by passing a stream of N_2 for 10 min through the solution and irradiated for 2 h using an LED with an emission centered at 415 nm (refer to Chapter 9.2). The solvent was removed under reduced pressure at 40°C water bath temperature yielding in a yellowish solid.

SEC characterization (THF, RI): $M_n = 15\,000 \text{ g mol}^{-1}$, $D = 1.54$.

$^1\text{H NMR}$ (500 MHz, CDCl_3) δ 7.74 – 6.21 (m, aromatic protons of $\text{S=PPh}_2\text{Sty}$, BMS and Sty), 5.01 (bs, $\text{CH}_2\text{-OOC}$), 4.42 (bs, CH_2Br), 3.96 – 3.22 (m, alkin- CH_3), 3.11 – 0.66 (m, aliphatic protons, backbone).

$^{31}\text{P}\{^1\text{H}\}$ NMR (203 MHz, CDCl_3) δ 42.7 (s, S=PPh_3).

9.6.2 SCNPs formation by cross-linking with dibromobimane **6** (SCNP2)

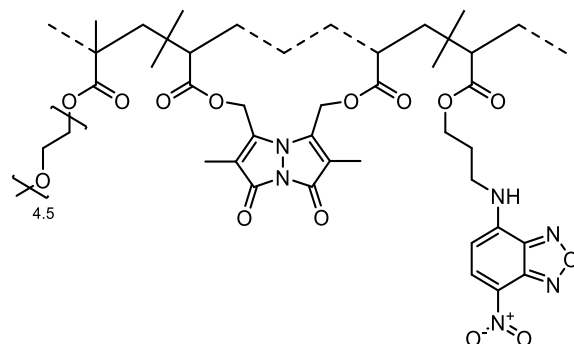


A solution of **P5** (150.00 mg, equivalent to 0.09 mmol AA units, 1.00 eq) and cesium carbonate (16.10 mg, 0.05 mmol, 0.50 eq) was dissolved in 750 mL of THF in a 1 L round bottom flask (brown glass). Dibromobimane **6** (16.10 mg, 0.05 mmol, 0.50 eq) was added and stirred for 48 h. Afterwards, the solvent was evaporated and the polymer was precipitated in cold Et_2O /pentane (5:1) and centrifuged yielding **SCNP2** which was stored in a solution of MeOH (10 mg mL) to prevent side reaction and precipitation.

SEC characterization (DMAc, RI): $M_n = 31.34 \cdot 10^3 \text{ g mol}^{-1}$, $\mathcal{D} = 1.49$.

$^1\text{H NMR}$ (400 MHz, CDCl_3) δ 4.08 (bs), 3.64 (bs), 3.55 (bs), 3.37 (bs), 2.09 – 1.64 (m), 1.14 – 0.74 (m).

9.6.3 Post-functionalization and SCNPs formation (SCNP3)

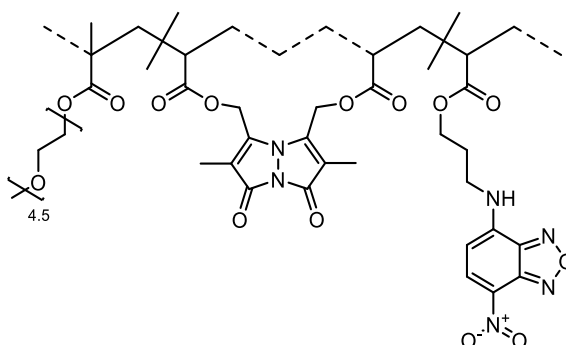


P5 (50.00 mg, equivalent to 30.74 μmol AA units, 1.00 eq) and cesium carbonate (5.01 mg, 15.37 μmol , 0.50 eq) was dissolved in 2.5 mL of THF in a 500 mL round bottom flask (brown glass). **12** (4.6 mg, 15.37 μmol , 0.50 eq) was added and stirred for 18 h. Subsequently, the reaction mixture was diluted with 250 mL THF and dibromobimane **6** (5.01 mg, 30.74 μmol , 0.50 eq) was added and stirred further 24 h. Next, the solvent was evaporated, and the polymer was purified by dialysis (cellulose membrane, 10 kDa MWCO) in methanol affording **SCNP3**, which was stored in a solution of MeOH (10 mg mL) to prevent side reaction and precipitation.

SEC characterization (DMAc, RI): $M_n = 35.67 \cdot 10^3 \text{ g mol}^{-1}$, $\mathcal{D} = 1.57$.

$^1\text{H NMR}$ (600 MHz, MeOD) δ 8.61 (s), 6.50 (s), 5.45 (bs), 4.13 (bs), 3.66 (bs), 3.56 (bs), 3.38 (bs), 2.30 – 1.66 (m), 1.25 – 0.79 (m).

9.6.4 Post-functionalization and SCNPs formation (SCNP4)

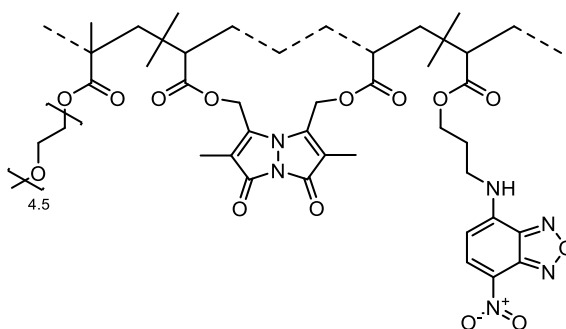


P5 (50.00 mg, equivalent to 30.74 μmol AA units, 1.00 eq) and cesium carbonate (5.01 mg, 15.37 μmol , 0.50 eq) was dissolved in 2.5 mL of THF in a 500 mL round bottom flask (brown glass). **12** (4.6 mg, 15.37 μmol , 0.50 eq) was added and stirred for 2 h. Subsequently, the reaction mixture was diluted with 250 mL of THF and dibromobimane **6** (5.01 mg, 30.74 μmol , 0.50 eq) was added and stirred further 3 h. Next, the solvent was evaporated and the polymer was purified by dialysis (cellulose membrane, 10 kDa MWCO) in methanol affording **SCNP4** which was stored in a solution of MeOH (10 mg mL) to prevent side reaction and precipitation.

SEC characterization (DMAc, RI): $M_n = 36.13 \cdot 10^3 \text{ g mol}^{-1}$, $D = 1.65$.

$^1\text{H NMR}$ (600 MHz, MeOD) δ 8.63 (s), 6.51 (s), 5.37 (bs), 4.13 (bs), 3.86 – 3.47 (m), 3.38 (bs), 2.34 – 1.41 (m), 1.22 – 0.72 (m).

9.6.5 Post-functionalization and SCNPs formation (SCNP5)



P5 (50.00 mg, equivalent to 30.74 μmol AA units, 1.00 eq) and cesium carbonate (5.01 mg, 15.37 μmol , 0.50 eq) was dissolved in 2.5 mL of THF in a 500 mL round bottom flask (brown glass). **12** (0.93 mg, 3.07 μmol , 0.10 eq) was added and stirred for 2 h. Subsequently, the reaction mixture was diluted with 250 mL THF and dibromobimane **6** (5.01 mg, 30.74 μmol , 0.50 eq) was added and stirred further for 3 h. Next, the solvent was evaporated and the polymer was purified by dialysis (cellulose membrane, 10 kDa MWCO) in methanol, affording

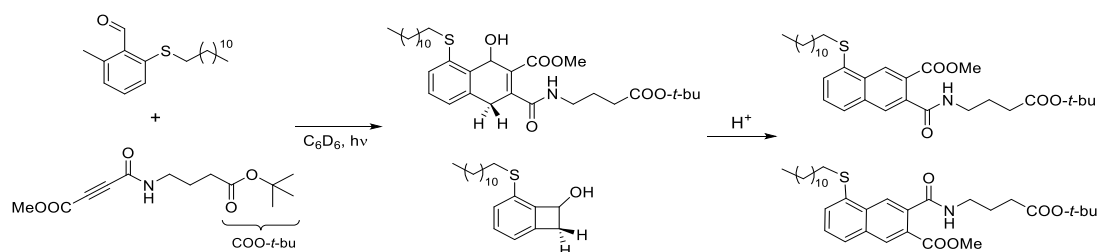
SCNP5 which was stored in a solution of MeOH (10 mg mL) to prevent side reaction and precipitation.

SEC characterization (DMAc, RI): $M_n = 38.62 \cdot 10^3 \text{ g mol}^{-1}$, $\bar{D} = 1.62$.

$^1\text{H NMR}$ (600 MHz, MeOD) δ 5.62 – 5.08 (m), 4.13 (bs), 3.91 – 3.46 (m), 3.38 (bs), 2.43 – 1.42 (m), 1.41 – 0.83 (m).

9.7 Photoreactions

9.7.1 Photoreaction of *ortho*-methylbenzaldehyde thioether (*o*MBA) with tert-butyl protected 4-(4-methoxy-4-oxobut-2-ynamido)butanoic acid (alkyne)

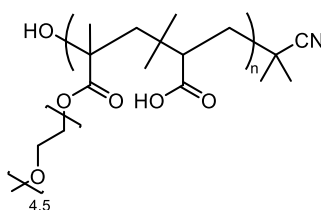


The procedure was adapted from Feist *et al.*, 2020.^[98] The batch photoreactions were performed using NMR-tubes (NORELL ST500-7 5mm, high-throughput 7" standard series) and LEDs with an emission centered at 415 nm (refer to Chapter 9.2). The reagents, *o*MBA (3.85 mg, 12.0 μmol , 1.00 eq) and methyl 4-(hexylamino)-4-oxobut-2-ynoate (alkyne) (2.70 mg, 13.0 μmol , 1.10 eq), were dissolved in 0.45 mL deuterated benzene (concentration of *o*-MBA 5 mmol L⁻¹), degassed by passing through a stream of nitrogen and irradiated for the respective time. Afterwards the reaction mixture was analyzed *via* ¹H NMR. The cycloadduct was converted further by adding a crystal of *p*-TsOH to obtain the naphthalene from the intermediate.

The crude product also contains the side product 1-hydroxybenzocyclobutane and is composed of two regioisomers and was not further purified.

¹H NMR (500 MHz, CDCl₃) δ 9.34 (s), 8.68 (s), 8.30 (s), 7.62 (s), 7.44 – 7.30 (m), 7.00 (t, $J = 7.6$ Hz), 6.69 (d, $J = 7.2$ Hz), 5.49 (t, $J = 6.1$ Hz), 5.16 – 5.11 (m), 5.01 (dd, $J = 4.6, 1.9$ Hz), 3.66 (s), 3.58 (s), 3.36 (q, $J = 6.8$ Hz), 3.26 (d, $J = 14.6$ Hz), 3.14 (s), 3.05 (dt, $J = 12.8, 7.2$ Hz), 2.95 (dt, $J = 12.7, 7.5$ Hz), 2.84 (q, $J = 6.6$ Hz), 2.74 – 2.60 (m), 1.85 (t, $J = 7.1$ Hz), 1.80 (q, $J = 7.0$ Hz), 1.62 (dd, $J = 15.1, 7.6$ Hz), 1.51 (h, $J = 6.8$ Hz), 1.43 – 1.11 (m), 0.95 – 0.89 (m).

9.7.2 Unfolding of SCNP1 by radiation with visible light (P5')



A solution of SCNP2 (25.00 mg, 2.50 mL in MeOH) was dissolved in 83 mL H₂O (0.3 mg mL⁻¹) and degassed by passing through a stream of N₂ for 10 min. The solution was irradiated for

30 min and subsequently freeze dried. The obtained polymer was purified by precipitation in cold Et₂O/Pentane (5:1) and centrifuged yielding **P5'**.

SEC characterization (DMAc, RI): $M_n = 37.29 \cdot 10^3 \text{ g mol}^{-1}$, $\bar{D} = 1.49$.

¹H NMR (600 MHz, CDCl₃) δ 4.19 – 3.88 (m), 3.65 – 3.53 (m), 3.51 – 3.46 (m), 3.31 (s), 2.05 – 1.65 (m), 1.01 – 0.88 (m), 0.84 – 0.78 (m).

9.7.3 Irradiation experiment of **10**

Compound **10** (30 μ L stock solution, 5 mg/mL) was diluted in 5 mL water and degassed by passing through a stream of nitrogen for 10 min using a 10 mL crimp cap vial. The solution was irradiated with 415 nm for 25 min. The reaction mixture was analyzed by fluorescence spectroscopy and LCMS. The photoreaction products were analyzed by LCMS.

9.7.4 Unfolding of **SCNP4** by radiation with 415 nm

A solution of **SCNP4** (2.00 mg, in 300 μ L MeOH) was dissolved in 10 mL H₂O (0.2 mg mL⁻¹) and degassed by passing a stream of N₂ through the solution for 10 min. The solution was subsequently irradiated with 415 nm for 3 h and analyzed by fluorescence spectroscopy and SEC. The SEC sample was prepared by adding 0.5 mL DMAc to the reaction mixture and evaporating the water under reduced pressure.

SEC characterization (DMAc, RI): $M_n = 38.95 \cdot 10^3 \text{ g mol}^{-1}$, $\bar{D} = 1.59$.

Bibliography

- [1] Y. Vo, M. D. Nothling, R. Raveendran, C. Cao, M. H. Stenzel, Effects of Drug Conjugation on the Biological Activity of Single-Chain Nanoparticles, *Biomacromolecules* **2024**.
- [2] A. Blazquez-Martín, E. Verde-Sesto, A. Arbe, J. A. Pomposo, Metamorphosis of a Commodity Plastic like PVC to Efficient Catalytic Single-Chain Nanoparticles, *Angew. Chem. Int. Ed.* **2023**, *62*, e202313502.
- [3] Y. Chen, Z. Hu, H. Pu, Macromolecular Metamorphosis in a Polymer Network via the Reversible Collapse of Single-Chain Nanoparticles, *Macromolecules* **2023**, *56*, 9277-9288.
- [4] B. Robles-Hernández, M. González-Burgos, P. Malo de Molina, I. Asenjo-Sanz, A. Radulescu, J. A. Pomposo, A. Arbe, J. Colmenero, Structure of Single-Chain Nanoparticles under Crowding Conditions: A Random Phase Approximation Approach, *Macromolecules* **2023**, *56*, 8971-8979.
- [5] A. Blázquez-Martín, S. Bonardd, E. Verde-Sesto, A. Arbe, J. A. Pomposo, Trimethylsilanol Cleaves Stable Azaylides As Revealed by Unfolding of Robust “Staudinger” Single-Chain Nanoparticles, *ACS Polymers Au* **2024**.
- [6] E. Verde-Sesto, A. Arbe, A. J. Moreno, D. Cangialosi, A. Alegría, J. Colmenero, J. A. Pomposo, Single-chain nanoparticles: opportunities provided by internal and external confinement, *Materials Horizons* **2020**, *7*, 2292-2313.
- [7] K. Mundsinger, A. Izuagbe, B. Tuten, P. Roesky, C. Barner-Kowollik, Single Chain Nanoparticles in Catalysis, *Angew. Chem. Int. Ed.* **2023**.
- [8] J. C. Chadwick, R. Duchateau, Z. Freixa, P. W. van Leeuwen, Homogeneous Catalysts: Activity - Stability - Deactivation, Wiley, **2011**.
- [9] S. Garmendia, A. P. Dove, D. Taton, R. K. O'Reilly, Reversible ionically-crosslinked single chain nanoparticles as bioinspired and recyclable nanoreactors for N-heterocyclic carbene organocatalysis, *Polym. Chem.* **2018**, *9*, 5286-5294.
- [10] R. Chen, E. B. Berda, 100th Anniversary of Macromolecular Science Viewpoint: Re-examining Single-Chain Nanoparticles, *ACS Macro Lett.* **2020**, *9*, 1836-1843.
- [11] C. K. Lyon, A. Prasher, A. M. Hanlon, B. T. Tuten, C. A. Tooley, P. G. Frank, E. B. Berda, A brief user's guide to single-chain nanoparticles, *Polym. Chem.* **2015**, *6*, 181-197.
- [12] N. Corrigan, K. Jung, G. Moad, C. J. Hawker, K. Matyjaszewski, C. Boyer, Reversible-deactivation radical polymerization (Controlled/living radical polymerization): From discovery to materials design and applications, *Prog. Polym. Sci.* **2020**, *111*, 101311.
- [13] A. Sathyan, S. Croke, A. M. Pérez-López, B. F. de Waal, A. Unciti-Broceta, A. R. Palmans, Developing Pd (ii) based amphiphilic polymeric nanoparticles for pro-drug activation in complex media, *Mol. Syst. Des. Eng.* **2022**.
- [14] L. Deng, L. Albertazzi, A. R. Palmans, Elucidating the Stability of Single-Chain Polymeric Nanoparticles in Biological Media and Living Cells, *Biomacromolecules* **2021**, *23*, 326-338.
- [15] S. Mavila, O. Eivgi, I. Berkovich, N. G. Lemcoff, Intramolecular cross-linking methodologies for the synthesis of polymer nanoparticles, *Chem. Rev.* **2016**, *116*, 878-961.
- [16] A. M. Hanlon, C. K. Lyon, E. B. Berda, What is next in single-chain nanoparticles?, *Macromolecules* **2016**, *49*, 2-14.
- [17] L. Oria, R. Aguado, J. A. Pomposo, J. Colmenero, A versatile “click” chemistry precursor of functional polystyrene nanoparticles, *Adv. Mater.* **2010**, *22*, 3038-3041.

- [18] A. P. P. Kröger, J. M. Paulusse, Single-chain polymer nanoparticles in controlled drug delivery and targeted imaging, *J. Controlled Release* **2018**, *286*, 326-347.
- [19] X. Chen, R. Li, S. H. D. Wong, K. Wei, M. Cui, H. Chen, Y. Jiang, B. Yang, P. Zhao, J. Xu, Conformational manipulation of scale-up prepared single-chain polymeric nanogels for multiscale regulation of cells, *Nat. Commun.* **2019**, *10*, 2705.
- [20] M. Longmire, P. L. Choyke, H. Kobayashi, Clearance properties of nano-sized particles and molecules as imaging agents: considerations and caveats, *Nanomedicine* **2008**, *3*, 703-717.
- [21] C.-C. Cheng, S.-Y. Huang, W.-L. Fan, A.-W. Lee, C.-W. Chiu, D.-J. Lee, J.-Y. Lai, Water-soluble single-chain polymeric nanoparticles for highly selective cancer chemotherapy, *ACS Appl. Polym. Mater.* **2020**, *3*, 474-484.
- [22] A. P. P. Kröger, N. M. Hamelmann, A. Juan, S. Lindhoud, J. M. Paulusse, Biocompatible single-chain polymer nanoparticles for drug delivery—a dual approach, *ACS Appl. Mater. Interfaces* **2018**, *10*, 30946-30951.
- [23] D. Kodura, H. A. Houck, F. R. Bloesser, A. S. Goldmann, F. E. Du Prez, H. Frisch, C. Barner-Kowollik, Light-fueled dynamic covalent crosslinking of single polymer chains in non-equilibrium states, *Chem. Sci.* **2021**, *12*, 1302-1310.
- [24] A. Levy, R. Feinstein, C. E. Diesendruck, Mechanical unfolding and thermal refolding of single-chain nanoparticles using ligand–metal bonds, *J. Am. Chem. Soc.* **2019**, *141*, 7256-7260.
- [25] P. J. Stals, C.-Y. Cheng, L. van Beek, A. C. Wauters, A. R. Palmans, S. Han, E. Meijer, Surface water retardation around single-chain polymeric nanoparticles: critical for catalytic function?, *Chem. Sci.* **2016**, *7*, 2011-2015.
- [26] A. Blazquez-Martín, E. Verde-Sesto, A. J. Moreno, A. Arbe, J. Colmenero, J. A. Pomposo, Advances in the Multi-Orthogonal Folding of Single Polymer Chains into Single-Chain Nanoparticles, *Polymers* **2021**, *13*, 293.
- [27] V. Kobernik, R. S. Phatake, J. Tzadikov, O. Reany, N. G. Lemcoff, Organometallic single-chain polymer nanoparticles via intra-chain cross-linking with dinuclear μ -halo (diene) Rh (I) complexes, *React. Funct. Polym.* **2021**, *165*, 104971.
- [28] J. F. Hoffmann, A. H. Roos, F.-J. Schmitt, D. Hinderberger, W. H. Binder, Fluorescent and Water Dispersible Single-Chain Nanoparticles: Core–Shell Structured Compartmentation, *Angew. Chem. Int. Ed.* **2021**, *60*, 7820-7827.
- [29] J. Engelke, B. T. Tuten, R. Schweins, H. Komber, L. Barner, L. Plüschke, C. Barner-Kowollik, A. Lederer, An in-depth analysis approach enabling precision single chain nanoparticle design, *Polym. Chem.* **2020**, *11*, 6559-6578.
- [30] R. Chen, S. J. Benware, S. D. Cawthorn, J. P. Cole, J. J. Lessard, I. M. Crawford-Eng, R. Saxena, E. B. Berda, Assessing structure/property relationships and synthetic protocols in the fabrication of poly (oxanorbornene imide) single-chain nanoparticles, *Eur. Polym. J.* **2019**, *112*, 206-213.
- [31] G. Odian, Principles of polymerization, John Wiley & Sons, **2004**.
- [32] K. Matyjaszewski, T. P. Davis, Handbook of radical polymerization, **2002**.
- [33] A. D. Jenkins, R. G. Jones, G. Moad, Terminology for reversible-deactivation radical polymerization previously called " controlled" radical or " living" radical polymerization (IUPAC Recommendations 2010), *Pure Appl. Chem.* **2009**, *82*, 483-491.
- [34] K. Matyjaszewski, Comparison and classification of controlled/living radical polymerizations, ACS Publications, **2000**.
- [35] M. Szwarc, 'Living' polymers, *Nature* **1956**, *178*, 1168-1169.
- [36] A. F. Halasa, Recent advances in anionic polymerization, *Rubber Chem. Technol.* **1981**, *54*, 627-640.
- [37] G. Moad, D. H. Solomon, The chemistry of radical polymerization, Elsevier, **2006**.

- [38] J. Nicolas, Y. Guillaneuf, C. Lefay, D. Bertin, D. Gignes, B. Charleux, Nitroxide-mediated polymerization, *Prog. Polym. Sci.* **2013**, *38*, 63-235.
- [39] T. Otsu, Iniferter concept and living radical polymerization, *J. Polym. Sci., Part A: Polym. Chem.* **2000**, *38*, 2121-2136.
- [40] T. Otsu, M. Yoshida, Role of initiator-transfer agent-terminator (iniferter) in radical polymerizations: Polymer design by organic disulfides as iniferters, *Makromol. Chem., Rapid Commun.* **1982**, *3*, 127-132.
- [41] D. H. Solomon, E. Rizzardo, P. Cacioli, Google Patents, **1986**.
- [42] G. Moad, E. Rizzardo, Alkoxyamine-initiated living radical polymerization: Factors affecting alkoxyamine homolysis rates, *Macromolecules* **1995**, *28*, 8722-8728.
- [43] H. B. Hass, E. F. Riley, The Nitroparaffins, *Chem. Rev.* **1943**, *32*, 373-430.
- [44] N. Kocherginsky, H. M. Swartz, Nitroxide spin labels: reactions in biology and chemistry, CRC press, **1995**.
- [45] C. J. Hawker, G. G. Barclay, J. Dao, Radical crossover in nitroxide mediated "living" free radical polymerizations, *J. Am. Chem. Soc.* **1996**, *118*, 11467-11471.
- [46] A. Goto, T. Fukuda, Kinetics of living radical polymerization, *Prog. Polym. Sci.* **2004**, *29*, 329-385.
- [47] D. Leifert, A. Studer, The persistent radical effect in organic synthesis, *Angew. Chem. Int. Ed.* **2020**, *59*, 74-108.
- [48] A. Studer, The persistent radical effect in organic synthesis, *Chem. - Eur. J.* **2001**, *7*, 1159-1164.
- [49] W. A. Braunecker, K. Matyjaszewski, Controlled/living radical polymerization: Features, developments, and perspectives, *Prog. Polym. Sci.* **2007**, *32*, 93-146.
- [50] J. Chiefari, Y. Chong, F. Ercole, J. Krstina, J. Jeffery, T. P. Le, R. T. Mayadunne, G. F. Meijs, C. L. Moad, G. Moad, Living free-radical polymerization by reversible addition-fragmentation chain transfer: the RAFT process, *Macromolecules* **1998**, *31*, 5559-5562.
- [51] X. Tian, J. Ding, B. Zhang, F. Qiu, X. Zhuang, Y. Chen, Recent advances in RAFT polymerization: novel initiation mechanisms and optoelectronic applications, *Polymers* **2018**, *10*, 318.
- [52] G. Moad, E. Rizzardo, S. H. Thang, Living radical polymerization by the RAFT process, *Aust. J. Chem.* **2005**, *58*, 379-410.
- [53] G. Moad, E. Rizzardo, S. H. Thang, Living radical polymerization by the RAFT process—a third update, *Aust. J. Chem.* **2012**, *65*, 985-1076.
- [54] S. Perrier, 50th Anniversary Perspective: RAFT Polymerization - A User Guide, *Macromolecules* **2017**, *50*, 7433-7447.
- [55] M. Coote, E. Krenske, E. Pas, Quantum-chemical studies of RAFT polymerization: methodology, structure-reactivity correlations and kinetic implications, Wiley-VCH Verlag GmbH & Co. KGaA, **2008**, pp. 5-49.
- [56] A. J. Inglis, S. Sinnwell, M. H. Stenzel, C. Barner-Kowollik, Ultrafast Click Conjugation of Macromolecular Building Blocks at Ambient Temperature, *Angew. Chem. Int. Ed.* **2009**, *48*, 2411-2414.
- [57] N. Zydziak, C. M. Preuss, V. Winkler, M. Bruns, C. Hübner, C. Barner-Kowollik, Hetero Diels-Alder Chemistry for the Functionalization of Single-Walled Carbon Nanotubes with Cyclopentadienyl End-Capped Polymer Strands, *Makromol. Rapid Commun.* **2013**, *34*, 672-680.
- [58] M. Villabona, S. Wiedbrauk, F. Feist, G. Guirado, J. Hernando, C. Barner-Kowollik, Dual-Wavelength Gated oxo-Diels-Alder Photoligation, *Org. Lett.* **2021**, *23*, 2405-2410.
- [59] G. Moad, E. Rizzardo, S. H. Thang, End-functional polymers, thiocarbonylthio group removal/transformation and reversible addition-fragmentation-chain transfer (RAFT) polymerization, *Polym. Int.* **2011**, *60*, 9-25.

- [60] M. Dietrich, M. Glassner, T. Gruending, C. Schmid, J. Falkenhagen, C. Barner-Kowollik, Facile conversion of RAFT polymers into hydroxyl functional polymers: a detailed investigation of variable monomer and RAFT agent combinations, *Polym. Chem.* **2010**, *1*, 634-644.
- [61] V. Mohanraj, Y. Chen, Nanoparticles-a review, *Trop. J. Pharm. Res.* **2006**, *5*, 561-573.
- [62] S. Mavila, I. Rozenberg, N. G. Lemcoff, A general approach to mono-and bimetallic organometallic nanoparticles, *Chem. Sci.* **2014**, *5*, 4196-4203.
- [63] H. Rothfuss, N. D. Knöfel, P. W. Roesky, C. Barner-Kowollik, Single-chain nanoparticles as catalytic nanoreactors, *J. Am. Chem. Soc.* **2018**, *140*, 5875-5881.
- [64] N. M. Hamelmann, J. M. Paulusse, Single-chain polymer nanoparticles in biomedical applications, *J. Controlled Release* **2023**, *356*, 26-42.
- [65] E. Harth, B. V. Horn, V. Y. Lee, D. S. Germack, C. P. Gonzales, R. D. Miller, C. J. Hawker, A facile approach to architecturally defined nanoparticles via intramolecular chain collapse, *J. Am. Chem. Soc.* **2002**, *124*, 8653-8660.
- [66] T. Mes, R. van der Weegen, A. R. Palmans, E. Meijer, Single-chain polymeric nanoparticles by stepwise folding, *Angew. Chem. Int. Ed.* **2011**, *50*, 5085-5089.
- [67] M. A. M. Alqarni, C. Waldron, G. Yilmaz, C. R. Becer, Synthetic Routes to Single Chain Polymer Nanoparticles (SCNPs): Current Status and Perspectives, *Macromol. Rapid Commun.* **2021**, *42*, 2100035.
- [68] O. Altintas, C. Barner-Kowollik, Single-chain folding of synthetic polymers: a critical update, *Macromol. Rapid Commun.* **2016**, *37*, 29-46.
- [69] Y. Shao, Y. L. Wang, Z. Tang, Z. Wen, C. Chang, C. Wang, D. Sun, Y. Ye, D. Qiu, Y. Ke, Scalable Synthesis of Photoluminescent Single-Chain Nanoparticles by Electrostatic-Mediated Intramolecular Crosslinking, *Angew. Chem.* **2022**, *134*, e202205183.
- [70] H. Rothfuß, thesis thesis, Thesis, Single-Chain Nanoparticle Formation Induced by Metal Complexation, Karlsruhe Institute of Technology **2019**.
- [71] N. Ormategui, I. García, D. Padro, G. Cabañero, H. J. Grande, I. Loinaz, Synthesis of single chain thermoresponsive polymer nanoparticles, *Soft Matter* **2012**, *8*, 734-740.
- [72] J. A. Pomposo, I. Perez-Baena, F. Lo Verso, A. J. Moreno, A. Arbe, J. Colmenero, ACS Publications, **2014**.
- [73] F. L. Verso, J. A. Pomposo, J. Colmenero, A. J. Moreno, Tunable slow dynamics in a new class of soft colloids, *Soft matter* **2016**, *12*, 9039-9046.
- [74] A. J. Moreno, F. Lo Verso, A. Sanchez-Sanchez, A. Arbe, J. Colmenero, J. A. Pomposo, Advantages of orthogonal folding of single polymer chains to soft nanoparticles, *Macromolecules* **2013**, *46*, 9748-9759.
- [75] D. Berek, Size exclusion chromatography—a blessing and a curse of science and technology of synthetic polymers, *J. Sep. Sci.* **2010**, *33*, 315-335.
- [76] S. M. Rowland, A. M. Striegel, Characterization of copolymers and blends by quintuple-detector size-exclusion chromatography, *Anal. Chem.* **2012**, *84*, 4812-4820.
- [77] R. W. Nunes, J. R. Martin, J. F. Johnson, Influence of molecular weight and molecular weight distribution on mechanical properties of polymers, *Polym. Eng. Sci.* **1982**, *22*, 205-228.
- [78] A. Latorre-Sánchez, A. Alegría, F. Lo Verso, A. J. Moreno, A. Arbe, J. Colmenero, J. A. Pomposo, A Useful Methodology for Determining the Compaction Degree of Single-Chain Nanoparticles by Conventional SEC, *Part. Part. Syst. Character.* **2016**, *33*, 373-381.
- [79] J. Stetefeld, S. A. McKenna, T. R. Patel, Dynamic light scattering: a practical guide and applications in biomedical sciences, *Biophysical reviews* **2016**, *8*, 409-427.
- [80] S.-i. Yusa, Chapter 6 - Polymer characterization (Ed.: R. Narain), Elsevier, **2020**, pp. 105-124.

- [81] E. Blasco, B. T. Tuten, H. Frisch, A. Lederer, C. Barner-Kowollik, Characterizing single chain nanoparticles (SCNPs): a critical survey, *Polym. Chem.* **2017**, *8*, 5845-5851.
- [82] A. D. McNaught, A. Wilkinson, Compendium of chemical terminology, Vol. 1669, Blackwell Science Oxford, **1997**.
- [83] E. Rabinowitch, Photosynthesis, *Annu. Rev. Phys. Chem.* **1951**, *2*, 361-382.
- [84] D. Mauzerall, Oceanic photochemistry and evolution of elements and cofactors in the early stages of the evolution of life, Elsevier, **2007**, pp. 7-19.
- [85] J. C. Maxwell, VIII. A dynamical theory of the electromagnetic field, *Philos. Trans. R. Soc. London* **1865**, 459-512.
- [86] J. Chen, J. Cen, X. Xu, X. Li, The application of heterogeneous visible light photocatalysts in organic synthesis, *Catal. Sci. Technol.* **2016**, *6*, 349-362.
- [87] U. E. Steiner, Fundamentals of Photophysics, Photochemistry, and Photobiology, Springer, **2014**, pp. 25-58.
- [88] D. Li, W. Hu, J. Wang, Q. Zhang, X.-M. Cao, X. Ma, H. Tian, White-light emission from a single organic compound with unique self-folded conformation and multistimuli responsiveness, *Chem. Sci.* **2018**, *9*, 5709-5715.
- [89] J. P. Hooker, Thesis, Photocycloadditions as tools for particle synthesis, Queensland University of Technology **2021**.
- [90] V. Balzani, P. Ceroni, A. Juris, Photochemistry and photophysics: concepts, research, applications, John Wiley & Sons, **2014**.
- [91] H. Frisch, D. E. Marschner, A. S. Goldmann, C. Barner-Kowollik, Wavelength-Gated Dynamic Covalent Chemistry, *Angew. Chem. Int. Ed.* **2018**, *57*, 2036-2045.
- [92] A. Beer, Bestimmung der absorption des rothen lichts in farbigen flussigkeiten, *Ann. Physik* **1852**, *162*, 78-88.
- [93] S. L. Walden, J. A. Carroll, A.-N. Unterreiner, C. Barner-Kowollik, Photochemical Action Plots Reveal the Fundamental Mismatch Between Absorptivity and Photochemical Reactivity, *Advanced Science* **2024**, *11*, 2306014.
- [94] I. M. Irshadeen, S. L. Walden, M. Wegener, V. X. Truong, H. Frisch, J. P. Blinco, C. Barner-Kowollik, Action Plots in Action: In-Depth Insights into Photochemical Reactivity, *J. Am. Chem. Soc.* **2021**, *143*, 21113-21126.
- [95] I. Erden, D. Kaufmann, Cycloadditionsreaktionen des heptafulvalens, *Tetrahedron Lett.* **1981**, *22*, 215-218.
- [96] J. L. Segura, N. Martin, o-Quinodimethanes: efficient intermediates in organic synthesis, *Chem. Rev.* **1999**, *99*, 3199-3246.
- [97] P. G. Sammes, Photoenolisation, *Tetrahedron* **1976**, *32*, 405-422.
- [98] F. Feist, L. L. Rodrigues, S. L. Walden, T. W. Krappitz, T. R. Dargaville, T. Weil, A. S. Goldmann, J. P. Blinco, C. Barner-Kowollik, Light-induced Ligation of o-Quinodimethanes with Gated Fluorescence Self-reporting, *J. Am. Chem. Soc.* **2020**, *142*, 7744-7748.
- [99] E. Kosower, A. Radkowsky, A. Fairlamb, S. Croft, R. Neal, Bimane cyclic esters, possible stereologues of trypanothione as antitrypanosomal agents. Bimanes 29, *Eur. J. Med. Chem.* **1995**, *30*, 659-671.
- [100] N. S. Kosower, E. M. Kosower, G. L. Newton, H. M. Ranney, Bimane fluorescent labels: labeling of normal human red cells under physiological conditions, *Proc. Natl. Acad. Sci.* **1979**, *76*, 3382-3386.
- [101] A. J. Horsfall, D. P. McDougal, D. B. Scanlon, J. B. Bruning, A. D. Abell, Approaches to Introduce Helical Structure in Cysteine-Containing Peptides with a Bimane Group, *ChemBioChem* **2021**, *22*, 2711-2720.
- [102] A. M. Jones Brunette, D. L. Farrens, Distance mapping in proteins using fluorescence spectroscopy: tyrosine, like tryptophan, quenches bimane fluorescence in a distance-dependent manner, *Biochemistry* **2014**, *53*, 6290-6301.

- [103] A. Chaudhuri, Y. Venkatesh, K. K. Behara, N. P. Singh, Bimane: A visible light induced fluorescent photoremovable protecting group for the single and dual release of carboxylic and amino acids, *Org. Lett.* **2017**, *19*, 1598-1601.
- [104] T. L. Kirley, K. D. Greis, A. B. Norman, Selective disulfide reduction for labeling and enhancement of Fab antibody fragments, *Biochem. Biophys. Res. Commun.* **2016**, *480*, 752-757.
- [105] T. Forster, Intermolecular energy transfer and fluorescence, *Ann. Phys. Leipzig.* **1948**, *2*, 55-75.
- [106] W. R. Algar, N. Hildebrandt, S. S. Vogel, I. L. Medintz, FRET as a biomolecular research tool—understanding its potential while avoiding pitfalls, *Nat. Methods* **2019**, *16*, 815-829.
- [107] P. Rajdev, S. Ghosh, Fluorescence resonance energy transfer (FRET): a powerful tool for probing amphiphilic polymer aggregates and supramolecular polymers, *J. Phys. Chem. B* **2018**, *123*, 327-342.
- [108] X. Wu, C. Barner-Kowollik, Fluorescence-readout as a powerful macromolecular characterisation tool, *Chem. Sci.* **2023**, *14*, 12815-12849.
- [109] A. S. K. Hashmi, F. D. Toste, Modern gold catalyzed synthesis, John Wiley & Sons, **2012**.
- [110] A. S. K. Hashmi, Gold-catalyzed organic reactions, *Chem. Rev.* **2007**, *107*, 3180-3211.
- [111] S. Coco, P. Espinet, J. M. Martín-Alvarez, A.-M. Levelut, Effects of isocyanide substituents on the mesogenic properties of halogeno (isocyanide) gold complexes: calamitic and discotic liquid crystals, *J. Mater. Chem.* **1997**, *7*, 19-23.
- [112] N. H. Dryden, J. G. Shapter, L. L. Coatsworth, P. R. Norton, R. J. Puddephatt, [CF₃Au(C. tpbond. NMe)] as a precursor for CVD of gold, *Chem. Mater.* **1992**, *4*, 979-981.
- [113] T. Basova, A. Hassan, N. Morozova, Chemistry of gold (I, III) complexes with organic ligands as potential MOCVD precursors for fabrication of thin metallic films and nanoparticles, *Coord. Chem. Rev.* **2019**, *380*, 58-82.
- [114] W. B. Jones, B. J. Yuan, R. Narayanaswamy, M. A. Young, R. Elder, A. E. Bruce, M. R. Bruce, Solid state EXAFS and luminescence studies of neutral, dinuclear gold (I) complexes. Gold (I)-gold (I) interactions in the solid state, *Inorg. Chem.* **1995**, *34*, 1996-2001.
- [115] S. Jain, D. Hirst, J. O'Sullivan, Gold nanoparticles as novel agents for cancer therapy, *Br. J. Radiol.* **2012**, *85*, 101-113.
- [116] C. I. Yeo, K. K. Ooi, E. R. Tiekink, Gold-based medicine: a paradigm shift in anti-cancer therapy?, *Molecules* **2018**, *23*, 1410.
- [117] A. Nijamudheen, A. Datta, Gold-catalyzed cross-coupling reactions: an overview of design strategies, mechanistic studies, and applications, *Chem. - Eur. J.* **2020**, *26*, 1442-1487.
- [118] J. L. Bohlen, B. Kulendran, H. Rothfuss, C. Barner-Kowollik, P. W. Roesky, Heterobimetallic Au(I)/Y(III) single chain nanoparticles as recyclable homogeneous catalysts, *Polym. Chem.* **2021**, *12*, 4016-4021.
- [119] P. van Leeuwen, Phosphines and Related Tervalent Phosphorus Systems, Wiley-VCH: Weinheim, **2019**.
- [120] N. D. Knöfel, H. Rothfuss, J. Willenbacher, C. Barner-Kowollik, P. W. Roesky, Platinum (II)-Crosslinked Single-Chain Nanoparticles: An Approach towards Recyclable Homogeneous Catalysts, *Angew. Chem. Int. Ed.* **2017**, *56*, 4950-4954.
- [121] A. Latorre-Sánchez, J. A. Pomposo, Recent bioinspired applications of single-chain nanoparticles, *Polym. Int.* **2016**, *65*, 855-860.
- [122] J. A. Pomposo, Single-Chain Polymer Nanoparticles: Synthesis, Characterization, Simulations, and Applications, John Wiley & Sons, **2017**.

- [123] K. Mundsinger, B. T. Tuten, L. Wang, K. Neubauer, C. Kropf, M. L. O'Mara, C. Barner-Kowollik, Visible Light Reactive Single-Chain Nanoparticles, *Angew. Chem. Int. Ed.* **2023**.
- [124] A. B. Benito, M. K. Aiertza, M. Marradi, L. Gil-Iceta, T. Shekhter Zahavi, B. Szczupak, M. Jiménez-González, T. Reese, E. Scanziani, L. Passoni, M. Matteoli, M. De Maglie, A. Orenstein, M. Oron-Herman, G. Kostenich, L. Buzhansky, E. Gazit, H.-J. Grande, V. Gómez-Vallejo, J. Llop, I. Loinaz, Functional Single-Chain Polymer Nanoparticles: Targeting and Imaging Pancreatic Tumors in Vivo, *Biomacromolecules* **2016**, *17*, 3213-3221.
- [125] H. Frisch, B. T. Tuten, C. Barner-Kowollik, Macromolecular superstructures: a future beyond single chain nanoparticles, *Isr. J. Chem.* **2020**, *60*, 86-99.
- [126] T. K. Claus, J. Zhang, L. Martin, M. Hartlieb, H. Mutlu, S. Perrier, G. Delaittre, C. Barner-Kowollik, Stepwise Light-Induced Dual Compaction of Single-Chain Nanoparticles, *Macromol. Rapid Commun.* **2017**, *38*, 1700264.
- [127] J. Y. J. Wang, M. T. Blyth, M. S. Sherburn, M. L. Coote, Tuning Photoenolization-Driven Cycloadditions Using Theory and Spectroscopy, *J. Am. Chem. Soc.* **2022**, *144*, 1023-1033.
- [128] H. Frisch, J. P. Menzel, F. R. Bloesser, D. E. Marschner, K. Mundsinger, C. Barner-Kowollik, Photochemistry in confined environments for single-chain nanoparticle design, *J. Am. Chem. Soc.* **2018**, *140*, 9551-9557.
- [129] D. Kodura, L. L. Rodrigues, S. L. Walden, A. S. Goldmann, H. Frisch, C. Barner-Kowollik, Orange-Light-Induced Photochemistry Gated by pH and Confined Environments, *J. Am. Chem. Soc.* **2022**, *144*, 6343-6348.
- [130] J. Fan, X. Chang, M. He, C. Shang, G. Wang, S. Yin, H. Peng, Y. Fang, Functionality-oriented derivatization of naphthalene diimide: a molecular gel strategy-based fluorescent film for aniline vapor detection, *ACS Appl. Mater. Interfaces* **2016**, *8*, 18584-18592.
- [131] R. A. Widenhoefer, X. Han, Gold-catalyzed hydroamination of C–C multiple bonds, *Eur. J. Org. Chem.* **2006**, *2006*, 4555-4563.
- [132] A. S. K. Hashmi, G. J. Hutchings, Gold catalysis, *Angew. Chem. Int. Ed.* **2006**, *45*, 7896-7936.
- [133] M. C. Dietl, V. Vethacke, A. Keshavarzi, F. F. Mulks, F. Rominger, M. Rudolph, I. A. Mkhaliid, A. S. K. Hashmi, Synthesis of Heterobimetallic Gold (I) Palladium (II) Bis (acyclic diaminocarbene) Complexes via the Isonitrile Route, *Organometallics* **2022**, *41*, 802-810.
- [134] F. Feist, J. P. Menzel, T. Weil, J. P. Blinco, C. Barner-Kowollik, Visible light-induced ligation via o-quinodimethane thioethers, *J. Am. Chem. Soc.* **2018**, *140*, 11848-11854.
- [135] J. P. Hooker, F. Feist, L. Delafresnaye, F. Cavalli, L. Barner, C. Barner-Kowollik, On-demand acid-gated fluorescence switch-on in photo-generated nanospheres, *Chem. Commun.* **2020**, *56*, 4986-4989.
- [136] T. K. Claus, J. Zhang, L. Martin, M. Hartlieb, H. Mutlu, S. Perrier, G. Delaittre, C. Barner-Kowollik, Stepwise Light-Induced Dual Compaction of Single-Chain Nanoparticles, *Macromol. Rapid Commun.* **2017**, *38*, 1700264.
- [137] C.-H. Wong, S. C. Zimmerman, Orthogonality in organic, polymer, and supramolecular chemistry: from Merrifield to click chemistry, *Chem. Commun.* **2013**, *49*, 1679-1695.
- [138] G. Dijkstra, W. H. Kruizinga, R. M. Kellogg, An assessment of the causes of the "cesium effect", *The Journal of Organic Chemistry* **1987**, *52*, 4230-4234.
- [139] K. Balenović, B. Gašpert, N. Štimac, Introduction of the N-phthaloyl group into heat-sensitive amino acid derivatives; N-phthaloyl-L-aspartic acid, *Croat. Chem. Acta* **1957**, *29*, 93-95.

- [140] J. Chen, K. Li, J. S. L. Shon, S. C. Zimmerman, Single-chain nanoparticle delivers a partner enzyme for concurrent and tandem catalysis in cells, *J. Am. Chem. Soc.* **2020**, *142*, 4565-4569.
- [141] D. Kim, P. V. Pikhitsa, H. Yang, M. Choi, Room temperature CO and H₂ sensing with carbon nanoparticles, *Nanotechnology* **2011**, *22*, 485501.
- [142] X. Tian, R. Xue, F. Yang, L. Yin, S. Luan, H. Tang, Single-chain nanoparticle-based coatings with improved bactericidal activity and antifouling properties, *Biomacromolecules* **2021**, *22*, 4306-4315.
- [143] K. A. Ryu, C. M. Kaszuba, N. B. Bissonnette, R. C. Oslund, O. O. Fadeyi, Interrogating biological systems using visible-light-powered catalysis, *Nat. Rev. Chem.* **2021**, *5*, 322-337.
- [144] P. Zhao, S. Huo, J. Fan, J. Chen, F. Kiessling, A. J. Boersma, R. Göstl, A. Herrmann, Activation of the Catalytic Activity of Thrombin for Fibrin Formation by Ultrasound, *Angew. Chem. Int. Ed.* **2021**, *60*, 14707-14714.
- [145] M. Liu, W. Wenzel, H. Frisch, Photocycloreversions within single polymer chains, *Polym. Chem.* **2020**, *11*, 6616-6623.
- [146] J. L. Pelloth, P. A. Tran, A. Walther, A. S. Goldmann, H. Frisch, V. X. Truong, C. Barner-Kowollik, Wavelength-Selective Softening of Hydrogel Networks, *Adv. Mater.* **2021**, *33*, 2102184.
- [147] E. M. Kosower, B. Pazhenchevsky, E. Hershkowitz, 1, 5-Diazabicyclo [3.3.0] octadienediones (9, 10-dioxabimanes). Strongly fluorescent syn isomers, *J. Am. Chem. Soc.* **1978**, *100*, 6516-6518.
- [148] P. H. Maag, F. Feist, H. Frisch, P. W. Roesky, C. Barner-Kowollik, Fluorescent and Catalytically Active Single Chain Nanoparticles, *Macromolecules* **2022**, *55*, 9918-9924.
- [149] V. Kobernik, I. Berkovich, A. Levy, N. G. Lemcoff, C. E. Diesendruck, Chemical Communication between Organometallic Single-Chain Polymer Nanoparticles, *Chem. Eur. J.* **2020**, *26*, 15835-15838.
- [150] I. Berkovich, S. Mavila, O. Iliashevsky, S. Kozuch, N. G. Lemcoff, Single-chain polybutadiene organometallic nanoparticles: an experimental and theoretical study, *Chem. Sci.* **2016**, *7*, 1773-1778.
- [151] P. A. Klonos, N. Patelis, E. Glynos, G. Sakellariou, A. Kyritsis, Molecular dynamics in polystyrene single-chain nanoparticles, *Macromolecules* **2019**, *52*, 9334-9340.
- [152] A. M. Hanlon, K. J. Rodriguez, R. Chen, E. Bright, E. B. Berda, Characterization of Single-Chain Polymer Nanoparticles: Analytical Techniques, *Single-Chain Polym. Nanopart.* **2017**, 91-138.
- [153] J. Steinkoenig, H. Rothfuss, A. Lauer, B. T. Tuten, C. Barner-Kowollik, Imaging single-chain nanoparticle folding via high-resolution mass spectrometry, *J. Am. Chem. Soc.* **2017**, *139*, 51-54.
- [154] E. Verde-Sesto, A. Blázquez-Martín, J. A. Pomposo, Advances in the Phototriggered Synthesis of Single-Chain Polymer Nanoparticles, *Polymers* **2019**, *11*, 1903.
- [155] S. Valdez, M. Robertson, Z. Qiang, Fluorescence resonance energy transfer measurements in polymer science: A review, *Macromol. Rapid Commun.* **2022**, *43*, 2200421.
- [156] T. Förster, Zwischenmolekulare energiewanderung und fluoreszenz, *Ann. Phys.* **1948**, *437*, 55-75.
- [157] A. Z. Mustafa, B. Kent, R. Chapman, M. H. Stenzel, Fluorescence enables high throughput screening of polyelectrolyte–protein binding affinities, *Polym. Chem.* **2022**, *13*, 6108-6113.
- [158] S. Jiwpanich, J.-H. Ryu, S. Bickerton, S. Thayumanavan, Noncovalent encapsulation stabilities in supramolecular nanoassemblies, *J. Am. Chem. Soc.* **2010**, *132*, 10683-10685.

- [159] M. P. Robin, S. A. Osborne, Z. Pikramenou, J. E. Raymond, R. K. O'Reilly, Fluorescent block copolymer micelles that can self-report on their assembly and small molecule encapsulation, *Macromolecules* **2016**, *49*, 653-662.
- [160] S. W. Reulen, M. Merckx, Exchange kinetics of protein-functionalized micelles and liposomes studied by Förster resonance energy transfer, *Bioconjugate Chem.* **2010**, *21*, 860-866.
- [161] A. Harriman, R. Ziessel, Exploring the effects of solvent polarity on the rate of Förster-type electronic energy transfer in a closely-spaced molecular dyad, *Photochem. Photobiol. Sci.* **2010**, *9*, 960-967.
- [162] K. Morishima, K. Terao, T. Sato, Structural analysis of hydrophobe-uptake micelle of an amphiphilic alternating copolymer in aqueous solution, *Langmuir* **2016**, *32*, 7875-7881.
- [163] P. Ebensperger, M. Zmyslia, P. Lohner, J. Braunreuther, B. Deuringer, A. Becherer, R. Süß, A. Fischer, C. Jessen-Trefzer, A Dual-Metal-Catalyzed Sequential Cascade Reaction in an Engineered Protein Cage, *Angew. Chem.* **2023**, *135*, e202218413.
- [164] F. H. Quina, G. T. M. Silva, The photophysics of photosensitization: A brief overview, *J. Photochem. Photobiol.* **2021**, *7*, 100042.
- [165] G. R. Fulmer, A. J. Miller, N. H. Sherden, H. E. Gottlieb, A. Nudelman, B. M. Stoltz, J. E. Bercaw, K. I. Goldberg, NMR chemical shifts of trace impurities: common laboratory solvents, organics, and gases in deuterated solvents relevant to the organometallic chemist, *Organometallics* **2010**, *29*, 2176-2179.
- [166] D. R. Lide, CRC handbook of chemistry and physics, Vol. 85, CRC press, **2004**.
- [167] S. Harrisson, P. Couvreur, J. Nicolas, SG1 nitroxide-mediated polymerization of isoprene: alkoxyamine structure/control relationship and α , ω -chain-end functionalization, *Macromolecules* **2011**, *44*, 9230-9238.
- [168] C. A. Goodwin, B. L. Réant, G. F. Vettese, J. G. Kragoskow, M. J. Giansiracusa, I. M. DiMucci, K. M. Lancaster, D. P. Mills, S. Sproules, Heteroleptic Samarium (III) Chalcogenide Complexes: Opportunities for Giant Exchange Coupling in Bridging σ - and π -Radical Lanthanide Dichalcogenides, *Inorg. Chem.* **2020**, *59*, 7571-7583.
- [169] M. J. Harper, E. J. Emmett, J. F. Bower, C. A. Russell, Oxidative 1, 2-difunctionalization of ethylene via gold-catalyzed oxyarylation, *J. Am. Chem. Soc.* **2017**, *139*, 12386-12389.
- [170] M. Avalos, R. Babiano, P. Cintas, A. Gómez-Carretero, J. L. Jiménez, M. Lozano, A. L. Ortiz, J. C. Palacios, A. Pinazo, A Family of Hydrogels Based on Ureido-Linked Aminopolyol-Derived Amphiphiles and Bolaamphiphiles: Synthesis, Gelation under Thermal and Sonochemical Stimuli, and Mesomorphic Characterization, *Chem. - Eur. J.* **2008**, *14*, 5656-5669.
- [171] A. G. Aioub, C. J. Higginson, M. Finn, Traceless Release of Alcohols Using Thiol-Sensitive Oxanorbornadiene Linkers, *Org. Lett.* **2018**, *20*, 3233-3236.
- [172] T. Zhou, D. Gao, J.-X. Li, M.-J. Xu, J. Xu, Identification of an α -Oxoamine Synthase and a One-Pot Two-Step Enzymatic Synthesis of α -Amino Ketones, *Org. Lett.* **2020**, *23*, 37-41.
- [173] G. Greco, N. D'Antona, G. Gambera, G. Nicolosi, Glycerophosphoinositols: Total Synthesis of the First Fluorescent Probe Derivative, *Synlett* **2014**, *25*, 2111-2114.
- [174] T. Buscher, Á. Barroso, C. Denz, A. Studer, Synthesis and photo-postmodification of zeolite L based polymer brushes, *Polym. Chem.* **2015**, *6*, 4221-4229.
- [175] I. M. Irshadeen, V. X. Truong, H. Frisch, C. Barner-Kowollik, Red light induced folding of single polymer chains, *Chem. Commun.* **2022**, *58*, 12975-12978.

Lists of Figures, Schemes and Tables

List of Figures

- Figure 1:** The Jablonski diagram shows the possible transitions after absorbing light from the ground state to excited state. 18
- Figure 2:** Light beam with full intensity (I_0) on the left side and with lower intensity (I) after passing through a solution of concentration c containing a substance with a wavelength-dependent molar absorptivity coefficient ϵ_λ 19
- Figure 3:** Concept of Förster resonance energy transfer (FRET) with fluorescence spectra and Jablonski diagram of FRET. 23
- Figure 4:** Overview of the SCNPs synthesis in 6 steps. Polymerization and exchange reaction affording a styrene-based copolymer containing S=PPh₂Sty (orange) ligand and bromomethylstyrene (BMS, yellow), followed by the post-functionalization with an *o*MBA (green) and an alkyne (red), which are utilized to fold the polymer chain into SCNPs with fluorescent naphthalene cross-links (light blue) in the third step. Finally, the phosphine ligands are deprotected and coordinated with a catalytically active gold complex (metallic yellow). Reprinted with permission from P. H. Maag *et al.*, *Macromolecules* **2022**, 55 (22), 9918-9924. Copyright 2022 American Chemical Society..... 31
- Figure 5:** **Left:** Photoreaction of *o*MBA with the alkyne (**2**) in benzene (red numbers), initially leading to the non-fluorescent 1,4-dihydro-1-naphthole (blue numbers) and benzocyclobutane as side product (pink numbers), resulting in two regioisomers of the fluorescent naphthalene through an E1-elimination (green numbers). **Right:** Reaction monitoring *via* ¹H NMR spectroscopy in benzene-d₆. The top spectrum was recorded prior to the irradiation. The middle spectrum was obtained after 20 min of irradiation at $\lambda_{\max} = 415$ nm. The bottom spectrum was recorded after the addition of p-TsOH. Reprinted with permission from P. H. Maag *et al.*, *Macromolecules* **2022**, 55 (22), 9918-9924. Copyright 2022 American Chemical Society..... 33
- Figure 6:** THF-SEC and diffusion coefficients, D , measured by DOSY of **P3**, **SCNP1** and **SCNP-AuCl**. Both analytic methods show a significant decrease in the hydrodynamic radius after cross-linking. Reprinted with permission from P. H. Maag *et al.*, *Macromolecules* **2022**, 55 (22), 9918-9924. Copyright 2022 American Chemical Society. 37
- Figure 7:** ³¹P{¹H} NMR spectra of **SCNP-AuCl**, AuCl-PPh₂Sty and **P1** recorded in CDCl₃, showing a resonance at 32.2 ppm for the gold(I) complex in comparison to the sulfur protected triphenylphosphine. Reprinted with permission from P. H. Maag *et al.*, *Macromolecules* **2022**, 55 (22), 9918-9924. Copyright 2022 American Chemical Society. 38
- Figure 8:** UV/VIS spectra of **SCNP-AuCl** showing an increasing absorption band below 300 nm compared to **SCNP1**. Reprinted with permission from P. H. Maag *et al.*, *Macromolecules* **2022**, 55 (22), 9918-9924. Copyright 2022 American Chemical Society..... 39

- Figure 9:** Fluorescence spectra of **SCNP1** and gold coordinated SCNPs (**SCNP-AuCl**) in comparison with the small molecule model of the fluorescent cross-linking units. The fluorescence spectra of the **SCNP1** and the small molecules **4** show an emission and excitation band at the same wavelength, but redshifted emission and excitation band for **SCNP-AuCl**. Reprinted with permission from P. H. Maag *et al.*, *Macromolecules* **2022**, 55 (22), 9918-9924. Copyright 2022 American Chemical Society..... 39
- Figure 10: Left:** Fluorescence spectra of **SCNP-AuCl** compared with **SCNP + CsAc**. **Right:** Fluorescence spectra of **SCNP-AuCl** compared with small molecule (**4**) before and after treatment with CsAc. Reprinted with permission from P. H. Maag *et al.*, *Macromolecules* **2022**, 55 (22), 9918-9924. Copyright 2022 American Chemical Society. 40
- Figure 11:** LCMS spectra of **4** after treatment with acetic acid and cesium hydroxide in DMF for 3 d under N₂. Reprinted with permission from P. H. Maag *et al.*, *Macromolecules* **2022**, 55 (22), 9918-9924. Copyright 2022 American Chemical Society. 41
- Figure 12:** ¹H NMR spectra of the hydroamination of **5** with 2 mol% **SCNP-AuCl** as a time series recorded in CDCl₃. The conversion was calculated from the marked resonances: internal standard ferrocene (4.19 ppm, grey), product (3.21 ppm, orange) and **5** (3.02 ppm, blue). Reprinted with permission from P. H. Maag *et al.*, *Macromolecules* **2022**, 55 (22), 9918-9924. Copyright 2022 American Chemical Society..... 42
- Figure 13:** Kinetics of the catalyzed intramolecular hydroamination monitored by ¹H NMR with calculated conversion for **SCNP-AuCl** (0.8 mol%, 0.4 mol% [Au]), **P4** (0.8 mol% [Au]) and AuCl-PPh₂Sty (1.5 mol% [Au]). Na[B(C₆F₅)₄] was used as cocatalyst and tested in a control experiment, which showed no catalytic activity (blank). Reprinted with permission from P. H. Maag *et al.*, *Macromolecules* **2022**, 55 (22), 9918-9924. Copyright 2022 American Chemical Society. 43
- Figure 14: Left:** [S] over time of the SCNP-AuCl catalyzed intramolecular hydroamination with 0.8 mol% [Au]. **Right:** ln([S]₀/[S]_t) over time and fitted with a straight line. Reprinted with permission from P. H. Maag *et al.*, *Macromolecules* **2022**, 55 (22), 9918-9924. Copyright 2022 American Chemical Society. 44
- Figure 15:** LC-MS trace (250 nm, 400 nm detector wavelength), absorption spectra and accumulated mass spectra of irradiation products and side products of **8**. Reprinted with permission from P. H. Maag *et al.* *Angew. Chem. Int. Ed.* **2023**, 62, e202309259. Open access under a CC BY-NC 4.0 DEED license by John Wiley & Sons. 51
- Figure 16:** ¹H NMR spectrum of the reaction mixture before and after copolymerization for 5 and 22 h. The spectrum obtained after 22h was used for the calculation of the copolymer composition. Reprinted with permission from P. H. Maag *et al.* *Angew. Chem. Int. Ed.* **2023**, 62, e202309259. Open access under a CC BY-NC 4.0 DEED license by John Wiley & Sons. 52
- Figure 17: Top left:** Kinetics of the folding reaction of **P5** to **SCNP2** monitored by UV/VIS absorption at 400 nm and apparent molecular weight determined by size SEC. The cross-linking of the polymer chain leads to a higher compaction and consequently to a smaller hydrodynamic volume appearing with a smaller

- molecular weight in the SEC. **Bottom left:** RID SEC traces of **P5** folding to **SCNP2**. **Top right:** Kinetics of the unfolding reaction of **SCNP2** to **P5'** by irradiation with visible light monitored by UV/VIS absorption at 400 nm and apparent molecular weight by SEC. The cleavage of the cross-links leads to unfolding and consequently to a higher hydrodynamic volume appearing with a higher molecular weight in the SEC. **Bottom right:** RID SEC traces of **SCNP2** unfolding to **P5'** compared to **P5**. Reprinted with permission from P. H. Maag *et al. Angew. Chem. Int. Ed.* **2023**, 62, e202309259. Open access under a CC BY-NC 4.0 DEED license by John Wiley & Sons. 55
- Figure 18:** pH-value over time during radiation of **SCNP2** (25 mg) in 80 mL water. Reprinted with permission from P. H. Maag *et al. Angew. Chem. Int. Ed.* **2023**, 62, e202309259. Open access under a CC BY-NC 4.0 DEED license by John Wiley & Sons..... 56
- Figure 19:** Diffusion coefficients (*D*) determined by diffusion-ordered spectroscopy (DOSY) in deuterated chloroform of integrated polymer resonances for the original polymer **P5**, the folded **SCNP2** and the unfolded **P5'**. The defined integrals are compared with the ¹H NMR spectrum of **P5** displayed above. The *D* of the corresponding chemical shifts is displayed as a colored square (■) within the integral areas. For each polymer, the arithmetic mean was calculated and displayed as a colored line (–), wherefrom the hydrodynamic radius (*R_H*) was calculated. *D* increased after folding, correlated with a smaller *R_H* and decreases after irradiation, indicating an unfolding of the SCNPs. Reprinted with permission from P. H. Maag *et al. Angew. Chem. Int. Ed.* **2023**, 62, e202309259. Open access under a CC BY-NC 4.0 DEED license by John Wiley & Sons..... 57
- Figure 20:** ¹H NMR of the original polymer (**P5**), folded (**SCNP2**) and unfolding (**P5'**) polymer with integrals areas compared to the backbone. Reprinted with permission from P. H. Maag *et al. Angew. Chem. Int. Ed.* **2023**, 62, e202309259. Open access under a CC BY-NC 4.0 DEED license by John Wiley & Sons..... 58
- Figure 21:** ¹H NMR spectra of **SCNP2** and **P5'** after irradiating for 20 min with 415 nm LED in D₂O. The resonances of the bimeane cross-link (CH₃, CH₂) are not separated from the polymer resonances, but can be observed after cleaved of as dihydroxybimeane **7** indicated by the blue numbers 3 and 4. Reprinted with permission from P. H. Maag *et al. Angew. Chem. Int. Ed.* **2023**, 62, e202309259. Open access under a CC BY-NC 4.0 DEED license by John Wiley & Sons..... 59
- Figure 22:** **Left:** Molar absorption of **3** in methanol with standard deviation. **Right:** Absorption spectra of **SCNP1** and **P1'** for similar concentrations. Reprinted with permission from P. H. Maag *et al. Angew. Chem. Int. Ed.* **2023**, 62, e202309259. Open access under a CC BY-NC 4.0 DEED license by John Wiley & Sons..... 60
- Figure 23:** Probability of double bonded and single bonded bimeane units for different conversion simulated by a Monte Carlo method. Reprinted with permission from P. H. Maag *et al. Angew. Chem. Int. Ed.* **2023**, 62, e202309259. Open access under a CC BY-NC 4.0 DEED license by John Wiley & Sons. 62
- Figure 24:** **Left:** UV traces (380-400 nm) of LC-MS during irradiation of **8**. Over time the ester groups are cleaved resulting in **9** and further into **7**. **Right:** Composition of **7**, **8** and **9** over time. Reprinted with permission from P. H. Maag *et al.*

- Angew. Chem. Int. Ed.* **2023**, 62, e202309259. Open access under a CC BY-NC 4.0 DEED license by John Wiley & Sons. 63
- Figure 25:** Experimental (scattered) and simulated (line) results of bimane ester photocleavage. Reprinted with permission from P. H. Maag *et al.* *Angew. Chem. Int. Ed.* **2023**, 62, e202309259. Open access under a CC BY-NC 4.0 DEED license by John Wiley & Sons. 64
- Figure 26:** Fluorescence of **SCNP2** and **P5'** in water under a UV lamp showing a lower intensity after unfolding. Reprinted with permission from P. H. Maag *et al.* *Angew. Chem. Int. Ed.* **2023**, 62, e202309259. Open access under a CC BY-NC 4.0 DEED license by John Wiley & Sons. 64
- Figure 27: Left:** Normalized emission and excitation spectra of **SCNP2** compared with **P5'**. **Right:** Emission and excitation spectra after purification by dialysis. The intensity at 475 nm decreases by 95% after unfolding. Reprinted with permission from P. H. Maag *et al.* *Angew. Chem. Int. Ed.* **2023**, 62, e202309259. Open access under a CC BY-NC 4.0 DEED license by John Wiley & Sons. 65
- Figure 28:** Spectral fluorescence slices obtained by HPLC coupled with a fluorescence detector of **8** after radiation with $\lambda_{\text{max}} = 415$ nm for 30 min showing the emission trace at 472 nm (pink) in comparison with the UV/VIS absorption trace at 400 nm (black). As well as the fluorescence spectra of the assigned signals. Reprinted with permission from P. H. Maag *et al.* *Angew. Chem. Int. Ed.* **2023**, 62, e202309259. Open access under a CC BY-NC 4.0 DEED license by John Wiley & Sons. 66
- Figure 29:** Folding of poly(MPEGMA-co-acrylic acid) (**P5**) with dibromobimane **6** and unfolding with visible light in a repetitive fashion. **Left:** The second cycle shows a similar shift of the SEC trace compared to the first cycle (Figure 17) resulting in a lower molecular weight for **SCNP2'** and increasing molecular weight for **P5''**. **Right:** Depicts the molecular weight and absorption at 400 nm for every step in the cycle showing alternating values. Reprinted with permission from P. H. Maag *et al.* *Angew. Chem. Int. Ed.* **2023**, 62, e202309259. Open access under a CC BY-NC 4.0 DEED license by John Wiley & Sons. 67
- Figure 30:** Top left: Overlaid fluorescence spectra of **7** and **11** in THF with spectral overlap of the donor emission spectrum with the acceptor excitation spectrum. Top right: Fluorescence spectrum of **10** in THF. Bottom: 3D Fluorescence spectra of **7** (left), **11** (middle) and **10** (right) in THF with indicated 2D slices of spectra above. Reproduced from P. H. Maag *et al.* *Chem. Sci.* **2024**, 15, 5218-5224 with permission from the Royal Society of Chemistry. Open access under a CC BY 3.0 DEED license. 72
- Figure 31:** 3D Fluorescence spectra of **10** in different solvents sorted by polarity. Less polar solvents show a more efficient energy transfer between donor (bimane) and acceptor (NBD) than polar solvents. Reproduced from P. H. Maag *et al.* *Chem. Sci.* **2024**, 15, 5218-5224 with permission from the Royal Society of Chemistry. Open access under a CC BY 3.0 DEED license. 73
- Figure 32:** Comparison of peak absorption (470 nm) to peak emission (550 nm) intensity for different volume fractions of a stock solution of **10** in water ($l = 1$ cm). Reproduced from P. H. Maag *et al.* *Chem. Sci.* **2024**, 15, 5218-5224

with permission from the Royal Society of Chemistry. Open access under a CC BY 3.0 DEED license. 74

Figure 33: Reaction pathway of photobleaching and cleavage followed by 3D fluorescence spectra in THF. To photo-bleach the acceptor NBD, **10** was irradiated in water for 13 h with $\lambda_{\text{max}} = 505$ nm, resulting in an increasing intensity of the bimane emission. The cleavage reaction was performed in water for 25 min with $\lambda_{\text{max}} = 415$ nm resulting in an increasing intensity of the bimane emission. Reproduced from P. H. Maag *et al. Chem. Sci.* **2024**, 15, 5218-5224 with permission from the Royal Society of Chemistry. Open access under a CC BY 3.0 DEED license. 75

Figure 34: LC-MS trace (254 nm, 500 nm detector wavelength), absorption spectra and accumulated mass spectra of **10** irradiated with 415 nm for 25 min. Reproduced from P. H. Maag *et al. Chem. Sci.* **2024**, 15, 5218-5224 with permission from the Royal Society of Chemistry. Open access under a CC BY 3.0 DEED license. 76

Figure 35: Left: RID SEC traces of **P5**, post-functionalized to **P6** and folded into **SCNP3**. Middle: UV/Vis absorption SEC trace at 380 nm and 450 nm normalized by RID of **P5**, **P6** and **SCNP3**. Right: Kinetics of the post-functionalization of **P5** to **P6** and folding of **P6** to **SCNP3** monitored by UV/Vis absorption and M_n by SEC. The cross-linking of the polymer chain leads to a compaction and consequently to a smaller hydrodynamic volume e.g. a smaller apparent molecular weight in the SEC. M_n : apparent molecular weight. Reproduced from P. H. Maag *et al. Chem. Sci.* **2024**, 15, 5218-5224 with permission from the Royal Society of Chemistry. Open access under a CC BY 3.0 DEED license. 77

Figure 36: 3D fluorescence spectra of **SCNP3-5** in water as well as an image of the cuvettes irradiated with $\lambda_{\text{max}} = 380$ nm. M_n : apparent molecular weight. Reproduced from P. H. Maag *et al. Chem. Sci.* **2024**, 15, 5218-5224 with permission from the Royal Society of Chemistry. Open access under a CC BY 3.0 DEED license. 78

Figure 37: Bottom: Illustration of SCNPs with different incorporation of NBD analyzed by SEC showing different absorption at 450 nm compared to the RID and similar incorporation of bimane units according to the absorption at 380nm. The apparent M_n (red) slightly increases after post-functionalization and decreases with folding to SCNPs. Reproduced from P. H. Maag *et al. Chem. Sci.* **2024**, 15, 5218-5224 with permission from the Royal Society of Chemistry. Open access under a CC BY 3.0 DEED license. 79

Figure 38: Left: **SCNP3** and **SCNP4** analyzed by SEC showing different absorption at 450 nm and 380 nm. The apparent M_n (red) increases after irradiating with 415 nm for 3 h in water indicating an unfolded of the SCNPs. M_n : apparent molecular weight. Reproduced from P. H. Maag *et al. Chem. Sci.* **2024**, 15, 5218-5224 with permission from the Royal Society of Chemistry. Open access under a CC BY 3.0 DEED license. 80

Figure 39: Left: RID SEC traces of **SCNP4** unfolding compared to **P5**. Right: 3D fluorescence spectrum of **SCNP4** irradiated with 505 nm for 8 h in water. Reproduced from P. H. Maag *et al. Chem. Sci.* **2024**, 15, 5218-5224 with permission from the Royal Society of Chemistry. Open access under a CC BY 3.0 DEED license. 81

Figure 40: Illustration of a photoinduced drug release and degradation of SCNPs.....	86
Figure 41: Illustration of two fluorophores attached to a linear polymer chain which get closer by folding the polymer chain into SCNPs and report their folding and increasing compaction by a strong FRET signal.	87
Figure 42: Left: Setup for small scale batch photoreactions performed in NMR-tubes. Right: Batch photoreaction setup for the cross-linking of linear polymers to SCNPs (Step 4). The LEDs and the reaction mixture were cooled using two small ventilators.....	94
Figure 43: Irradiation setup for the photo cleavage of bimane with pH electrode to track the pH over time. The degassed sample in water was stirred with an electric stir bar and further flushed with N ₂ to prevent contamination with oxygen. The LED and reaction mixture was cooled by small electric fans to maintain ambient temperature. Both pictures show the same setup from different angles without and under irradiation in a lightproof box.	94
Figure 44: Emission spectrum of 415 nm (green) and 505 nm (blue) 10 W LEDs and absorbance spectrum of bimane and NBD (black).	95
Figure 45: LC-MS trace (254 nm, 215 nm detector wavelength), accumulated mass spectra of Methyl 4-((4-(tert-butoxy)-4-oxobutyl)amino)-4-oxobut-2-ynoate (2).	141
Figure 46: LC-MS trace (250 nm, 400 nm detector wavelength), absorption spectra and accumulated mass spectra of 8	141
Figure 47: LC-MS trace (250 nm, 400 nm detector wavelength), absorption spectra and accumulated mass spectra of radiation products and side products of 8	142
Figure 48: LC-MS trace (250 nm, 400 nm detector wavelength), absorption spectra and accumulated mass spectra of radiation products and side products of 8	142
Figure 49: LC-MS trace (250 nm, 400 nm detector wavelength), absorption spectra and accumulated mass spectra of radiation products and side products of 8	143
Figure 50: LC-MS trace (250 nm, 400 nm detector wavelength), absorption spectra and accumulated mass spectra of radiation products and side products of 8	143
Figure 51: LC-MS trace (250 nm, 400 nm detector wavelength), absorption spectra and accumulated mass spectra of 7	144
Figure 52: LC-MS trace (250 nm, 400 nm detector wavelength), absorption spectra and accumulated mass spectra of 7 after radiation for 30 min.	144
Figure 53: LC-MS trace (254 nm, 500 nm detector wavelength), absorption spectra and accumulated mass spectrum of <i>tert</i> -butyl (7-nitrobenzo[<i>c</i>][1,2,5]oxadiazol-4-yl)glycinate (NBD-Gly- <i>tert</i>).	145
Figure 54: LC-MS trace (254 nm, 500 nm detector wavelength), absorption spectra and accumulated mass spectrum of 11	145
Figure 55: LC-MS trace (254 nm, 500 nm detector wavelength), absorption spectra and accumulated mass spectrum of 10	146
Figure 56: LC-MS trace (254 nm, 500 nm detector wavelength), absorption spectra and accumulated mass spectrum of 12	146
Figure 57: LC-MS trace (254 nm, 500 nm detector wavelength), absorption spectra and accumulated mass spectrum of 7	147

Figure 58: Overview of the detailed synthetic strategy and THF-SEC RI traces of poly(Sty-co-BMS-co-S=PPh ₂ Sty) (P2) and the post-functionalization with the DA reagents, i.e. <i>o</i> MBA and alkyne (P3), as well as the resulting cross-links of SCNP1 and the final gold(I) coordinated SCNPs (SCNP-AuCl).....	148
Figure 59: SEC traces of P5 , SCNP2 and P5' . Left: Processed data as normalized intensity of RID over molecular weight compared with PMMA standards. Middle: Normalized intensity of RID over elution time. Right: Unprocessed data of RID and UV detector at 400 nm over elution time.	148
Figure 60: ¹ H NMR spectra of the hydroamination of 5 with 2 mol% SCNP-AuCl as a time series recorded in CDCl ₃ . The conversion was calculated from the marked resonances: internal standard ferrocene (4.19 ppm, grey), product (3.21 ppm, orange) and 5 (3.02 ppm, blue).	149
Figure 61: ¹ H NMR spectra of the hydroamination of 5 with 0.4 mol% SCNP-AuCl as a time series recorded in CDCl ₃ . The conversion was calculated from the marked resonances: internal standard ferrocene (4.19 ppm, grey), product (3.21 ppm, orange) and 5 (3.02 ppm, blue).	149
Figure 62: ¹ H NMR spectra of the hydroamination of 5 with AuCl-PPh ₂ Sty as a time series recorded in CDCl ₃ . The conversion was calculated from the marked resonances: internal standard ferrocene (4.19 ppm, grey), product (3.21 ppm, orange) and 5 (3.02 ppm, blue).	150
Figure 63: ¹ H NMR spectra of the hydroamination of 5 with P4 as a time series recorded in CDCl ₃ . The conversion was calculated from the marked resonances: internal standard ferrocene (4.19 ppm, grey), product (3.21 ppm, orange) and 5 (3.02 ppm, blue).	150
Figure 64: ¹ H NMR spectra of the hydroamination of 5 without catalyst as a time series recorded in CDCl ₃ . The conversion was calculated from the marked resonances: internal standard ferrocene (4.19 ppm, grey), product (3.21 ppm, orange) and 5 (3.02 ppm, blue).	151
Figure 65: 3D Fluorescence spectrum of 10 in water with emission and excitation slices (<i>l</i> = 10 mm, sample concentration around 0.1 % absorption).....	154
Figure 66: 3D Fluorescence spectrum of 11 in water with emission and excitation slices (<i>l</i> = 10 mm, sample concentration around 0.1 % absorption).....	154
Figure 67: 3D Fluorescence spectrum of 7 in water with emission and excitation slices (<i>l</i> = 10 mm, sample concentration around 0.1 % absorption).....	155
Figure 68: 3D Fluorescence spectrum of 10 in THF with emission and excitation slices (<i>l</i> = 10 mm, sample concentration around 0.1 % absorption).....	155
Figure S69: 3D Fluorescence spectrum of 11 in THF with emission and excitation slices (<i>l</i> = 10 mm, sample concentration around 0.1 % absorption).....	156
Figure 70: Overlap of the excitation spectrum ($\lambda_{EM} = 525$ nm) and the absorption spectrum of 11 in THF.	156
Figure 71: 3D Fluorescence spectrum of 7 in THF with emission and excitation slices (<i>l</i> = 10 mm, sample concentration around 0.1 % absorption).....	157
Figure 72: 3D Fluorescence spectrum of Ac ₂ -Bimane 8 in THF with emission and excitation slices (<i>l</i> = 10 mm, sample concentration around 0.1 % absorption).	157

Figure 73: 3D Fluorescence spectrum of 10 irradiated with 415 nm for 30 min recorded in THF with emission and excitation slices ($l = 10$ mm, sample concentration around 0.1 % absorption).	158
Figure 74: 3D Fluorescence spectrum of 10 irradiated with 505 nm for 16 h recorded in THF with emission and excitation slices ($l = 10$ mm, sample concentration around 0.1 % absorption).	158
Figure 75: Fluorescence spectra of 10 before and after irradiating with 505 nm for 16 h recorded in THF ($l = 10$ mm, sample concentration around 0.1 % absorption, 3D experiment, PMT voltage = 570V).	159
Figure 76: 3D Fluorescence spectrum of SCNP3 in water with emission and excitation slices ($l = 10$ mm, sample concentration around 0.1 % absorption).	159
Figure 77: 3D Fluorescence spectrum of SCNP3 in THF with emission and excitation slices ($l = 10$ mm, sample concentration around 0.1 % absorption).	160
Figure 78: 3D Fluorescence spectrum of SCNP3 in methanol (MeOH) with emission and excitation slices ($l = 10$ mm, sample concentration around 0.1 % absorption).	160
Figure 79: 3D Fluorescence spectrum of SCNP3 in dimethylformamide (DMF) with emission and excitation slices ($l = 10$ mm, sample concentration around 0.1 % absorption).	161
Figure 80: 3D Fluorescence spectrum of SCNP4 in water with emission and excitation slices ($l = 10$ mm, sample concentration around 0.1 % absorption).	161
Figure 81: 3D Fluorescence spectrum of SCNP5 in water with emission and excitation slices ($l = 10$ mm, sample concentration around 0.1 % absorption).	162
Figure 82: Absorption spectra of SCNP3-5 in water showing different absorptivity in the bimeane (390 nm) and NBD (475 nm) region.	162
Figure 83: 3D Fluorescence spectrum of SCNP4 before irradiating with 505 nm in water with emission and excitation slices ($l = 10$ mm, sample concentration around 0.1 % absorption).	163
Figure 84: 3D Fluorescence spectrum of SCNP4 after irradiating with 505 nm for 3 h in water with emission and excitation slices ($l = 10$ mm, sample concentration around 0.1 % absorption).	163
Figure 85: ^1H NMR spectrum of 2,2,6,6-tetramethyl-1-(1-phenylethoxy)piperidine recorded in CDCl_3 and assigned resonances.	164
Figure 86: $^{13}\text{C}\{^1\text{H}\}$ NMR spectrum of 2,2,6,6-tetramethyl-1-(1-phenylethoxy)piperidine recorded in CDCl_3 and assigned resonances.	164
Figure 87: ^1H NMR spectrum of 4-(diphenylphosphino)styrene sulfide ($\text{S}=\text{PPh}_2\text{Sty}$) recorded in CDCl_3 and assigned resonances.	165
Figure 88: $^{31}\text{P}\{^1\text{H}\}$ NMR spectrum of 4-(diphenylphosphino)styrene sulfide ($\text{S}=\text{PPh}_2\text{Sty}$) recorded in CDCl_3 and assigned resonances.	165
Figure 89: ^1H NMR spectrum of 4-(diphenylphosphino)styrene gold complex ($\text{ClAu}-\text{PPh}_2\text{Sty}$) recorded in CDCl_3 and assigned resonances.	166
Figure 90: $^{31}\text{P}\{^1\text{H}\}$ NMR spectrum of 4-(diphenylphosphino)styrene gold complex ($\text{ClAu}-\text{PPh}_2\text{Sty}$) recorded in CDCl_3 and assigned resonances.	166

Figure 91: ^1H NMR spectrum of <i>tert</i> -butyl 4-isocyanatobutanoate recorded in CDCl_3 and assigned resonances.....	167
Figure 92: ^{13}C -APT NMR spectrum of <i>tert</i> -butyl 4-isocyanatobutanoate recorded in CDCl_3 and assigned resonances.....	167
Figure 93: ^1H NMR spectrum of methyl 4-((4-(<i>tert</i> -butoxy)-4-oxobutyl)amino)-4-oxobut-2-ynoate (2) in CDCl_3 and assigned resonances.....	168
Figure 94: ^{13}C -APT NMR spectrum of methyl 4-((4-(<i>tert</i> -butoxy)-4-oxobutyl)amino)-4-oxobut-2-ynoate (2) recorded in CDCl_3 and assigned resonances.	168
Figure 95: ^1H NMR spectrum of 4-(4-methoxy-4-oxobut-2-ynamido)butanoic acid recorded in CDCl_3 and assigned resonances.	169
Figure 96: ^{13}C -APT NMR spectrum of 4-(4-methoxy-4-oxobut-2-ynamido)butanoic acid recorded in CDCl_3 and assigned resonances.	169
Figure 97: ^1H NMR spectrum of 4-(4-methoxy-4-oxobut-2-ynamido)butanoic acid recorded in CDCl_3 and assigned resonances.	170
Figure 98: ^{13}C -APT NMR spectrum of 4-(4-methoxy-4-oxobut-2-ynamido)butanoic acid recorded in CDCl_3 and assigned resonances.	170
Figure 99: ^1H NMR spectrum of 2,2-diphenylhept-4-yn-1-amine recorded in CDCl_3 and assigned resonances.....	171
Figure 100: ^{13}C -APT NMR spectrum of 2,2-diphenylhept-4-yn-1-amine recorded in CDCl_3 and assigned resonances.....	171
Figure 101: ^1H NMR spectrum of 8 recorded in CDCl_3 and assigned resonances.....	172
Figure 102: ^{13}C DEPTQ135 NMR spectrum of 8 recorded in CDCl_3 and assigned resonances.....	172
Figure 103: ^1H NMR spectrum of <i>tert</i> -butyl (7-nitrobenzo[<i>c</i>][1,2,5]oxadiazol-4-yl)glycinate (NBD-Gly- <i>tert</i>) recorded in CD_3CN and assigned resonances.	173
Figure 104: $^{13}\text{C}\{^1\text{H}\}$ NMR spectrum of <i>tert</i> -butyl (7-nitrobenzo[<i>c</i>][1,2,5]oxadiazol-4-yl)glycinate (NBD-Gly- <i>tert</i>) recorded in CD_3CN and assigned resonances.	173
Figure 105: ^1H NMR spectrum of 11 recorded in CD_3OD and assigned resonances.	174
Figure 106: $^{13}\text{C}\{^1\text{H}\}$ NMR spectrum of 11 recorded in CD_3OD and assigned resonances. ...	174
Figure 107: ^1H NMR spectrum of 10 recorded in CD_3CN and assigned resonances. The resonance at 1.29 ppm results from high boiling alkanes as part of impurity of cyclohexane and are difficult to avoid for small scale reactions. We assume that high boiling alkanes do not interfere with the photochemical reactions.....	175
Figure 108: $^{13}\text{C}\{^1\text{H}\}$ NMR spectrum of 10 recorded in CD_3CN and assigned resonances.....	175
Figure 109: ^1H NMR spectrum of 12 recorded in CD_3CN and assigned resonances.....	176
Figure 110: $^{13}\text{C}\{^1\text{H}\}$ NMR spectrum of 12 recorded in CD_3CN and assigned resonances.....	176
Figure 111: ^1H NMR spectrum of poly(Sty- <i>co</i> -CMS- <i>co</i> -S=PPh ₂ Sty) recorded in CDCl_3 and assigned resonances (Step 1, P1).	177
Figure 112: $^{31}\text{P}\{^1\text{H}\}$ NMR spectrum of poly(Sty- <i>co</i> -CMS- <i>co</i> -S=PPh ₂ Sty) recorded in CDCl_3 and assigned resonances (Step 1, P1).	177
Figure 113: ^1H NMR spectrum of poly(Sty- <i>co</i> -BMS- <i>co</i> -S=PPh ₂ Sty) recorded in CDCl_3 and assigned resonances (Step 2, P2).	178

Figure 114: $^{31}\text{P}\{^1\text{H}\}$ NMR spectrum of poly(Sty-co-BMS-co-S=PPh ₂ Sty) recorded in CDCl ₃ and assigned resonances (Step 2, P2).....	178
Figure 115: ^1H NMR spectrum of the post-functionalized poly(Sty-co-BMS-co-S=PPh ₂ Sty) recorded in CDCl ₃ and assigned resonances (Step 3, P3).....	179
Figure 116: ^1H NMR spectrum of the cross-linked poly(Sty-co-BMS-co-S=PPh ₂ Sty) recorded in CDCl ₃ and assigned resonances (Step 4, SCNP1).....	179
Figure 117: ^1H NMR spectrum of the cross-linked and protected poly(Sty-co-BMS-co-S=PPh ₂ Sty) recorded in CDCl ₃ and assigned resonances (Step 5).....	180
Figure 118: $^{31}\text{P}\{^1\text{H}\}$ NMR spectrum of the deprotected SCNP recorded in CDCl ₃ and assigned resonances (Step 6).....	180
Figure 119: ^1H NMR spectrum of the SCNP-AuCl recorded in CDCl ₃ and assigned resonances (Step 6, SCNP-AuCl).....	181
Figure 120: $^{31}\text{P}\{^1\text{H}\}$ NMR spectrum of SCNP-AuCl recorded in CDCl ₃ and assigned resonances (Step 6, SCNP-AuCl).....	181
Figure 121: ^1H NMR spectrum of poly(Sty-co-CMS-co-AuCl-PPh ₂ Sty) recorded in CDCl ₃ and assigned resonances (P4).....	182
Figure 122: $^{31}\text{P}\{^1\text{H}\}$ NMR spectrum of poly(Sty-co-CMS-co- AuCl-PPh ₂ Sty) recorded in CDCl ₃ and assigned resonances (P4).....	182
Figure 123: ^1H NMR spectrum of end group modification poly(MPEGMA-co-AA) recorded in CDCl ₃ and assigned resonances (P5).....	183
Figure 124: ^1H NMR spectrum bimane cross-linked SCNPs recorded in CDCl ₃ and assigned resonances (SCNP2).....	183
Figure 125: ^1H NMR spectrum of unfolded poly(MPEGMA-co-AA) recorded in CDCl ₃ and assigned resonances (P5').....	184
Figure 126: ^1H NMR spectrum of NBD post-functionalized and bimane cross-linked poly(MPEGMA-co-AA) recorded in CD ₃ OD and assigned resonances (SCNP3).....	184
Figure 127: ^1H NMR spectrum of NBD post-functionalized and bimane cross-linked poly(MPEGMA-co-AA) recorded in CD ₃ OD and assigned resonances (SCNP4).....	185
Figure 128: ^1H NMR spectrum of NBD post-functionalized and bimane cross-linked poly(MPEGMA-co-AA) recorded in CD ₃ OD and assigned resonances (SCNP5).....	185

List of Schemes

Scheme 1: Styryl-TEMPO alkoxyamine used in the current thesis for the polymerization of styrene derivatives, allowing thermal fragmentation into a persistent nitroxide radical and an initiating alkyl radical.....	5
Scheme 2: Mesomeric structures of nitroxides showing the delocalization of the unpaired electron. ^[38]	5

Scheme 3: Mechanism of the NMP process. Starting with an alkoxyamine in the pre-equilibrium to generate a living chain. The main equilibrium shows the propagating chain. The monomer (M) is in this case styrene. ^[38]	6
Scheme 4: General mechanism of a RAFT-polymerization. The activated initiator (I [•]) reacts with monomer units (M) forming a propagating chain (P _n [•]). In the presence of a RAFT agent, the P _n [•] forms a RAFT adduct radical which undergoes fragmentation, leading to a new propagating chain (P _m [•]). Step 4 describes the main equilibrium between the active chain and a dormant species. ^[51]	8
Scheme 5: RAFT agent with a free-radical leaving group R and Z-group which controls the reactivity of the C=S bond.	9
Scheme 6: Different Z- and R-groups for more activated monomers (MAMs) and less activated monomers (LAMs).	9
Scheme 7: End group modification of a RAFT polymer with dithiobenzoate group. A radical oxidation cycle initiated by AIBN yielding hydroperoxide groups which were reduced with triphenylphosphine to hydroxides.	10
Scheme 8: Examples of different ways of cross-linking polymer chains to obtain SCNPs with pendant groups and external cross-linker.....	13
Scheme 9: Folding of polymers <i>via</i> repeat unit folding and selective point folding. ^[68]	13
Scheme 10: Schematic overview of a [4+2] Diels-Alder cycloaddition between butadiene and ethene.	20
Scheme 11: Photoinduced mechanism for the formation of <i>o</i> -quinodimethanes and side products.	21
Scheme 12: Photoinduced cleavage mechanism of bimane diesters in the presence of water.....	22
Scheme 13: Mechanism for the Au(I)-catalyzed intramolecular hydroamination of an aminoalkyne.	26
Scheme 14: Synthesis of 4-(4-methoxy-4-oxobut-2-ynamido)butanoic acid (3) starting with tert-butyl 4-aminobutanoate (1).	32
Scheme 15: Step 1, NMP copolymerization to form P1 using 2,2,6,6-Tetramethyl-1-(1-phenylethoxy)piperidine as initiator, incorporating styrene, CMS and S=PPh ₂ Sty.....	34
Scheme 16: Overview of the detailed synthetic strategy showing the poly(Sty- <i>co</i> -BMS- <i>co</i> -S=PPh ₂ Sty) (P2) and the post-functionalization with the DA reagents the <i>o</i> MBA (B) and alkyne (A) (P3), as well as the resulting cross-links of SCNP1 and the final gold(I) coordinated SCNPs (SCNP-AuCl). Reprinted with permission from P. H. Maag <i>et al.</i> , <i>Macromolecules</i> 2022 , 55 (22), 9918-9924. Copyright 2022 American Chemical Society.....	35
Scheme 17: <i>o</i> MBA and alkyne used for the light introduced [4+2] cycloaddition, leading to fluorescent cross-links of the polymer chains. To attach both to the polymer backbone, the carboxylic acid group is used, which allows a post-functionalization with the BMS repeating units.....	36
Scheme 18: Proposed reaction scheme for the naphthalene formation within SCNPs.	41

Scheme 19: Intramolecular hydroamination of 2,2-diphenylhept-4-yn-1-amine (5) utilizing SCNP-AuCl as catalyst and Na[B(C ₆ F ₅) ₄] as cocatalysts forming a nitrogen-containing heterocycle.	42
Scheme 20: Folding and unfolding of poly(MPEGMA-co-acrylic acid), utilizing dibromobimane 1 as fluorescent, photoreactive cross-linker. In the folding reaction, the acrylic acid (AA) units react in a base-mediated SN ₂ reaction with 1 . The generated cross-links can be cleaved by visible light resulting in the original polymer and dihydroxybimane 2 . Reprinted with permission from P. H. Maag <i>et al. Angew. Chem. Int. Ed.</i> 2023 , 62, e202309259. Open access under a CC BY-NC 4.0 DEED license by John Wiley & Sons.	49
Scheme 21: Bimane caged acetate ester ((2,6-dimethyl-1,7-dioxo-1H,7H-pyrazolo[1,2-a]pyrazole-3,5-diyl)bis(methylene) diacetate, 8).....	50
Scheme 22: Synthesis route for folding poly(MPEGMA-co-acrylic acid) (P5) with dibromobimane 6 in an esterification reaction with the AA units using cesium carbonate as base resulting in SCNP2 . The bimane caged esters – functioning as cross-links – can be cleaved by visible light, resulting in the original polymer and dihydroxybimane 7 as side product. Reprinted with permission from P. H. Maag <i>et al. Angew. Chem. Int. Ed.</i> 2023 , 62, e202309259. Open access under a CC BY-NC 4.0 DEED license by John Wiley & Sons.	54
Scheme 23: Linear polymer chain P6 with incorporated FRET acceptor (NBD, green), folded <i>via</i> intramolecular cross-links utilizing dibromobimane (6 , blue). The introduced bimane units act as energy donor, absorbing light at shorter wavelengths and transferring this energy to the NBD units, which emits light in its unique spectral range, allowing the optical read out of the folding state <i>via</i> the characteristic FRET spectrum. Reproduced from P. H. Maag <i>et al. Chem. Sci.</i> 2024 , 15, 5218-5224 with permission from the Royal Society of Chemistry. Open access under a CC BY 3.0 DEED license.....	71
Scheme 24: Structure of the molecular FRET pair (10) composed of bimane (blue) and NBD (green), connected with a short linker. Bimane, the energy donor, absorbs light at shorter wavelengths and transfers this energy to the acceptor (NBD), which in turn emits light in its characteristic spectra. Reproduced from P. H. Maag <i>et al. Chem. Sci.</i> 2024 , 15, 5218-5224 with permission from the Royal Society of Chemistry. Open access under a CC BY 3.0 DEED license.....	72
Scheme 25: Post-functionalization of P5 with the fluorophores 12 and 6 to incorporating the FRET pair. 6 concomitantly acts as cross-linker, folding P5 into SCNP3 . Reproduced from P. H. Maag <i>et al. Chem. Sci.</i> 2024 , 15, 5218-5224 with permission from the Royal Society of Chemistry. Open access under a CC BY 3.0 DEED license.	77

List of Tables

Table 1: Analysis of the copolymer composition by monomer conversion.....	34
Table 2: Analysis of copolymer composition calculated from ¹ H NMR of the polymer.....	35
Table 3: TON and TOF for the catalyzed intramolecular hydroamination of 5	45
Table 4: Analysis of copolymer composition by conversion of the polymerization.	52

Table 5: Calculation of the cross-linking density for SCNP1 and P1'	60
Table 6: Experimental and theoretical m/z of radiation products and side products of 8	143
Table 7: Experimental and theoretical m/z of radiation products and side products of 7	144
Table 8: Experimental and theoretical m/z of small molecule synthesis products.....	147

Appendices

Appendix A: LCMS

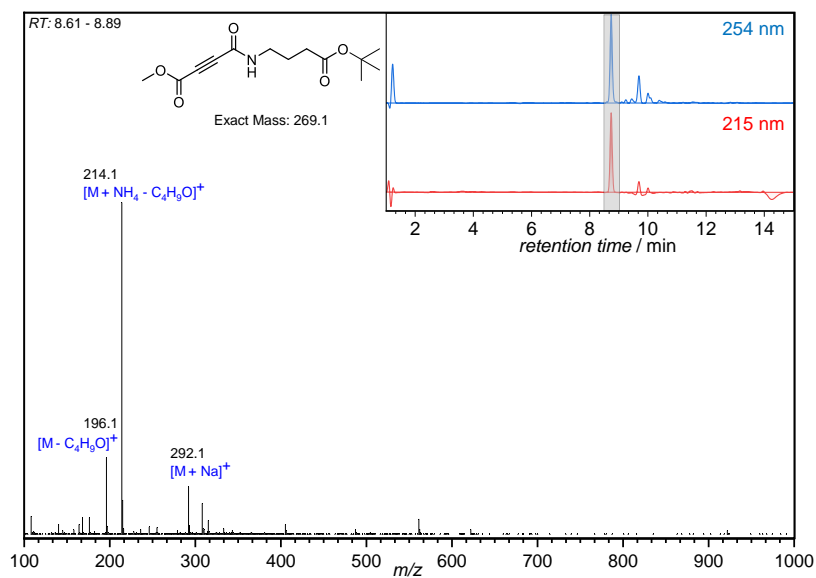


Figure 45: LC-MS trace (254 nm, 215 nm detector wavelength), accumulated mass spectra of Methyl 4-((4-(tert-butoxy)-4-oxobutyl)amino)-4-oxobut-2-ynoate (**2**).

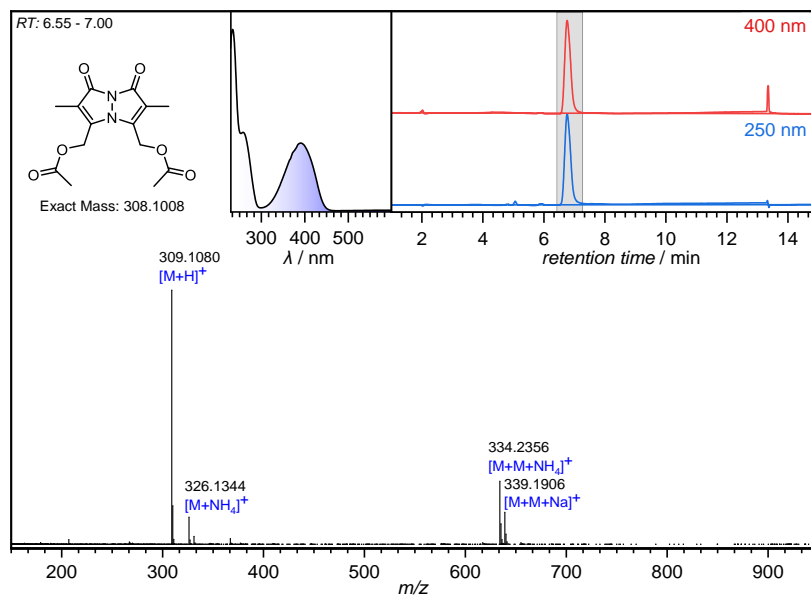


Figure 46: LC-MS trace (250 nm, 400 nm detector wavelength), absorption spectra and accumulated mass spectra of **8**.

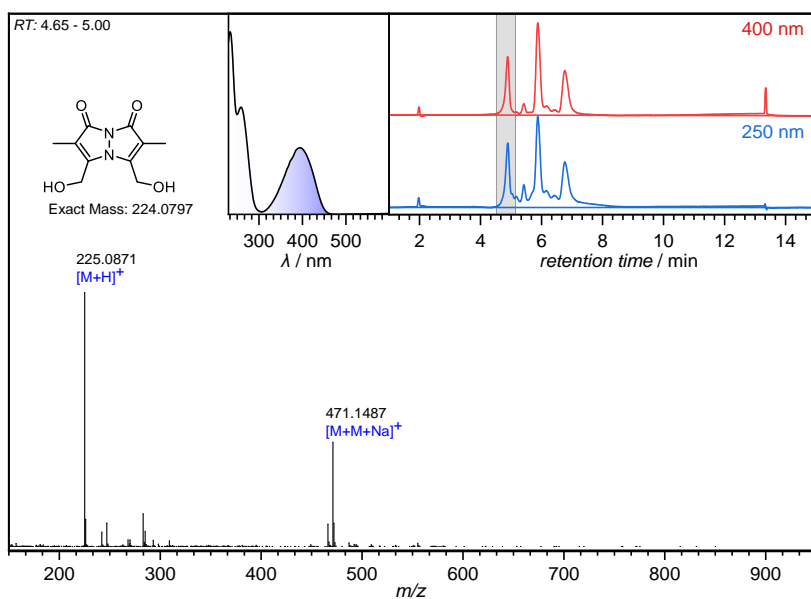


Figure 47: LC-MS trace (250 nm, 400 nm detector wavelength), absorption spectra and accumulated mass spectra of radiation products and side products of **8**.

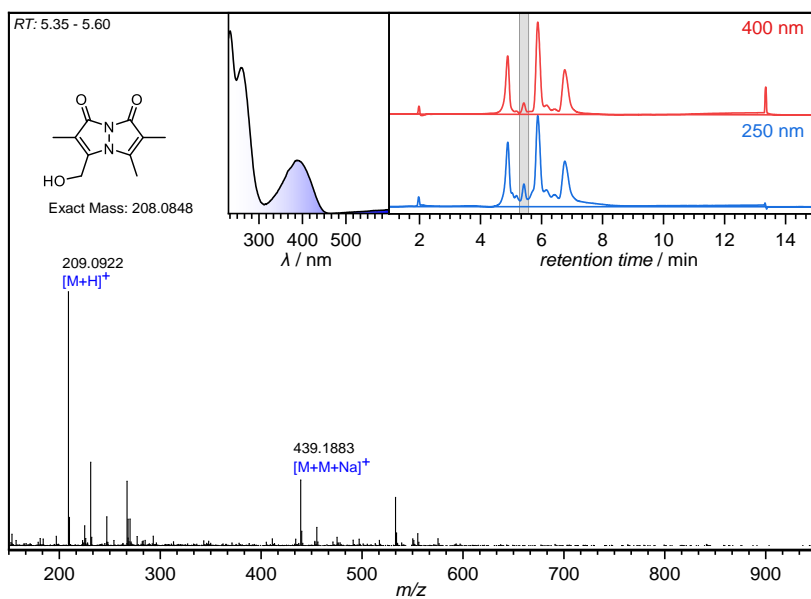


Figure 48: LC-MS trace (250 nm, 400 nm detector wavelength), absorption spectra and accumulated mass spectra of radiation products and side products of **8**.

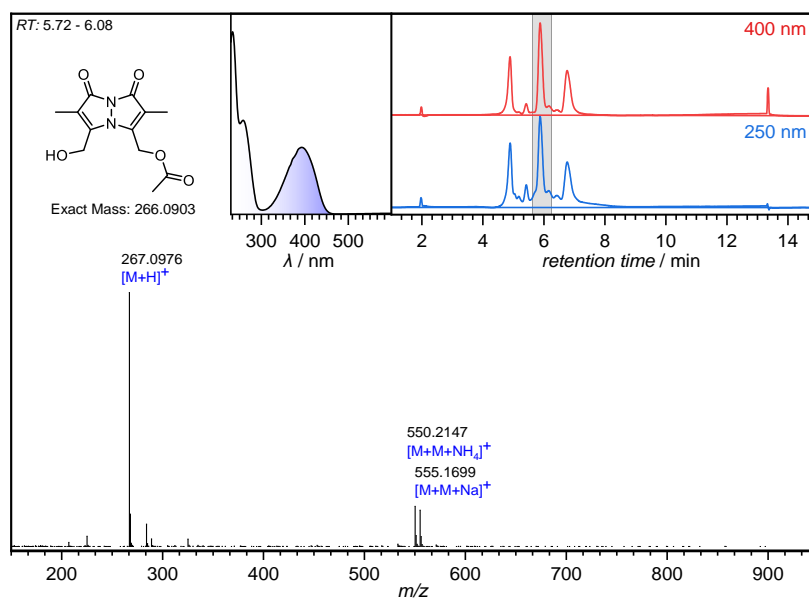


Figure 49: LC-MS trace (250 nm, 400 nm detector wavelength), absorption spectra and accumulated mass spectra of radiation products and side products of **8**.

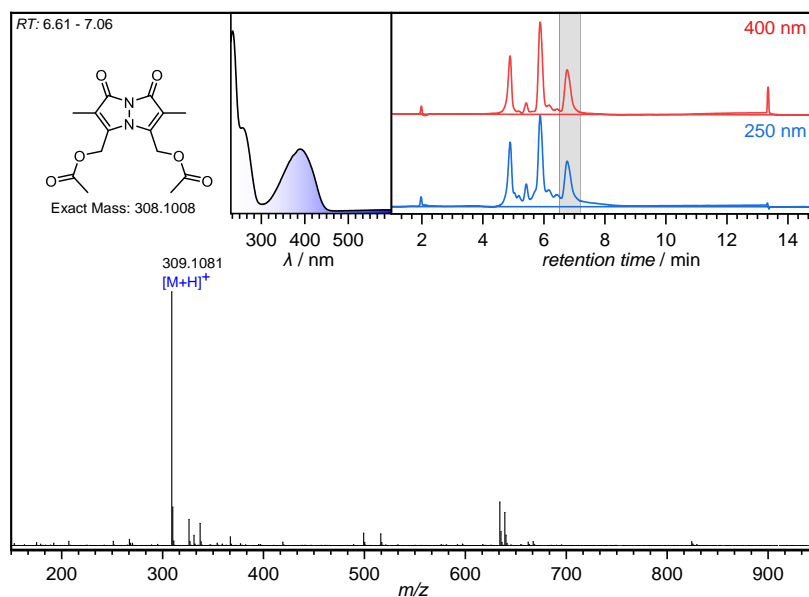


Figure 50: LC-MS trace (250 nm, 400 nm detector wavelength), absorption spectra and accumulated mass spectra of radiation products and side products of **8**.

Table 6: Experimental and theoretical m/z of radiation products and side products of **8**.

Symbol	m/z^{exp}	m/z^{theor}	m/z^{H^+}	Δ_{ppm}
$[M+H]^+$	309.108	308.1008	1.0073	0.26
$[M+H]^+$	225.0871	224.0797	1.0073	0.54
$[M+H]^+$	209.0922	208.0848	1.0073	0.58
$[M+H]^+$	267.0976	266.0903	1.0073	0.08
$[M+H]^+$	309.1081	308.1008	1.0073	0.06

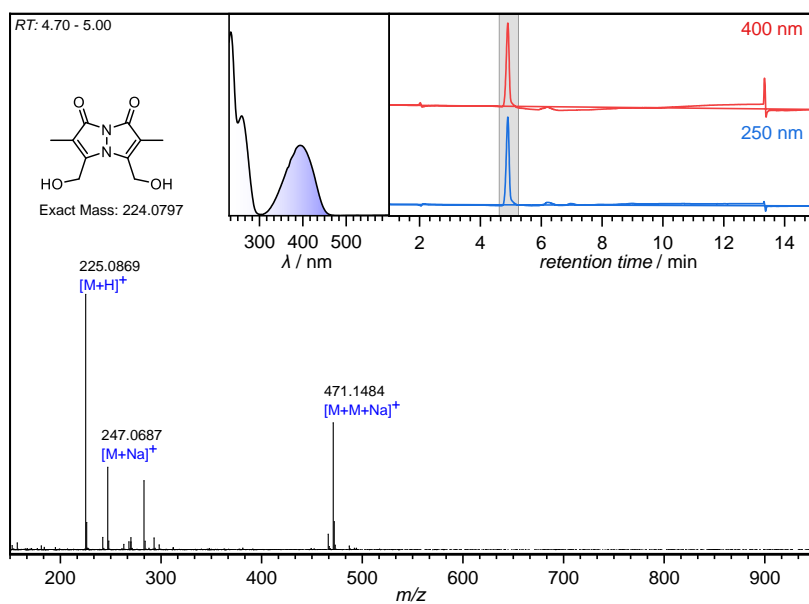


Figure 51: LC-MS trace (250 nm, 400 nm detector wavelength), absorption spectra and accumulated mass spectra of **7**.

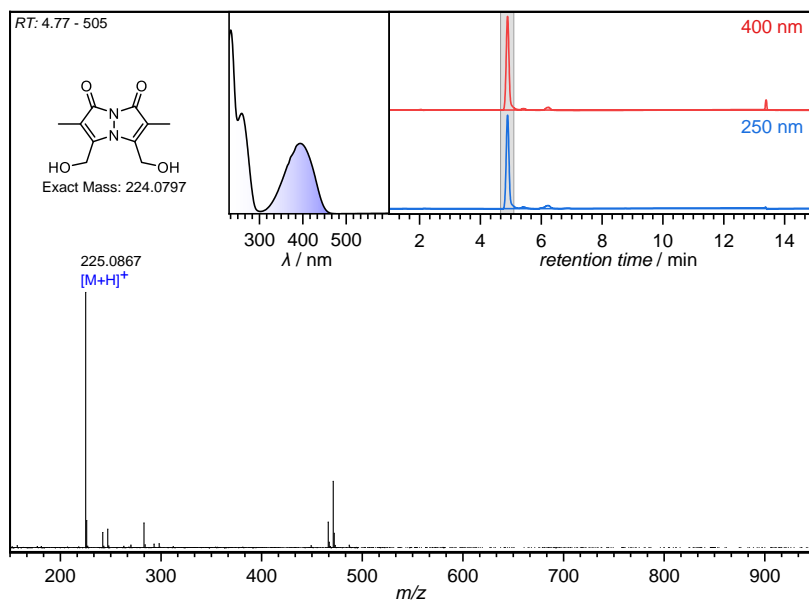


Figure 52: LC-MS trace (250 nm, 400 nm detector wavelength), absorption spectra and accumulated mass spectra of **7** after radiation for 30 min.

Table 7: Experimental and theoretical m/z of radiation products and side products of **7**.

Symbol	m/z^{exp}	m/z^{theor}	m/z^{H^+}	Δ_{ppm}
$[M+H]^+$	225.0869	224.0797	1.0073	0.36
$[M+H]^+$	225.0867	224.0797	1.0073	1.25

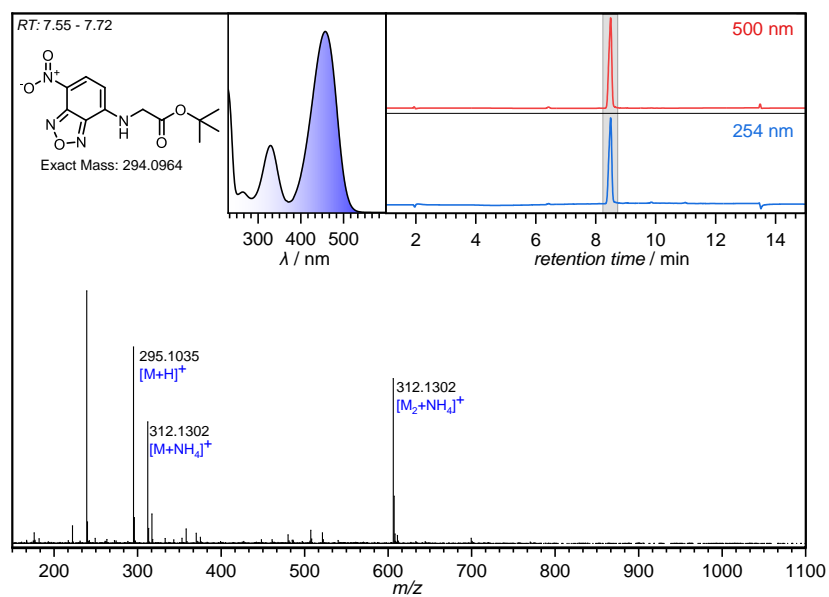


Figure 53: LC-MS trace (254 nm, 500 nm detector wavelength), absorption spectra and accumulated mass spectrum of *tert*-butyl (7-nitrobenzo[*c*][1,2,5]oxadiazol-4-yl)glycinate (NBD-Gly-*tert*).

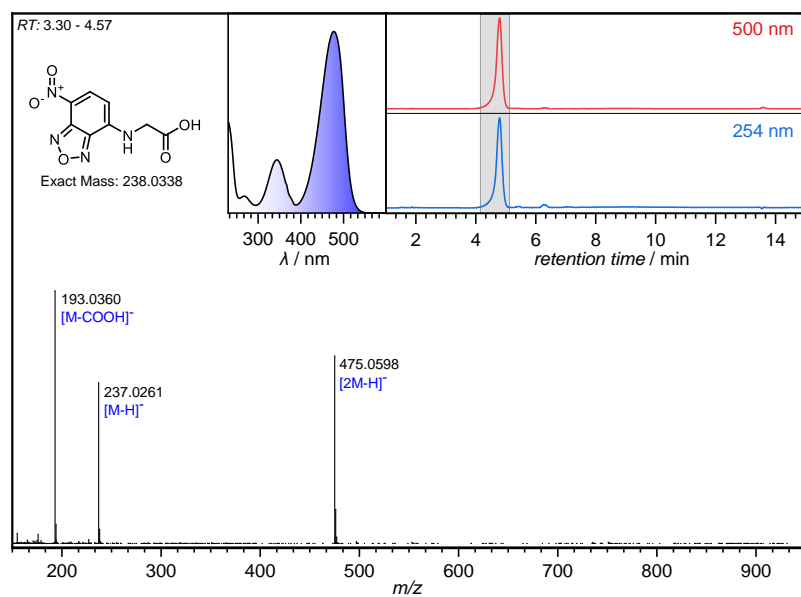


Figure 54: LC-MS trace (254 nm, 500 nm detector wavelength), absorption spectra and accumulated mass spectrum of **11**.

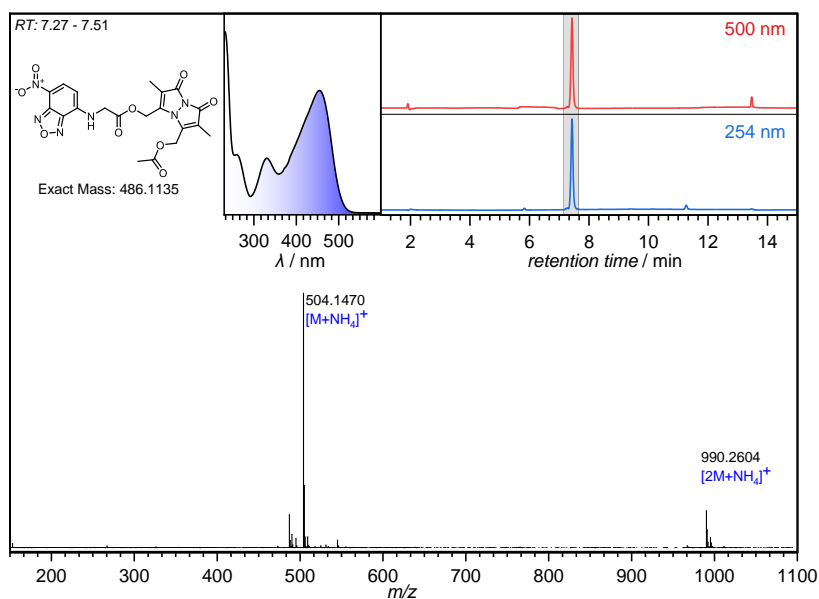


Figure 55: LC-MS trace (254 nm, 500 nm detector wavelength), absorption spectra and accumulated mass spectrum of **10**.

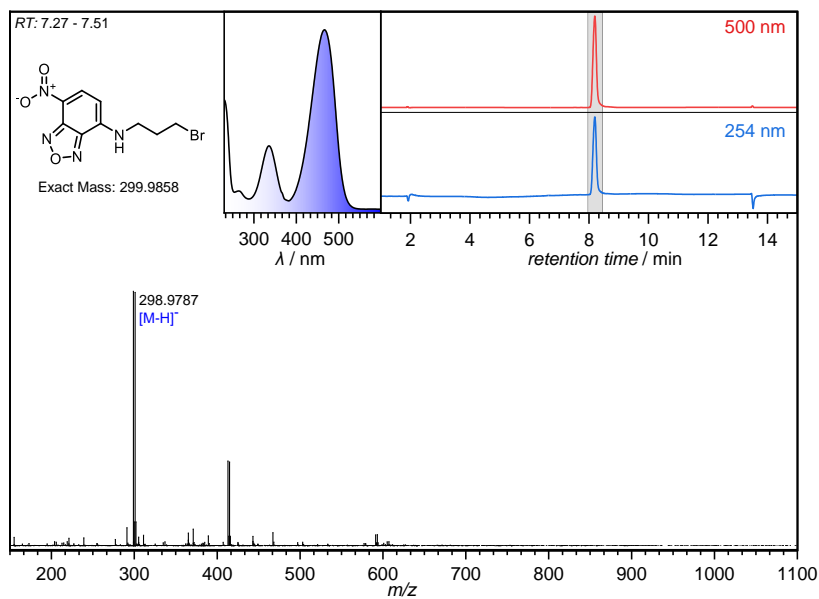


Figure 56: LC-MS trace (254 nm, 500 nm detector wavelength), absorption spectra and accumulated mass spectrum of **12**.

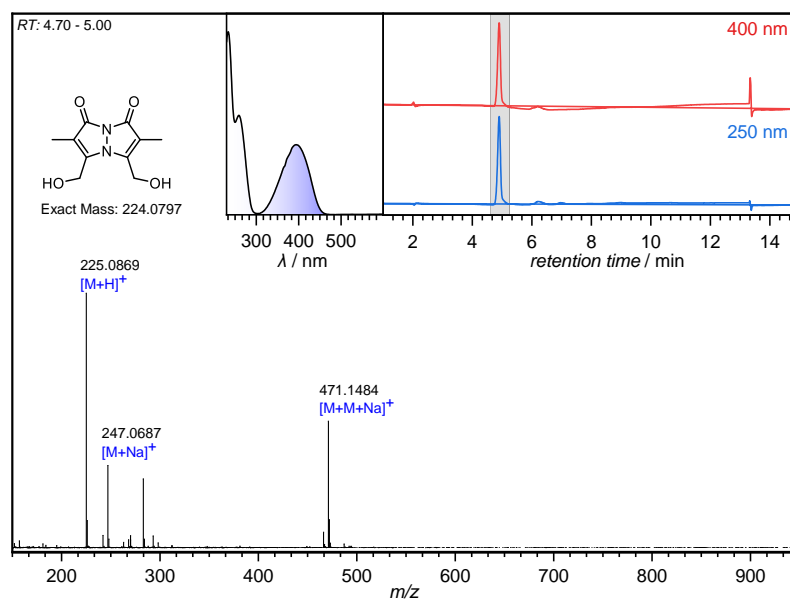


Figure 57: LC-MS trace (254 nm, 500 nm detector wavelength), absorption spectra and accumulated mass spectrum of **7**.

Table 8: Experimental and theoretical m/z of small molecule synthesis products.

Product	Symbol	m/z^{exp}	m/z^{theor}	m/z^{adduct}	Δ_{ppm}
NBD-Gly-tert	$[M+H]^+$	295.1035	294.0964	1.0073	0.61
4	$[M-H]^-$	237.0261	238.0338	1.0073	1.76
1	$[M+NH_4]^+$	504.1470	486.1135	18.0338	0.62
5	$[M-H]^-$	298.9787	299.9858	1.0073	0.60
3	$[M+H]^+$	225.0869	224.0797	1.0073	0.36

Appendix B: SEC

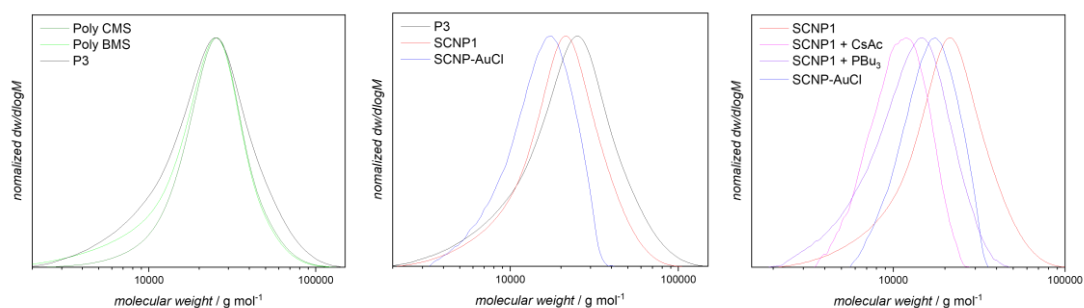


Figure 58: Overview of the detailed synthetic strategy and THF-SEC RI traces of poly(Sty-co-BMS-co-S=PPh2Sty) (P2) and the post-functionalization with the DA reagents, i.e. *o*MBA and alkyne (**P3**), as well as the resulting cross-links of SCNP1 and the final gold(I) coordinated SCNPs (SCNP-AuCl).

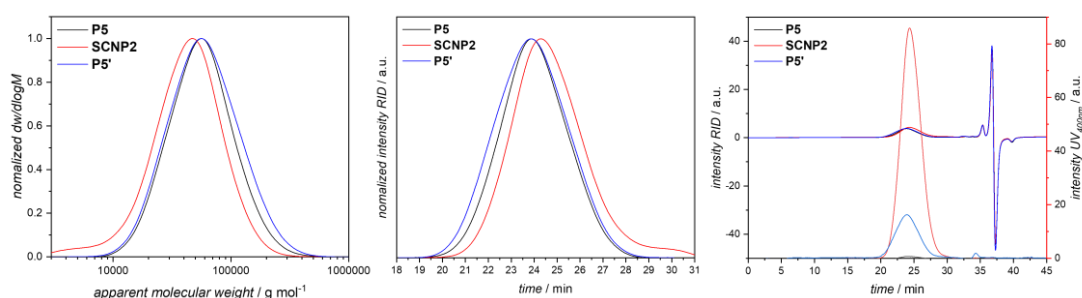


Figure 59: SEC traces of **P5**, **SCNP2** and **P5'**. **Left:** Processed data as normalized intensity of RID over molecular weight compared with PMMA standards. **Middle:** Normalized intensity of RID over elution time. **Right:** Unprocessed data of RID and UV detector at 400 nm over elution time.

Appendix C: NMR kinetics of catalyzed Intramolecular Hydroamination

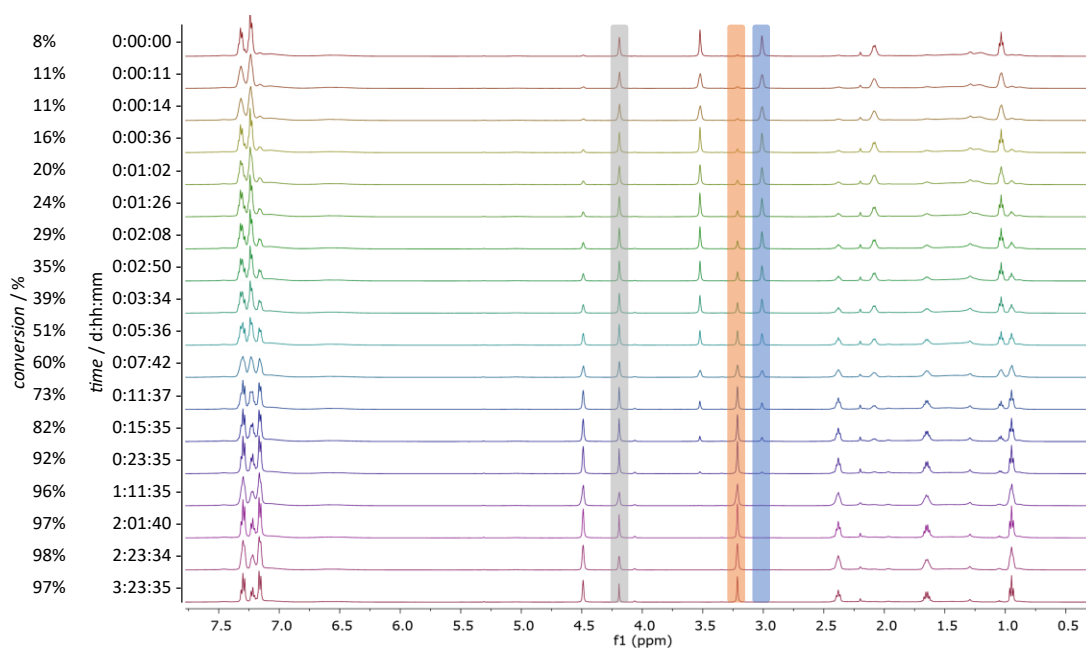


Figure 60: ^1H NMR spectra of the hydroamination of **5** with 2 mol% SCNP-AuCl as a time series recorded in CDCl_3 . The conversion was calculated from the marked resonances: internal standard ferrocene (4.19 ppm, grey), product (3.21 ppm, orange) and **5** (3.02 ppm, blue).

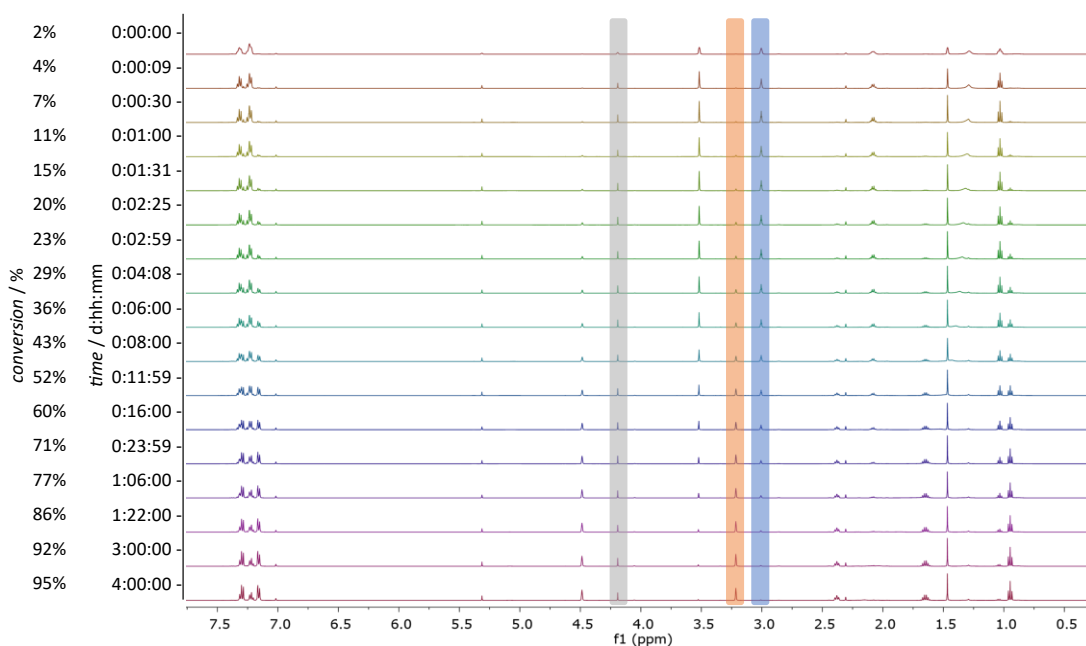


Figure 61: ^1H NMR spectra of the hydroamination of **5** with 0.4 mol% SCNP-AuCl as a time series recorded in CDCl_3 . The conversion was calculated from the marked resonances: internal standard ferrocene (4.19 ppm, grey), product (3.21 ppm, orange) and **5** (3.02 ppm, blue).

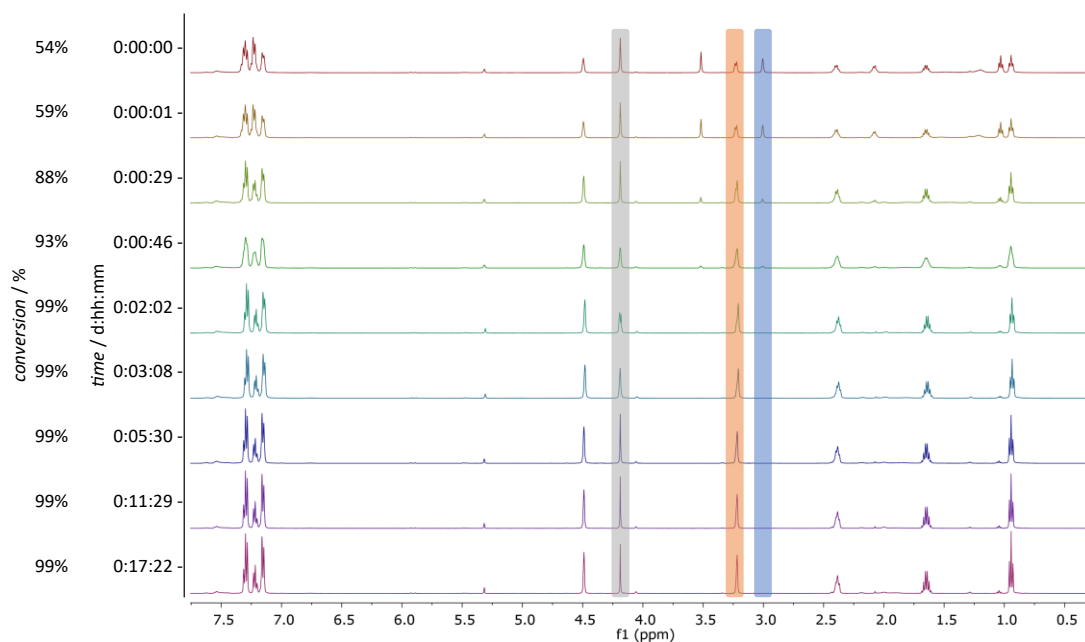


Figure 62: ^1H NMR spectra of the hydroamination of **5** with AuCl-PPH₂Sty as a time series recorded in CDCl₃. The conversion was calculated from the marked resonances: internal standard ferrocene (4.19 ppm, grey), product (3.21 ppm, orange) and **5** (3.02 ppm, blue).

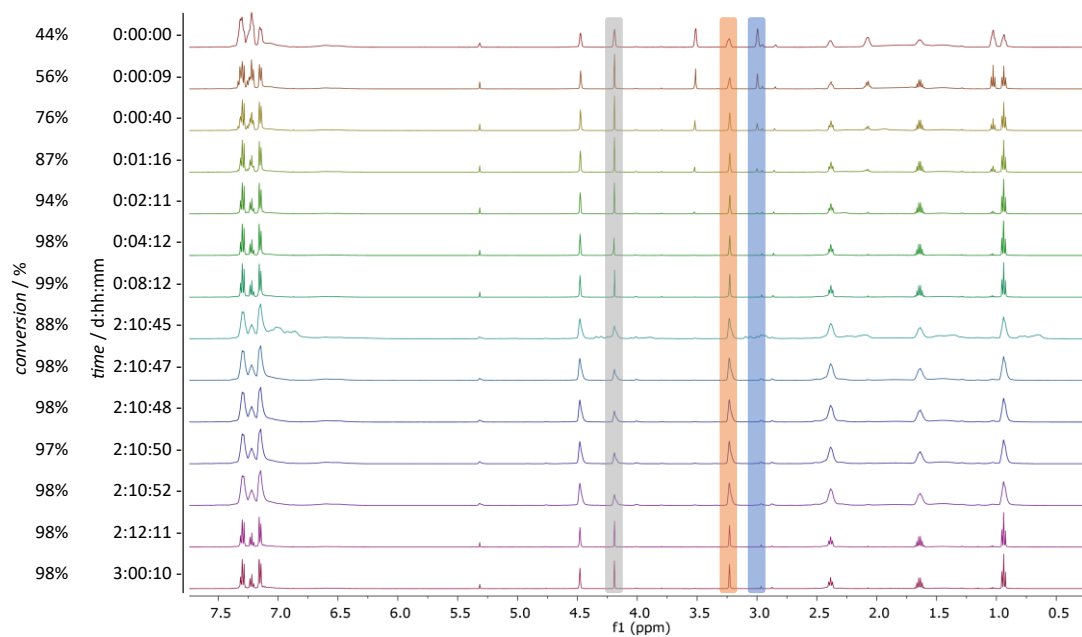


Figure 63: ^1H NMR spectra of the hydroamination of **5** with **P4** as a time series recorded in CDCl₃. The conversion was calculated from the marked resonances: internal standard ferrocene (4.19 ppm, grey), product (3.21 ppm, orange) and **5** (3.02 ppm, blue).

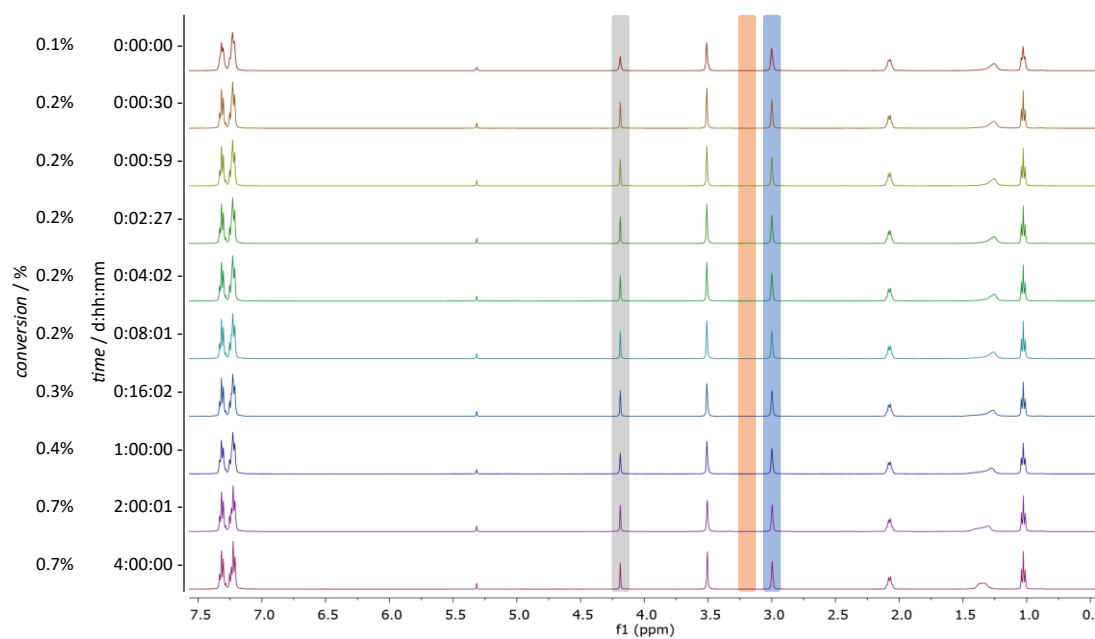


Figure 64: ^1H NMR spectra of the hydroamination of **5** without catalyst as a time series recorded in CDCl_3 . The conversion was calculated from the marked resonances: internal standard ferrocene (4.19 ppm, grey), product (3.21 ppm, orange) and **5** (3.02 ppm, blue).

Appendix D: MatLab code

The cleavage simulation was performed on MatLab R2022b using an adapted code written by an AI-powered language model (*Microsoft (2023) Bing, Copilot*).

```
% Initialize the number of simulations
num_sims = 10000;

% Initialize the range of bimanane units remaining in the polymer for different
conversions
bimane_remaining_range = 0:5:100;

% Initialize a table to store the results
results = table('Size', [length(bimane_remaining_range), 3], 'VariableTypes',
{'double', 'double', 'double'}, 'VariableNames', {'BimaneRemaining',
'ProbNeverReacted', 'ProbReactedOnce'});

% Run the Monte Carlo simulation for each conversion
for i = 1:length(bimane_remaining_range)
    % Get the current number of bimanane units remaining in the polymer
    bimane_remaning = bimane_remaining_range(i);

    % Initialize counts for unreacted bimananes and bimananes cleaved once
    never_reacted_count = 0;
    reacted_once_count = 0;

    % Run the Monte Carlo simulation
    for sim = 1:num_sims
        % Initialize the polymer chain with 100 distinguishable bimananes
        chain = 1:100;

        % Initialize a vector to keep track of which bimananes reacted
        reacted_bimananes = zeros(1,100);

        % Continue cleaving bimananes until there are bimane_remaining left in the
polymer chain
        while length(chain) > bimane_remaning
            % Randomly choose a bimanane to react
            bimane = chain(randi(length(chain)));

            % Check if the chosen bimanane has reacted before
            if reacted_bimananes(bimane) == 1
                % If yes, cleave it off completely
                chain(chain == bimane) = [];
            else
                % If no, remember that this specific bimanane unit has reacted
once
                reacted_bimananes(bimane) = 1;
            end
        end

        % Count the number of bimananes remaining in the polymer chain that have
been cleaved once
        num_cleaved_once = sum(reacted_bimananes(chain));

        % Count the number of bimananes remaining in the polymer chain that has
not reacted at all
        num_not_reacted = length(chain) - num_cleaved_once;

        % Update counts for bimananes never reacted and bimananes reacted once
        never_reacted_count = never_reacted_count + num_not_reacted;
        reacted_once_count = reacted_once_count + num_cleaved_once;
    end

    % Estimate probabilities for bimanane units never reacted and cleaved once
    prob_never_reacted = never_reacted_count / num_sims;
    prob_reacted_once = reacted_once_count / num_sims;
end
```



```
% Store results in table
results.BimaneRemaining(i) = bimane_remaning;
results.ProbNeverReacted(i) = prob_never_reacted;
results.ProbReactedOnce(i) = prob_reacted_once;
end

% Display results table
disp(results)
```

Appendix E: Fluorescence spectra

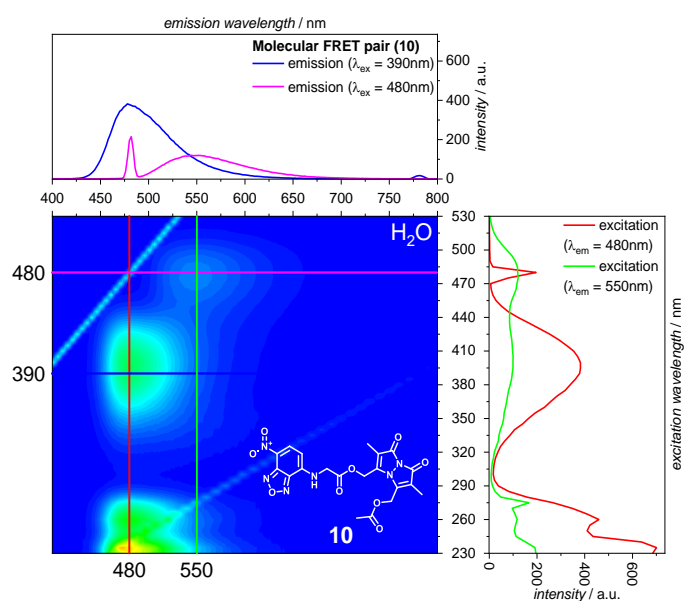


Figure 65: 3D Fluorescence spectrum of **10** in water with emission and excitation slices ($l = 10$ mm, sample concentration around 0.1 % absorption).

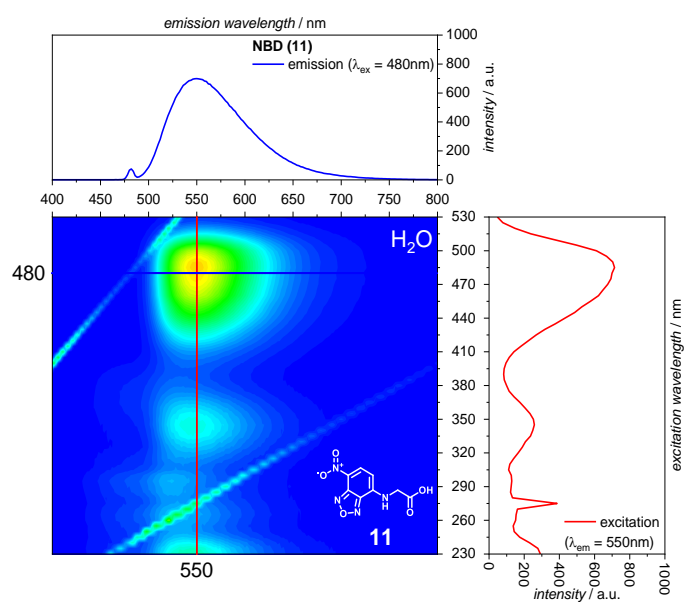


Figure 66: 3D Fluorescence spectrum of **11** in water with emission and excitation slices ($l = 10$ mm, sample concentration around 0.1 % absorption).

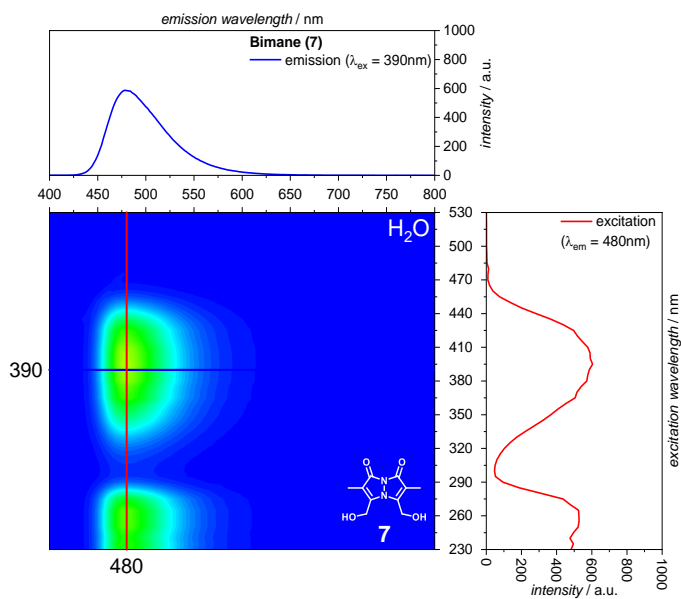


Figure 67: 3D Fluorescence spectrum of **7** in water with emission and excitation slices ($l = 10$ mm, sample concentration around 0.1 % absorption).

Fluorophores in THF

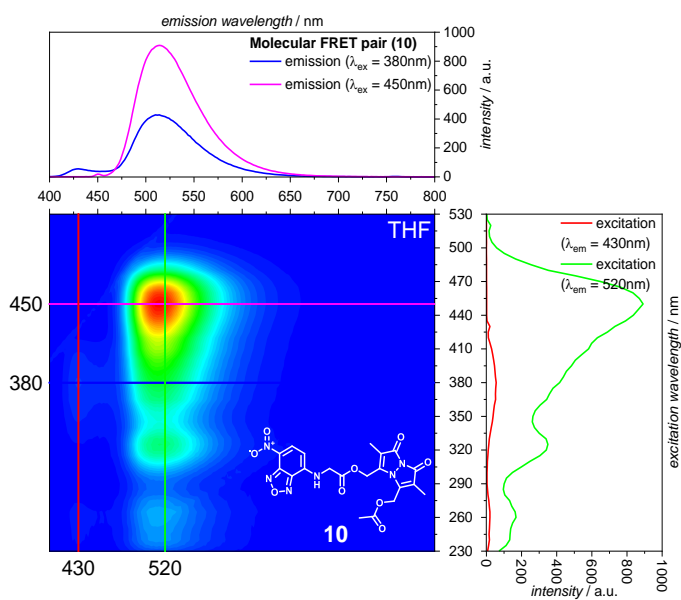


Figure 68: 3D Fluorescence spectrum of **10** in THF with emission and excitation slices ($l = 10$ mm, sample concentration around 0.1 % absorption).

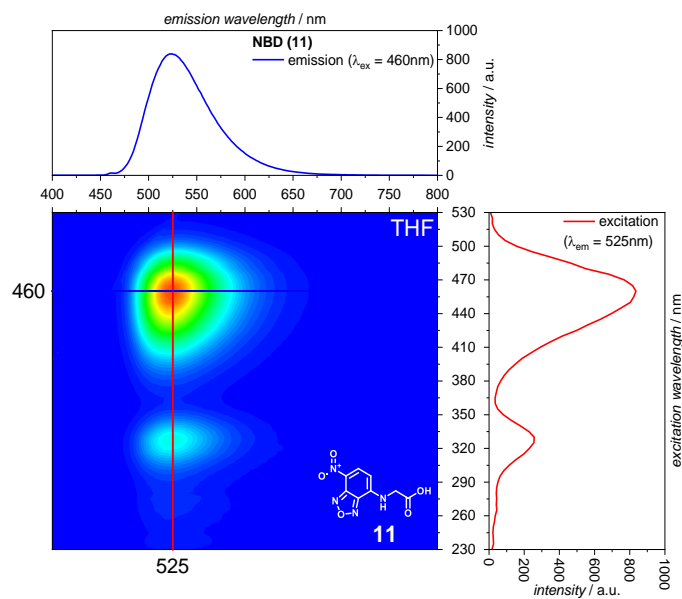


Figure S69: 3D Fluorescence spectrum of **11** in THF with emission and excitation slices ($l = 10$ mm, sample concentration around 0.1 % absorption).

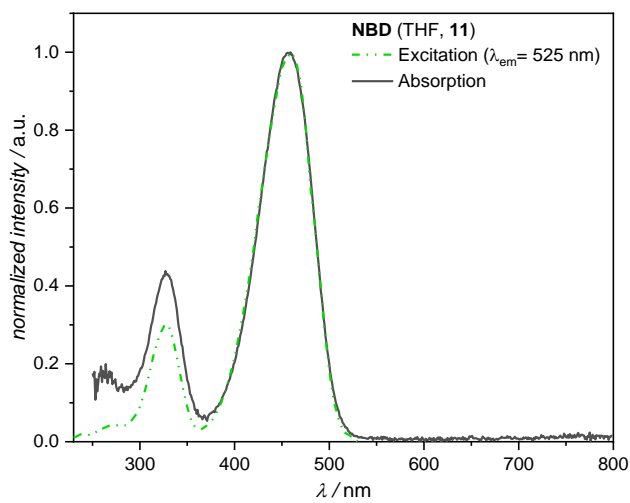


Figure 70: Overlap of the excitation spectrum ($\lambda_{EM} = 525$ nm) and the absorption spectrum of **11** in THF.

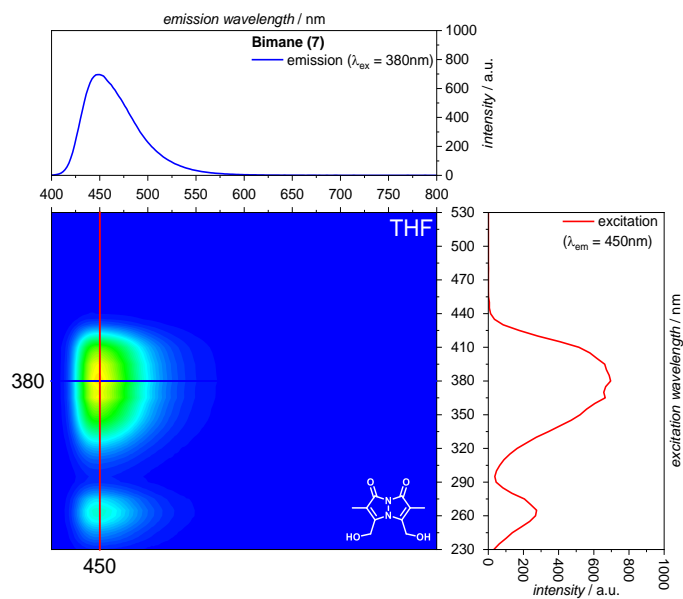


Figure 71: 3D Fluorescence spectrum of **7** in THF with emission and excitation slices ($l = 10$ mm, sample concentration around 0.1 % absorption).

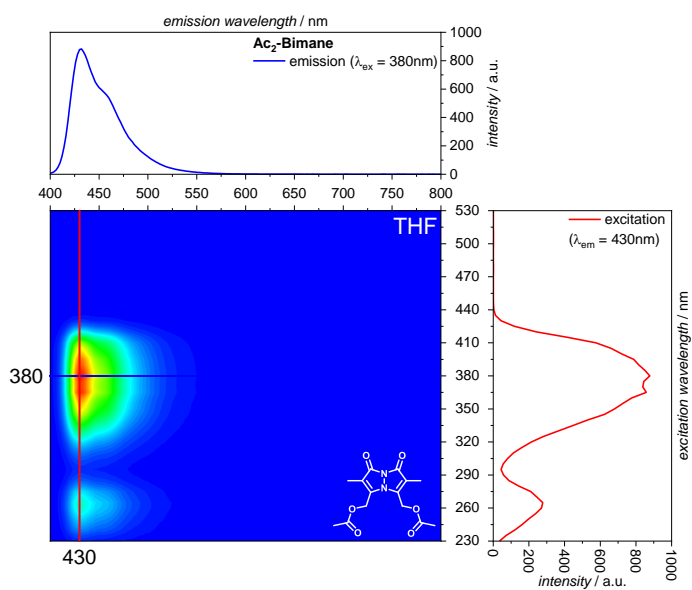


Figure 72: 3D Fluorescence spectrum of Ac₂-Bimane **8** in THF with emission and excitation slices ($l = 10$ mm, sample concentration around 0.1 % absorption).

Irradiation Experiments

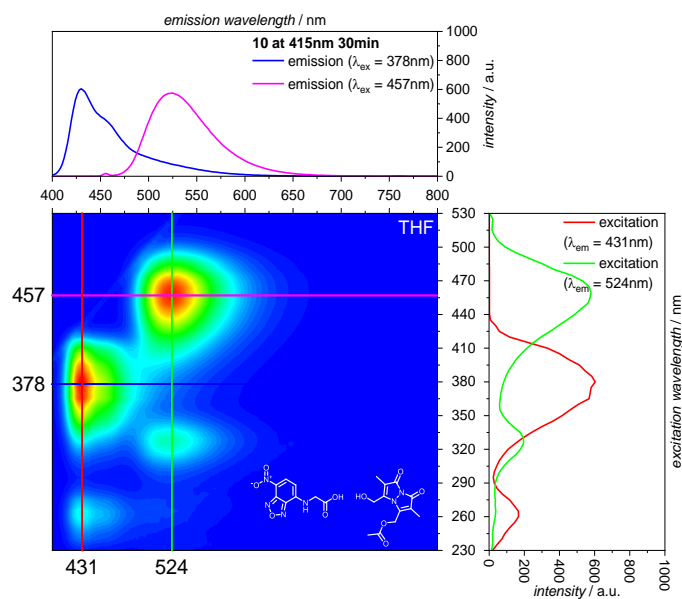


Figure 73: 3D Fluorescence spectrum of **10** irradiated with 415 nm for 30 min recorded in THF with emission and excitation slices ($l = 10\text{ mm}$, sample concentration around 0.1 % absorption).

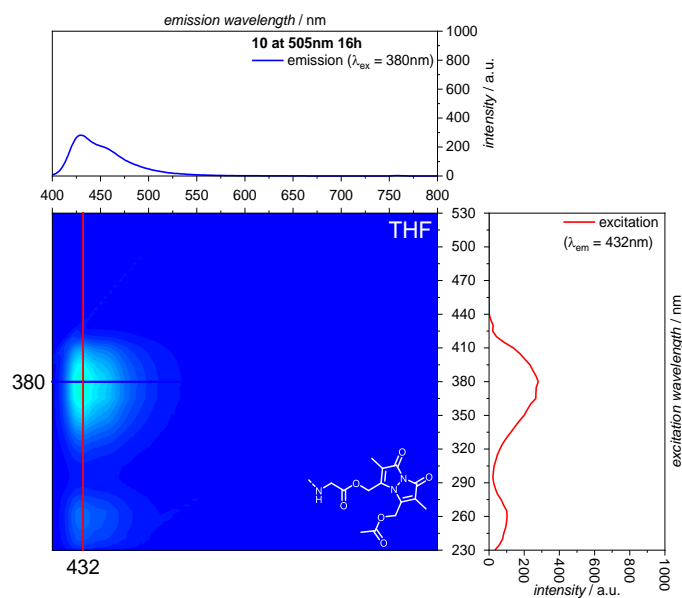


Figure 74: 3D Fluorescence spectrum of **10** irradiated with 505 nm for 16 h recorded in THF with emission and excitation slices ($l = 10\text{ mm}$, sample concentration around 0.1 % absorption).

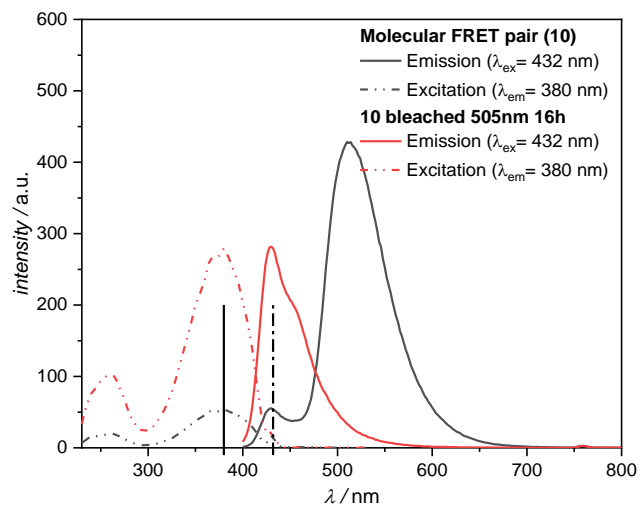


Figure 75: Fluorescence spectra of **10** before and after irradiating with 505 nm for 16 h recorded in THF ($l = 10$ mm, sample concentration around 0.1 % absorption, 3D experiment, PMT voltage = 570V).

Polymers

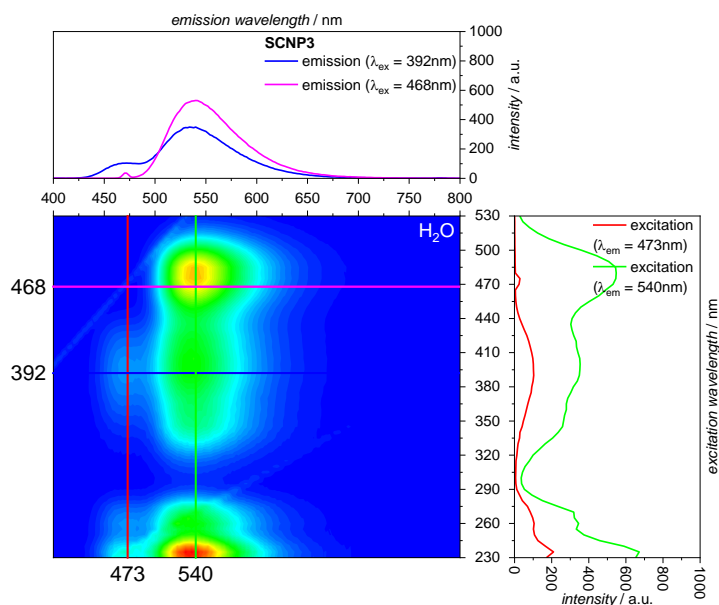


Figure 76: 3D Fluorescence spectrum of **SCNP3** in water with emission and excitation slices ($l = 10$ mm, sample concentration around 0.1 % absorption).

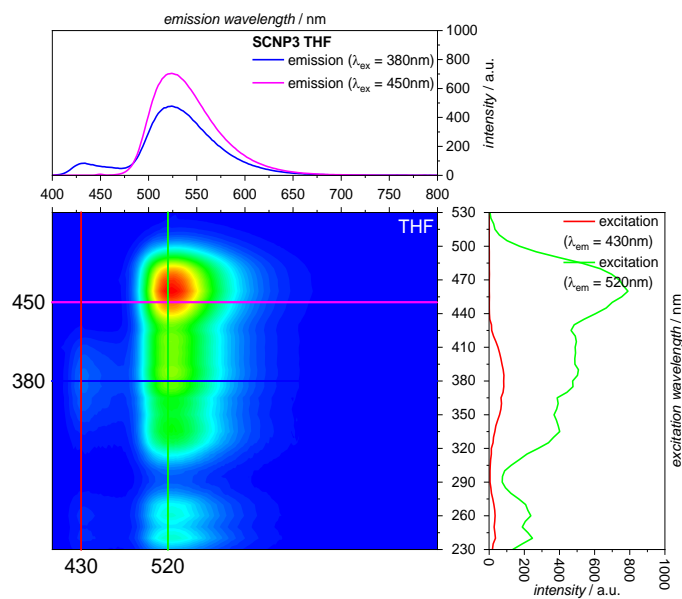


Figure 77: 3D Fluorescence spectrum of **SCNP3** in THF with emission and excitation slices ($l = 10$ mm, sample concentration around 0.1 % absorption).

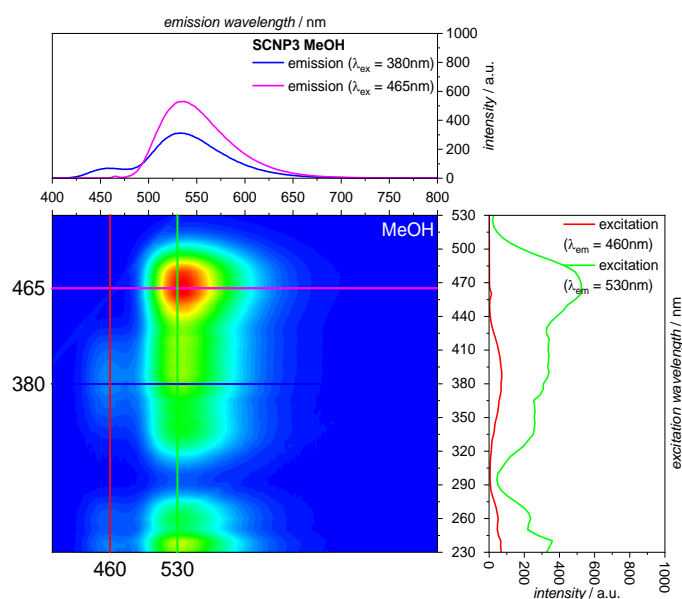


Figure 78: 3D Fluorescence spectrum of **SCNP3** in methanol (MeOH) with emission and excitation slices ($l = 10$ mm, sample concentration around 0.1 % absorption).

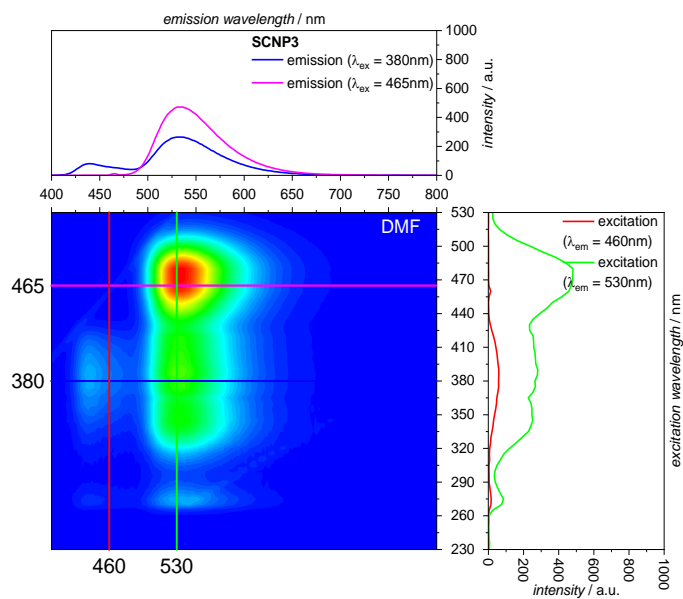


Figure 79: 3D Fluorescence spectrum of **SCNP3** in dimethylformamide (DMF) with emission and excitation slices ($l = 10$ mm, sample concentration around 0.1 % absorption).

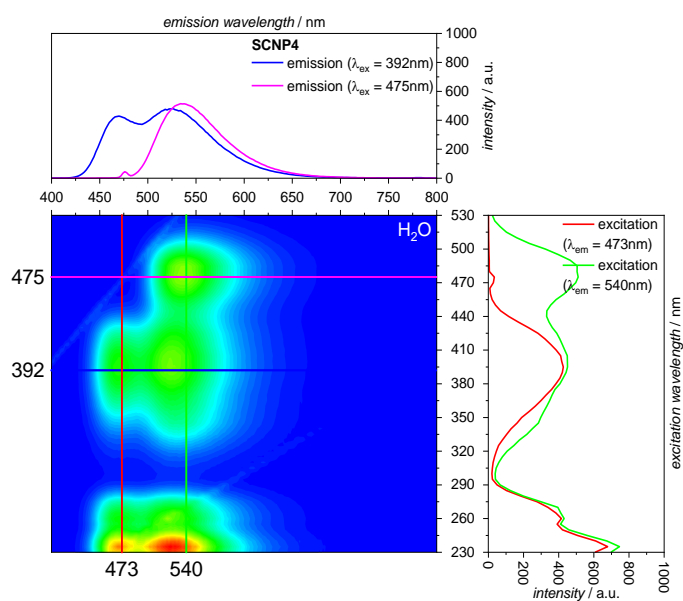


Figure 80: 3D Fluorescence spectrum of **SCNP4** in water with emission and excitation slices ($l = 10$ mm, sample concentration around 0.1 % absorption).

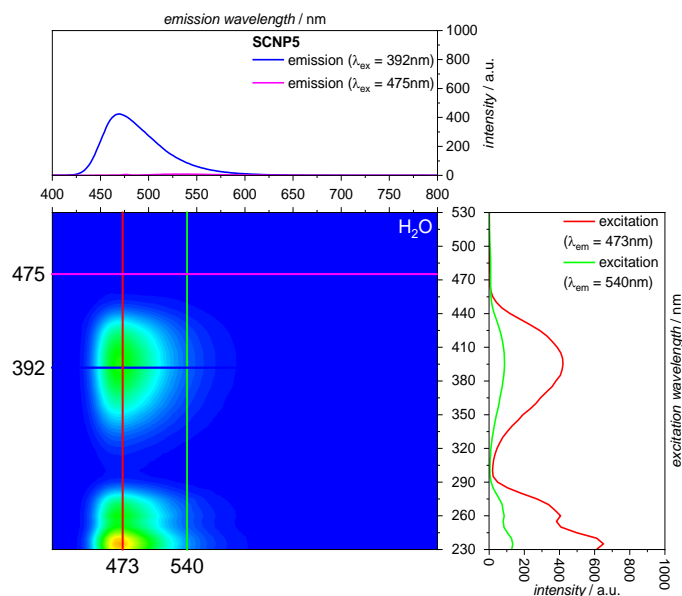


Figure 81: 3D Fluorescence spectrum of SCNP5 in water with emission and excitation slices ($l = 10$ mm, sample concentration around 0.1 % absorption).

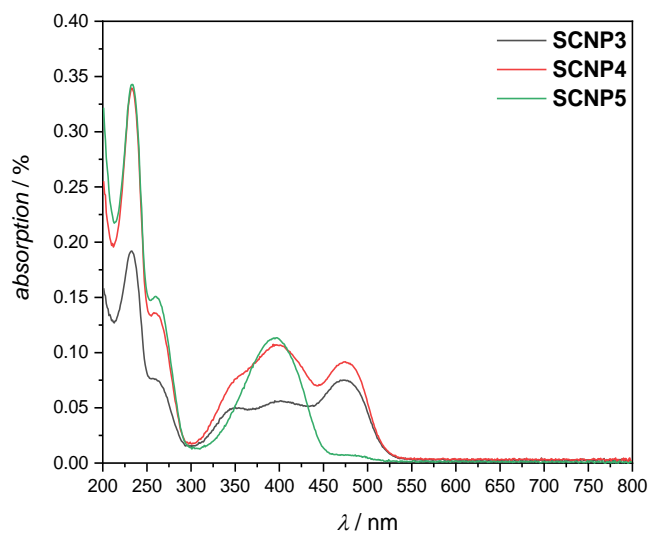


Figure 82: Absorption spectra of SCNP3-5 in water showing different absorptivity in the bimane (390 nm) and NBD (475 nm) region.

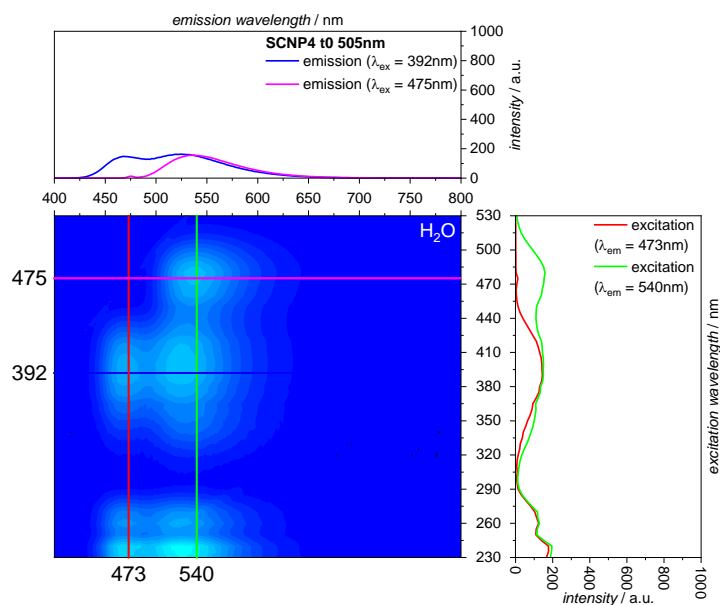


Figure 83: 3D Fluorescence spectrum of **SCNP4** before irradiating with 505 nm in water with emission and excitation slices ($l = 10$ mm, sample concentration around 0.1 % absorption).

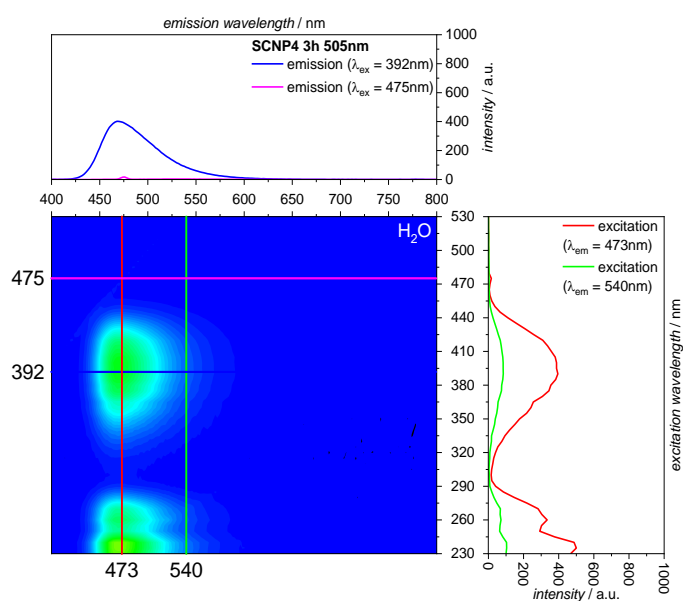


Figure 84: 3D Fluorescence spectrum of **SCNP4** after irradiating with 505 nm for 3 h in water with emission and excitation slices ($l = 10$ mm, sample concentration around 0.1 % absorption).

Appendix F: NMR-Spectra of Small Molecules

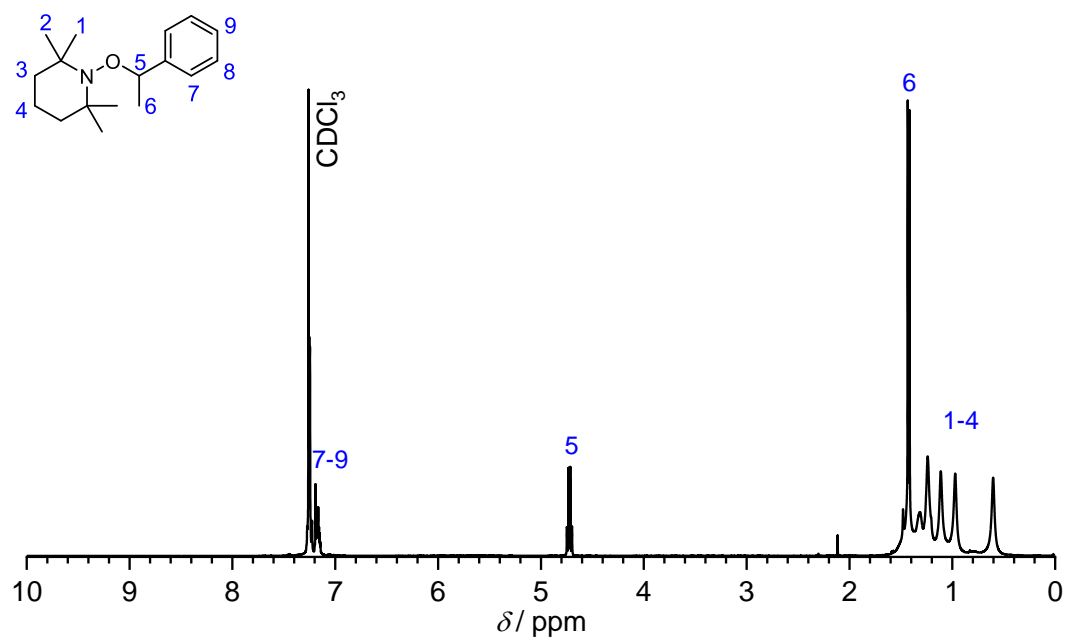


Figure 85: ¹H NMR spectrum of 2,2,6,6-tetramethyl-1-(1-phenylethoxy)piperidine recorded in CDCl₃ and assigned resonances.

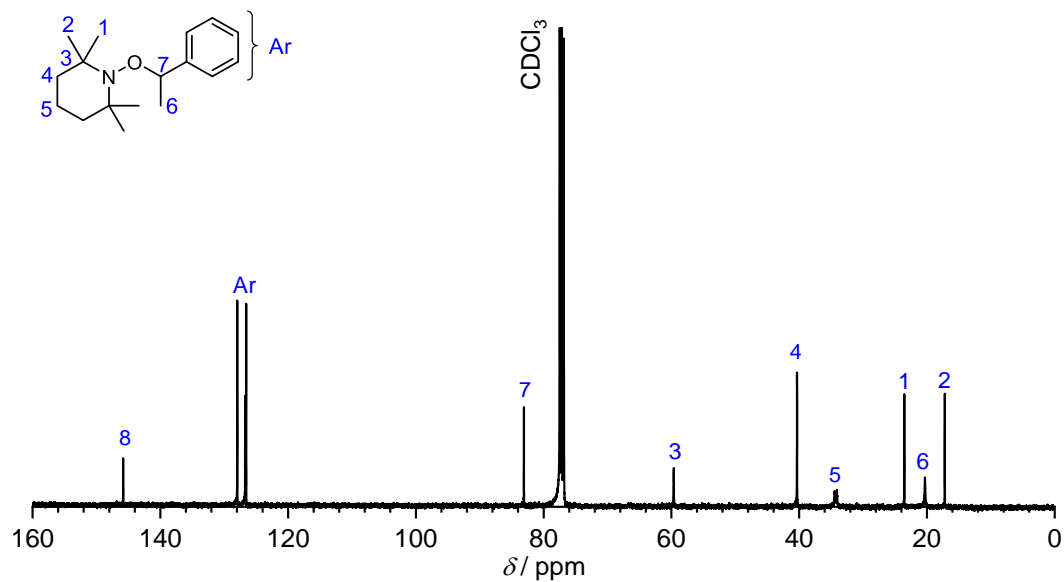


Figure 86: ¹³C{¹H} NMR spectrum of 2,2,6,6-tetramethyl-1-(1-phenylethoxy)piperidine recorded in CDCl₃ and assigned resonances.

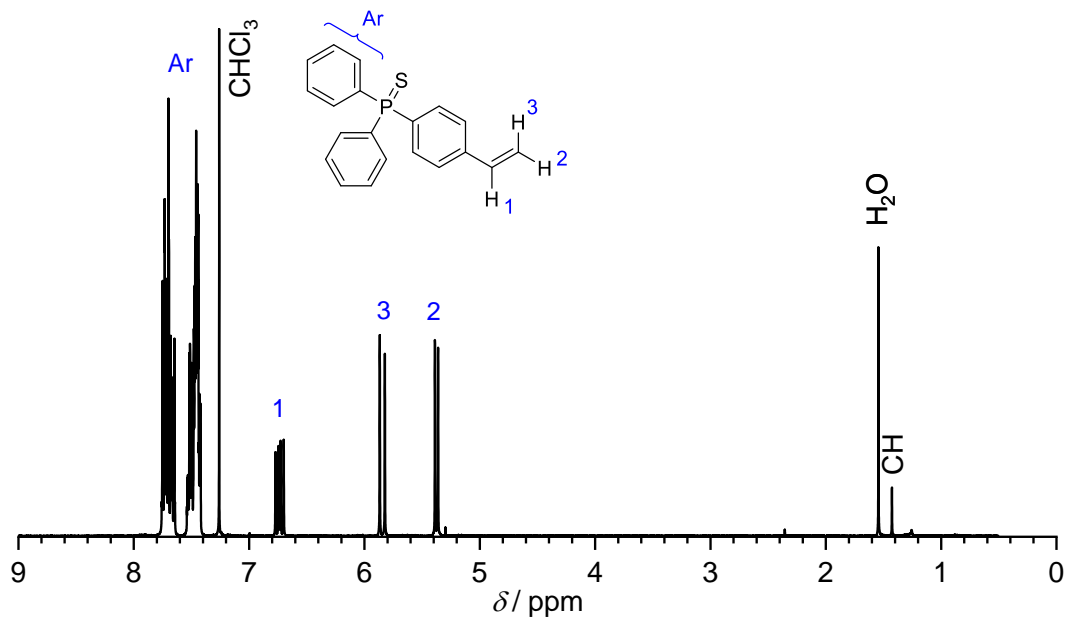


Figure 87: ^1H NMR spectrum of 4-(diphenylphosphino)styrene sulfide ($\text{S}=\text{PPh}_2\text{Sty}$) recorded in CDCl_3 and assigned resonances.

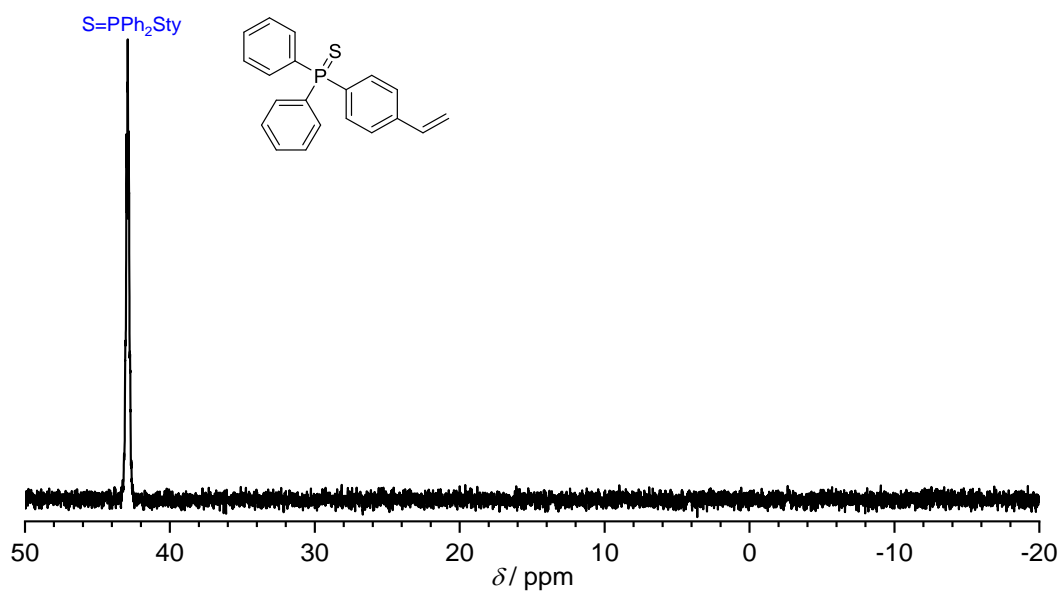


Figure 88: $^{31}\text{P}\{^1\text{H}\}$ NMR spectrum of 4-(diphenylphosphino)styrene sulfide ($\text{S}=\text{PPh}_2\text{Sty}$) recorded in CDCl_3 and assigned resonances.

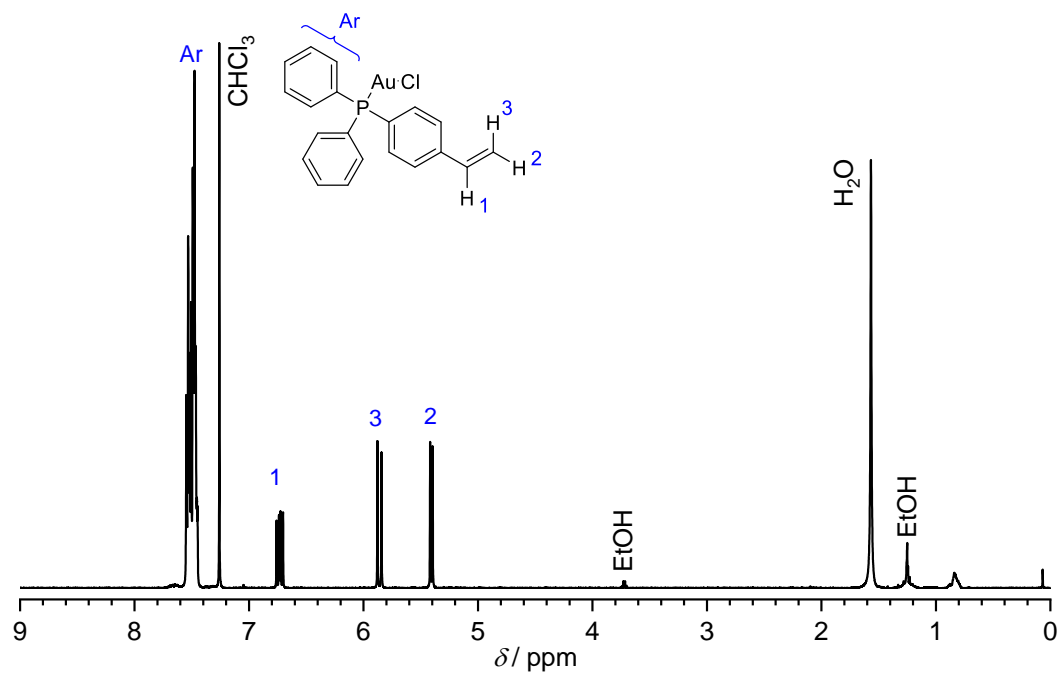


Figure 89: ^1H NMR spectrum of 4-(diphenylphosphino)styrene gold complex (ClAu-PPh₂Sty) recorded in CDCl₃ and assigned resonances.

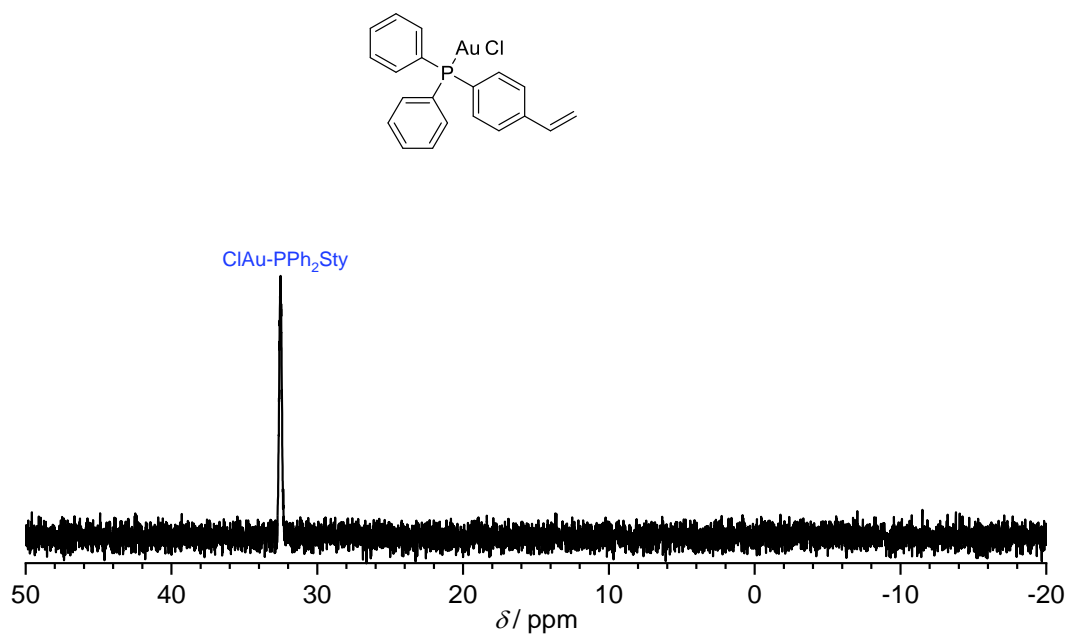


Figure 90: $^{31}\text{P}\{^1\text{H}\}$ NMR spectrum of 4-(diphenylphosphino)styrene gold complex (ClAu-PPh₂Sty) recorded in CDCl₃ and assigned resonances.

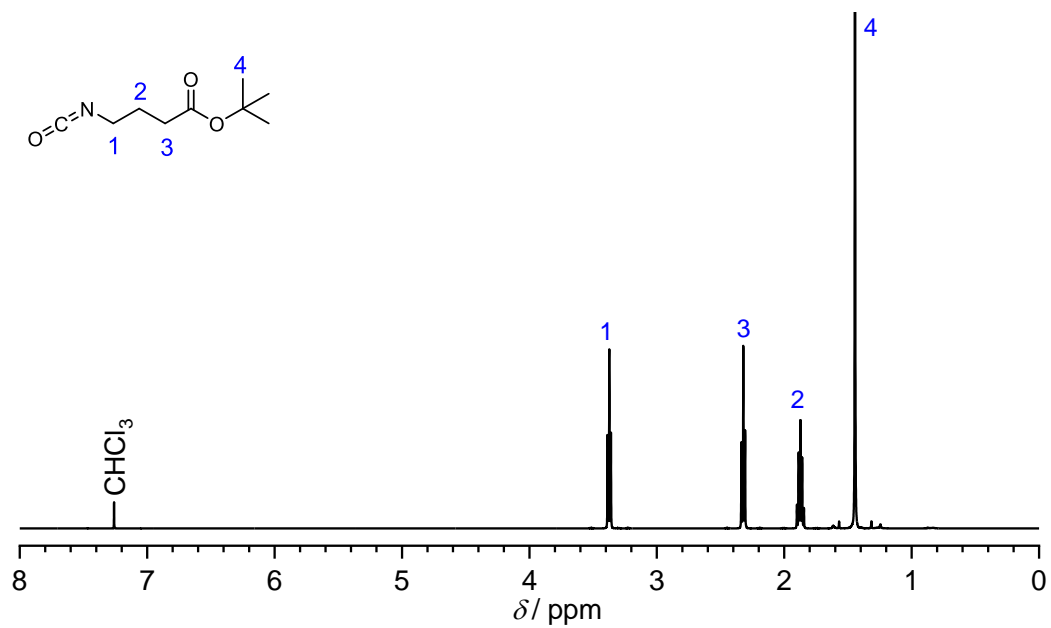


Figure 91: ^1H NMR spectrum of tert-butyl 4-isocyanatobutanoate recorded in CDCl_3 and assigned resonances.

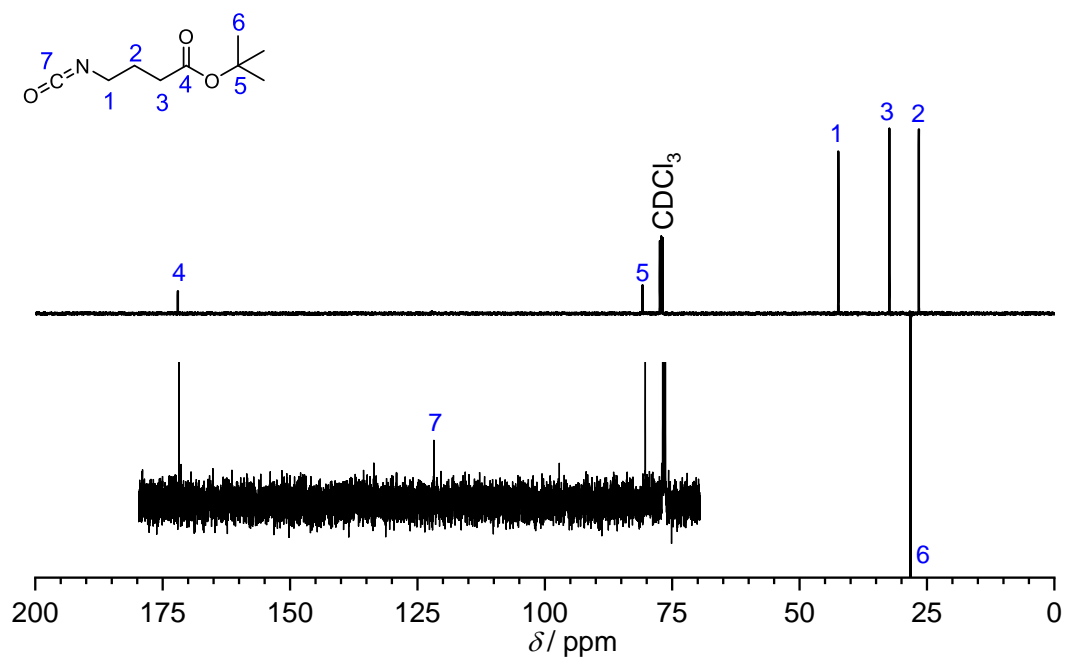


Figure 92: ^{13}C -APT NMR spectrum of tert-butyl 4-isocyanatobutanoate recorded in CDCl_3 and assigned resonances.

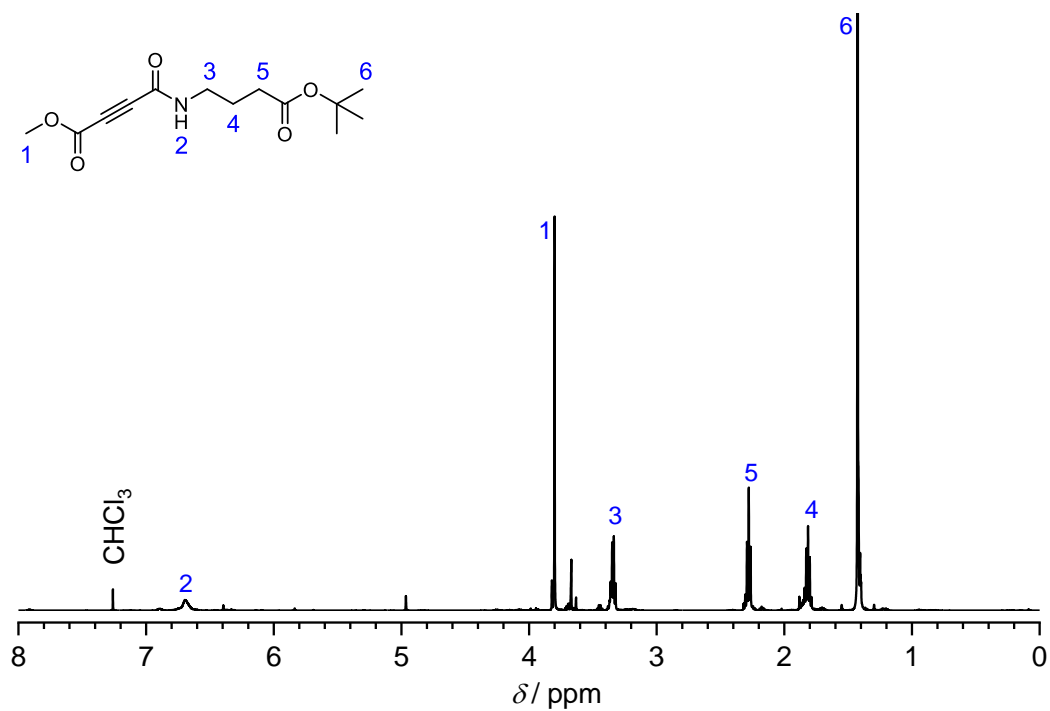


Figure 93: ^1H NMR spectrum of methyl 4-((4-(tert-butoxy)-4-oxobutyl)amino)-4-oxobut-2-ynoate (2) in CDCl_3 and assigned resonances.

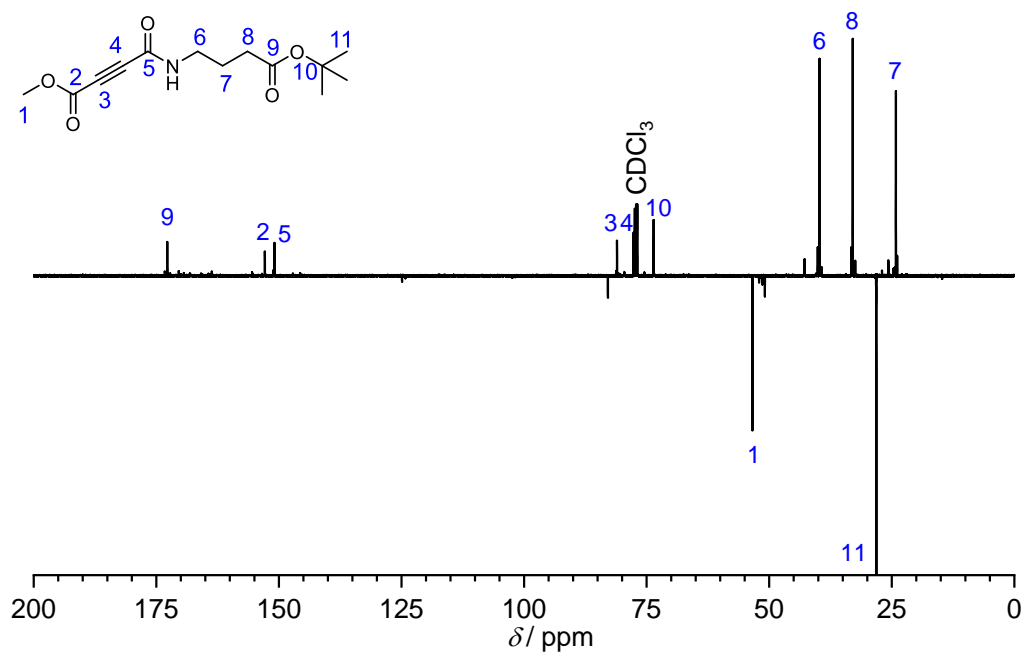


Figure 94: ^{13}C -APT NMR spectrum of methyl 4-((4-(tert-butoxy)-4-oxobutyl)amino)-4-oxobut-2-ynoate (2) recorded in CDCl_3 and assigned resonances.

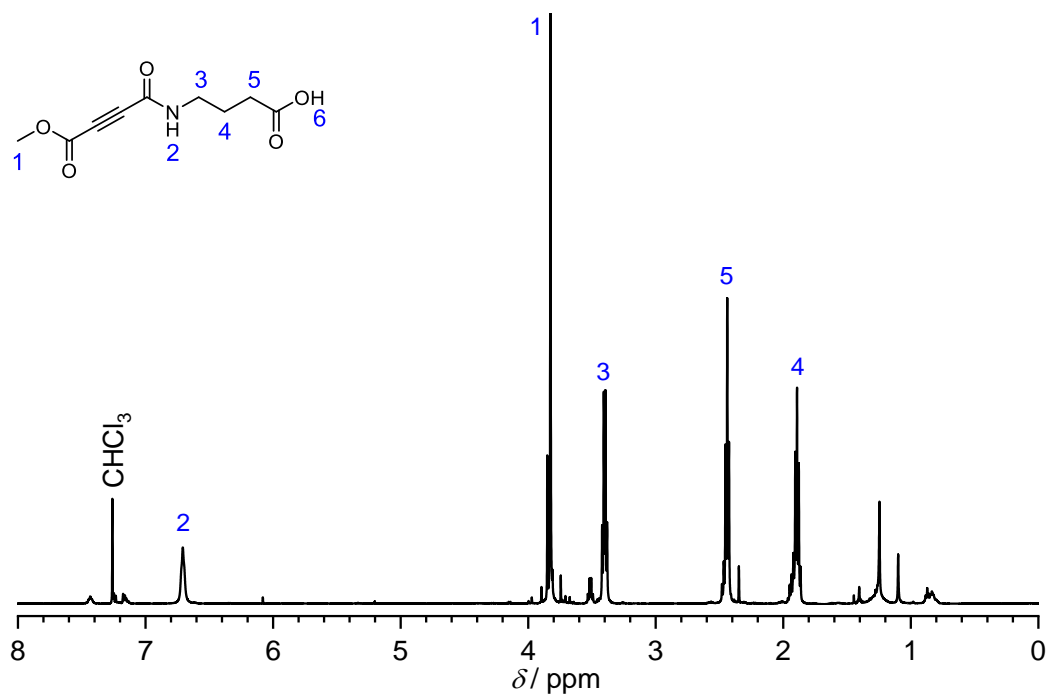


Figure 95: ^1H NMR spectrum of 4-(4-methoxy-4-oxobut-2-ynamido)butanoic acid recorded in CDCl_3 and assigned resonances.

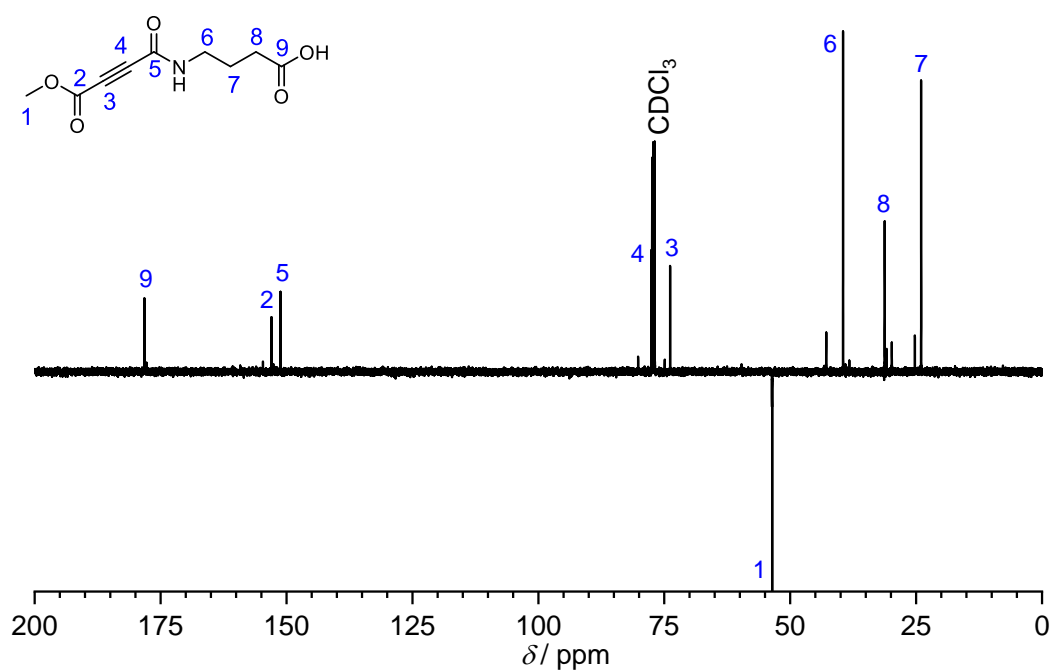


Figure 96: ^{13}C -APT NMR spectrum of 4-(4-methoxy-4-oxobut-2-ynamido)butanoic acid recorded in CDCl_3 and assigned resonances.

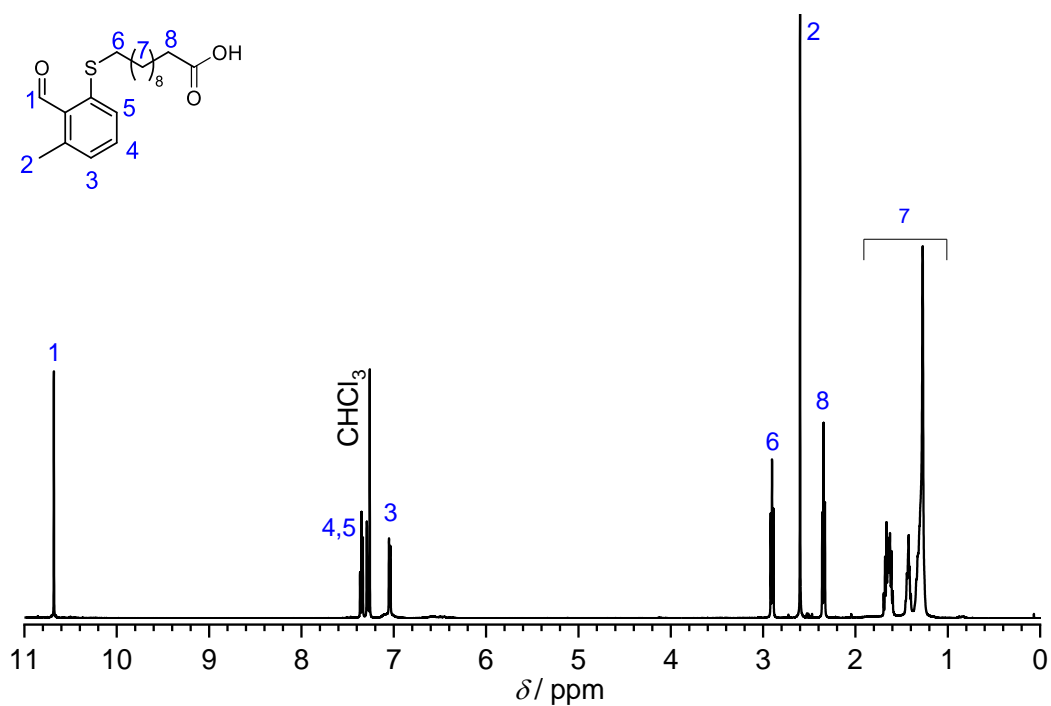


Figure 97: ^1H NMR spectrum of 4-(4-methoxy-4-oxobut-2-ynamido)butanoic acid recorded in CDCl_3 and assigned resonances.

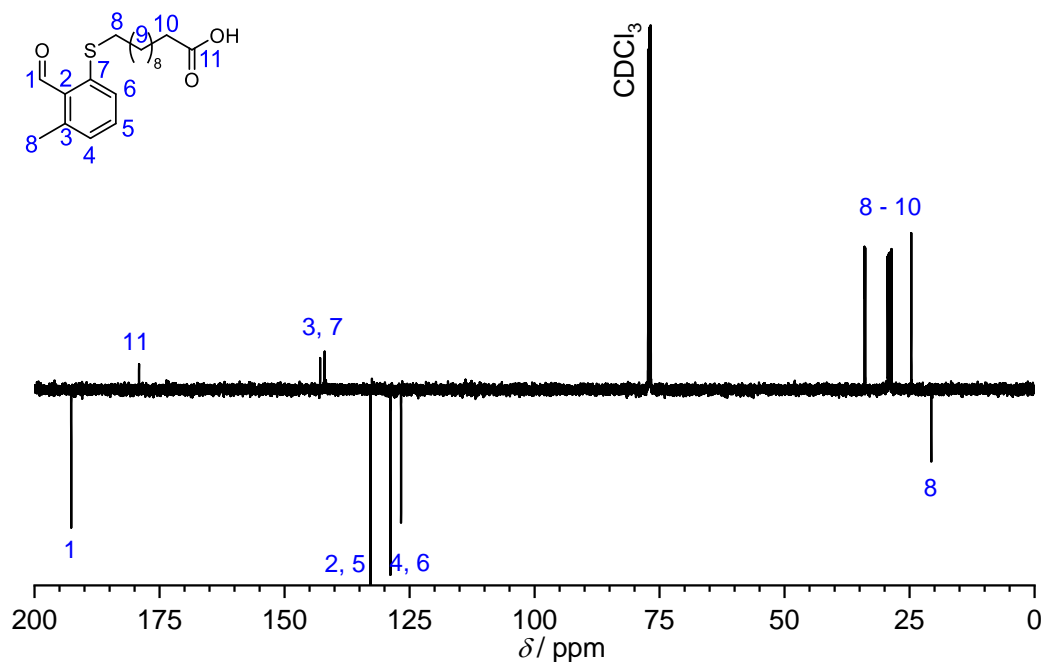


Figure 98: ^{13}C -APT NMR spectrum of 4-(4-methoxy-4-oxobut-2-ynamido)butanoic acid recorded in CDCl_3 and assigned resonances.

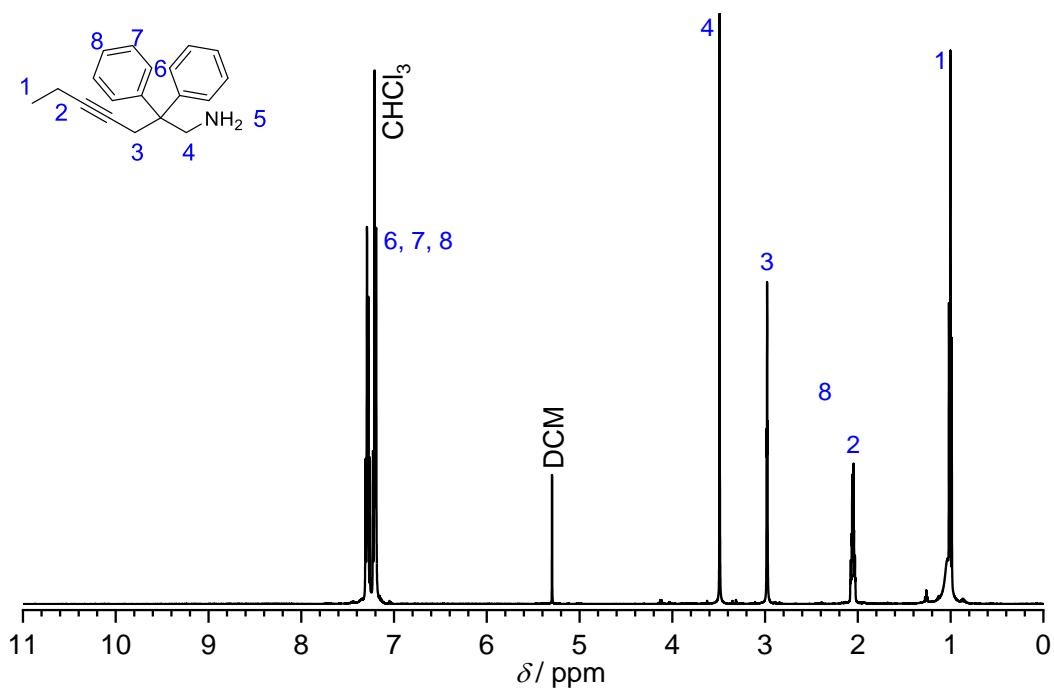


Figure 99: ¹H NMR spectrum of 2,2-diphenylhept-4-yn-1-amine recorded in CDCl₃ and assigned resonances.

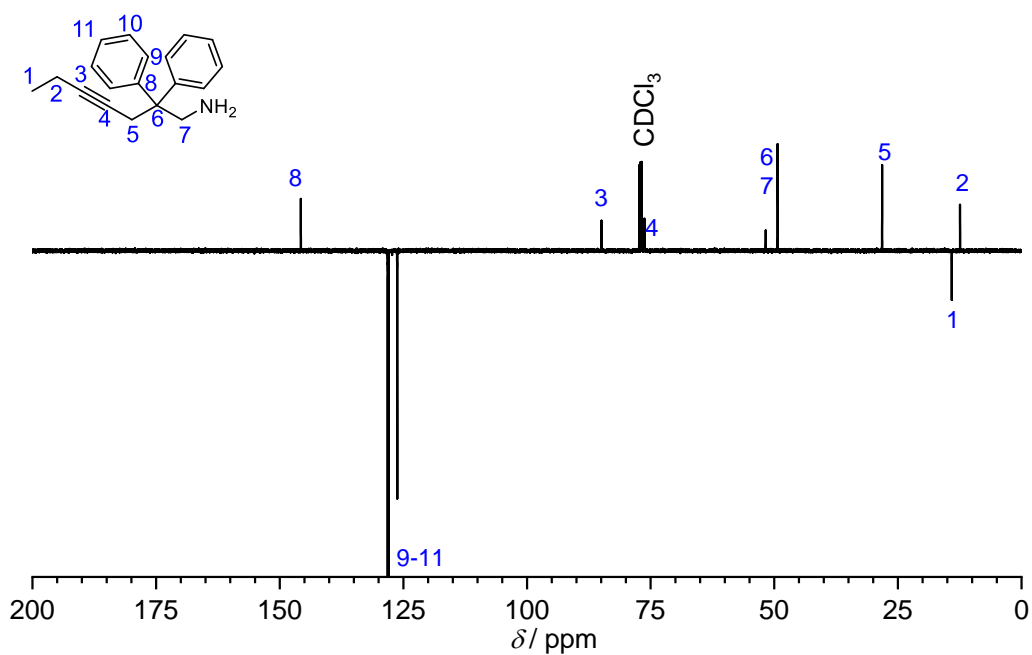


Figure 100: ¹³C-APT NMR spectrum of 2,2-diphenylhept-4-yn-1-amine recorded in CDCl₃ and assigned resonances.

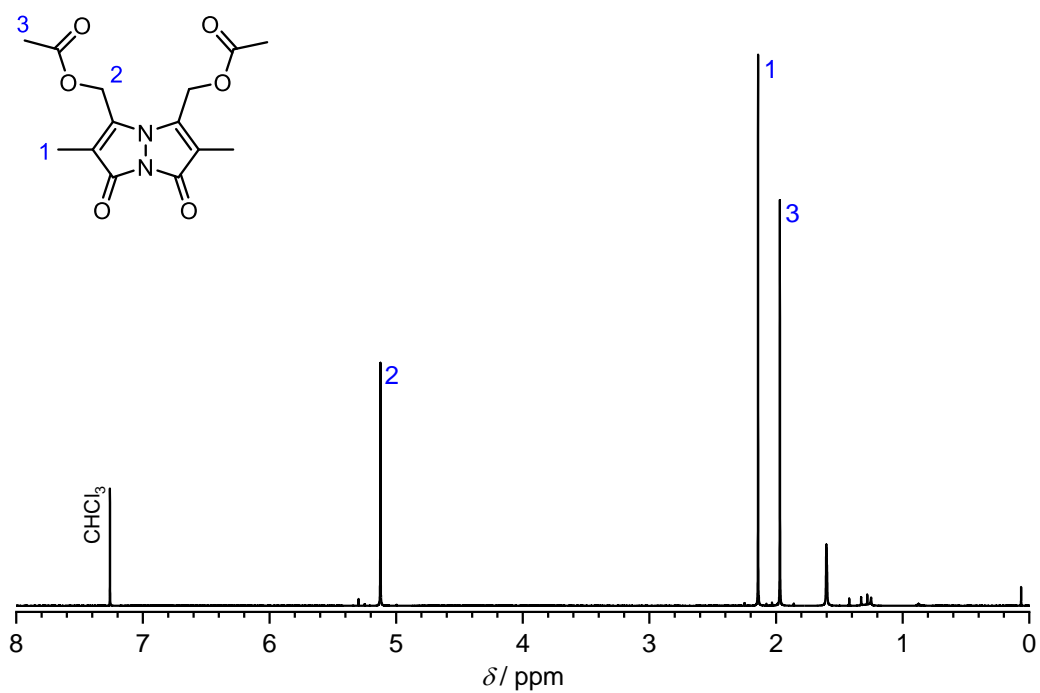


Figure 101: ^1H NMR spectrum of **8** recorded in CDCl_3 and assigned resonances.

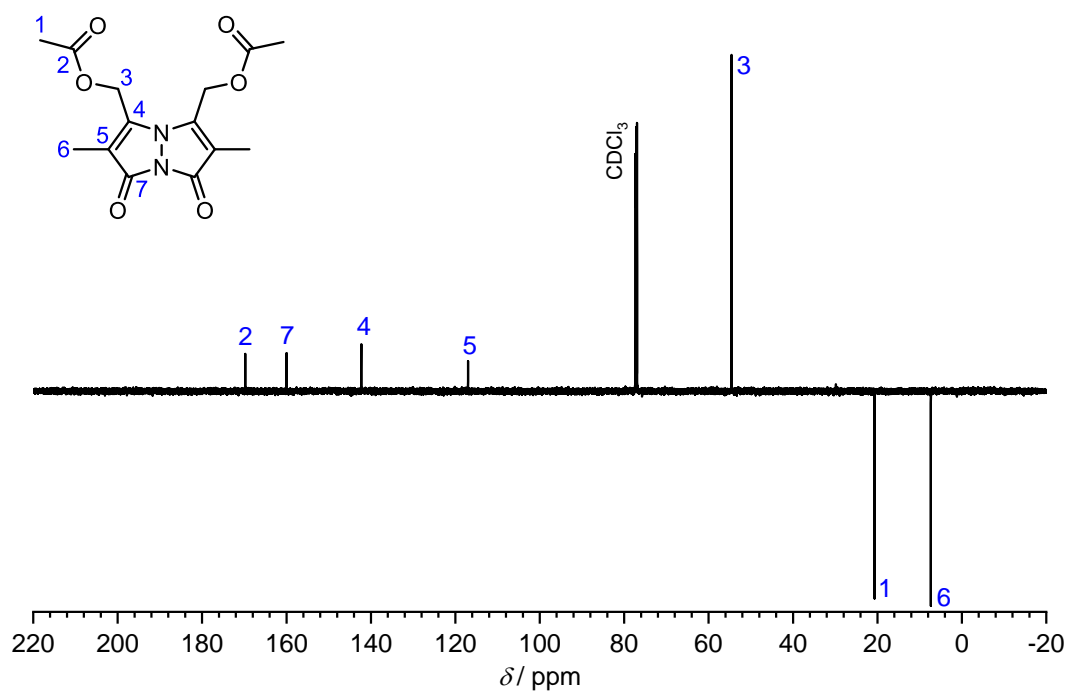


Figure 102: ^{13}C DEPTQ135 NMR spectrum of **8** recorded in CDCl_3 and assigned resonances.

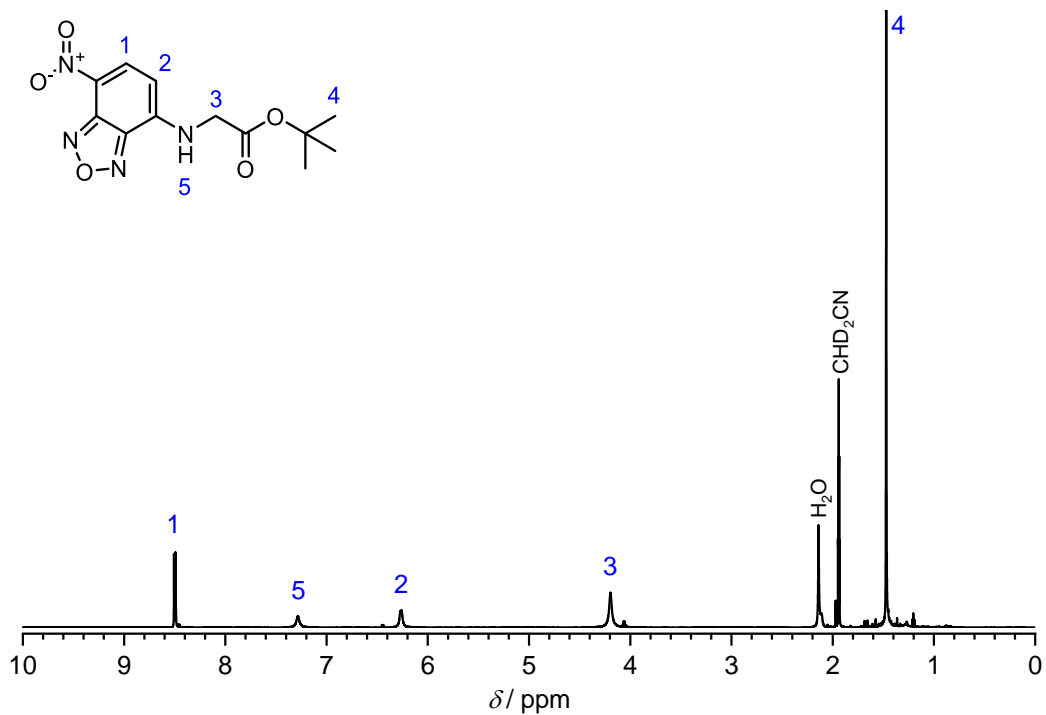


Figure 103: ^1H NMR spectrum of *tert*-butyl (7-nitrobenzo[*c*][1,2,5]oxadiazol-4-yl)glycinate (NBD-Gly-*tert*) recorded in CD_3CN and assigned resonances.

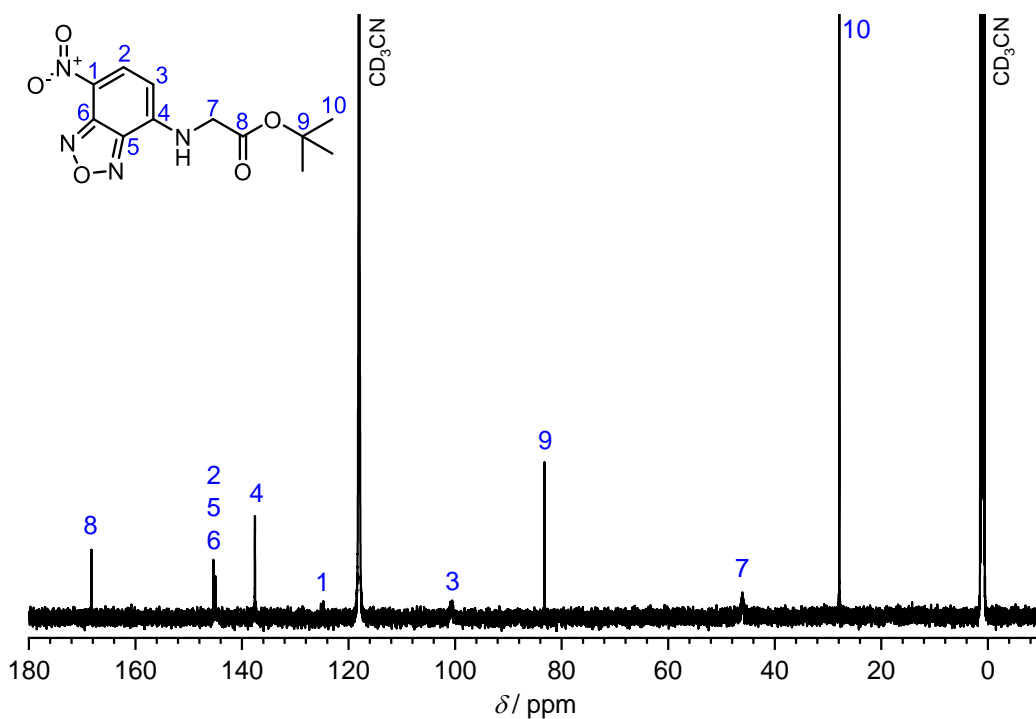


Figure 104: $^{13}\text{C}\{^1\text{H}\}$ NMR spectrum of *tert*-butyl (7-nitrobenzo[*c*][1,2,5]oxadiazol-4-yl)glycinate (NBD-Gly-*tert*) recorded in CD_3CN and assigned resonances.

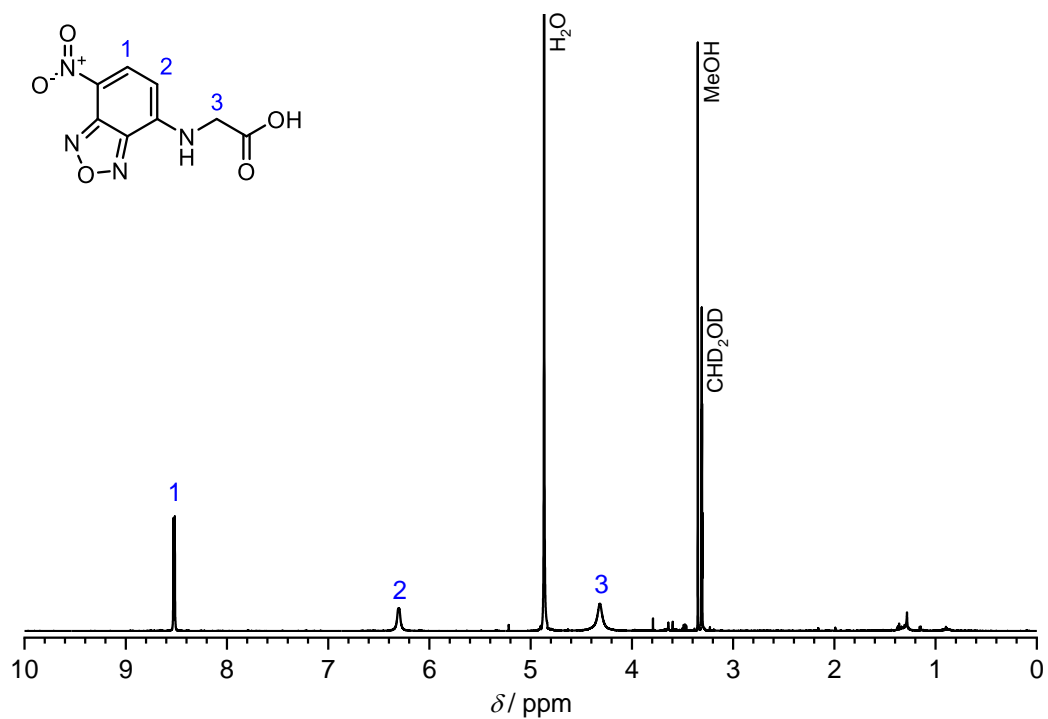


Figure 105: ^1H NMR spectrum of **11** recorded in CD_3OD and assigned resonances.

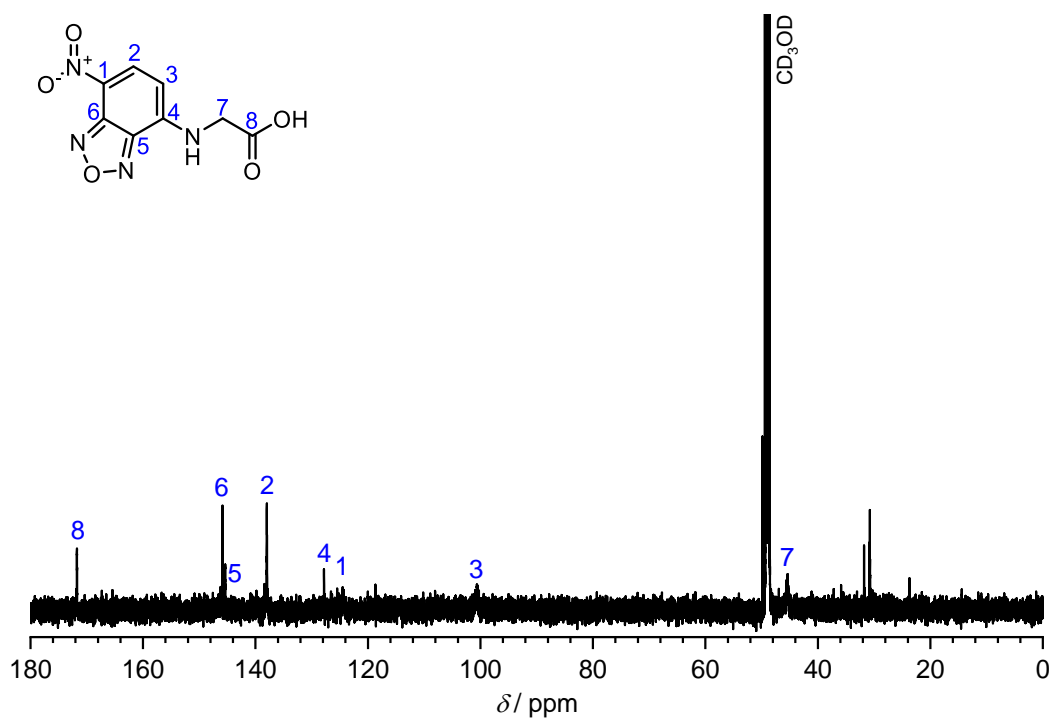


Figure 106: $^{13}\text{C}\{^1\text{H}\}$ NMR spectrum of **11** recorded in CD_3OD and assigned resonances.

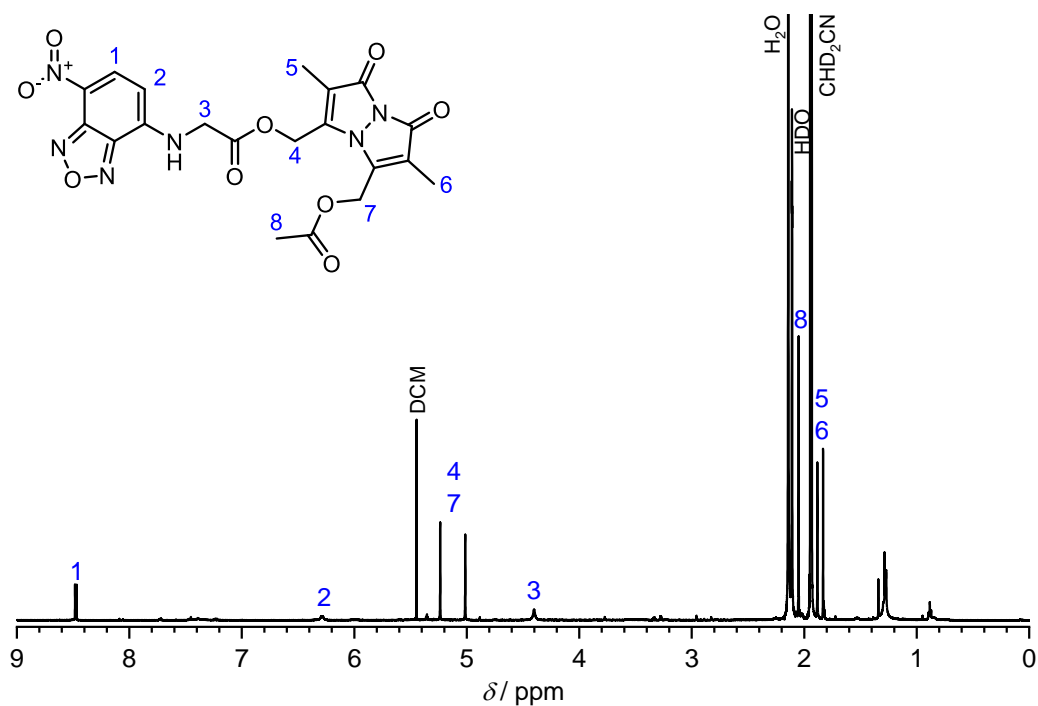


Figure 107: ^1H NMR spectrum of **10** recorded in CD_3CN and assigned resonances. The resonance at 1.29 ppm results from high boiling alkanes as part of impurity of cyclohexane and are difficult to avoid for small scale reactions. We assume that high boiling alkanes do not interfere with the photochemical reactions.

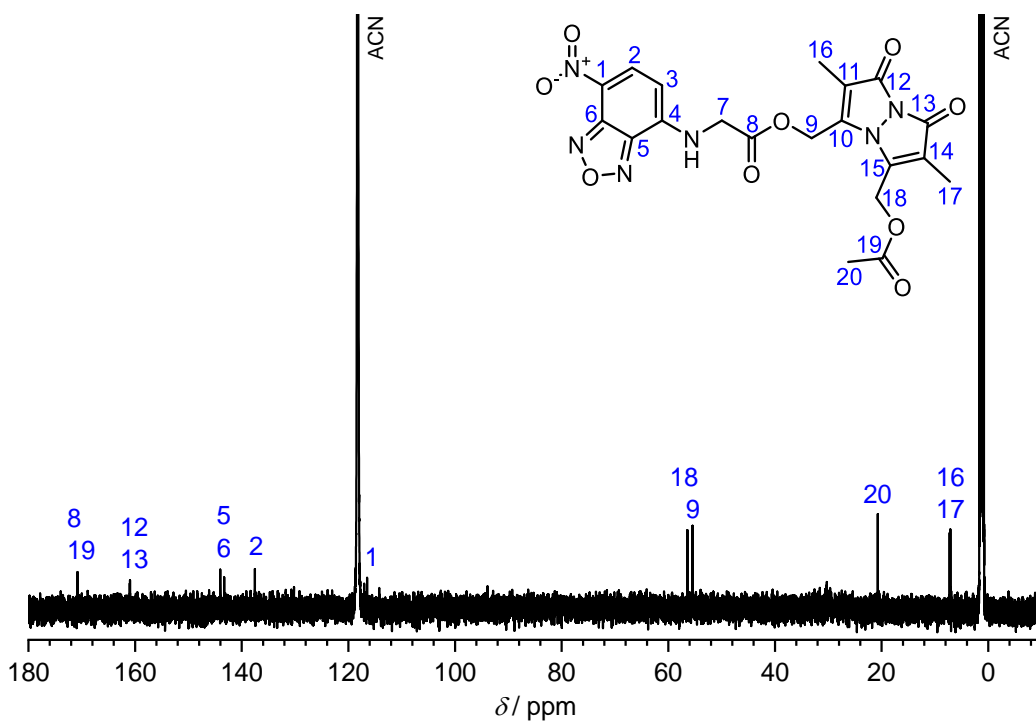


Figure 108: $^{13}\text{C}\{^1\text{H}\}$ NMR spectrum of **10** recorded in CD_3CN and assigned resonances.

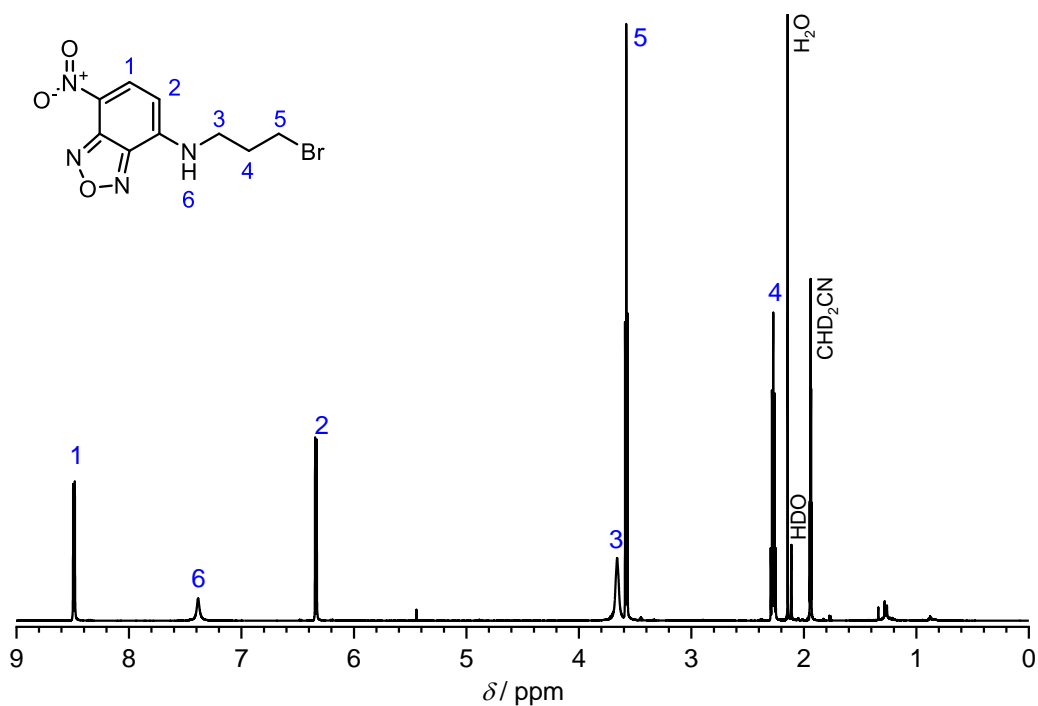


Figure 109: ^1H NMR spectrum of **12** recorded in CD_3CN and assigned resonances.

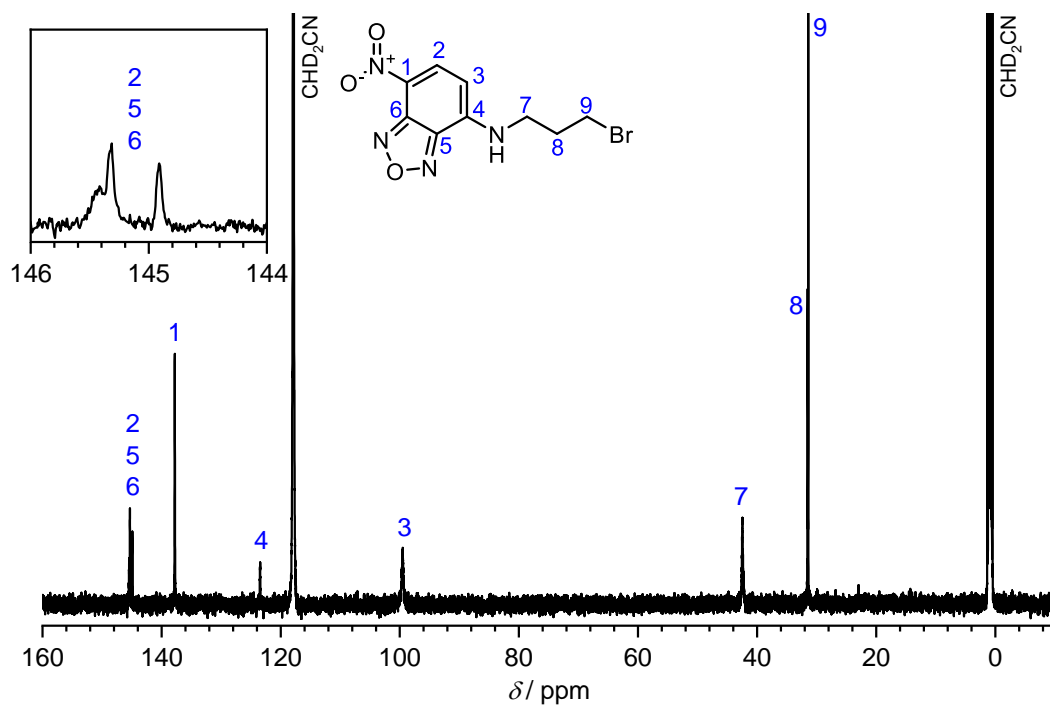


Figure 110: $^{13}\text{C}\{^1\text{H}\}$ NMR spectrum of **12** recorded in CD_3CN and assigned resonances.

Appendix G: NMR-Spectra of polymers

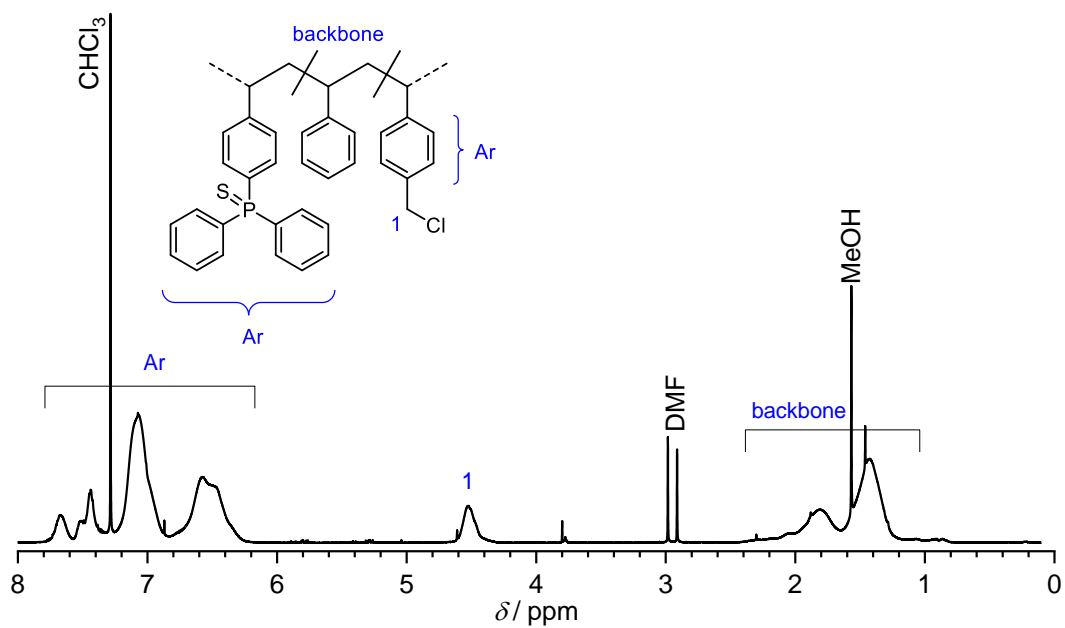


Figure 111: ^1H NMR spectrum of poly(Sty-co-CMS-co-S=PPh₂Sty) recorded in CDCl₃ and assigned resonances (Step 1, P1).

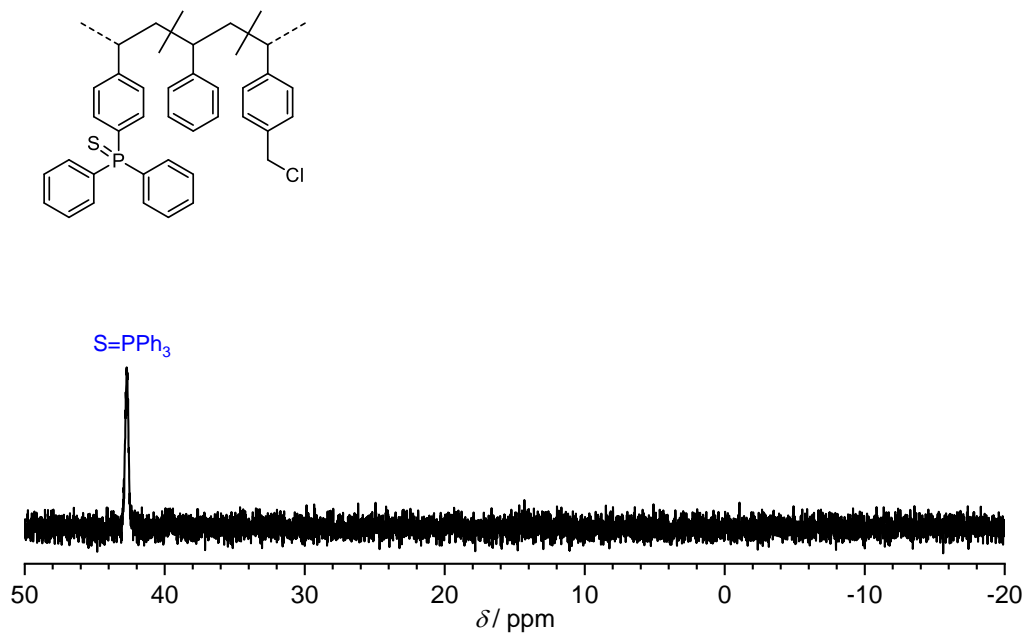


Figure 112: $^{31}\text{P}\{^1\text{H}\}$ NMR spectrum of poly(Sty-co-CMS-co-S=PPh₂Sty) recorded in CDCl₃ and assigned resonances (Step 1, P1).

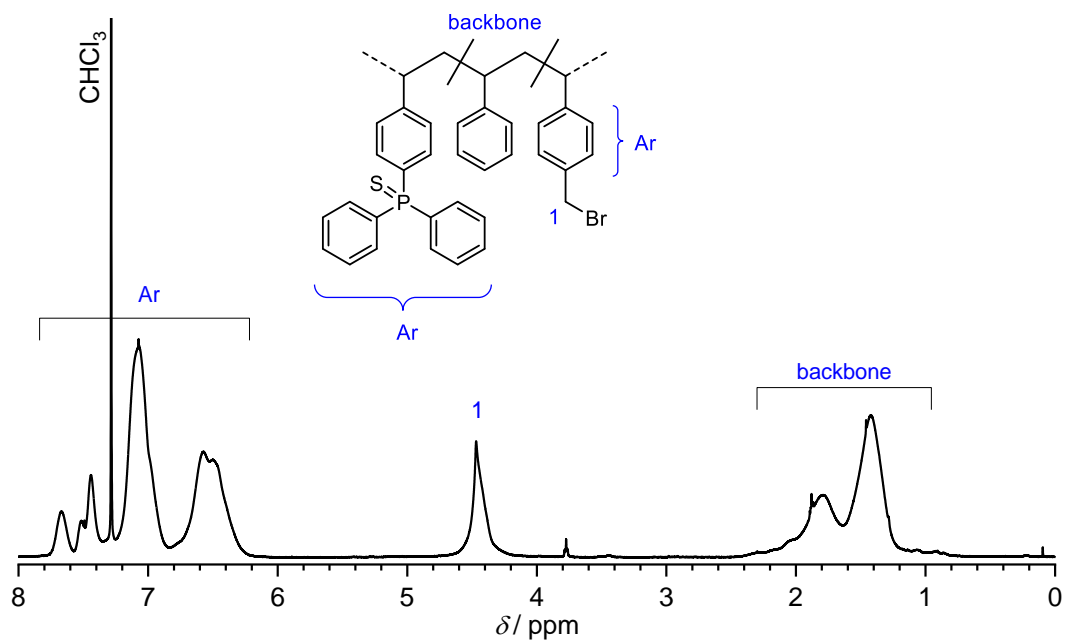


Figure 113: ^1H NMR spectrum of poly(Sty-co-BMS-co-S=PPh₂Sty) recorded in CDCl₃ and assigned resonances (Step 2, P2).

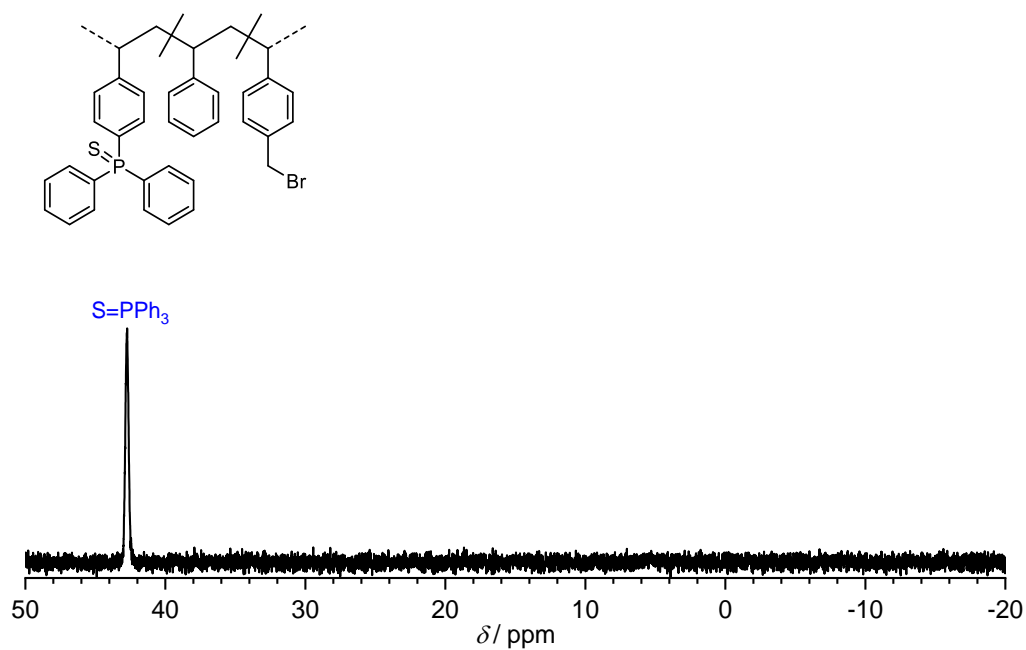


Figure 114: $^{31}\text{P}\{^1\text{H}\}$ NMR spectrum of poly(Sty-co-BMS-co-S=PPh₂Sty) recorded in CDCl₃ and assigned resonances (Step 2, P2).

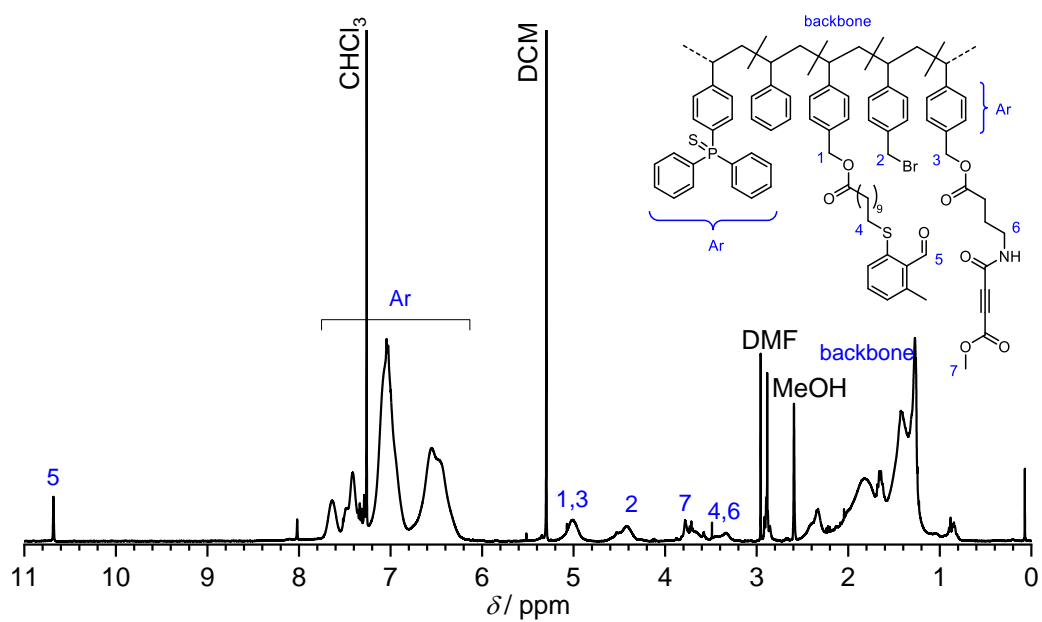


Figure 115: ¹H NMR spectrum of the post-functionalized poly(Sty-co-BMS-co-S=PPh₂Sty) recorded in CDCl₃ and assigned resonances (Step 3, **P3**).

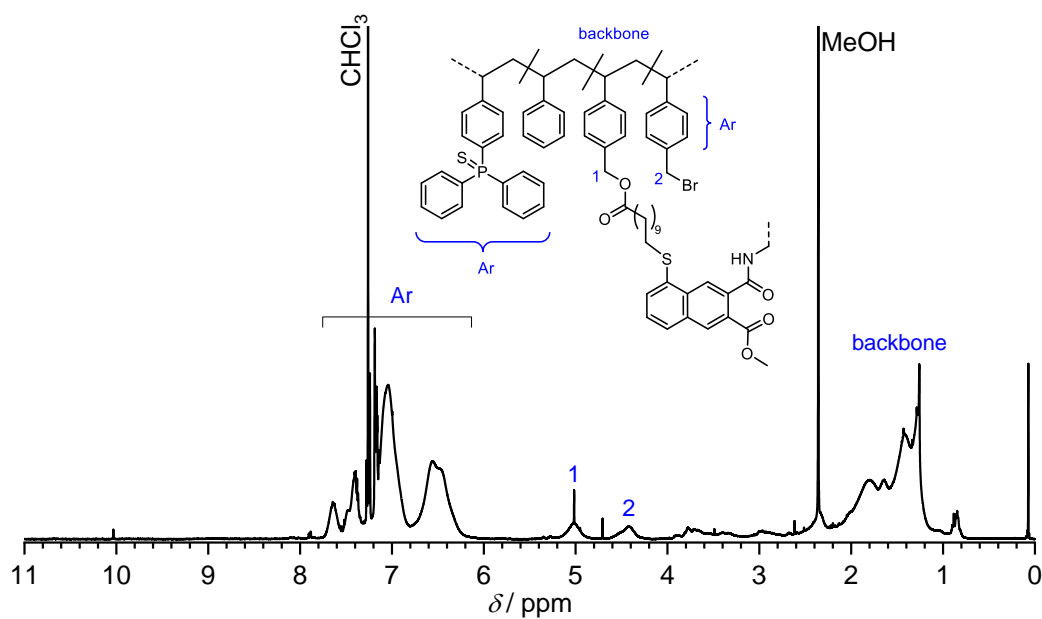


Figure 116: ¹H NMR spectrum of the cross-linked poly(Sty-co-BMS-co-S=PPh₂Sty) recorded in CDCl₃ and assigned resonances (Step 4, **SCNP1**).

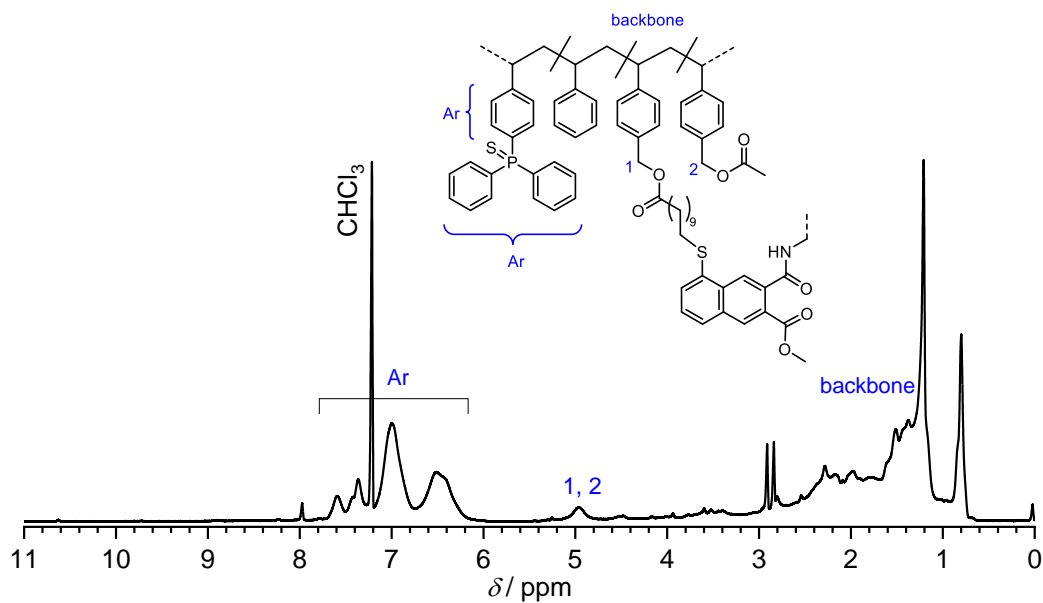


Figure 117: ^1H NMR spectrum of the cross-linked and protected poly(Sty-co-BMS-co-S=PPh₂Sty) recorded in CDCl₃ and assigned resonances (Step 5).

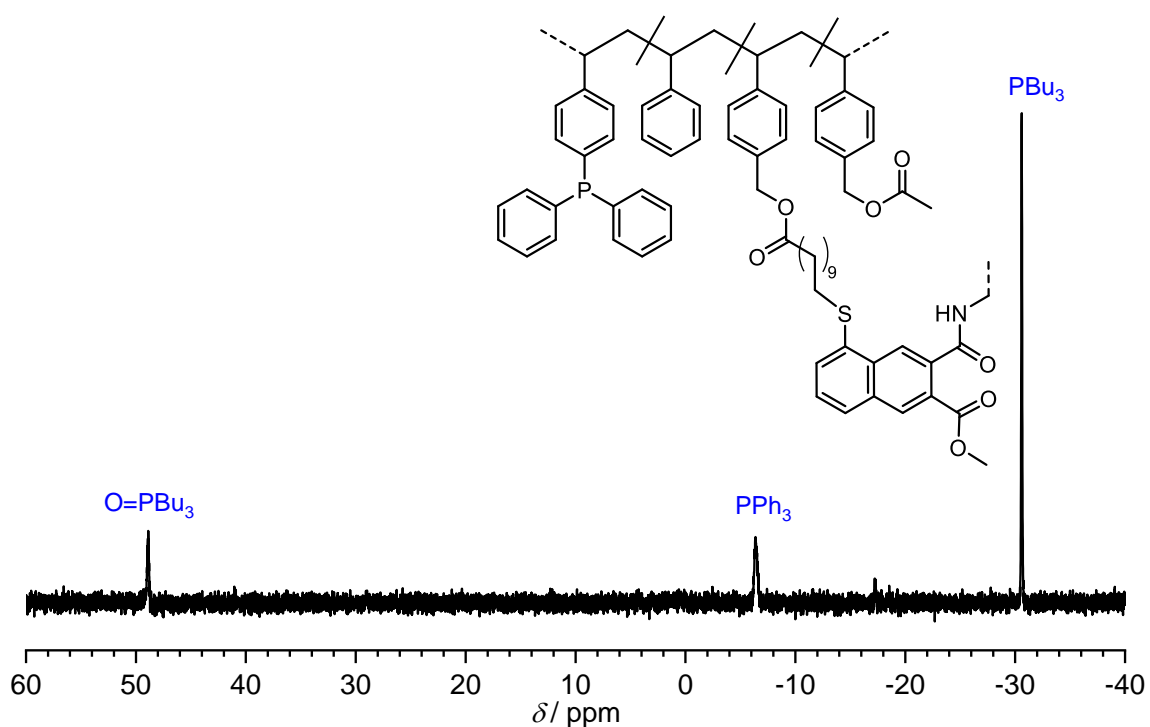


Figure 118: $^{31}\text{P}\{^1\text{H}\}$ NMR spectrum of the deprotected SCNPs recorded in CDCl₃ and assigned resonances (Step 6).

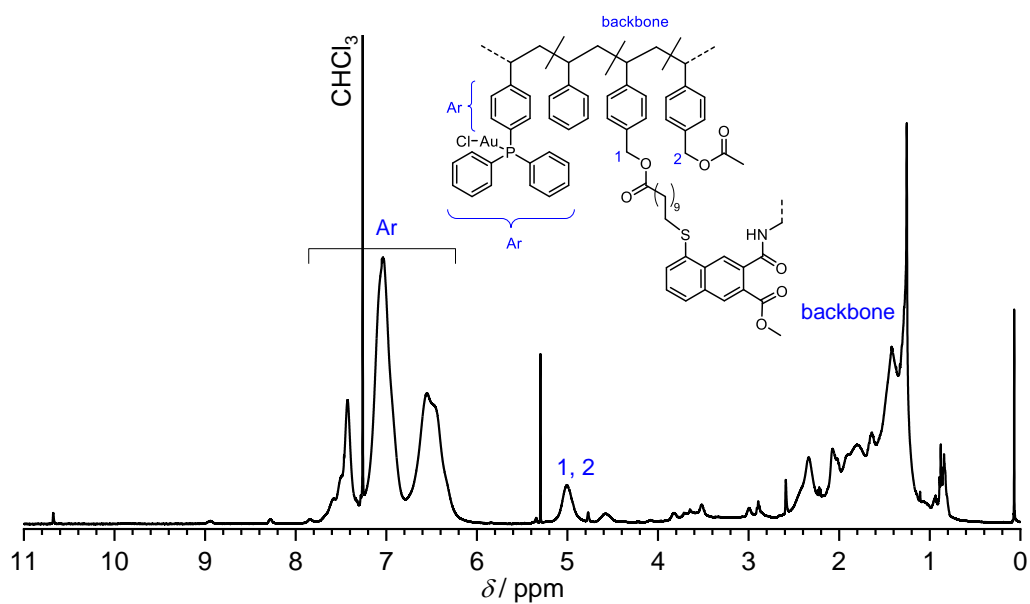


Figure 119: ^1H NMR spectrum of the SCNPAuCl recorded in CDCl_3 and assigned resonances (Step 6, SCNPAuCl).

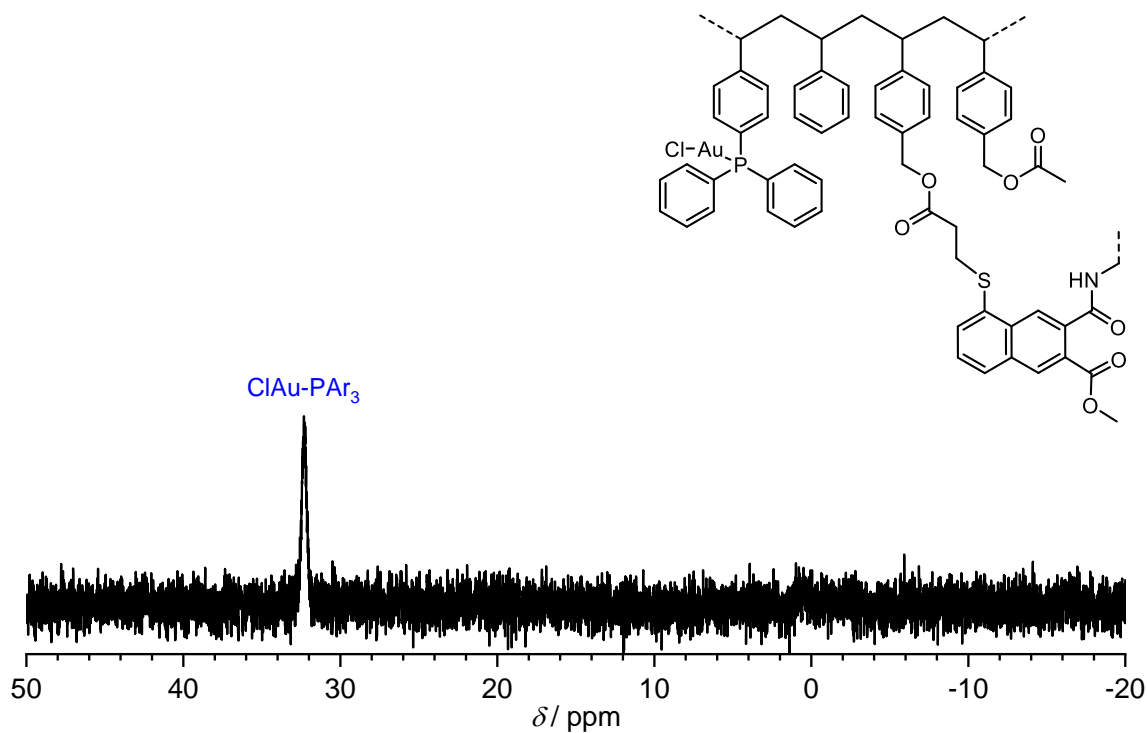


Figure 120: $^{31}\text{P}\{^1\text{H}\}$ NMR spectrum of SCNPAuCl recorded in CDCl_3 and assigned resonances (Step 6, SCNPAuCl).

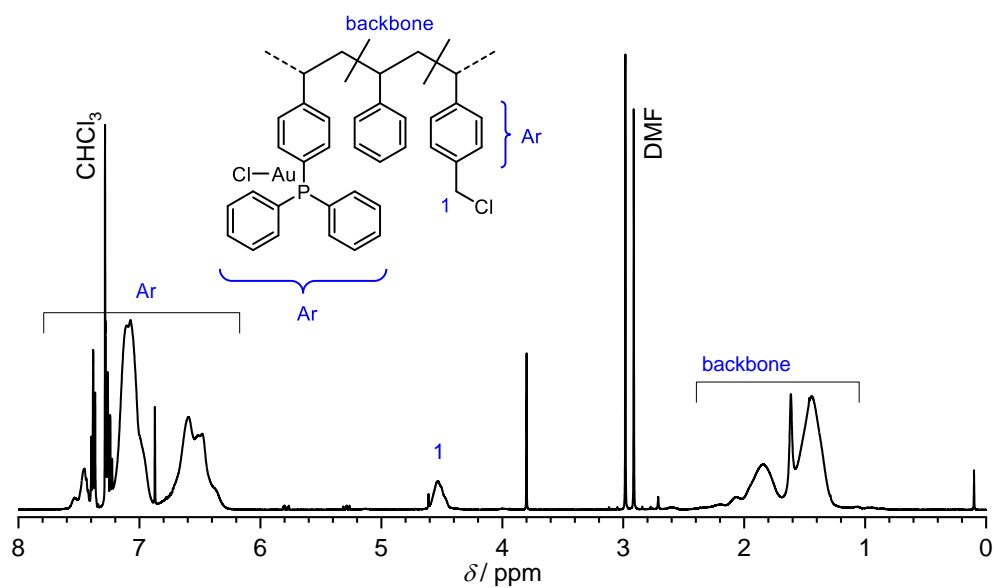


Figure 121: ^1H NMR spectrum of poly(Sty-co-CMS-co-AuCl-PPh₂Sty) recorded in CDCl_3 and assigned resonances (**P4**).

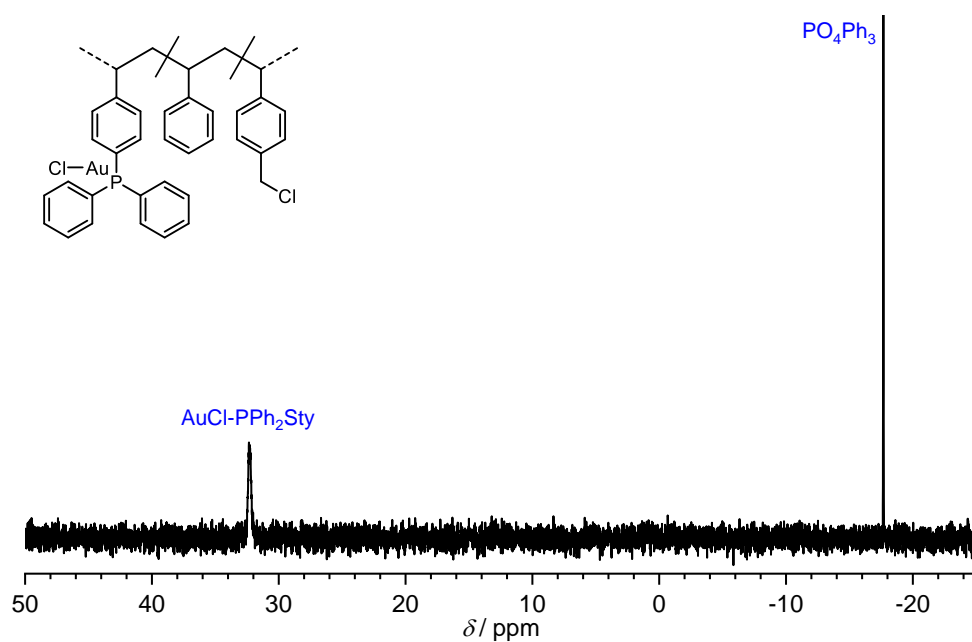


Figure 122: $^{31}\text{P}\{^1\text{H}\}$ NMR spectrum of poly(Sty-co-CMS-co-AuCl-PPh₂Sty) recorded in CDCl_3 and assigned resonances (**P4**).

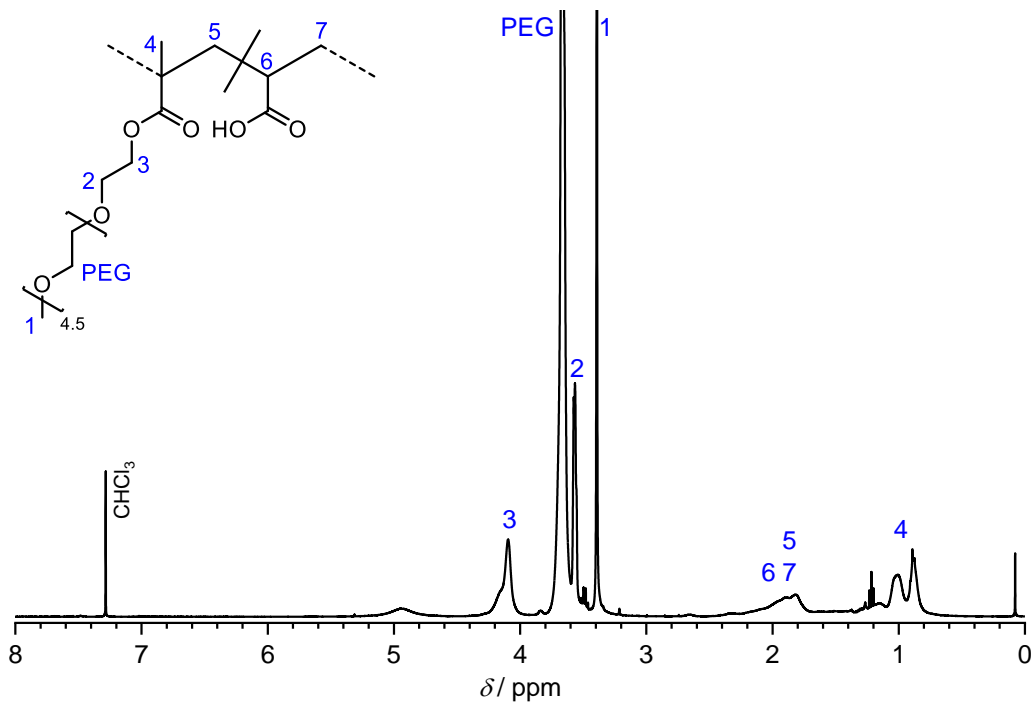


Figure 123: ¹H NMR spectrum of end group modification poly(MPEGMA-co-AA) recorded in CDCl₃ and assigned resonances (**P5**).

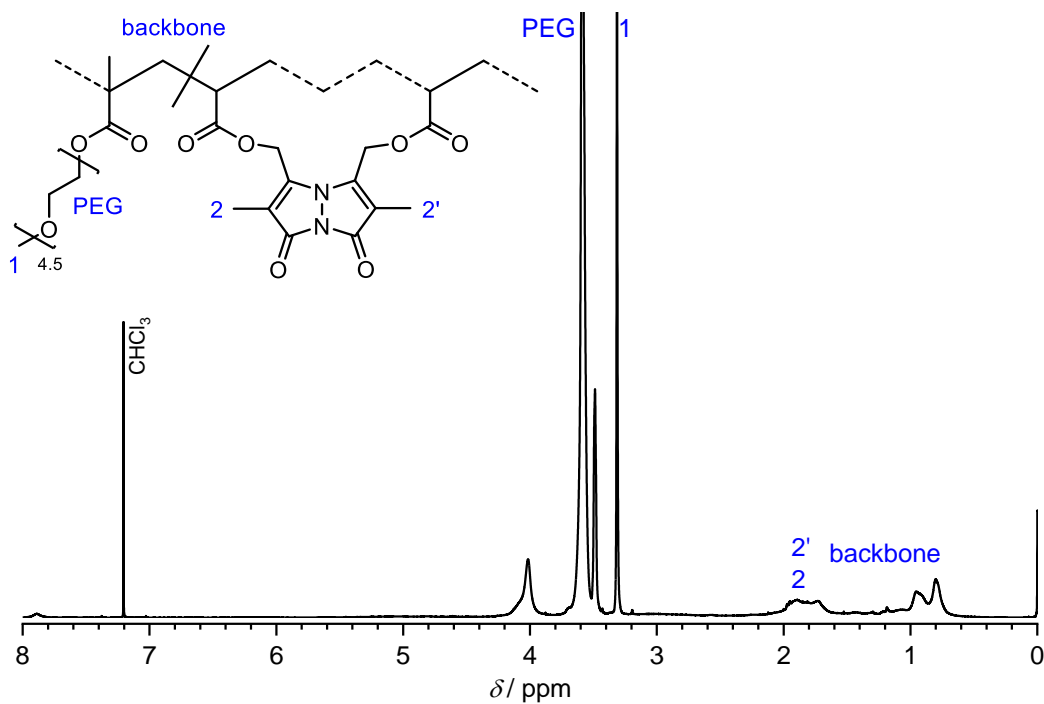


Figure 124: ¹H NMR spectrum bimane cross-linked SCNP2 recorded in CDCl₃ and assigned resonances (**SCNP2**).

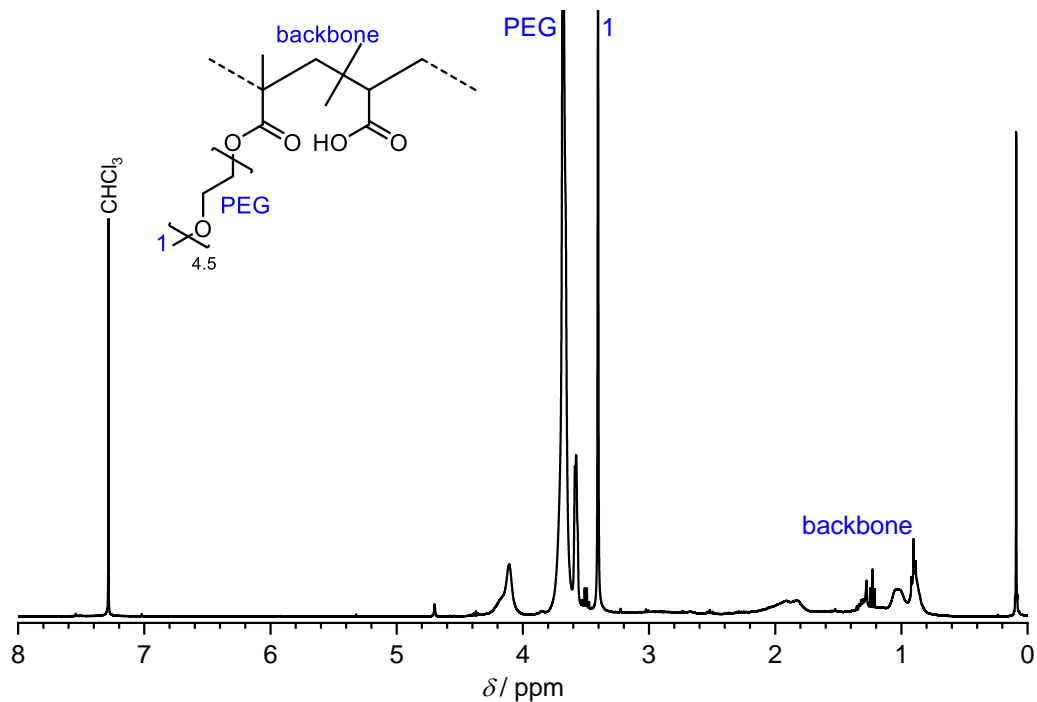


Figure 125: ¹H NMR spectrum of unfolded poly(MPEGMA-co-AA) recorded in CDCl₃ and assigned resonances (**P5'**).

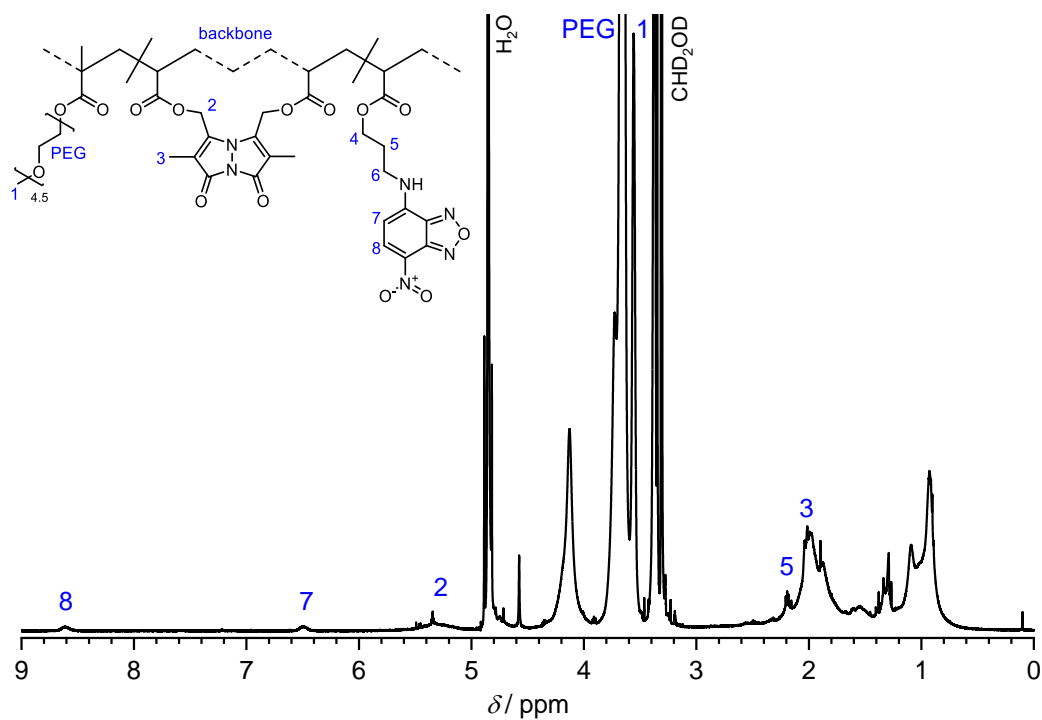


Figure 126: ¹H NMR spectrum of NBD post-functionalized and bimane cross-linked poly(MPEGMA-co-AA) recorded in CD₃OD and assigned resonances (**SCNP3**).

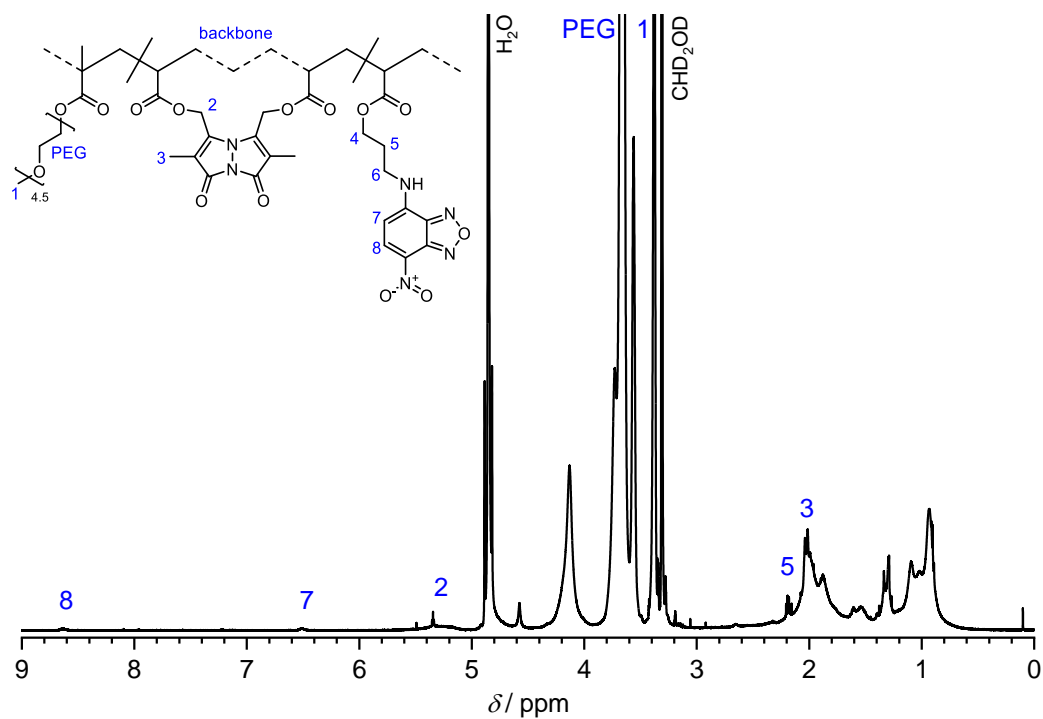


Figure 127: ^1H NMR spectrum of NBD post-functionalized and bimane cross-linked poly(MPEGMA-co-AA) recorded in CD_3OD and assigned resonances (**SCNP4**).

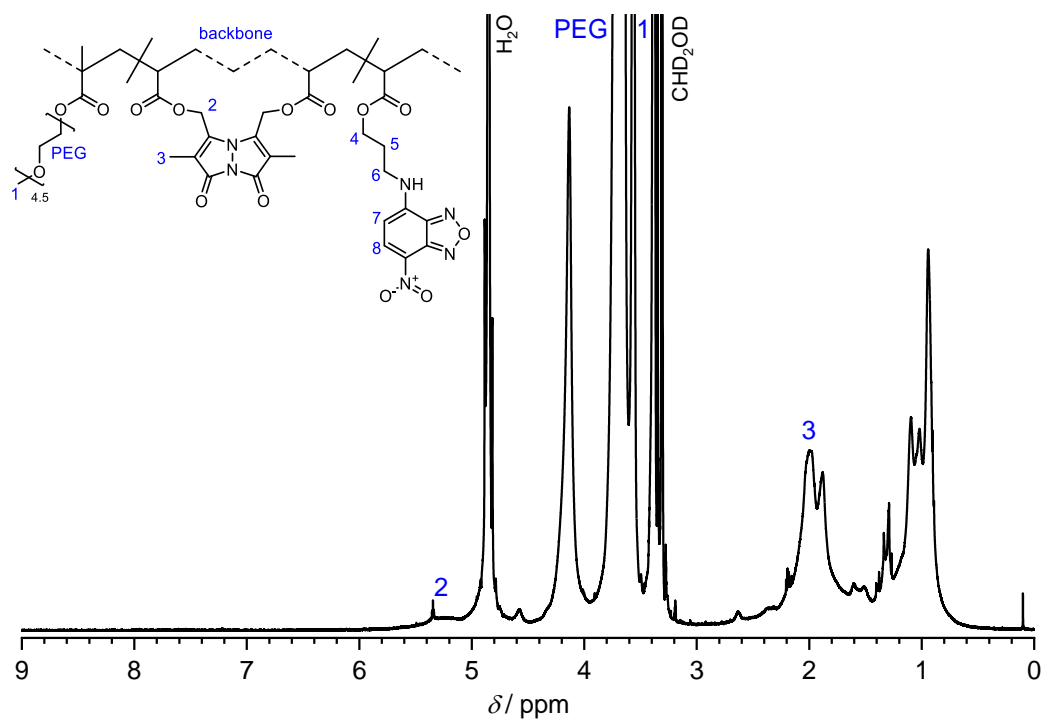


Figure 128: ^1H NMR spectrum of NBD post-functionalized and bimane cross-linked poly(MPEGMA-co-AA) recorded in CD_3OD and assigned resonances (**SCNP5**).